RESEARCH ARTICLE

DOI: 10.54926/jnamt.2025.247

J Nav Architect Mar Technol 2025;227(1):1-21

A Comprehensive CFD Analysis of Tandem Foils With and Without Ground Effect

Mehmet Delikan, Şakir Bal

İstanbul Technical University Faculty of Naval Architecture and Marine Sciences, Department of Naval Architecture and Ocean Engineering, İstanbul, Türkiye

To cite this article: M. Delikan, and Ş. Bal. A comprehensive CFD analysis of tandem foils with and without ground effect. *J Nav Architect Mar Technol*. 2025;227(1):1-21.

Received: 12.11.2024 - **Revised:** 10.02.2025 - **Accepted:** 05.03.2025 - **Publication Date:** 06.05.2025

Abstract

The flow dynamics and performance of tandem foils, both with and without ground effect (GE), continue to present challenges that are critical to understanding and optimizing aero/hydrodynamic systems, particularly for applications in next-generation wing-in-ground (WIG) effect vehicles, sailing yachts, and hydrofoil vessels. The performance of foils in GE (IGE) versus out of GE has not been extensively compared. This comprehensive study investigates the aero/hydrodynamic performance and flow dynamics of tandem foils using NACA 4412 section at moderate Reynolds number. To isolate the effects of spacing and ground clearance (H), both foils were set at a fixed angels of attack to negate the influence of decalage angle. The design variables examined include horizontal and vertical spacing between the foils, as well as H. Performance comparisons in both GE and out-of-GE conditions were presented, focusing on lift-to-drag ratio, lift and drag, and foil-to-foil interaction dynamics. Numerical simulations were conducted using the finite-volume method to solve the incompressible Reynolds-averaged-Navier-Stokes equations with the shear-stress transport k-ω turbulence model with gamma-transition model. Results indicate that the superiority of tandem foils is highly configuration-dependent. IGE, tandem foils exhibit a significantly higher lift-to-drag ratio than in out-of-GE conditions, where their performance is often lower than that of isolated foils. Positive G between the foils were found to enhance aero/hydrodynamic efficiency, suggesting that optimizing the gap distance can lead to performance improvements. The stagger distance plays a critical role in altering the static pressure distribution due to foil-to-foil interactions. Notably, under certain interference conditions, the fore foil can experience reduced drag or even generate thrust, offering potential advantages for specific aero/hydrodynamic applications. These findings provide new insights into the behaviour of tandem foils and may inform the design of next-generation WIG vehicles, hydrofoil vessels, tandem sails, and other systems where foil interactions are significant.

Keywords: Ground effect, lift, drag, interference effect, RANS, tandem foil

1. Introduction

Ground effect (GE) and finite depth phenomena have been the subject of extensive research, with the primary goal of understanding the complex flow dynamics and hydrodynamic responses of lifting surfaces when operating in close proximity to a boundary such as the ground or water surface. This comprehensive study investigates how the GE influences vehicle performance, where the reduced distance to the surface enhances the lift and modifies the overall aero/hydrodynamic behaviour [1-3]. The flow characteristics and hydrodynamic behaviour in GE (IGE) are distinct from those encountered in freestream flow conditions, necessitating further analysis.

Address for Correspondence: Mehmet Delikan, İstanbul Technical University Faculty of Naval Architecture and Marine Sciences, Department of Naval Architecture and Ocean Engineering, İstanbul, Türkiye
E-mail: delikan22@itu.edu.tr
ORCID ID: orcid.org/0009-0009-5244-4731

Copyright© 2025 The Author. Published by Galenos Publishing House on behalf of UCTEA Turkish Chamber of Naval Architects and Marine Engineers. Licensed under a Creative Commons Attribution-NonCommercial-NoDerivatives 4.0 (CC BY-NC-ND) International License

While conventional aircraft experience GE during critical phases such as take-off and landing, wing-in-ground (WIG) vehicles are specifically designed to leverage this phenomenon to achieve higher lift-to-drag ratios by flying just above the water surface. These vehicles combines the naval architecture and aerospace engineering principles, enabling them to operate efficiently in a hover-like state over the water [4]. By bridging the operational gap between ships and airplanes, WIG vehicles offer a compelling transportation solution that combines the fuel efficiency and higher cruising speeds of aircraft with the stability and endurance of marine vessels [5]. Compared to conventional craft, WIG vehicles exhibit enhanced aerodynamic and hydrodynamic efficiency, which contributes to significant improvements in fuel economy and operational speed. This combination of benefits has sparked growing international interest and investment in the development of WIG technology, driving further research into the aerodynamics and hydrodynamics of GE to optimize vehicle design and performance.

1.1. Literature Survey

The impact of ground proximity on aero/hydrodynamic performance has been explored experimentally since the early 20th century. One of the earliest methods was the fixed ground simulation, where the ground is represented by a stationary surface, such as a wind tunnel bottom [6]. A second approach, the image method, involves using two identical wind tunnel models, one inverted, to create a symmetrical flow about an imaginary ground plane [7]. However, this method mainly simulates inviscid GE and presents challenges in achieving perfect symmetry. The most precise technique for modelling GE is the moving belt system, which simulates the relative motion of the ground by running a belt at freestream velocity, though it comes with practical difficulties, including vibrations and belt flatness [8]. Werle's work in the 1960's further highlighted the significant differences between these methods, particularly in flow separation and vortex behaviour under various conditions [9].

GE phenomena are generally classified into two categories: two-dimensional (2D) chord-dominated GE and three-dimensional (3D) span-dominated GE [10]. In 2D chord-dominated GE, the proximity to the ground increases the pressure on the lower surface (pressure side) of the foil, resulting in a significant enhancement in lift, an improved performance of foil. In contrast, for 3D wings, GE causes the outward displacement of wingtip vortices, which reduces downwash and consequently lowers induced drag.

Previous studies have extensively explored 2D GE at low to moderate angles of attack (AoA). For instance, Hsiun and Chen [11] investigated a NACA 4412 foil at 5° and 10° AoA and found that lift increased as ground clearance (H) decreased, peaking at specific height-to-chord ratios. However, at very close distances, lift dropped sharply due to recirculation zones and increased adverse pressure near the ground. Similarly, Chun [12] used numerical simulations on the NACA 4412 and Clark Y foils, demonstrating that lift and pitching moment predictions were similar for both static and moving ground models, though drag was lower in the fixed-ground setup.

An investigation was performed to assess the aerodynamic behaviour of the NACA 4412 foil under GE, using a moving belt apparatus to replicate ground proximity. Flow data were gathered via particle image velocimetry at a Reynolds number (Re) of 3×10^5, with AoA ranging from 0° to 10°. Findings indicated that at smaller AoA ($\alpha\leq4°$), the lift coefficient (C_L) tended to decrease as the foil neared the simulated ground. This outcome was attributed to an elevated pressure along the lower surface and a reduction in suction on the upper surface. Conversely, at larger angles ($\alpha\geq6°$), an increase in C_L was observed due to substantial pressure buildup beneath the foil. Furthermore, drag coefficient (C_D) values were noted to rise with reduced H, particularly at higher angles, influenced by the specific contour of the passage between the foil and the ground, which impacted the lift force [13].

An investigation was undertaken to study the WIG effect using a Tyrrell 026 Formula 1 car's front wing in a wind tunnel. Their findings demonstrated that aerodynamic performance was highly dependent on ride height, with significant changes noted as the wing moved closer to the ground. In particular, they noted the onset of boundary layer separation near the trailing edge, which became more pronounced at reduced ride heights. The reduction in aerodynamic force was attributed to a balance between minimal downforce loss from flow separation and increased velocity on the lower surface at reduced ride heights [14].

Qu et al. [15], conducted a numerical study examining the aerodynamic properties of NACA 4412 foil IGE while simulating a moving ground surface at a Re of $6\text{x}10^6$. The investigation encompassed a wide range of AoA, from -4° to 20°, and H ratios (H/c) ranging from 0.05 to infinity. They found that, for AoA between 2° and 12°, the C_L initially decreased as the foil approached the ground, followed by a significant increase in lift at very close proximity (region I). This behaviour was linked to a reduction in the effective AoA, which raised the pressure on the suction side while lowering it on the lower surface. Additionally, a blockage effect caused further pressure buildup on the lower surface. In region II, the reduction in effective AoA had a stronger influence than the blockage effect, causing a decrease in lift. However, as the foil transitioned into region I, the blockage

effect became more pronounced, taking precedence and resulting in a substantial lift increase. Moreover, at elevated AoA, the transition from region II to region I occurred at smaller Hs. For AoA greater than 12°, airflow separation became more pronounced, expanding in response to the increasingly adverse pressure gradient as H decreased. This condition caused a notable increase in pressure on the upper surface (suction side), resulting in reduced lift across all Hs, with C_L decreasing as the foil close to the ground. Stall conditions were observed to occur earlier and more abruptly at lower H/c values due to the intensified adverse pressure gradient close to the ground.

Hayashi and Endo [16], reported an increase in the separation region during their experimental and numerical investigations of the wake behind a NACA 4412 foil operating at 15° AoA (post-stall) and a Re of $3.2x10^5$. Their findings indicated that as the foil approached the ground, the wake region expanded significantly, resulting in an earlier onset of stalling compared to scenarios out of ground effect (OGE). These observations aligned with those noted by Qu et al. [15].

As previously mentioned, the ground conditions in experimental setups can vary considerably. In addition to various experimental studies examining these ground types, numerous numerical analyses have been conducted. A study by Barber et al. [17] explored four distinct ground conditions to assess their effects on aerodynamic performance. Beyond the traditional stationary and moving ground conditions, the researchers also investigated two additional models: A "slip" boundary condition, defined by the absence of shear stress at the boundary, and an "image" ground condition, which involved simulating two identical bodies reflected across a symmetry plane to mimic the effects of the ground.

In addition to viscous flow solvers, previous research has examined GEs on foils operating above free surfaces. While many studies have investigated various ground conditions, including fixed and moving boundaries, a notable body of work focuses specifically on foils above free surfaces [18-23]. Iterative numerical methods have been extensively employed to evaluate the performance of foils and wings in close proximity to free surfaces. The Iterative Boundary Element Method (IBEM) is used to predict the hydrodynamic behavior of WIG effect vehicles flying above a free water surface. Originally designed for submerged hydrofoils, IBEM has been extended to account for WIG-specific conditions. The method divides the problem into two parts: One for the wing and wake effects, and one for the free surface. These parts interact iteratively using Green's theorem. Both components are modeled with panels that have dipole and source distributions, enabling analysis of how factors like Froude number, H, and wing geometry affect the lift and drag forces on WIG vehicles [18]. Bal [19] adapted a method initially designed for submerged cavitating hydrofoils to analyse 2D foils and 3D wings above free water surfaces. Their perturbation potential formulation effectively resolved interactions between the foil and the free surface, yielding strong agreement with experimental C_L data for NACA 0004 and NACA 0015 foils across various Froude numbers and clearance ratios. The study highlighted that higher Froude numbers generally enhanced aerodynamic loading on the foil, with free surface effects, particularly wave patterns, becoming more pronounced at reduced clearance ratios.

Building on this foundation, Dogrul and Bal [20] applied an IBEM combined with a finite volume approach to predict the aerodynamic performance of a 3D wing steadily moving above a free water surface. Their findings showed that the free surface significantly increased aero/hydrodynamic loading compared to unbounded flow, particularly at smaller clearance ratios. They also noted the development of a Kelvin wave pattern on the free surface, with an increase in the wing aspect ratio further causing an increase in loading. These insights suggest that unsteady and viscous effects are critical factors in the aerodynamic design of wings and foils operating near free surfaces, warranting further investigation in future work.

Kinaci and Bal [21] utilized a similar approach to investigate a foil near the ground under inviscid flow conditions, comparing solid ground and free surface scenarios. Their validation against experimental data revealed that lift and C_Ds increased with decreasing clearance ratios due to GEs, while wave heights and wavelengths on the free surface grew larger with higher Froude numbers, emphasizing the importance of these effects in design considerations.

Bal [22] presents an analytical model using a lumped vortex element to calculate the C_L of a 2D flat plate flying over a free water surface. The study focuses on high-speed conditions and applies potential flow theory, satisfying boundary conditions both on the plate and the water surface. Results show that the C_L is significantly affected by the Froude number, clearance height, and AoA, influencing wave formation on the surface. This work provides insights into the performance of WIG marine vehicles, such as racing boats.

Bal [23] presents an analytical solution for the hydrodynamics of a 2D flat plate moving beneath a free surface in finite depth water. Using a lumped vortex element and the method of images, the study calculates the C_L and analyses wave deformation. Key findings show that lower Froude numbers increase lift, while higher Froude numbers and shallower depths result in larger wave heights. The study also highlights the influence of finite depth and AoA on the hydrodynamic performance of submerged bodies, providing valuable insights for marine applications.

Despite the extensive body of research on GE in single-wing configurations, relatively little attention has been devoted to tandem wing setups, particularly in the context of GE. The benefits of tandem wing designs have been recognized since the early stages of aviation development. From Prandtl's early biplane theory to advanced Navier-Stokes simulations, studies have consistently highlighted the aerodynamic advantages of tandem wings. However, it is important to note that there is no universally applicable design criterion for all tandem configurations. Each configuration demands a comprehensive analysis that considers the mission requirements, specific size and weight limitations, as well as the desired aerodynamic characteristics.

Tandem foil configurations hold significant promise for enhancing the performance of both sail and hydrofoil vessels by improving lift, reducing drag, and optimizing overall hydrodynamic efficiency. In sail vessels, tandem foils can be employed to distribute aerodynamic loads more evenly, improving stability and increasing sailing speed. By adjusting the lift-to-drag ratio, these configurations help mitigate leeway drift and reduce the risk of capsizing, particularly under varying wind and sea conditions. This has been particularly relevant in competitive yacht racing, where optimizing the aerodynamic efficiency of the vessel is paramount. For instance, in America's Cup racing yachts, tandem or multi-element foils have been explored to enhance upwind and downwind performance through reduced induced drag and improved load distribution [24].

In hydrofoil vessels, tandem foil configurations are beneficial for maintaining stability and efficiency at high speeds. By lifting the hull out of the water, hydrofoil boats reduce drag and increase fuel efficiency. Tandem foils improve lift distribution between the fore and aft foils, which leads to enhanced stability, particularly in rough sea conditions, while reducing wave-making resistance [25,26]. This configuration also helps mitigate issues related to cavitation at high speeds, a common problem in hydrofoil systems. As a result, tandem hydrofoil arrangements are increasingly being considered for high-speed ferries and naval applications where efficiency, stability, and safety are critical [27].

The potential of tandem foils to contribute to green shipping initiatives is also being explored, as these configurations can significantly enhance energy efficiency in marine vessels. By reducing drag and improving lift, tandem foils offer an opportunity to design faster and more sustainable ships, aligning with current environmental objectives. These benefits, along with future developments in adaptive or morphing foil technologies, position tandem foil configurations as a promising area of continued research and innovation in marine technology [28].

Khan and Mueller [29] examined the influence of the vortical wake generated by a finite-span canard on the aerodynamic performance of a low Re wing, emphasizing that the position of the canard's tip vortex and wake significantly alters wing performance. Building on prior research, Rokhsaz [30] employed vortex panel methods to analyse tandem configurations of NACA 62-215 and NACA 0012 foils, confirming the aerodynamic benefits identified by earlier studies while elucidating the underlying mechanisms of drag reduction.

Fanjoy and Dorney [31] explored the aerodynamic characteristics of tandem foil systems, observing that reducing the horizontal distance between foils leads to an increase in drag on the aft foil, while the fore foil exhibits improved aero/hydrodynamic efficiency through an expanded drag bucket and a higher performance. In a comprehensive investigation of turbulent flow around tandem foils in a T-configuration, Faure et al. [32] focused on high AoA at moderate Re. Their study detailed how the wake generated by the fore foil affects the aerodynamic performance of the aft foil, including changes in C_L and vortex dynamics. Their statistical analysis of the velocity field revealed critical features such as wake velocity deficits, recirculation zones, and turbulence intensities that play a key role in describing the flow characteristics within the detached region.

Further advancing this field, Yin et al. [33] conducted a study on the aero/hydrodynamic performance of tandem NACA 0012 foils operating in IGE case at ultra-low Re (Re=500). Their findings demonstrated that tandem configurations provide superior aerodynamic performance compared to single foil setups, especially when vertical distance between foils is positive. Their analysis also highlighted the influence of horizontal and vertical distance between foils, and ride height (H/c) on flow dynamics, including the formation of laminar separation bubbles. These bubbles, observed within the wake of the fore foil, were found to induce oscillations in the flow, ultimately impacting the lift and drag of the aft foil and offering insights into optimizing aerodynamic efficiency.

1.2. Objectives of the Study

Despite considerable research on the aero/hydrodynamics of 2D foils, there is a critical gap in understanding the flow characteristics of tandem foils operating IGE, particularly at moderate Re. This study seeks to address this gap by conducting a comprehensive numerical investigation of NACA 4412 foils arranged in a tandem configuration near a moving ground. By fixing the AoA at $\alpha=4°$ for both foils, the study eliminates decalage effects, allowing for a focused analysis at $Re=3\times10^5$.

This extensive study methodically examines the impact of horizontal and vertical spacing between foils, as well as ride

height (H/c), on the lift, drag, and overall performance of the tandem configuration. The findings are benchmarked against baseline data from isolated foil cases to assess the impact of foil-to-foil interactions. In addition, the aero/hydrodynamic performance of the tandem foils is evaluated under both GE and non-GE conditions. This approach provides valuable insights into how ground proximity affects aero/hydrodynamic efficiency and the overall aero/hydrodynamic behaviour of the tandem system.

2. Model Geometries and Parameter Definition

This study examines the aero/hydrodynamic efficiency of NACA 4412 foils in tandem arrangements, considering both IGE and OGE conditions. The relative positioning of the foils is defined by three key parameters: horizontal separation (S), vertical offset (G), and H. S is characterized as the distance from the trailing edge of the front foil to the leading edge of the rear foil. G indicates the vertical distance between the trailing edges of both foils, with positive values signifying that the front foil is positioned higher than the rear foil. H is defined as the vertical distance from the trailing edge of the front foil to the ground surface. These parameters, as illustrated in Figure 1, are critical in analysing the interaction effects and overall hydrodynamic efficiency of the tandem foil configuration.

NACA 0012 foil was validated in case of OGE in the thesis [34], and the NACA 4412 foil was similarly validated in the conference paper [35]. As these validations are documented in those works, they are not repeated here. Upon successful validation, twenty tandem configurations are investigated, encompassing scenarios both with and without the influence of GE. Table 1 provides an overview of the parameters for these configurations.

3. Solution Method

The unsteady, incompressible Reynolds-averaged Navier-Stokes (RANS) equations were employed in the analyses. In Cartesian tensor form, these equations can be represented as follows:

$$\frac{\partial U_i}{\partial x_i} = 0 \tag{1}$$

$$\rho \frac{\partial (U_i)}{\partial t} + \rho \frac{\partial (U_J U_i)}{x_j} = -\frac{\partial P}{\partial x_i} + \frac{\partial}{\partial x_j}\left(\mu S_{ij} - \overline{\rho \acute{U}_i \acute{U}_j}\right) \tag{2}$$

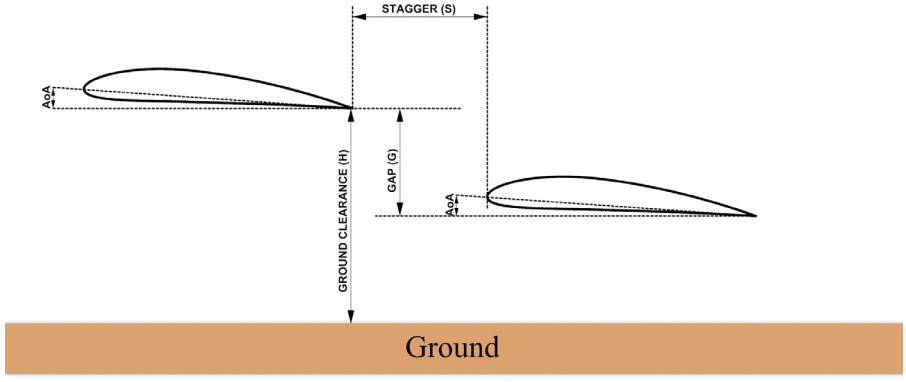


Figure 1. Geometric configuration of foils in tandem case.

AoA: Angle of attack

Table 1. Test cases.

Case no	Stagger distance (S)	Gap (G)	Ground clearance (H)	Case no	Stagger distance (S)	Gap (G)	Ground clearance (H)
Case 1	0.25c	-0.4c	0.4c	Case 11	0.25c	-0.4c	-
Case 2	0.50c	-0.4c	0.4c	Case 12	0.50c	-0.4c	-
Case 3	1c	-0.4c	0.4c	Case 13	1c	-0.4c	-
Case 4	2c	-0.4c	0.4c	Case 14	2c	-0.4c	-
Case 5	4c	-0.4c	0.4c	Case 15	4c	-0.4c	-
Case 6	0.25c	0.4c	0.8c	Case 16	0.25c	0.4c	-
Case 7	0.50c	0.4c	0.8c	Case 17	0.50c	0.4c	-
Case 8	1c	0.4c	0.8c	Case 18	1c	0.4c	-
Case 9	2c	0.4c	0.8c	Case 19	2c	0.4c	-
Case 10	4c	0.4c	0.8c	Case 20	4c	0.4c	-

in this context ρ, μ, U, P and Ú refer to the fluid's density, dynamic viscosity, average velocity, mean static pressure, and fluctuating velocity, respectively. S_{ij} term in equation (2), corresponds to the mean strain rate tensor, while the expression $-\rho\overline{Ú_I Ú_j}$ accounts for the stresses resulting from turbulent fluctuations, known as Reynolds stresses, with the overbar signifying a time-averaged value. ANSYS Fluent was utilized for the simulations, with the k-ω Shear Stress Transport (SST) turbulence model [36], grounded in the Boussinesq approximation [37]. This approach incorporates two extra transport equations for turbulence kinetic energy and its dissipation to capture the effects of Reynolds stresses in the RANS equations.

The RANS and turbulence transport equations were solved using the finite volume method with the coupled algorithm for pressure-velocity coupling. A second-order upwind scheme was used for flow simulation, while PRESTO and first-order implicit schemes were applied for pressure and transient formulations, respectively. In unsteady simulations, the time step was set for a CFL number of 1. Convergence was confirmed with scaled residuals below 10^{-5}, and the stability of aero/hydrodynamic forces was monitored. Simulation accuracy was verified through mesh quality assessments and comparison with experimental data.

4. Verification and Validation of NACA 4412 IGE

2D flow characteristics around the foil were analysed through computational fluid dynamics (CFD) simulations performed using ANSYS fluent. The unsteady RANS equations were resolved with a coupled solver, under the assumption of constant fluid density. Convergence was successfully attained across all simulations, with residuals decreased to a threshold of 10^5, thereby validating the accuracy and reliability of the computational solutions.

The simulations implemented the k-ω SST turbulence model with gamma transition model. The computational domain was specifically designed to extend 20 chord lengths (20c) in front of the foil's leading edge, 25 chord lengths behind the trailing edge, and to a vertical extent of 20c.

GE aerodynamics were investigated through both steady and unsteady CFD simulations, building upon insights from prior studies [38,39]. The results indicated that unsteady simulations, while requiring greater computational resources, produced findings that exhibited closer alignment with experimental data. In contrast, steady simulations demonstrated higher error margins, particularly regarding the C_D across all ride height (H/c) ratios. The ride height (H) refers to the vertical distance between the trailing edge of the foil and the ground surface, consistent with established conventions in the literature [40]. This alignment facilitates meaningful comparisons with existing research.

A second-order upwind scheme was employed for the unsteady flow simulations surrounding the foil, with the exception of pressure and transient formulations, which utilized the PRESTO! scheme and a first-order implicit method, respectively. The time step size for the unsteady simulations was selected to ensure CFL number of 1. The accuracy of the simulations was rigorously validated through comprehensive assessments of mesh quality, grid independence, and by comparing the resulting lift and drag against established experimental data.

Due to the significant impact of ground proximity on flow pattern around the foil, a refined mesh was implemented in the area between the foil and the ground to accurately resolve the steep flow gradients. The foil surface was subjected to no-slip boundary conditions, ensuring an average y+ value close to 1 for precise boundary layer resolution.

The conditions applied for the simulation were specified as: left side was set as a velocity inlet, the right side served as a pressure outlet, and the upper boundary was configured as a symmetry plane. The moving ground condition, aligned with the incoming flow velocity, was implemented to effectively replicate the GE. This configuration resulted in a chord Re of $3x10^5$, aligning with the experimental conditions reported by Ahmed et al. [13].

The validation of the simulations for the baseline NACA 4412 foil IGE was achieved by comparing the computed C_L and C_D with experimental wind tunnel data from Ahmed et al. [13]. A GCI study was conducted at a 4-degree AoA and a ride height (H/c) was 0.15, employing the k-ω SST turbulence model with the gamma transition model. To assess numerical uncertainty and determine an appropriate grid resolution, a GCI analysis was performed following Roache's methodology. Three distinct grids with varying levels of refinement were employed: the coarsest mesh (G), the moderately refined mesh (H), and the finest mesh (I), as shown in Figure 2. The results presented in Table 2 indicate that the relative errors (e_L) and (e_D) and GCI values between mesh configurations H and I were sufficiently low, confirming grid independence. Based on this analysis, mesh H was selected for all subsequent validation runs to ensure a balance between computational efficiency and numerical accuracy.

The simulations employed the k-ω SST model, with a gamma transition, to evaluate the performance characteristics of the NACA 4412 foil. A systematic comparison was conducted against experimental data collected at heights ranging from 15% to 80% of the chord length above a moving ground surface, all while maintaining a constant AoA of 4 degrees. Figure 3 displays a comparison of the calculated C_L and C_D with the measured values. The k-ω SST model

demonstrated a remarkable accuracy in predicting both lift and drag, effectively capturing the dynamics associated with the laminar-turbulent transition. Additionally, the surface pressure distributions confirmed the model's effectiveness in accurately predicting the occurrence of a laminar separation bubble on the upper surface of the foil, consistent with the results described by Ahmed et al. [13]. The numerical results align with those presented by Qu et al. [15], providing further validation of the laminar separation bubble's presence. Consequently, the findings of this study are consistent with the established literature, underscoring the robustness of the modelling approach adopted.

Figure 3 displays a comparative analysis between the findings of this study and the corresponding experimental results. Although employing high-fidelity CFD techniques, such as detached-eddy simulation or large-eddy simulation, could potentially mitigate these discrepancies, computational resource limitations constrain the breadth of cases explored within this investigation. The average-C_D error recorded within the range of 0.15 to 0.8 H/c is 3.5%, while the average C_L error for the same interval is 4.9%. The strong correlation observed in Figures 3 and 4 between the numerical outcomes and Ahmed's experimental findings validates the effectiveness of the employed methodology, underscoring its adequacy for accurately capturing the relevant flow dynamics.

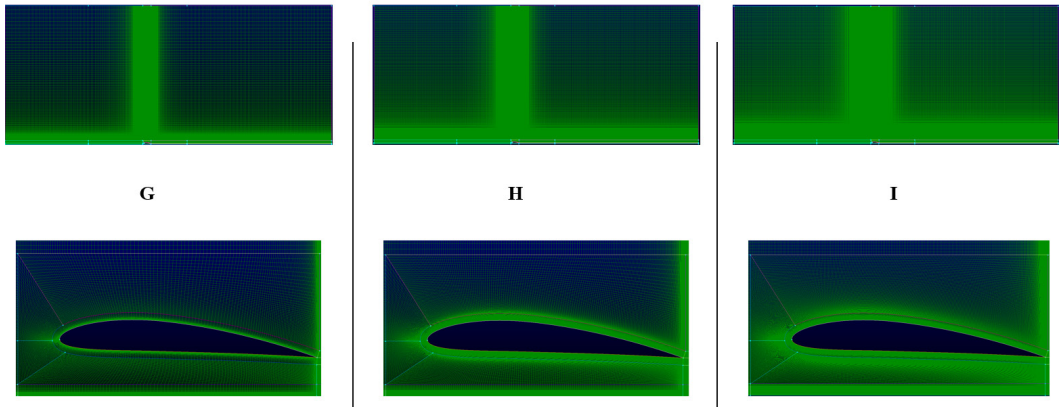


Figure 2. Grid refinement for NACA 4412 in ground effect.

Table 2. Grid convergence index results for NACA 4412 in ground effect.

Case	Mesh name	C_L	C_D	e_L	e_D	GCI_L	GCI_D	Average y+	Cell number
NACA4412 AoA=4° H/c=0.15	**G**	0.894	0.01145	-	-	-	-	0.89	248860
	H	0.929	0.00992	0.03753	0.15389	0.01073	0.04401	0.94	500498
	I	0.935	0.00975	0.00694	0.01754	0.00198	0.00276	0.87	1006946

AoA: Angle of attack, C_D: Drag coefficient, C_L: Lift coefficient, GCI: Grid convergence index, G: Coarsest mesh, H: Moderately refined mesh, I: Finest mesh

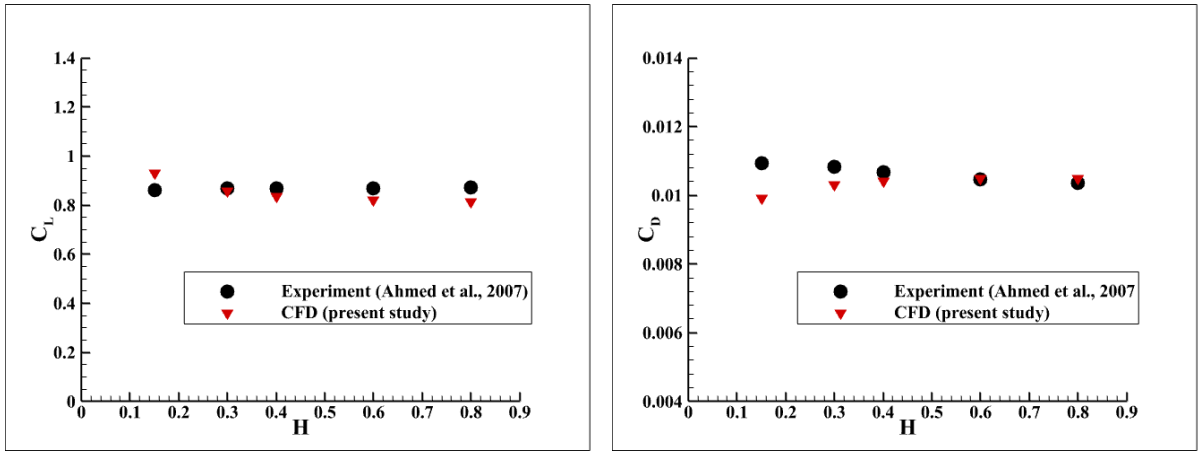


Figure 3. Comparison of results of present study and experimental results.

CFD: Computational fluid dynamic, C_D: Drag coefficient, C_L: Lift coefficient

5. Computational Domain and Mesh Configuration for Tandem Foils

In the simulations of two tandem foils, both assumed to have a NACA 4412 profile, the AoA is fixed at 4°, indicating no decalage between the foils. The Re is maintained constant at $3x10^5$.

5.1. Tandem Foils OGE Case

Figure 5 illustrates the computational domain and mesh arrangement for the tandem foils operating in an unbounded flow domain. The domain covers 20 chord lengths (20c) starting from the front foil's leading edge to the left side and extends 25c from the aft foil's trailing edge to the right side, with a total height of 40c. Velocity inlet conditions are applied on the left, top, and bottom sides, while a pressure outlet is set on the right side.

5.2. Tandem Foils in IGE Case

In the analysis of tandem foils operating within GE, the NACA 4412 foil profile is employed with a fixed AoA of 4° and a Re of 3×10^5. The computational domain for these simulations is depicted in Figure 6. Here, the inlet boundary is positioned 20c from the leading edge of the fore foil, while the outlet boundary is 25c from the trailing edge of the aft foil, with the total domain height set at 20c. The boundary conditions implemented include a velocity inlet on the left side, a symmetry condition along the upper boundary, and a pressure outlet on the right. The bottom boundary, which simulates the ground, is modelled as a moving wall to effectively reduce the formation of a viscous boundary layer. Furthermore, the surface of the foil, characterized by the NACA 4412 profile, is treated as a no-slip wall, achieving an average y+ value close to 1.

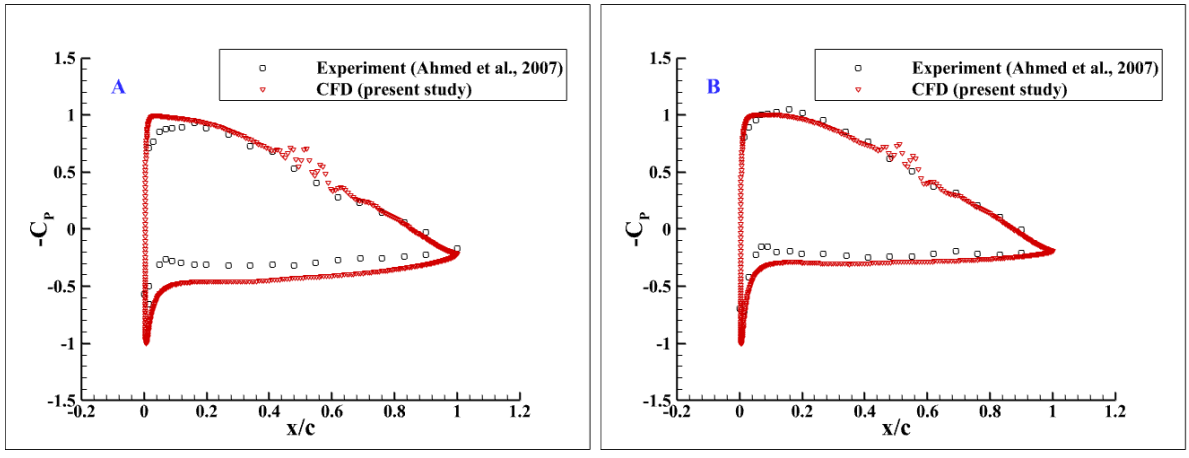


Figure 4. Pressure distribution comparison. **A)** H/c=0.15, **B)** H/c=0.40.

CFD: Computational fluid dynamic, C_p: Pressure coefficient

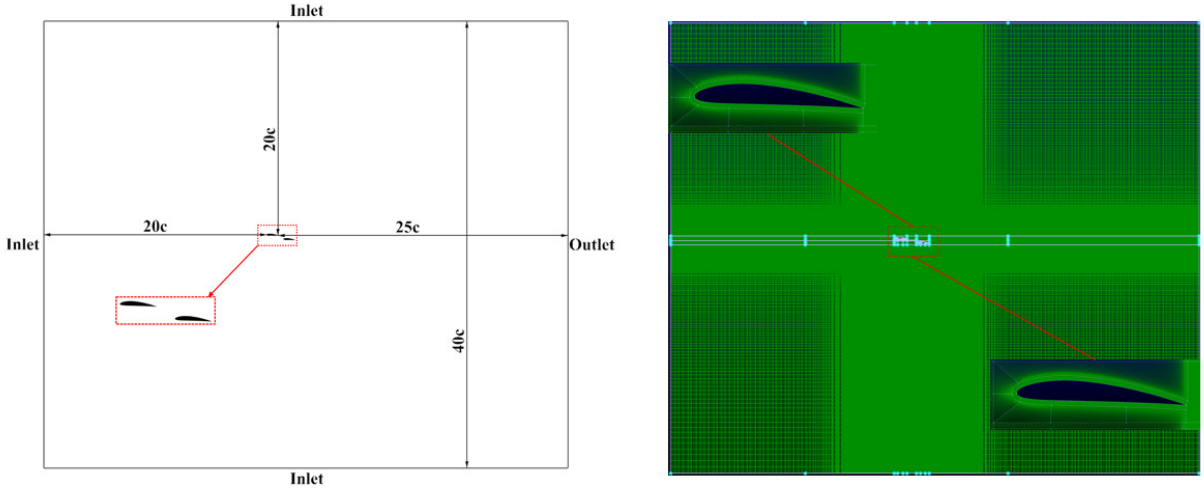


Figure 5. Computational domain and mesh configuration for the tandem foils outside of ground effect.

5.3. Meshing and Simulation Parameters for Tandem Cases

Figures 5 and 6 illustrate the computational mesh, featuring increased resolution near the foil surfaces to accurately capture velocity gradients, as well as additional refinement in the wake region to enhance flow field resolution. The mesh configuration supports the numerical approaches outlined in section 4, ensuring effective turbulence modelling and numerical stability. These figures provide a visual representation of the computational framework that facilitates the detailed analysis of the flow characteristics around the foils.

6. Results and Discussion

The comprehensive findings of present study are organized into three sub-sections to enhance clarity and depth of analysis. Section 6.1 presents a comprehensive examination of a single foil operating IGE, emphasizing the intricate flow dynamics associated with this configuration. Section 6.2 offers an in-depth analysis of selected scenarios involving the foil operating OGE, providing a meticulous assessment of the flow characteristics in these instances. Finally, section 6.3 focuses on a thorough evaluation of specific cases within GE, similarly detailing the related flow behaviour and aero/hydrodynamic performance.

6.1. Single Foil IGE

The analysis of the NACA 4412 foil IGE was conducted at a 4-degree AoA across a range of ride heights. As demonstrated in previous study [15], the pressure distribution of the airflow between the lower surface of the foil and the ground is critical in influencing the WIG effect. Figure 7 illustrates the airflow passage, which can be classified as either convergent or divergent. In instances of a convergent passage, where the inlet area (A1) exceeds the outlet area (A2), the airflow accelerates, leading to a decrease in static pressure, in accordance with the venturi effect. This phenomenon underscores the importance of flow geometry in optimizing the aerodynamic performance of foils operating IGE.

Figures 8 and 9 show the distribution of the pressure coefficient (C_p) for the NACA 4412 foil at different H/c. Figure 8 offers a graphical representation of the C_p along the foil, while Figure 9 presents a contour plot that delineates the pressure distribution over the foil's surface.

As illustrated in Figure 8, when the foil moves closer to the ground, the stagnation point shifts toward the trailing edge, increasing pressure on the lower surface. Notably, pressure on the suction surface, particularly close to the leading edge, rises due to GE. The maximum negative pressure occurs near this leading edge area on the suction side, where the slower airflow reduces suction pressure.

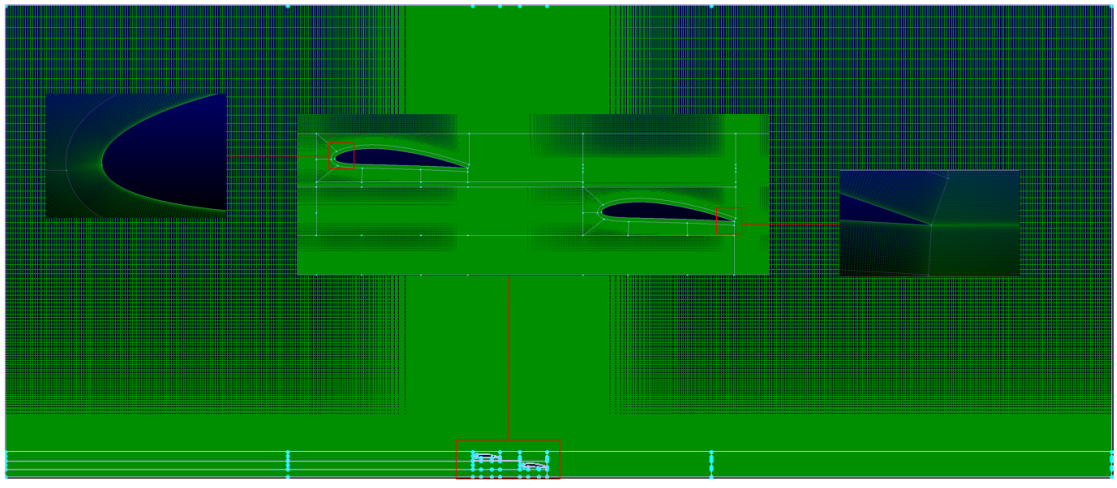


Figure 6. Computational mesh for tandem NACA 4412 foils in ground effect.

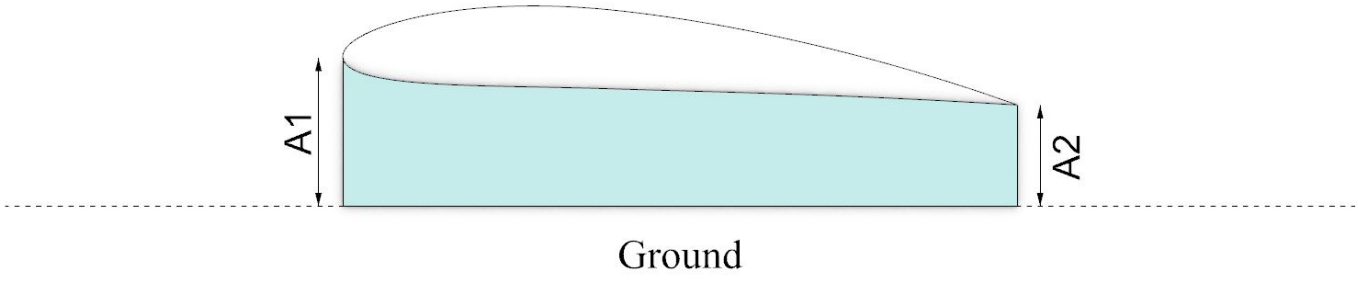


Figure 7. A convergent-divergent flow passage in proximity to the ground.

Conversely, the highest pressure on the lower surface is found near the leading edge at the stagnation point, where an increase in flow velocity corresponds to a reduction in static pressure. The fluid velocity beneath the foil significantly diminishes as it nears the ground. When the ride height (H/c) is reduced, the C_P correspondingly increased, indicating that the rise in static pressure beneath the foil consistently surpasses the reduction in suction pressure above it. This observation suggests that GE positively influences the C_L. Furthermore, the position of the positive pressure peak, corresponding to the stagnation point, shifts toward the trailing edge at reduced ride heights, a phenomenon that can

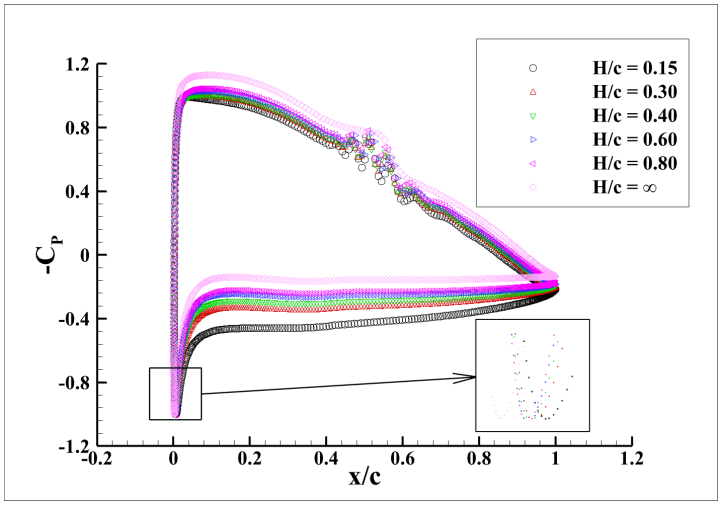


Figure 8. Pressure distribution across varying ground clearances.

C_P: Pressure coefficient

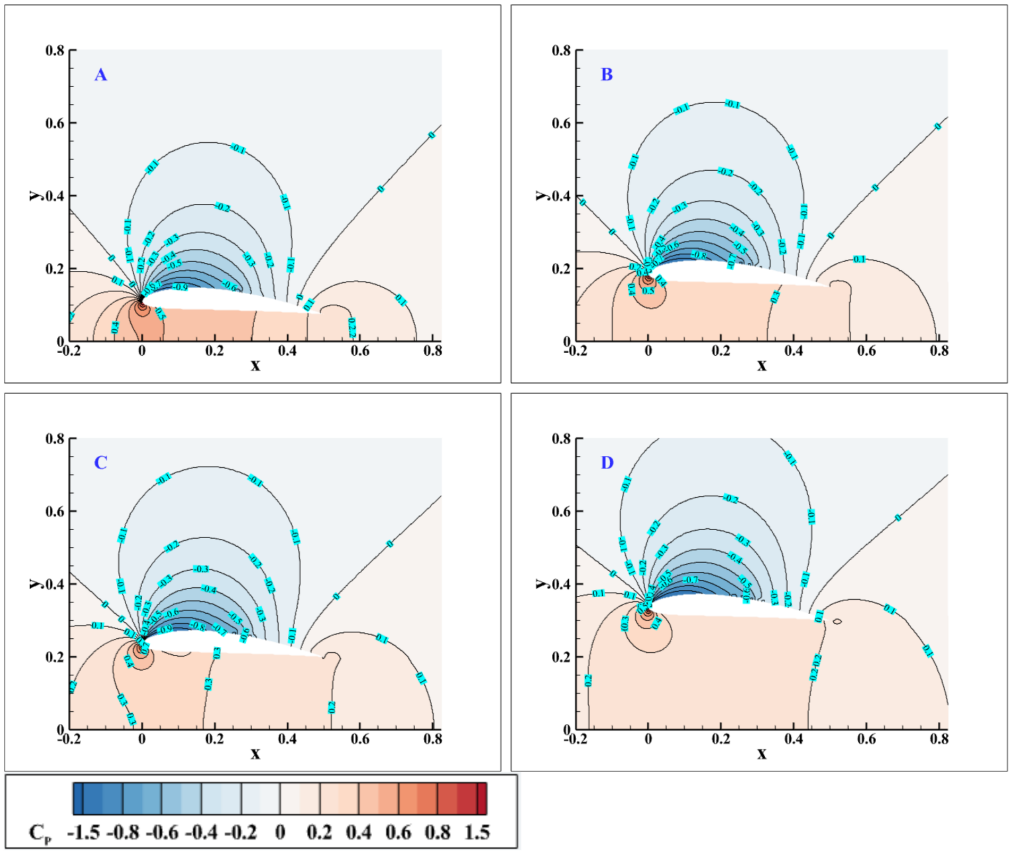


Figure 9. Comparison of pressure distribution for different ground clearances; **A)** H/c=0.15, **B)** H/c=0.30, **C)** H/c=0.40, **D)** H/c=0.60.

C_P: Pressure coefficient

be ascribed to the characteristics of the convergent-divergent flow region illustrated in Figure 7.

In the present study, Figure 8 reveals that the separation bubble is evident on the upper surface of the foil across all tested H/c, as well as in conditions where the foil is OGE. Notably, the bubble's position relative to the chord length (x/c) remains unchanged, irrespective of the proximity to the ground. As previously discussed, the decrease in airflow velocity over the upper surface of the foil, induced by GE, results in a reduction in suction pressure. This observation suggests that GE adversely affects the suction pressure on the upper surface of the foil. Consequently, the C_P curve for the suction side experiences a downward shift, while the position of the separation bubble remains unaffected.

As the H diminishes, the convergence-to-divergence ratio increases, resulting in more pronounced airflow acceleration or deceleration. This effect is illustrated in the pressure distribution for varying height-to-chord (H/c) ratios, as depicted in Figure 8. Furthermore, the influence of ground proximity on pressure distribution is clearly represented in Figure 9.

Figure 10 demonstrates the existence of a separation bubble on the upper surface of the foil, a physical phenomenon that aligns with the observations made by Winslow et al. [41]. Their research indicated that for AoA ranging from 0° to 8°, the separation bubble migrates from the trailing edge toward the leading edge, effectively altering the transition point from laminar to turbulent flow. However, this migration was not observed at higher Res, specifically at $Re=1\times10^6$.

Figure 11 illustrates the ratio of velocity magnitude to freestream velocity around a NACA 4412 foil operating at an AoA of 4° for various ride heights (H/c). As the foil approaches the ground, a notable decrease in velocity magnitude on its lower surface occurs, leading to a rise in static pressure beneath the foil.

The pressure distribution on the suction side of the foil exhibits a maximum negative pressure near the leading edge. This reduction in air velocity across the upper surface of the foil, attributed to GE, corresponds with a decrease in suction pressure. It appears that GE adversely impacts the suction pressure experienced by the foil. Conversely, the maximum static pressure on the lower surface of the foil is noted near the leading edge, especially at the stagnation point, where increases in flow velocity result in decreases in static pressure.

Furthermore, the fluid velocity close to ground significantly decreases beneath the foil. It is noteworthy that with a reduction in ride height (H/c), the C_P tends to increase. The augmentation of static pressure below the foil consistently exceeds the reduction in suction pressure above its upper surface. Thus, proximity to the ground is anticipated to positively contribute to the lift force C_L generated by the foil. Additionally, the proximity of the foil to the ground results in an expansion of the wake region, which suggests an increase in the pressure drag component.

To elucidate the observed reduction in streamline deflection within GE, we employ the mirror-image model. This theoretical framework introduces an imaginary foil positioned below the ground, effectively mirroring the real foil situated above. The real foil exhibits clockwise circulation, denoted as -Γ, while the image foil displays anticlockwise circulation, represented as Γ, as illustrated in Figure 12. The circulation generated by the image foil induces downwash in the upstream region and upwash in the downstream region, thereby significantly influencing the behaviour of streamlines in proximity to the ground [42].

IGE flow fields, the proximity of the ground and the induced flows from the image foil lead to a predominantly straight configuration of streamlines until they approach the foil closely. This phenomenon results in a more localized region of streamline deflection in comparison to the expansive

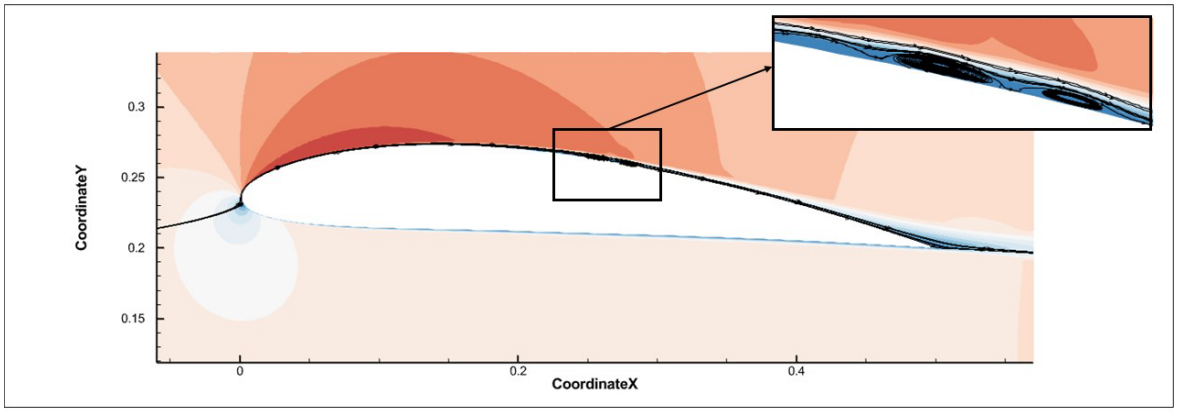


Figure 10. Separation bubble observed at a reynolds number of $3x10^5$. The red arrow indicates the location of the separation bubble.

deflection region observed in unbounded flow case. As the clearance decreases, the point at which streamline deflection commences migrates closer to the foil, further concentrating this deflection zone. Thus, the mirror-image model offers a robust theoretical framework for elucidating the observed reduction in streamline deflection underground-effect conditions.

For AoA that generate positive lift, the presence of the foil induces an upward deflection of the surrounding streamlines, as depicted in Figure 13. In an unbounded flow field, this region of deflection extends substantially from the inlet to the outlet. However, in a ground-effect flow field, the deflection is markedly more constrained, occurring primarily in the immediate vicinity of the foil. In this scenario, the streamlines tend to remain predominantly straight until they near the leading edge of the foil [15].

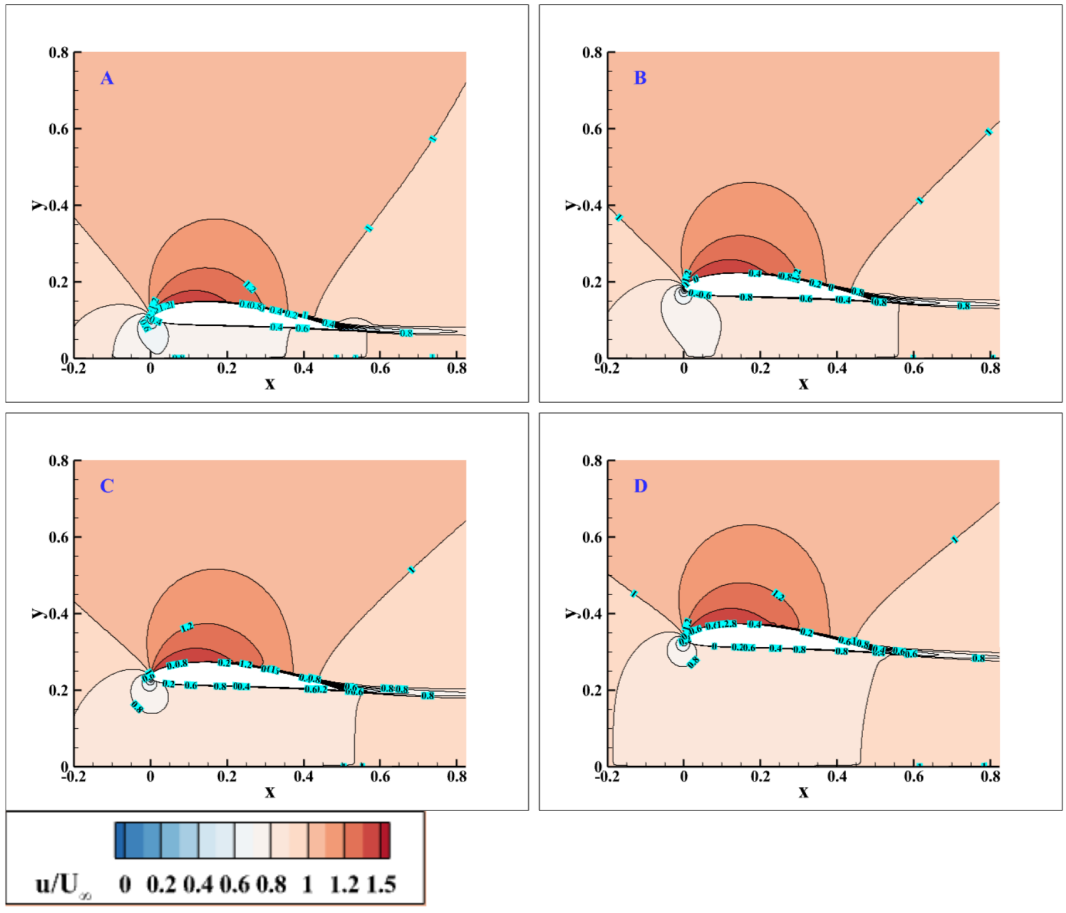


Figure 11. Velocity magnitude to freestream velocity around NACA 4412 foil. **A)** H/c=0.15, **B)** H/c=0.30, **C)** H/c=0.40, **D)** H/c=0.60.

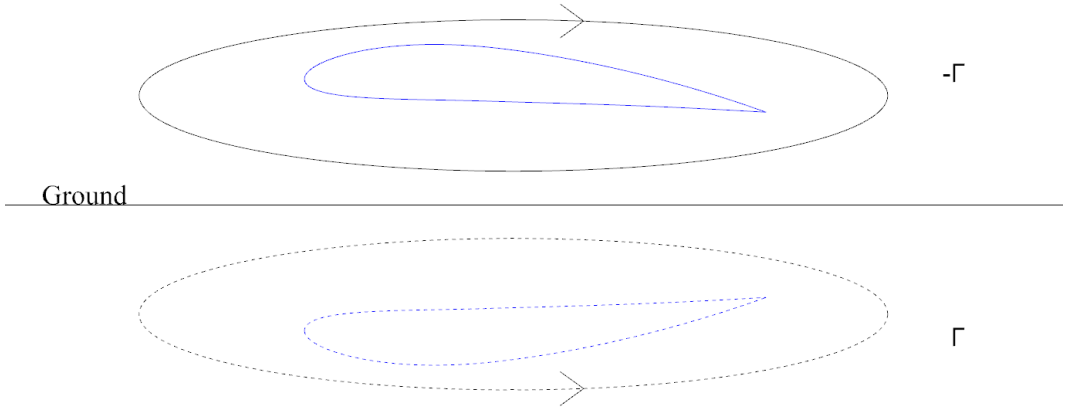


Figure 12. Mirror-image model.

When a foil operates IGE, the surrounding airflow characteristics undergo substantial changes compared to those in an unbounded flow environment. For a foil generating positive lift, the induced circulation leads to a notable upward deflection of adjacent streamlines. In an unbounded flow condition, this deflection region is extensive, significantly influencing the overall airflow dynamics from the inlet to the outlet.

In the context of GE, the reduced upward deflection of streamlines leads to two critical outcomes: A decrease in the effective AoA and an obstruction of airflow beneath the foil.

6.2. Tandem Cases

6.2.1. Reference data: Foil only configuration without interaction effects

To assess the interaction effects between the tandem foils, the results obtained from the tandem configuration were compared against baseline data derived from the analysis of each foil. This comparison effectively eliminates any interaction influences and establishes a benchmark for reference. The baseline data were generated through simulations of each foil in isolation, maintaining consistent conditions for Re and AoA in both IGE and OGE scenarios. The reference values for the C_L and C_D of the leading foil were obtained from simulations conducted at the same H used in the tandem configuration. Likewise, the reference data for the aft foil were derived from isolated simulations at the same clearance distance. The average reference values for the tandem configuration were calculated by taking the mean of the coefficients from the individual foil analyses. Convergence was confirmed when fluctuations in lift and C_D fell below $1x10^{-5}$, indicating negligible numerical dispersion.

In the reference framework, the lift and drag aero/hydrodynamic coefficients are expressed as:

$$C_{l(reference)} = \frac{C_{l(individual\ fore)} + C_{l(invididual\ aft)}}{2} \quad (3)$$

$$C_{d(reference)} = \frac{C_{d(individual\ fore)} + C_{d(invididual\ aft)}}{2} \quad (4)$$

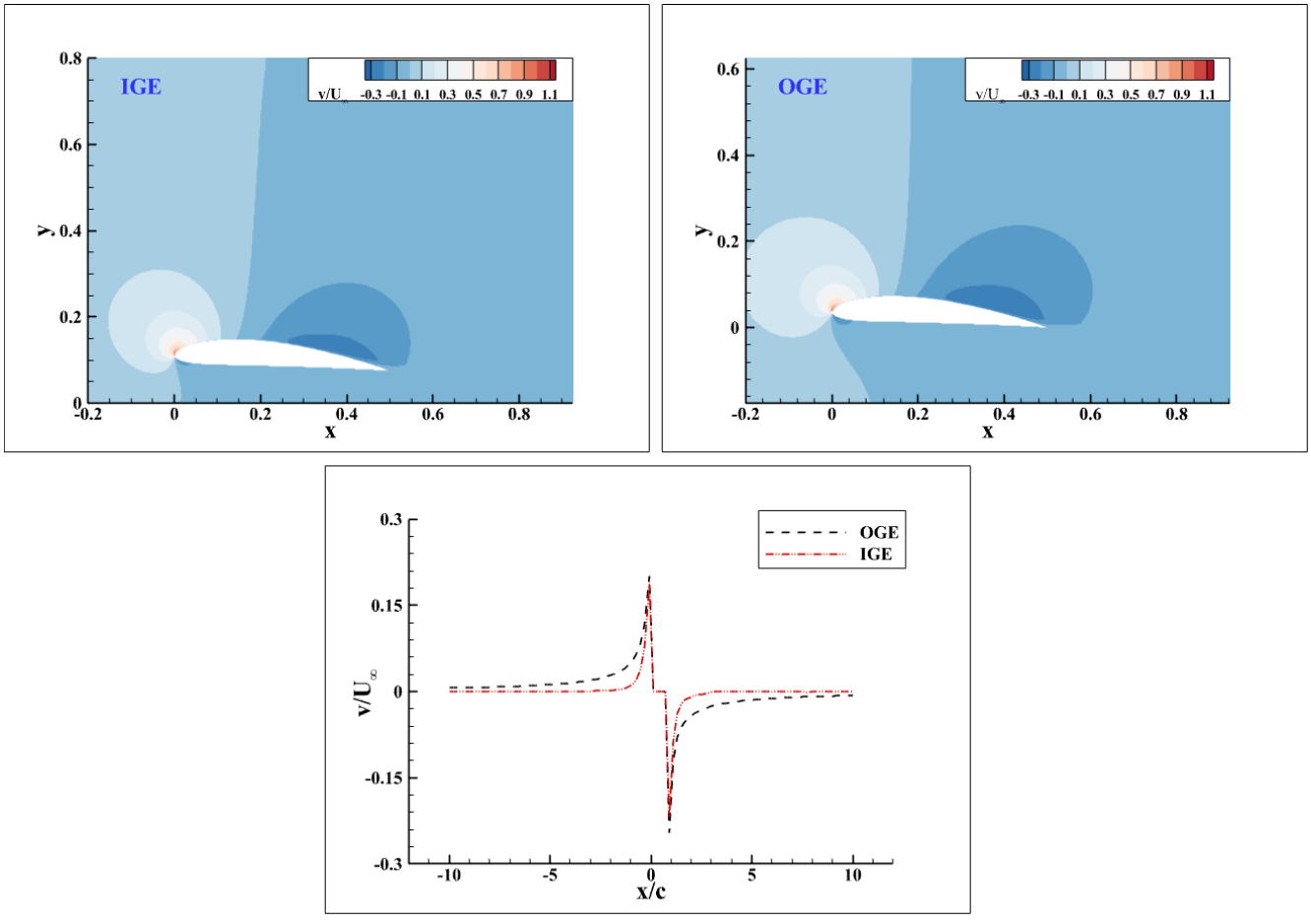


Figure 13. Non-dimensional velocity contour plot (top), non-dimensional velocity distribution along x-axis (bottom).

In the tandem framework, the lift and drag aero/hydrodynamic coefficients are expressed as:

$$C_{l(tandem)} = \frac{C_{l(fore)} + C_{l(aft)}}{2} \quad (5)$$

$$C_{d(tandem)} = \frac{C_{d(fore)} + C_{d(aft)}}{2} \quad (6)$$

6.2.2. Effect of gap distance in OGE case

Presented in Figure 14, the pressure distributions for the isolated foil, the fore foil in the negative gap configuration (case 13) (see Table 1), and the positive gap configuration (case 18) at a constant stagger distance (S) of (S=1c) reveal that the presence of the aft foil significantly influences the pressure distribution on the fore foil. Specifically, the stagnation point on the fore foil shifts slightly towards the trailing edge compared to the isolated foil scenario. This shift is evident in both tandem configurations; however, the distinction between the negative and positive gap cases is subtle. Notably, case 18 exhibits a more pronounced shift in the location of the minimum C_P relative to case 13, which can be attributed to the more favourable aero/hydrodynamic positioning of the fore foil in the positive gap configuration.

The impact of gap distance on the aero/hydrodynamic performance of tandem foils in the absence of GE has been rigorously analysed by examining the C_L and C_D as functions of S, as depicted in Figure 15. These figures illustrate the variations in C_L and C_D, along with the performance of foils, for gap distances between -0.4c and 0.4c.

Figure 15 shows the C_L of both the aft and fore foils under negative and positive gap conditions. Notably, the C_L of the aft foil consistently remains lower than the corresponding reference value across both gap configurations, exhibiting minimal sensitivity to variations in gap distance. Conversely, the fore foil demonstrates an increased C_L relative to the reference, with a more pronounced enhancement observed in positive gap conditions, indicating a heightened sensitivity of the fore foil lift to positive gaps.

The presence of the fore foil significantly influences the aerodynamic performance of the aft foil. Notably, the stagnation points on the aft foil shift towards the leading edge compared to the isolated foil scenario, resulting in a reduced maximum suction coefficient C_P value. This shift indicates a decrease in the effective AoA for the aft foil, despite both foils maintaining the same geometric AoA. Furthermore, the area under the C_P curve for the aft foil is smaller than that of the isolated foil, which can be attributed to the momentum deficit created by the wake of the fore foil.

In contrast, the lift curve for the fore foil demonstrates an upward trend with an increase in gap distance, while its C_D remains relatively stable, suggesting enhanced aerodynamic efficiency under these conditions. The lift and C_D for the aft foil, however, exhibit minimal changes with variations in gap distance, indicating a lower sensitivity to adjustments in gap spacing.

The tandem configuration exhibits a diminished lift-to-drag ratio in both positive and negative gap conditions relative to the reference values. This reduction arises from the fore foil's enhanced lift and decreased drag, which are counterbalanced by a reduction in lift and an increase in drag for the aft foil. As a result, the beneficial aero/hydrodynamic performance of the fore foil is partially offset by the suboptimal performance of the aft foil, leading to an overall decline in the aero/hydrodynamic efficiency of the tandem system, regardless of the gap condition.

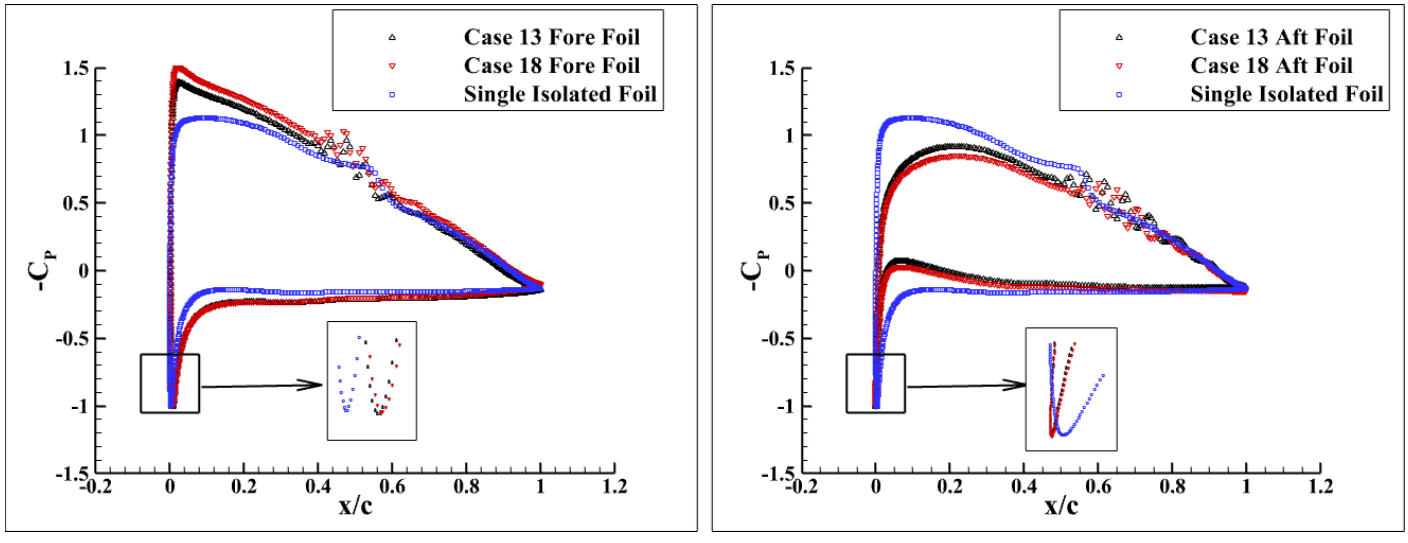


Figure 14. Influence of stagnation point variations on pressure distributions.

C_P: Pressure coefficient

6.2.3. Effect of S in OGE case

This section examines the effect of S on the aero/hydrodynamic characteristics of the system under both positive and negative gap configurations. As previously established, the results indicate a consistent reduction in performance across both gap scenarios. Figures 15 illustrates the variations in C_L and C_D, as well as the performance of foil, in relation to S for each gap condition.

As the S increases in both negative and positive gap configurations, a notable trend emerges: the C_L of the fore foil decreases, whereas the C_L of the aft foil increases. This phenomenon is indicative of diminishing interference effects between the foils as the S increases. Notably, the reduction in lift for the fore foil is more pronounced in the positive gap configuration, suggesting that the favourable interference effects enhancing lift in this configuration are less effective at greater S.

As the S between the foils increases, the C_D of the fore foil rises, while that of the aft foil decreases. Despite the reduction in drag on the aft foil and the corresponding increase on the fore foil, the overall mean C_D for the tandem configuration remains slightly elevated compared to the value observed for isolated foils. This trend is likely due to the formation of a high-pressure region between the foils, which generates an upstream force on the fore foil and a downstream force on the aft foil, as depicted in Figure 16.

6.3. Effect of Gap Distance in IGE Case

The influence of gap distance on the aero/hydrodynamic performance of tandem foils in proximity to the ground was analysed by evaluating C_L and C_D as functions of S, as presented in Figure 17. The findings indicate that the lift generated by the aft foil is significantly diminished compared to that of an isolated foil, while concurrently, the aft foil exhibits increased drag relative to the reference values. This

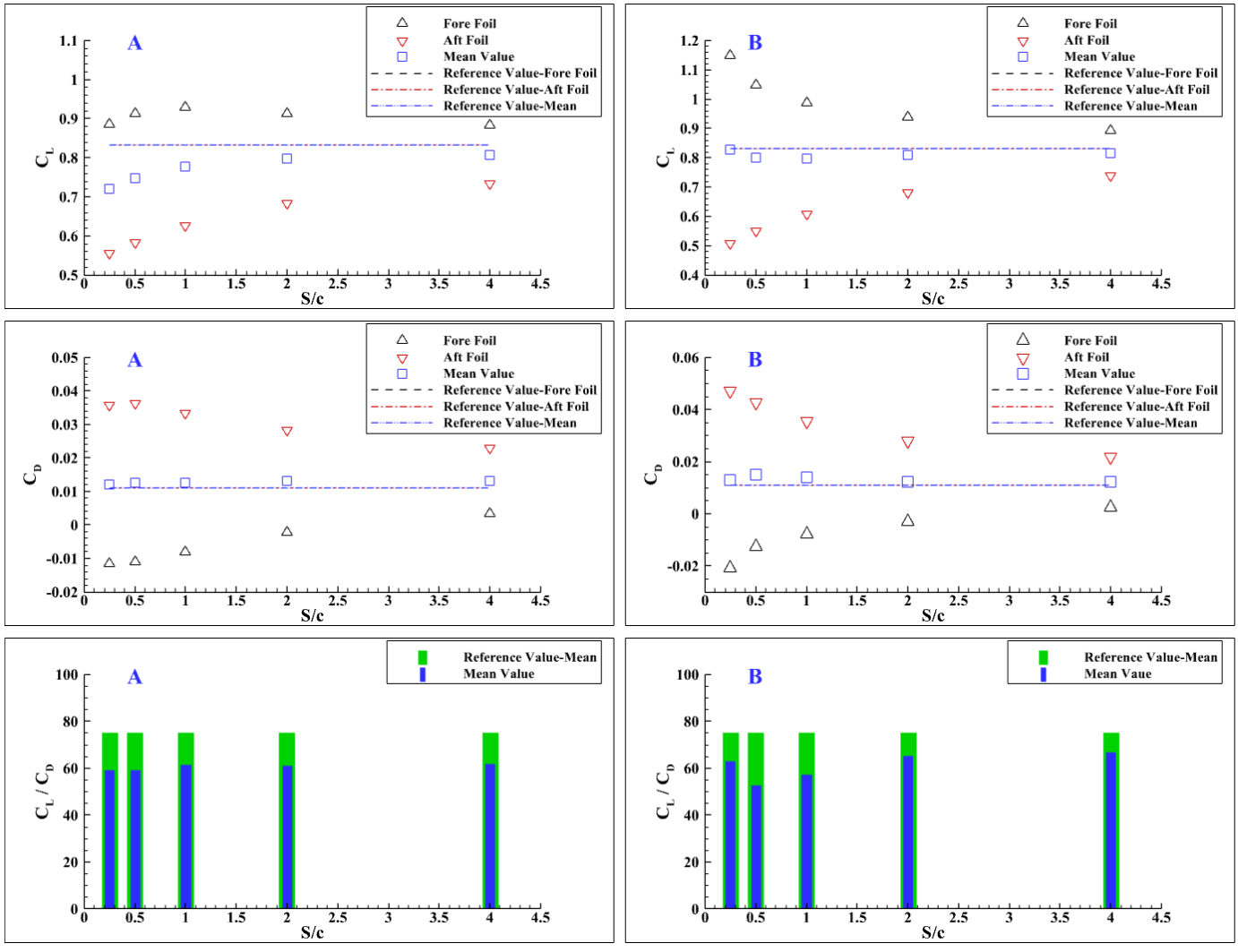


Figure 15. Lift coefficient, drag coefficient, performance of foils in the absence of ground effect. **A)** G=-0.4c, **B)** G=0.4c.

C_D: Drag coefficient, C_L: Lift coefficient

decline in performance is attributed to the aft foil interaction with the intricate wake structures induced by the fore foil, which adversely affects its overall aero/hydrodynamic efficiency.

When the gap height (G) is positive, there is a significant increase in the C_L of the fore foil, despite its greater distance from the ground. This phenomenon can be attributed to the aft foil influence, which causes high pressure on the lower (pressure) side of the fore foil, thereby offsetting the reduction in lift associated with diminished GE. Conversely, in cases where G is negative, the aft foil enhances the pressure on the suction side of the fore foil, as illustrated in Figure 18.

The tandem configuration exhibits improved performance as G increases, primarily driven by the increase in lift on the fore foil and the aft foil ability to mitigate the adverse effects of wake interference near the ground. As a result, with a positive gap, the tandem system achieves significantly higher performance compared to the reference single foil. While a similar trend is observed with negative gap values, the performance enhancement is markedly more pronounced when G is positive.

The fore foil demonstrates a significant reduction in drag across both negative and positive gap configurations, primarily due to the presence of the aft foil, which induces a beneficial interference drag effect. This reduction in overall drag is consistently observed across all tested gap spacings. Moreover, in the positive gap configuration, the lift curve for the fore foil increases while drag remains relatively constant, reflecting improved aero/hydrodynamic efficiency. These findings indicate that a tandem foil configuration can achieve enhanced aero/hydrodynamic performance compared to two isolated foils, particularly when the gap between the foils is positive.

6.3.1. Effect of S in IGE case

As detailed in the preceding section, the aero/hydrodynamic efficiency of tandem foils shows marked improvement when the G between the foils is positive. However, to

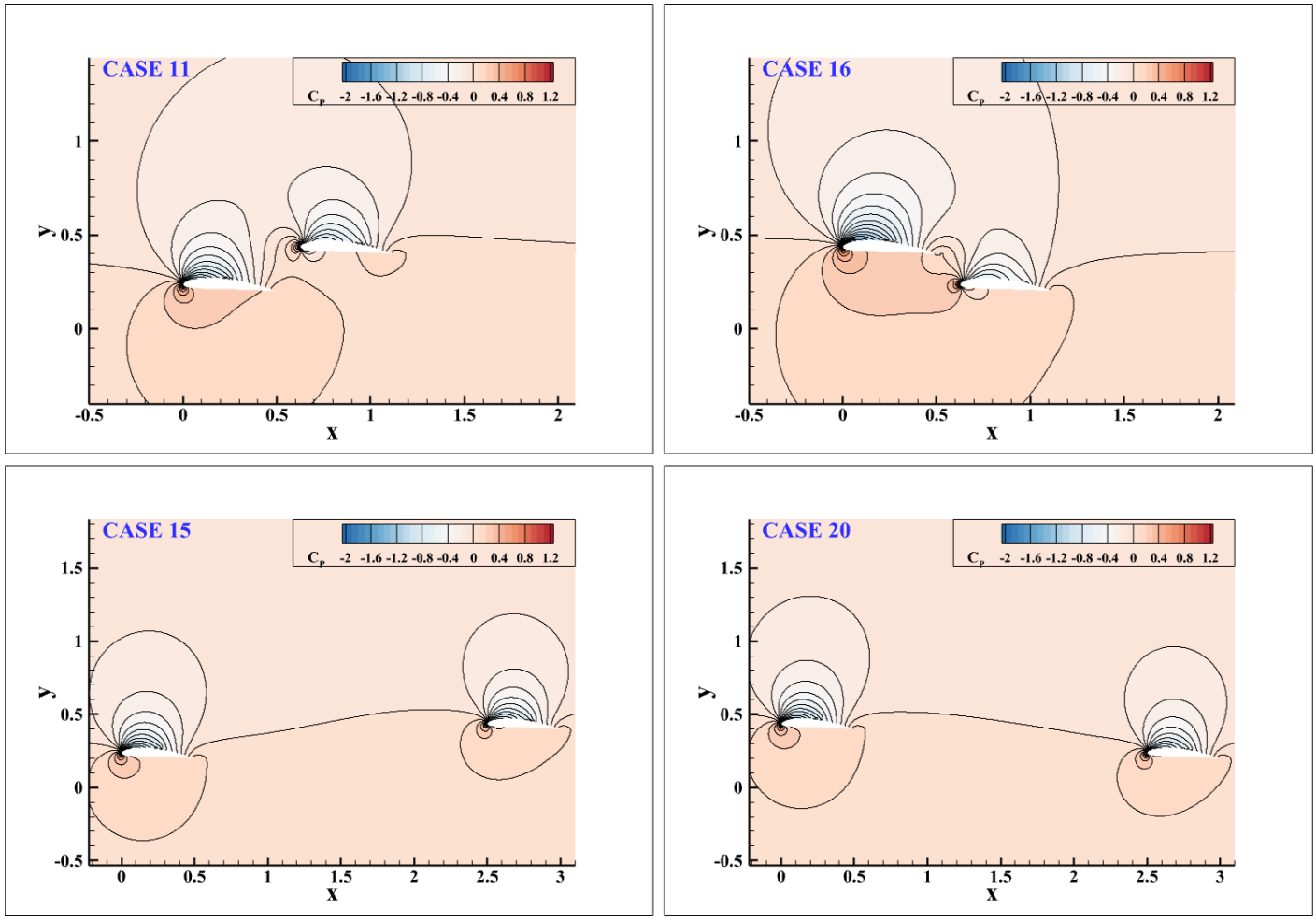


Figure 16. Contours depicting the pressure distribution for the various tested configurations in the absence of ground effect.

C_p: Pressure coefficient

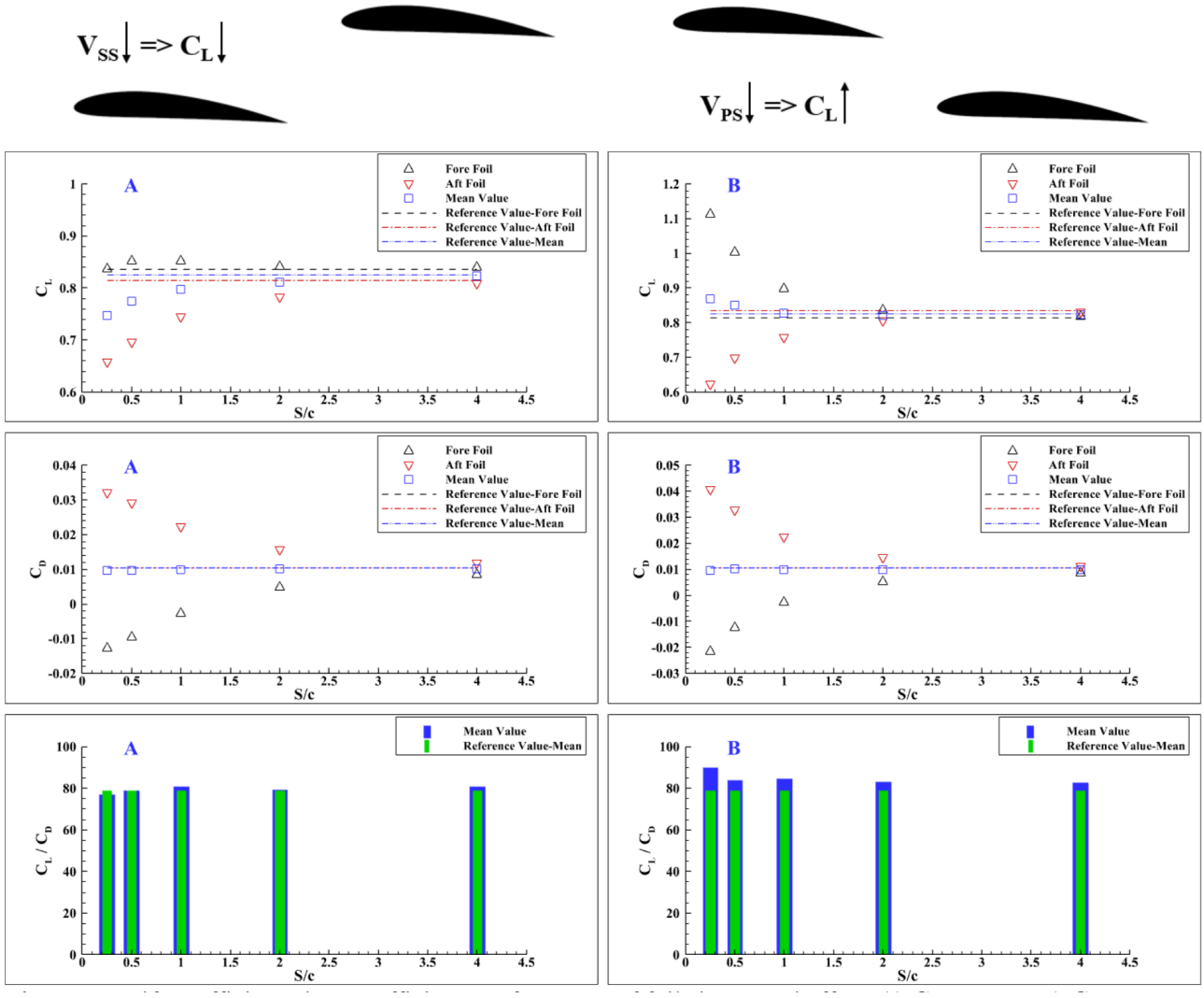


Figure 17. Lift coefficient, drag coefficient, performance of foils in ground effect. **A)** Gap=-0.4c, **B)** Gap=0.4c.

C_D: Drag coefficient, C_L: Lift coefficient

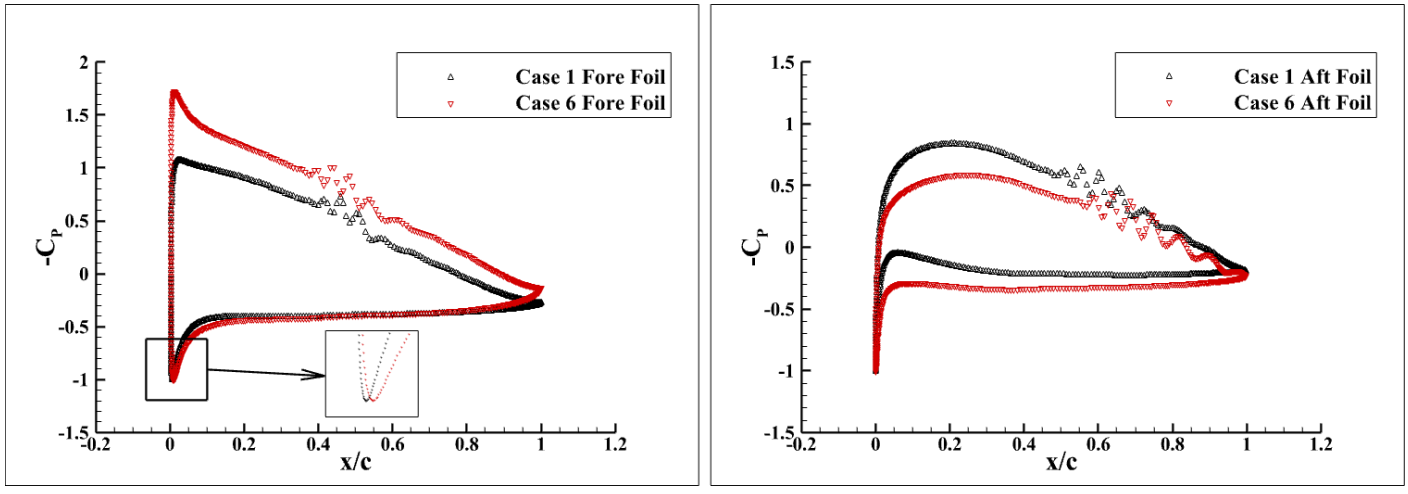


Figure 18. Pressure distributions in tandem configurations with ground effect.

C_P: Pressure coefficient

comprehensively evaluate the influence of S on the system's aero/hydrodynamic behaviour, both positive and negative gap configurations are examined in this section. Figure 17 illustrates the variation in C_L and C_D as functions of S, providing insights into how these parameters evolve with changes in the foil arrangement.

The analysis of drag characteristics reveals that the C_D of the fore foil decreases due to the elevated pressure region created by the aft foil, as demonstrated in Figure 19. Nevertheless, the mean C_D of the tandem system remains comparable to the reference value, indicating a compensatory relationship between the reduced drag on the fore foil and the drag exerted by the aft foil. As the S increases, the C_D of the fore foil exhibits an upward trend, while that of the aft foil decreases. This behaviour can be attributed to the diminishing interference effects between the foils, resulting in a reduced influence of each foil wake and pressure fields on the other as the S increases.

The results of this study are consistent with the trends presented in the experimental work of Biermann and Herrnstein [43], despite the absence of GE in their investigations. Analysing the lift-to-drag ratio (C_L/C_D) reveals that the mean ratio for the tandem system decreases as the S increases, although it remains elevated compared to the reference values for isolated foils. This observation suggests that closer S confer beneficial interference effects, which diminish as the foils are spaced further apart. Notably, at a S of four times the chord length, the aero/hydrodynamic performance metrics of the tandem system converge towards those of a single isolated foil, indicating a significant reduction in aero/hydrodynamic interference between the two foils.

The influence of S on aero/hydrodynamic performance is discernible in both negative and positive gap configurations, with a more significant effect observed in the positive gap scenario as shown Figure 19. Specifically, case 6 illustrates that, despite sharing the same H ratio (H/c=0.80) as in case 9, the fore foil in case 6 generates a higher C_L. This

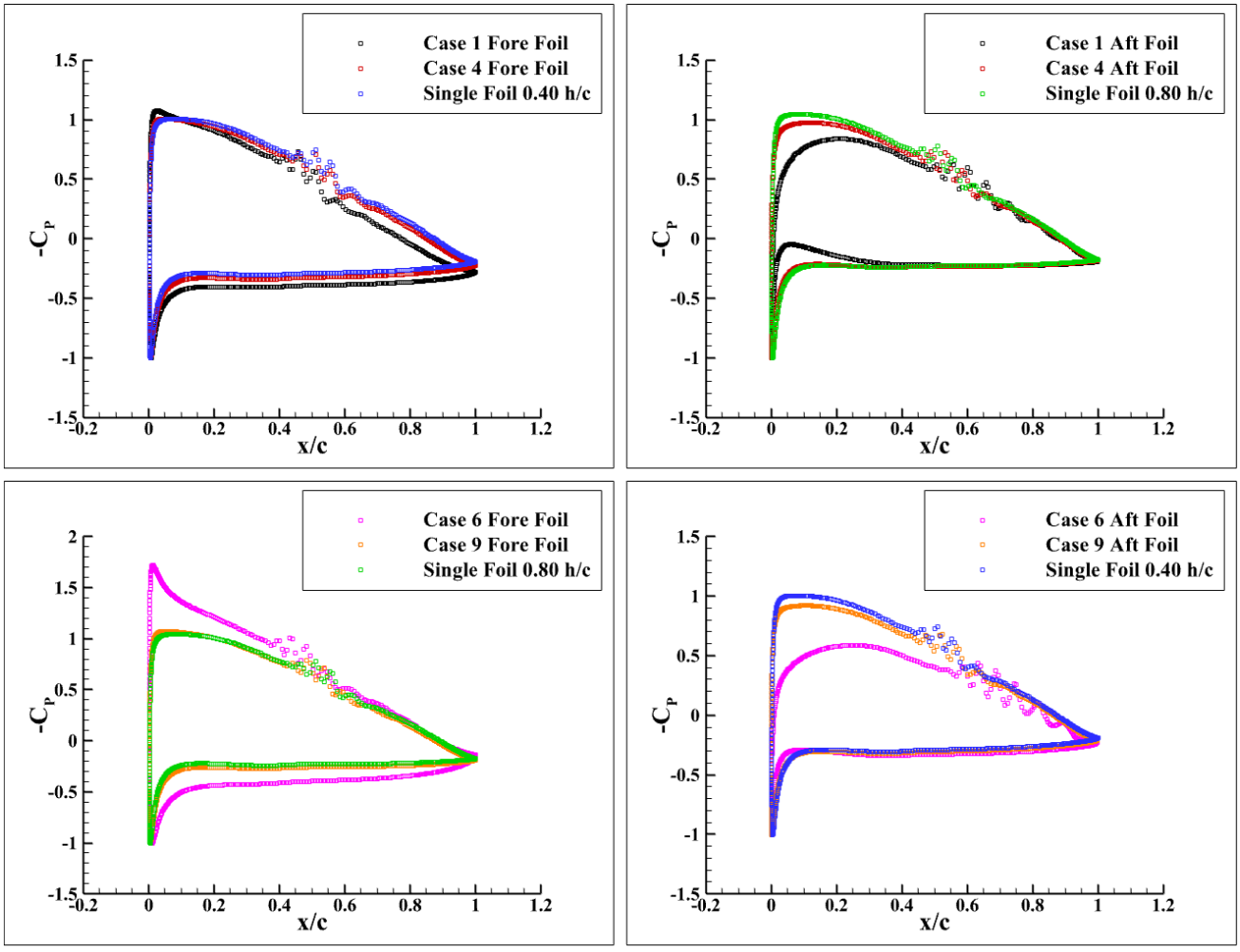


Figure 19. Tested cases pressure distribution in IGE cases.

C_P: Pressure coefficient, IGE: In ground effect

enhancement is attributable to the shorter (S=0.25c in case 6 compared to S=2c in case 9), which facilitates the development of a high-pressure region behind the fore foil due to the presence of the aft foil. As the S increases, this positive pressure region diminishes, signifying a reduction in foil-to-foil interaction effects.

The positive pressure region created by the convergent-divergent zone, alleviates the flow tendency to approach the trailing edge of the fore foil, thereby resulting in a higher suction peak than observed in the isolated case. Furthermore, the positive pressure field generated by the aft foil contributes to a deceleration of the flow on the pressure side of the fore foil, facilitating an increase in pressure in this region. Collectively, these effects enhance the lift production of the fore foil in case 6.

In conclusion, the findings underscore the critical influence of both gap and S on the aero/hydrodynamic performance of tandem foils operating within the GE. Specifically, configurations with positive gaps generally yield enhanced performance. Conversely, increased S diminish the interaction between the foils, leading to performance metrics that approach those of isolated foils (Figure 20).

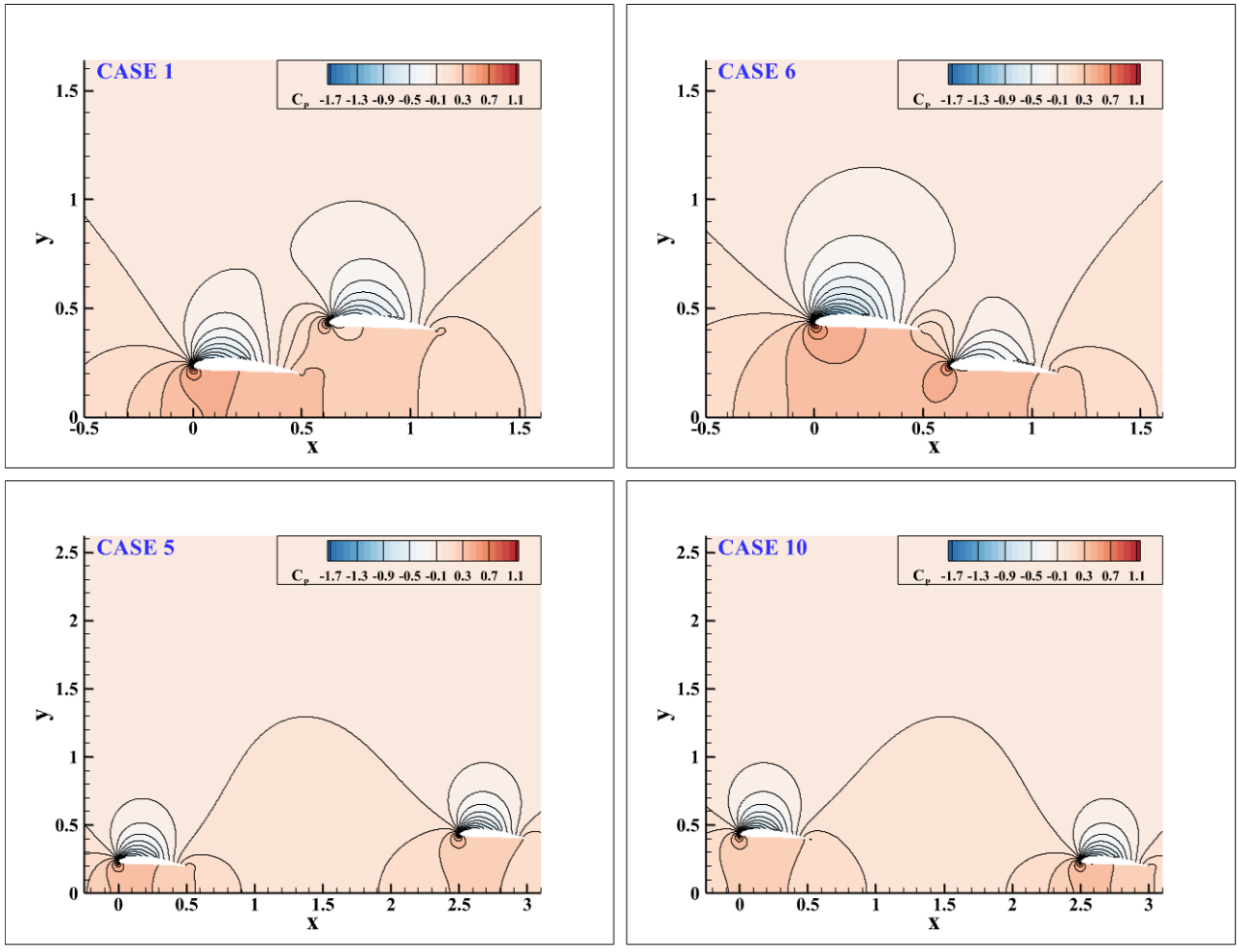


Figure 20. Pressure distribution for various tested configurations in IGE case.

C_P: Pressure coefficient, IGE: In ground effect

7. Conclusion

This original study provides an extensive analysis of the aero/hydrodynamic performance of tandem foils, emphasizing the effects of G, S, and ground. By contrasting tandem configurations with isolated foil cases, the research enhances the understanding of aero/hydrodynamic interactions between the foils. The investigation encompasses a series of simulations and comparative analyses to elucidate how these parameters influence C_L and C_D, as well as the efficiency. The findings yield valuable insights into the effect of these factors on the aero/hydrodynamic efficiency of tandem configurations in both IGE and OGE scenarios.

The main conclusions are as follows:

• It is challenging to assert a single configuration as universally superior without considering specific performance criteria. For instance, achieving maximum range and endurance necessitates an optimal lift-to-drag ratio. In contrast, applications demanding substantial lift forces, regardless of efficiency, or requiring significant drag forces for low-speed flight or short take-off and landing capabilities may prioritize different configurations.

• The tandem system demonstrates a superior lift-to-drag ratio IGE compared to out-of-ground configurations at equivalent stagger and gap distances. While the tandem system OGE exhibits a lower lift-to-drag ratio than the corresponding reference value, the tandem system IGE achieves a higher lift-to-drag ratio in comparison to the reference.

• The aero/hydrodynamic performance of the tandem system is enhanced with a positive G, indicating that an optimal gap can significantly improve system efficiency.

• S significantly affects the performance of the tandem system, primarily due to foil-to-foil interactions that modify the static pressure distribution across the foils.

• In instances of pronounced interference between the foils, the fore foil may experience thrust rather than drag, presenting a considerable advantage for specific applications.

• OGE, the fore foil typically attains a higher C_L than IGE for identical gap and stagger. This variance is attributed to the reduction in the effective AoA induced by GE, which is defined as the angle between the chord line of the foil and the relative airflow impacting the foil. IGE, the proximity of the ground alters the flow field, effectively reducing AoA experienced by the fore foil, resulting in decreased lift. Although both ground and out-of-ground conditions present a notable reduction in lift for the aft foil relative to the reference value, aft foils IGE demonstrate higher C_L compared to their out-of-ground counterparts. This can be explained by the increased pressure on the pressure side of the aft foil due to its closeness to the ground.

In summary, the results indicate that a tandem wing configuration IGE can provide distinct advantages over a single wing design, particularly regarding enhanced aero/hydrodynamic performance under specific conditions.

Footnotes

Authorship Contributions

Concept: M. Delikan, and Ş. Bal, Design: M. Delikan, and Ş. Bal, Data Collection or Processing: M. Delikan, Analysis or Interpretation: M. Delikan, and Ş. Bal, Literature Review: M. Delikan, Writing: M. Delikan, and Ş. Bal.

Conflict of Interest: No conflict of interest was declared by the authors.

Financial Disclosure: The authors declared that this study received no financial support.

9. References

[1] M. R. Ahmed, and S. D. Sharma, "An investigation on the aerodynamics of a symmetrical airfoil in ground effect," *Exp. Therm. Fluid Sci.*, vol. 29, no. 6, pp. 633-647, Jul 2005.

[2] J. Smith, H. Graham, and J. Smith, "The validation of an airfoil in the ground effect regime using 2-D CFD analysis," in *26th AIAA Aerodynamic Measurement Technology and Ground Testing Conference*, Seattle, Washington: American Institute of Aeronautics and Astronautics, Jun 2008.

[3] S. C. Luo, and Y. S. Chen, "Ground effect on flow past a wing with a NACA0015 cross-section," *Experimental Thermal and Fluid Science,* vol. 40, pp. 18-28, Jul 2012.

[4] T. Barber, "Aerodynamic ground effect: a case study of the integration of CFD and experiments," *International Journal of Vehicle Design,* vol. 40, no. 4, pp. 299-316, 2006.

[5] H. Wang, C. J. Teo, B. C. Khoo, and C. J. Goh, "Computational aerodynamics and flight stability of wing-in-ground (WIG) craft," *Procedia Engineering*, vol. 67, pp. 15-24, 2013.

[6] A. F. Zahm, and R. M. Bear, "Ground-plane influence on airplane wings," *Journal of the Franklin Institute,* vol. 191, no. 5, pp. 687-693, May 1921.

[7] K. Park, and J. Lee, "Influence of endplate on aerodynamic characteristics of low-aspect-ratio wing in ground effect," *Journal of Mechanical Science and Technology,* vol. 22, no. 12, pp. 2578-2589, Dec 2008.

[8] A. Klemin, "A belt method of representing the ground," *Journal of the Aeronautical Sciences,* vol. 1, no. 4, pp. 198-199, Oct 1934.

[9] X. Zhang, W. Toet, and J. Zerihan, "Ground effect aerodynamics of race cars," *Appl. Mech. Rev.*, vol. 59, no. 1, pp. 33-49, Jan 2006.

[10] K. V. Rozhdestvensky, "Wing-in-ground effect vehicles," *Progress in Aerospace Sciences,* vol. 42, no. 3, pp. 211-283, May 2006.

[11] C.-M. Hsiun, and C.-K. Chen, "Aerodynamic characteristics of a two-dimensional airfoil with ground effect," *Journal of Aircraft*, vol. 33, no. 2, pp. 386-392, Mar 1996.

[12] H. H. Chun, "Turbulence flow simulation for wings in ground effect with two ground conditions: fixed and moving ground," *International Journal of Maritime Engineering,* vol. 145, pp. 18, 2003.

[13] M. R. Ahmed, T. Takasaki, and Y. Kohama, "Aerodynamics of a NACA4412 Airfoil in Ground Effect," *AIAA J.*, vol. 45, no. 1, pp. 37-47, Jan 2007.

[14] J. Zerihan, and X. Zhang, "Aerodynamics of a single element wing in ground effect," *Journal of Aircraft*, vol. 37, no. 6, pp. 1058-1064, Nov 2000.

[15] Q. Qu, W. Wang, P. Liu, and R. K. Agarwal, "Airfoil aerodynamics in ground effect for wide range of angles of attack," *AIAA Journal*, vol. 53, no. 4, pp. 1048-1061, Apr 2015.

[16] E. Hayashi, and M. Endo, "Measurement of flow fields around an airfoil section with separation," *Transactions of the Japan Society for Aeronautical and Space Sciences,* vol. 21, no. 52, pp. 69-75, 1978.

[17] T. J. Barber, E. Leonardi, and R. D. Archer, "Causes for discrepancies in ground effect analyses," *The Aeronautical Journal,* vol. 106, no. 1066, pp. 653-668, Dec 2002.

[18] S. Bal, "Prediction of hydrodynamic performance of 3-D wig by IBEM," *International Journal of Maritime Engineering*, vol. 160, no. A3, Dec 2021.

[19] S. Bal, "Free surface effects on 2-D airfoils and 3-D wings moving over water," *Ocean Systems Engineering,* vol. 6, no. 3, pp. 245-264, Sep 2016.

[20] A. Dogrul, and S. Bal, "Performance prediction of wings moving above free surface," in *Advances in Boundary Element and Meshless Techniques XVI*, Ankara, Turkey: Middle East Technical University, Ankara, Turkey, 2016, pp. 85-92.

[21] O. K. Kinaci, and S. Bal, "Performance prediction of 2D foils moving above and close to free surface," in *Advances in Boundary Element and Meshless Techniques XVII*, Ankara, Turkey: Middle East Technical University, Ankara, Turkey, 2016, pp. 43-50.

[22] S. Bal, "Lumped vortex element flying over free water surface," *Bulletin of the Technical University of Istanbul,* vol. 55, no. 1, pp. 1-6, 2023.

[23] S. Bal, "Analytic solution for flat-plate under a free surface with finite depth effects," *Ocean Systems Engineering,* vol. 14, no. 3, pp. 301-314, 2024.

[24] J.-B. R. G. Souppez, "*Hydrofoil configurations for sailing superyachts: hydrodynamics, stability, and performance,*" Conference: Design & Construction of Super & Mega YachtsAt: Genoa, Italy, May 2019.

[25] K. I. Matveev, and I. I. Matveev, "Tandem hydrofoil system," *Ocean Engineering*, vol. 28, no. 2, pp. 253-261, Jan 2001.

[26] D. Speranza, S. Papa, C. Pensa, and R. Di Bernardo, "Hydrofoil technology: current applications and future developments for sustainable boating," in *Design Tools and Methods in Industrial Engineering III*, M. Carfagni, R. Furferi, P. Di Stefano, L. Governi, and F. Gherardini, Eds., in Lecture Notes in Mechanical Engineering, Cham: Springer Nature Switzerland, 2024, p. 339-346.

[27] Y. Shang, and J. J. Horrillo, "Numerical simulation and hydrodynamic performance predicting of 2 two-dimensional hydrofoils in tandem configuration," *Journal of Marine Science and Engineering,* vol. 9, no. 5, p. 462, Apr 2021.

[28] O. K. Kinaci, "A numerical parametric study on hydrofoil interaction in tandem," *International Journal of Naval Architecture and Ocean Engineering,* vol. 7, no. 1, pp. 25-40, Jan 2015.

[29] F. A. Khan, and T. J. Mueller, "Tip vortex/airfoil interaction for a low Reynolds number canard/wingconfiguration," *Journal of Aircraft*, vol. 28, no. 3, pp. 181-186, Mar 1991.

[30] K. Rokhsaz, "*Analytical investigation of the aerodynamic characteristics of dual wing systems*," University of Missouri-Rolla, 1980.

[31] D. W. Fanjoy, and D. J. Dorney, "*Numerical simulations of tandem-airfoil aerodynamics*," presented at the Aerospace Atlantic Conference & Exposition, p. 961295, May 1996.

[32] T. M. Faure, L. Hétru, and O. Montagnier, "Aerodynamic features of a two-airfoil arrangement," *Experiments in Fluids*, vol. 58, no. 10, pp. 146, Oct 2017.

[33] B. Yin, Y. Guan, A. Wen, N. Karimi, and M. H. Doranehgard, "Numerical simulations of ultra-low-Re flow around two tandem airfoils in ground effect: isothermal and heated conditions," *Journal of Thermal Analysis and Calorimetry,* vol. 145, no. 4, pp. 2063-2079, Aug 2021.

[34] M. Delikan, "Computational analysis of 2D foils with and without ground effect in tandem," Master Thesis, *Istanbul Technical University*, İstanbul, 2024.

[35] M. Delikan, and S. Bal, "*Moderate-reynolds number flow around tandem foils with ground effect by CFD,*" presented at the 3rd International Shipbuilding and Maritime Technology Congress (GMO - Shipmar 2024), Trabzon, 2024.

[36] F. R. Menter, "Two-equation eddy-viscosity turbulence models for engineering applications," *AIAA Journal*, vol. 32, no. 8, pp. 1598-1605, Aug 1994.

[37] H. Tennekes, and J. L. Lumley, *A first course in turbulence*, Nachdruck des Originals von 1972. Cambridge, Massachusetts: The MIT Press, 1972.

[38] A. Aslani, A. Shires, A. Shahsavari, and K. C. Kim, "Short-takeoff marine vehicle with circulation flow control of wing-in-ground effect," *Ocean Engineering*, vol. 262, pp. 112074, Oct 2022.

[39] H. Zhi, T. Xiao, S. Deng, M. Tong, P. Chen, and B. Wu, "Distinct wing-in-ground effect of airfoil in proximity to water waves", *AIAA Journal,* vol. 60, no. 6, pp. 3789-3804, Jun 2022.

[40] Y.-H. Im and K.-S. Chang, "Unsteady aerodynamics of a wing-in-ground-effect airfoil flying over a wavy wall", *Journal of Aircraft*, vol. 37, no. 4, pp. 690-696, Jul 2000.

[41] J. Winslow, H. Otsuka, B. Govindarajan, and I. Chopra, "Basic understanding of airfoil characteristics at low reynolds numbers (104-105)", *Journal of Aircraft*, vol. 55, no. 3, pp. 1050-1061, May 2018.

[42] A. O. Nuhait, and D. T. Mook, "Numerical simulation of wings in steady and unsteady ground effects," *Journal of Aircraft,* vol. 26, no. 12, pp. 1081-1089, Dec 1989.

[43] D. Biermann, and W. H. Herrnstein Jr., "The interference between struts in various combinations," *NACA*, United States, Technical Report NACA-TR-468, Jan 1934.

REVIEW ARTICLE

DOI: 10.54926/jnamt.2025.2412

J Nav Architect Mar Technol 2025;227(1):22-33

Technological Transformation and Future Perspectives in Autonomous Maritime Systems

Sadık Kula[1], Uğur Buğra Çelebi[2]

[1]Yıldız Technical University Faculty of Administrative and Social Sciences, Department of Political Science and International Relations, İstanbul, Türkiye

[2]Yıldız Technical University Naval Architecture and Maritime Faculty, İstanbul, Türkiye

To cite this article: S. Kula, and U. B. Çelebi. Technological transformation and future perspectives in autonomous maritime systems. *J Nav Architect Mar Technol*. 2025;227(1):22-33.

Received: 03.12.2024 - **Revised:** 26.01.2025 - **Accepted:** 25.04.2025 - **Publication Date:** 14.05.2025

Abstract

This article examines the growing role of autonomous systems in the defense and maritime sectors within the context of the historical and societal transformations driven by technology. It highlights how technological innovations, particularly since the Industrial Revolution, have shaped systemic transformations, while information and communication technologies have redefined societal life and global dynamics. In the military domain, the use of unmanned systems and artificial intelligence (AI)-supported platforms is emphasized as replacing traditional warfare tools with more effective and flexible technologies. The study focuses on the development of autonomous maritime vehicles, emphasizing their operational advantages and strategic importance for national security. Unmanned maritime vehicles undertake critical missions, ranging from combating asymmetric threats to environmental monitoring, while offering significant benefits such as cost efficiency and risk reduction. However, the limitations of autonomous systems include deficiencies in communication infrastructure, susceptibility to electronic jamming, and legal and ethical challenges. It is anticipated that future warfare technologies will derive strategic advantages from swarm intelligence, machine learning, and AI-based systems. These systems have the potential to perform complex tasks in a coordinated manner without human intervention. However, challenges such as cybersecurity threats, legal and ethical regulations, and societal acceptance must be addressed carefully for the widespread adoption of these technologies. In this context, the integrated development of autonomous systems, supported by innovation and collaboration processes, is expected to lead to significant transformations in military and civilian domains in the future. These systems, leveraging advancements in information technologies, AI, and sensor systems, will achieve more efficient and sustainable operational capabilities, offering both economic and strategic advantages. In conclusion, as the importance of autonomous systems continues to grow in the coming years, innovative strategies and disciplined management approaches will be required for their effective use. In the future, the adaptability of autonomous systems and capabilities such as swarm intelligence will play a game-changing role in both military and commercial operations.

Keywords: Autonomous maritime systems, artificial intelligence, robotics, sensor technologies

Address for Correspondence: Sadık Kula, Yıldız Technical University Faculty of Administrative and Social Sciences, Department of Political Science and International Relations, İstanbul, Türkiye

E-mail: kulasadik@yahoo.com

ORCID ID: orcid.org/0009-0008-9586-6865

Copyright© 2025 The Author. Published by Galenos Publishing House on behalf of UCTEA Turkish Chamber of Naval Architects and Marine Engineers.
Licensed under a Creative Commons Attribution-NonCommercial-NoDerivatives 4.0 (CC BY-NC-ND) International License

1. Introduction

Technology has always played a central role in historical and societal transformations and continues to be one of the most critical drivers of global change processes today. The formation and institutionalization of industrial societies shaped by economic developments largely resulted from technological innovations. Additionally, the integration of knowledge accumulated during the information revolution into this process has laid the groundwork for the development of modern production facilities.

Technological advancements are progressively reducing the demand for human labor across various sectors, with automation and artificial intelligence (AI)-powered robots replacing manual work. This transformation creates favorable conditions for the transition to knowledge-based economic systems while also revealing a direct relationship between economic growth facilitated by technology and military power. Today, civil and military sectors exhibit an interdependent structure through shared knowledge and technology networks.

When examining historical processes, it is evident that early wars were predominantly aimed at territorial expansion. However, during the 19th and 20th centuries, the focus of warfare shifted to expanding economic resources and increasing production capacity. In the present era, the core of conflicts revolves around the control and management of information [1]. Historically, technological leadership in the policies of major powers has often focused on military technology [2]. Therefore, technological advancement has progressed in parallel with the transformation of military power throughout history [3].

The maritime industry has been one of the sectors most significantly impacted by the Industrial Revolution. The development of armored warships facilitated technological advancements in weapons and devices, while the growth of the shipbuilding industry played a crucial role in strengthening nations' maritime dominance. For instance, European states' development of gunpowder-based weaponry and long-range ocean-going ships enhanced their superiority over other nations, allowing them to expand their spheres of hegemony both on land and at sea. These advancements provided a significant foundation for the establishment of Western colonial dominance in the early 19th century [4].

Throughout human history, the development of military technology has been shaped by numerous significant milestones, including the use of gunpowder in firearms, the advent of steam-powered ships, the introduction of armored vehicles on the battlefield, and the invention of submarines, radar, and military jets. Today, information and communication technologies, AI, and robotic systems are permeating every aspect of social life, especially in economic, political, and sociological domains, driving rapid and comprehensive transformations.

In this context, militarily powerful states are increasingly relying on the capabilities provided by unmanned systems while reducing the number and costs of manned systems. Unmanned aerial vehicles have emerged as one of the most effective tools of warfare in this regard. In the near future, the concept of military security is expected to be reshaped based on the capabilities of autonomous or remotely controlled combat platforms equipped with AI.

In addition to the challenges of operating large manned platforms, shrinking military budgets and smaller force structures are key factors driving nations toward unmanned systems. Consequently, security agencies must effectively leverage the technological transformation brought about by unmanned vehicles and systems to provide strategic, swift, flexible, and agile responses to current and future crises.

Future wars are anticipated to be shaped by semi-autonomous and fully autonomous systems powered by AI technologies. These systems are expected to be significantly more effective than traditional manned warfare platforms. As the use of unmanned systems in combat and conflict surpasses the use of manned weapons and systems, a fundamental shift in the nature of wars and conflicts will occur, leading to an era dominated by autonomous devices and weapons.

Unmanned systems not only have the potential to reduce human-related risks and perform tasks beyond the capabilities of manned vehicles, but they also act as force multipliers, creating synergy among operational elements by enhancing the execution of assigned tasks.

2. General Requirements and Methods for Autonomous Systems

With the enhancement of weapon systems' capabilities through information technologies, the design of systems equipped with AI and various algorithms, capable of autonomously selecting the most effective methods in warfare and operating automatically, emerges as a transformative phenomenon for the culture of conflict. Parties achieving technological superiority have the opportunity to leverage this advantage to establish a form of technological dominance. Today, the most effective technological dominance is achieved through autonomous systems managed by computer programs and equipped with automated functions (Table 1) [5].

Autonomous maritime vehicles have significant potential as force multipliers in the realm of unmanned systems. These vehicles reduce risks to manned vessels and personnel, providing a cost-effective and human-resource-efficient solution for a wide range of applications, from traditional

Table 1. Algorithm distribution analysis for autonomous maritime systems

Method	Typical application areas	Common use	Example studies/Projects
PID	Heading control, station keeping, path following	High	YARA Birkeland (NTNU), low-level control loops in most commercial systems
LQR	Optimal stabilization, linear model-based control	Medium	Research vessels with model-based state feedback (e.g., maritime testbeds)
MPC	Collision avoidance, constrained path planning	High	Rolls-Royce autonomous vessels, ASV-Global path tracking
RL	Learning-based maneuvering, dynamic environments	Emerging	Sea Hunter DARPA (U.S. Navy), RL-based harbor navigation studies
DL	Environmental perception, sensor fusion	Experimental	Object recognition in autonomous harbor monitoring (LiDAR/Camera fusion)
Fuzzy Logic	Obstacle avoidance, uncertain environments	Low	Fuzzy ship heading control under changing sea state
Heuristic (e.g., GA, PSO, ACO)	Route planning, multi-agent coordination	Medium	NATO MUSCLE Project-multi-agent formation control with GA

PID: Proportional-Integral-Derivative, LQR: Linear Quadratic Regulator, MPC: Model Predictive Control, RL: Reinforcement Learning, DL: Deep Learning, ASV: Autonomous Surface Vehicles, LiDAR: Laser Detection and Ranging

warfare to small-scale regional conflicts. Additionally, they address defense needs such as combating asymmetric threats and terrorism, contributing to nations' ability to achieve their strategic goals.

Rapidly advancing technology, along with commercial and military requirements, has expanded the autonomous maritime vehicle market, creating substantial opportunities for both established manufacturers and new entrants aiming to join the sector. However, among the three primary categories of unmanned vehicles (air, land, and maritime), maritime vehicles have received the least attention and funding in recent years. Nevertheless, considering the cost efficiency and risk-reducing advantages of unmanned maritime vehicles, this trend is expected to shift significantly in favor of maritime systems in the near future. Today, the global unmanned maritime vehicle market has evolved into a dynamic ecosystem driven by new research, development, and procurement initiatives.

From a military perspective, unmanned maritime vehicles are primarily used for missions such as reconnaissance, surveillance, mine countermeasures, anti-submarine warfare, and combating terrorism and smuggling. Additionally, nations rely on these systems to address challenges such as irregular migration and illegal activities, safeguard commercial maritime logistics, protect offshore energy infrastructure, and monitor the marine environment. These vehicles play a critical role in observing relevant activities and enabling effective and timely responses in these areas.

Unmanned Maritime Systems (UMS) can operate on or beneath the surface of the sea. Surface-based unmanned vehicles are referred to as Autonomous Surface Vehicles (ASVs), while those operating underwater are known as Unmanned Underwater Vehicles [6].

Unmanned ships are defined as vessels capable of operating autonomously or via remote control without requiring a crew. In this context, unmanned systems are positioned as an overarching concept that also encompasses autonomous ships.

In European maritime circles and by the International Maritime Organization (IMO), unmanned ships are defined as vessels "capable of operating with varying degrees of independence from human interaction". For such vessels, the terms "Unmanned Surface Vehicles" (USVs) and "Maritime Autonomous Surface Ships" are commonly used (Figure 1) [7,8].

The primary vulnerabilities of unmanned systems include the limited range of operations due to their short range, the need for protection, the requirement for interoperability with other systems, the demand for wide bandwidth for communication, sensitivity to electronic jamming, and limited capability in handling uncertainties compared to manned systems [9]. Another significant vulnerability of autonomous weapons and systems is that their software is often open-source, making it susceptible to being purchased or copied.

Unmanned systems used autonomously offer various advantages, such as immunity to communication interruptions since they are not controlled from a remote command center, resistance to electronic jamming, and the difficulty of determining their location (Table 2) [5].

Advancements in engineering, sensor technology, and particularly computer systems and information technology,

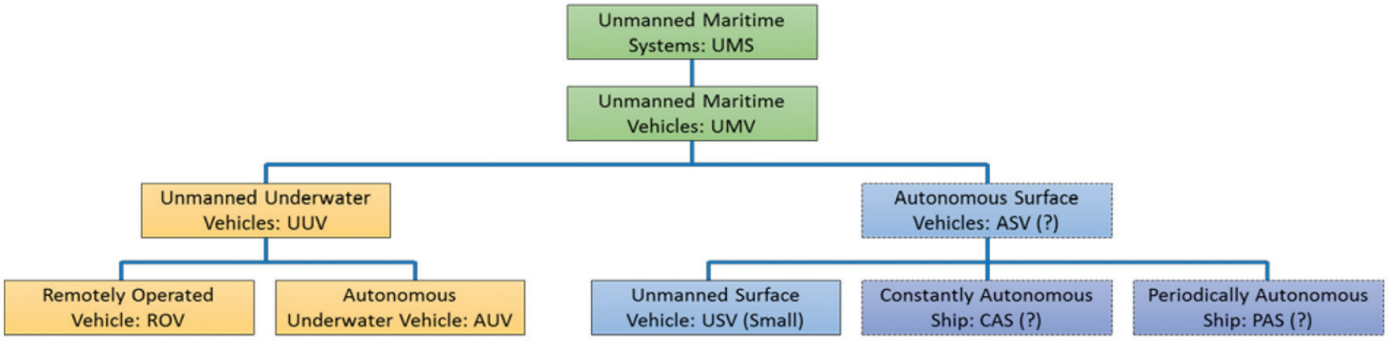


Figure 1. General classification of unmanned maritime systems [8]

Table 2. Comparative analysis of algorithms in autonomous systems under real-world maritime conditions

Algorithm	Accuracy	Robustness	Computational efficiency	Adaptability
PID	Good	Moderate	Excellent	Low
LQR	Excellent	Moderate	Good	Moderate
MPC	Excellent	Good	Moderate	Moderate
RL	Excellent	Excellent	Low	Excellent
DL	Excellent	Good	Low	Excellent
Fuzzy logic	Moderate	Excellent	Moderate	Moderate
Heuristic (GA, PSO, etc.)	Moderate	Moderate	Moderate	Moderate

PID: Proportional-Integral-Derivative, LQR: Linear Quadratic Regulator, MPC: Model Predictive Control, RL: Reinforcement Learning, DL: Deep Learning

have enabled greater utilization of the potential of unmanned systems. However, today's unmanned systems are far from being fully autonomous in making and executing decisions as often perceived. Due to the sensitive nature of tasks such as weapon usage, these systems currently operate primarily through methods that involve human oversight.

The Unmanned Systems Integrated Roadmap published by the U.S. Department of Defense defines unmanned systems as either "self-administered" or "self-decision-making" systems based on their capabilities and designs. In this context, unmanned systems are categorized into three main types: semi-autonomous (human in the loop), supervised autonomous (human on the loop), and fully autonomous (human out of the loop) [10]. The fundamental assumption of this classification is that future unmanned systems will require more advanced capabilities than the current systems, which possess limited autonomy. Furthermore, these capabilities are expected to include the simultaneous sharing of critical data, such as situational awareness and targeting information, with other unmanned systems and manned platforms. This will necessitate an enhancement in the interoperability capacity of unmanned systems [6].

The United Nations Convention on the Law of the Sea states that ensuring adequate crew onboard ships, in accordance with international standards, is the responsibility of the flag state. Additionally, the International Convention for the Safety of Life at Sea, which establishes minimum safety standards for the construction, equipment, and operation of commercial ships, mandates that flag states ensure an adequate number of personnel to guarantee the safe navigation of ships.

In this context, Lloyd's Register, IMO and Society of Automotive Engineers has classified the levels of autonomy and control methods for maritime vessels as outlined below (Table 2) [11].

Table 3. Comparison of autonomy level definitions by Lloyd's register [12], International Maritime Organization, and Society of Automotive Engineers International

Level	Lloyd's Register-Maritime	IMO-Maritime Autonomous Surface Ships	SAE-Automotive
0	No automation; all decisions and actions by human crew	Not formally defined	No automation-Full human control of all operations
1	Decision-support only; onboard crew makes all final decisions	Ship with automated processes and decision support	Driver assistance-System assists with steering or acceleration (e.g., cruise control)
2	Automated control with human-in-the-loop onboard	Remotely controlled ship with crew onboard	Partial automation-System controls both steering and acceleration; driver monitors
3	Automated decision-making and control; remote control capability	Remotely controlled ship without crew onboard	Conditional automation-Vehicle handles all tasks, but human must intervene when requested
4	Remotely controlled or supervised from shore, with high automation	Fully autonomous ship: capable of operating independently without human intervention	High automation-Vehicle performs all tasks under defined conditions; no driver attention needed
5	Fully autonomous ship, no human involvement at any time	(Covered under level 4 implicitly)	Full automation-Vehicle can handle all conditions, no human driver required

IMO: International Maritime Organization, SAE: Society of Automotive Engineers

Autonomous systems, while operating as programmed, require robust protection against external interference. Exploiting gaps in engagement rules poses a potential risk of disrupting these systems. Additionally, unlike humans, autonomous systems lack empathy - at least at present - which prevents them from exercising judgment in avoiding escalation or disproportionate actions during conflicts.

Despite the advantages offered by unmanned systems, any vulnerabilities within the system could be exploited, potentially escalating tensions and leading to conflict. Therefore, a highly cautious approach must be adopted when deploying such systems, particularly in sensitive operations [13].

Recent advancements in artificial intelligence, sensor technology, and communication systems have enabled the development of more advanced unmanned maritime vehicles with autonomous operation and real-time data collection capabilities. These systems utilize sophisticated sensors, sonars, and imaging technologies to gather valuable data for scientific research, defense, and commercial applications in marine and underwater environments (Figure 2).

Today's electronic technologies have the capability to distinguish between a warship and a commercial vessel. Additionally, maritime and civil aviation regulations, along with navigational and flight safety measures, ensure that neutral and friendly entities do not enter the operational area, thereby minimizing the risk of collateral damage. Due to the nature of naval warfare, autonomous weapon systems can be programmed to target only military objectives for ethical and legal reasons, ensuring full compliance with the principles of military necessity, target discrimination, and proportionality.

Automation and robotics are among the most critical elements in the development of unmanned systems, enabling these vehicles to operate autonomously or semi-autonomously without human control. These technologies play a pivotal role in enhancing the capabilities, efficiency, and effectiveness of unmanned systems across various domains.

Automation facilitates autonomous navigation and the execution of predefined tasks in unmanned systems. This allows the vehicles to plan their routes and missions, avoid obstacles, and adapt to changing environments without human intervention. Operators can program tasks, set routes, and define targets through software interfaces. Moreover, automation optimizes the operation of payloads, sensors, and onboard devices, managing processes such as automatic control systems, fault detection and response mechanisms, sensor calibration, data collection, and image processing. These processes enable unmanned vehicles to collect and analyze information in real time (Figure 3).

The rapid advancements in AI and maritime technologies allow UMS to operate in a coordinated manner at predefined levels of autonomy. The success of joint maritime operations involving unmanned systems relies on reliable and robust information networks to support propulsion, machinery operation, and mission execution. Manned warships, in turn, must enhance their capabilities in monitoring the maintenance and repair processes of the unmanned vessels they host, as well as in effectively utilizing weaponry and information systems [16].

Integrating a hybrid fleet composed of manned and unmanned platforms poses several challenges under existing

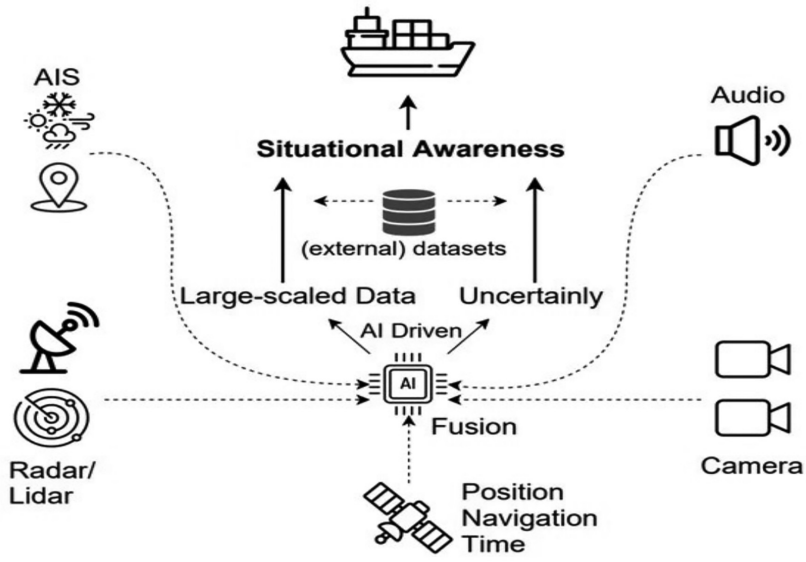


Figure 2. General overview of an AI-focused maritime situational awareness system [14]

AI: Artificial intelligence

international laws. These challenges include conducting operations in compliance with the rules of armed conflict, determining the legal status of unmanned platforms as ships, and implementing regulations to ensure safe navigation at sea.

3. Advances in Autonomous Maritime Systems: AI, Decision-Making, and Simulation Platforms

Significant progress has been made in machine learning applications for autonomous systems, particularly in decision-making, prediction, optimization, and threat detection processes. These advancements are driving developments in areas such as more powerful computational capabilities and intelligent algorithmic functionality. Optimizing the capabilities of autonomous systems increasingly requires specialized computational technologies, including software models for simulation purposes, software development processes for autonomy and mission planning, large data repositories integrating analytics and machine learning, and the integration of open-source commercial software into systems [Figure 4) [17].

AI-based navigation systems enable unmanned maritime vehicles to operate autonomously in complex environments such as open seas, ports, and coastal areas. These systems utilize route planning algorithms to optimize navigation paths based on factors such as weather and sea conditions, maritime traffic, and mission-specific objectives, ensuring efficient and safe operation of unmanned vehicles.

Machine learning algorithms play a crucial role in tasks such as real-time map creation, obstacle detection, underwater object identification and classification, and safe route planning for autonomous platforms. During these processes, data collected from sensors like satellite positioning systems, radar, and sonar are analyzed. With the assistance of AI and machine learning techniques, UMS can effectively perform tasks such as environmental sensing, monitoring, search and rescue operations, maritime security and surveillance, control and decision-making, preventive maintenance, and system fault monitoring (Table 4).

The integration of AI and machine learning algorithms into UMS has revolutionized these systems, significantly enhancing autonomy, systemic intelligence, and operational effectiveness across a wide range of applications. Dr. Jacquelyn Schneider, an assistant professor at the U.S. Naval War College, asserts that the winners of future wars will be nations that can most effectively leverage autonomy and human-machine integration [19].

Research continues to integrate robotic technologies with autonomous systems in areas such as big data processing, motion sensor technology, voice and image recognition, human-machine interaction, and decision-making processes. The design of unmanned ships must focus on developing obstacle detection and avoidance capabilities that account for real-world conditions to ensure navigational safety. Additionally, supporting remote control requires a range of sensor components, including visual and thermal camera systems, long- and short-range precision radars, laser detection and ranging devices, GPS, Automatic Identification System (AIS), and Electronic Chart Display and Information System (Figure 5) [20].

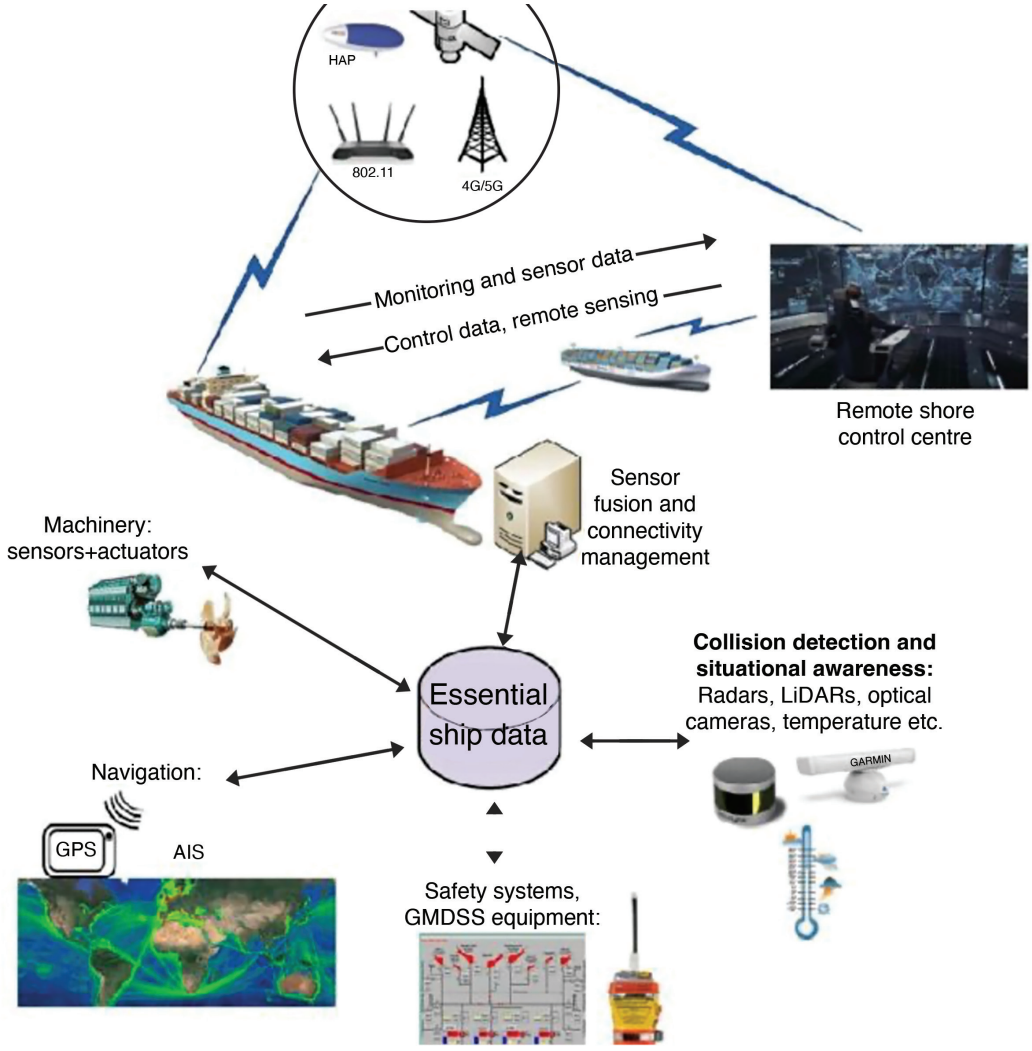


Figure 3. Communication architecture of an autonomous ship [15]

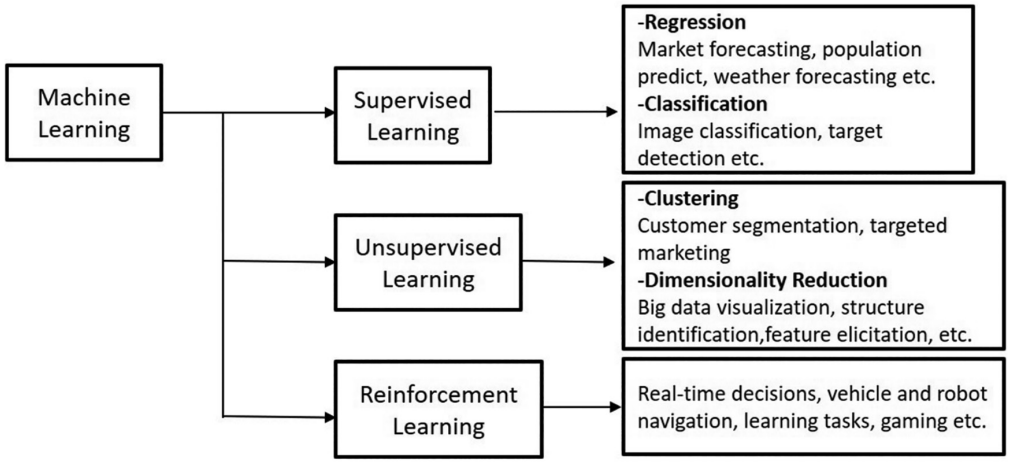


Figure 4. Different types of machine learning in autonomous systems [18]

Table 4. Software tools and simulation platforms for autonomous maritime systems

Tool/Platform	Purpose	Description/Use case
MATLAB marine toolbox	Modeling & control design	Toolbox for marine vehicle dynamics, control design (PID, LQR, MPC), wave modeling
Simulink	Block-diagram simulation	Used for simulating marine autopilots, mission control, sensor integration
MOOS-IvP	Autonomy engine for marine vehicles	Open-source tool for mission planning, behavior-based control, especially for USVs/UUVs
ROS2	Middleware for robotic control	Widely used in autonomous robotics; marine extensions available; works with sensors & navigation
Gazebo + ROS2 (UUV Simulator)	3D physics-based marine simulation	Used for simulating autonomous underwater vehicles (AUVs/UUVs), sensor feedback, physics
ArduPilot/Mission planner	Real-time USV firmware and GCS	Open-source autopilot with USV mode; good for building and testing small-scale autonomous boats
Unity/Unreal engine	Visualization & HMI simulation	Ideal for simulating human-machine interaction and visual autonomy environments
OpenSeaLab	Real-time ocean data visualization	For training, testing algorithms with real-world oceanographic and vessel data
QGIS + AIS data	Geospatial traffic data analysis	Useful for analyzing vessel movement patterns and creating data-driven navigation models
BlueROV2/BlueSim	Commercial AUV with associated simulation	Often used in research labs; ROS-compatible underwater platform for algorithm testing

ROV: Robot Operating System, PID: Proportional-Integral-Derivative, LQR: Linear Quadratic Regulator, MPC: Model Predictive Control, AUV: Autonomous Underwater Vehicles, UUV: Unmanned Underwater Vehicle, AIS: Automatic Identification System

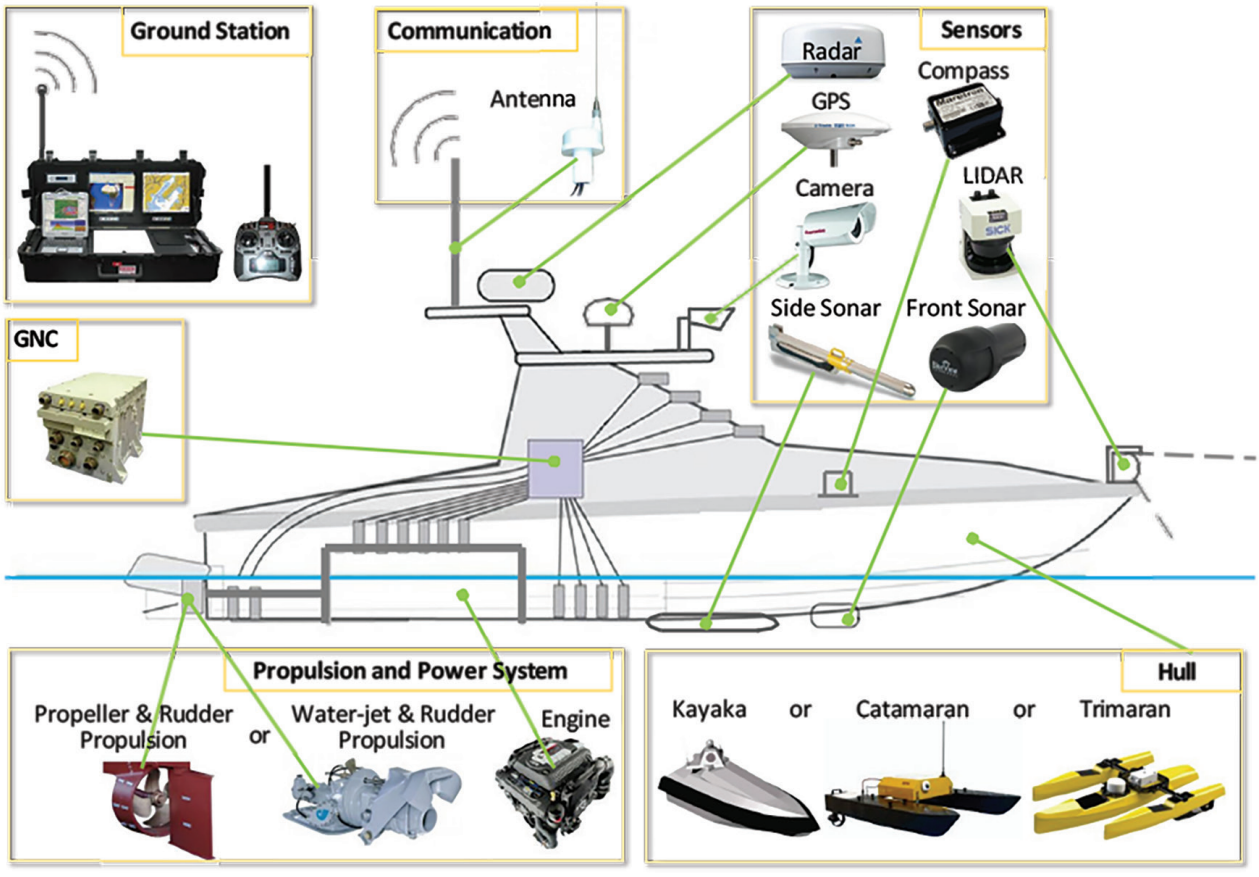


Figure 5. System requirements for autonomous maritime vehicles [21]

UMS are equipped with various technologies designed to address the following tasks and requirements:

• **Environmental Sensing and Monitoring:** Sonar and radar systems, along with hydrophones, are used for underwater activity surveillance. Environmental sensors measure parameters such as water temperature, salinity, and pH levels.

• **Accurate Positioning and Route Planning:** For precise navigation in open seas and coastal areas, global navigation satellite systems (GNSS) are utilized. In cases of GNSS signal interruptions, inertial measurement units, Doppler velocity units for seabed-referenced speed measurement, and dynamic positioning systems are essential.

• **Surveillance and Reconnaissance:** Optical and infrared cameras, radar systems, and AIS are employed to monitor maritime traffic and detect threats.

• **Sensor Data Integration:** Sensor data fusion techniques integrate information from multiple sensors. Machine learning algorithms analyze this data to enhance maritime security and surveillance capabilities. Predictive analytics techniques are used to anticipate potential risks in dynamic marine environments, plan proactive responses, and optimize mission outcomes.

• **Route Optimization and Decision Support:** Decision support systems are utilized to optimize navigation routes, minimize travel time, fuel consumption, and environmental impact, and provide real-time insights, recommendations, and situational awareness.

These technologies enable UMS to perform their tasks efficiently, safely, and effectively.

Autonomous systems, which enhance operational efficiency, reduce costs, and provide strategic advantages in the defense and maritime sectors, are recognized as innovative technologies. In this context, Multi-Criteria Decision-Making (MCDM) methods offer a comprehensive and scientific framework to evaluate the strategic importance and operational impacts of autonomous systems.

One such method, the Analytic Hierarchy Process (AHP), quantitatively contributes to decision-making by analyzing the relative importance of criteria within a hierarchical structure, systematically prioritizing the identified criteria. Another method, Technique for Order Preference by Similarity to Ideal Solution (TOPSIS), ranks alternatives based on their proximity to the ideal solution, enabling the objective selection of the most suitable option.

These methods provide decision-makers with the opportunity to develop scientific and objective strategies by addressing autonomous maritime systems in the context of technology, operational requirements, safety, and ethical-legal standards. Consequently, the analyses offered by MCDM methods serve as valuable tools for strategic planning and play a significant role in shaping technology and defense policies.

4. Future Outlook of Autonomous Systems: Findings

The future of autonomous unmanned systems presents significant potential for innovation and societal impact. Advances in artificial intelligence, robotics, and sensor technologies are expected to further enhance the capabilities of autonomous systems, enabling them to perform increasingly complex tasks in diverse environments. However, challenges such as cybersecurity threats, ethical and legal issues, and societal acceptance of autonomous technologies highlight the need for interdisciplinary collaboration and the development of appropriate policies. Nevertheless, it is evident that AI and robotics hold the potential to revolutionize industries and enhance efficiency.

In the future, unmanned systems are expected to be equipped with more advanced autonomous capabilities. These platforms will need enhanced capabilities to communicate directly with each other without human intervention to perform tasks in a coordinated manner. Furthermore, their interoperability is anticipated to surpass current levels [6].

Below are some of the challenges and development opportunities for autonomous systems in the future:

• **Energy Storage:** Advances in energy storage technologies, such as fuel cells and advanced batteries, will enable unmanned and autonomous maritime systems to operate for extended durations and achieve greater operational ranges. Continuous operations will facilitate long-term research activities and consistent monitoring of marine environments.

• **Underwater Communication:** Improving underwater communication capabilities remains a critical challenge for autonomous underwater systems. Developing reliable, high-bandwidth communication systems for data transmission, command-and-control, and remote operation will enhance the effectiveness and autonomy of these systems.

• **Regulatory Frameworks:** Clear regulatory frameworks and guidelines are essential to ensure the safe and compliant operation of autonomous maritime systems in marine environments. Addressing navigation and collision avoidance rules, data privacy, and environmental protection regulations will facilitate the broader integration of these systems into maritime operations and ensure their compatibility with other systems.

• **Sensor Technology and Data Analytics:** The effective use of sensor technologies and data analytics will remain a critical component of UMS. These advancements will allow autonomous systems to operate efficiently in challenging

marine environments and navigate with situational awareness.

• **Cybersecurity Threats:** Operations involving the transmission of large volumes of information or the use of classified weapon systems through cyber technologies could overwhelm critical platforms, such as aircraft carriers and air defense systems, within the operational theater. To successfully execute operations aimed at denying access to physical and informational domains, planning cybersecurity measures and countermeasures is essential [22].

To minimize risks and prevent accidents associated with the use of autonomous systems, prioritizing security, reliability, and resilience is critical. Cybersecurity measures, fault-prevention mechanisms, and backup procedures must be incorporated into the design, testing, and operation of these systems. Additionally, developing legal, ethical, and sustainable solutions will reduce risks for both personnel and civilians. Supporting innovation in unmanned system technologies should be a key part of research and development efforts.

Designing autonomous systems with a modular structure to adapt to various task types is of great importance. Defining weapon, system, and device configurations suitable for mission profiles will increase the flexibility of these systems. Furthermore, software infrastructure should be designed to allow easy integration of new versions and updates in parallel with technological advancements.

In the coming years, autonomous systems equipped with swarm intelligence are expected to work in coordination, enhancing operational efficiency. These systems can minimize risks and maximize mission success in complex tasks. Supported by AI, swarm intelligence, and machine learning techniques, these systems must be integrated into national defense ecosystems with a comprehensive strategy to ensure the sustainability of unmanned vehicles.

Collaboration between academia and industry should be prioritized strategically to strengthen the knowledge and technological infrastructure of the autonomous maritime systems sector. Developing creative solutions for training qualified human resources, effectively utilizing this infrastructure, and enhancing competitiveness is essential. In the near future, the concept of military security is expected to be reshaped by the capabilities of AI-supported autonomous platforms. These platforms can increase situational awareness, enable faster and more accurate decision-making, and effectively handle tasks that pose risks to human life (Table 5).

The sustainability and effectiveness of autonomous maritime systems depend on successfully managing the risks and limitations these technologies may encounter. In particular, making these systems resilient against cybersecurity threats and compliant with ethical and legal standards will significantly enhance their success and societal acceptance. Addressing legal gaps, ethical concerns, and aligning with international regulations will support the broader adoption of autonomous maritime systems.

Moreover, combining MCDM methods such as AHP and TOPSIS with innovative approaches supported by machine learning, swarm intelligence, and AI-based technologies will enhance the sustainability and effectiveness of these systems in both military and civilian applications.

Advances in autonomous surface and underwater systems offer new opportunities for maritime surveillance, environmental monitoring, commercial operations, and scientific research. Progress in technology, integration, and collaboration will enhance the capabilities and effectiveness of these systems, paving the way for safer, more efficient, and sustainable maritime operations. Unmanned systems provide unique capabilities for reconnaissance, surveillance, and naval operations, granting strategic advantages to navies. As technology evolves, these systems will offer innovative solutions to address challenges and threats, shaping the future of maritime operations.

5. Conclusion and Evaluation

The proliferation of autonomous systems plays a significant role in transforming 21st-century military power. Robotics, autonomous systems, and AI-based capabilities have become the cornerstones of modern warfare strategies. These technologies reduce the reliance on human involvement while enabling the successful execution of more complex and risky missions.

Rapid technological advancements compel a reevaluation of traditional practices and the development of innovative strategies. Enhancing capabilities in areas such as data analytics, cybersecurity, and autonomous systems necessitates a flexible and proactive approach. To establish a more effective defense structure against modern threats, traditional strategies must be reinterpreted within the framework of emerging technologies, with existing strategies modified as needed.

Continuous advancements in sensor technology, AI, and unmanned systems are increasingly shaping the future of naval operations. These systems also assist navies in operating more cost-effectively in challenging maritime environments. In this context, it is crucial to clearly define strategic objectives and establish appropriate task groups. Smaller, highly capable unmanned assets, which are likely to constitute the future combat fleet, can also serve as part of task groups, contributing to the achievement of these strategic goals [23].

Table 5. Selected case studies of control methods in real-world autonomous maritime systems

Project/Vessel	Application domain	Method used	Performance highlights	Type
Sea hunter-DARPA (USA)	Long-range autonomous patrol and ASW	RL + Classical control (PID/LQR)	Robust navigation in dynamic environments; adaptive obstacle avoidance	Military
Rolls-Royce AAWA project	Commercial cargo ship autonomy	MPC + Deep RL	Accurate route planning, real-time collision avoidance	Commercial
NTNU-YARA Birkeland	Autonomous zero-emission cargo ship	PID/Classical control	Energy-efficient station keeping and harbor maneuvers	Commercial
NATO MUSCLE	Multi-agent underwater & surface surveillance	GA + Distributed RL	Optimized multi-vehicle coordination under communication constraints	Military
Kongsberg maritime-ASV	Autonomous harbor and offshore operations	Fuzzy Logic + PID	Reliable control in uncertain marine conditions (e.g., weather, currents)	Commercial
MIT-USV experimental platform	Experimental adaptive path planning	RL + MPC hybrid	Dynamic decision making in simulated real-time maritime environments	Research

ASW: Anti-submarine Warfare, PID: Proportional-Integral-Derivative, RL: Reinforcement Learning, MPC: Model Predictive Control, GA: Genetic Algorithms, ASV: Autonomous Surface Vehicles

To strengthen the strategic advantages of autonomous maritime systems and optimize their performance, the broader application of MCDM methods, such as AHP and TOPSIS, is considered essential. These methods not only enhance the current performance of systems but also contribute to the development of more resilient configurations capable of addressing future risks. This approach, supported by MCDM methods, ensures the sustainability of autonomous maritime systems while establishing a solid foundation for achieving strategic objectives. As a result, innovative technologies in the defense and maritime sectors can be utilized more effectively and reliably.

Once countries develop unmanned vehicles, they must equip them with the necessary sensors, information technology, and AI capabilities to ensure seamless functionality without personnel shortages. Additionally, a guiding and proactive management approach should be adopted when defining strategic objectives related to the use of these vehicles. Parallel to advancements in information technology, the integration of innovations into systems, the creation of purpose-built modular designs, and the operation of a disciplined process to align new investments with existing resources and strategic needs are imperative [24].

In conclusion, capabilities such as swarm intelligence and machine learning, which enable autonomous systems to perceive their environment, adapt to threats, and perform complex tasks, will play a game-changing role in the future of warfare technologies.

Footnotes

Authorship Contributions

Concept: U. B. Çelebi, Design: U. B. Çelebi, Data Collection or Processing: S. Kula, Analysis or Interpretation: U. B. Çelebi, Literature Review: S. Kula, Writing: S. Kula.

Conflict of Interest: No conflict of interest was declared by the authors.

Financial Disclosure: The authors declared that this study received no financial support.

References

[1] B. İğlikçi, *Deep force intelligence*, İstanbul: AZ Yayıncılık, 2020, p. 65.

[2] G. Diesen, *Great power politics in the fourth industrial revolution*, New York: Bloomsbury Publishing, 2021, p. 43.

[3] E. Karakoç, and B. Yılmaz, "Military power and technological transformation," *International Journal of Social Research,* vol. 13, no. 72, pp. 229-241, Aug 2020.

[4] G. Agoston, "Ottoman firearms and the debate on military revolution," 2020.

[5] O. Tekinalp, *Introduction to strategy and naval strategy: Basic concepts, tactical information, and historical examples*, İstanbul: Doruk Yayınevi, 2020.

[6] D. Gonzales, and S. Harting, *Designing unmanned systems with greater autonomy*, Santa Monica, CA: RAND Corporation, 2014.

[7] F. Gözüyeşil, "Good seamanship principle and look-out duty on unmanned and autonomous ships in the context of the convention on the international regulations for preventing collisions at sea, 1972 (COLREGs)," *Adalet Dergisi,* vol. 1, no. 66, pp. 193-225, 2021.

[8] NFAS, "*Definition of autonomy levels for merchant ships*," in Norwegian Forum for Autonomous Ships, 2017.

[9] R. Erdağ, "The changing nature of war and conflict: The demilitarization of weapons," *Journal of Security Strategies,* vol. 22, no. 1, pp. 16, 2020.

[10] C. Kasapoğlu, and B. Kırdemir, "The emerging unmanned systems power: Turkey on the verge of a military breakthrough," *EDAM Foreign Policy and Security Journal*, vol. 5, p. 13, 2018.

[11] F. Bolat, and Ö. Koşaner, "Current status of unmanned ships," *European Journal of Science and Technology,* vol. 23, pp. 346-358, Apr 2021.

[12] L. Register, "*Levels of autonomy according to Lloyd's Register,*" [Online]. Available: https://www.researchgate.net/figure/Fig-Levels-of-autonomy-according-to-Lloyds-Register_fig2_354922331

[13] P. Scharre, *Unmanned armies: Killer robots, autonomous weapons, and machine wars* (K.A. Çetinalp Trans.), Istanbul: Kronik Kitap, 2020.

[14] J. Yoo, "*Formulating cybersecurity requirements for autonomous ships using the SQUARE methodology*," 2023.

[15] M. Höyhtyä, J. Huusko, M. Kiviranta, K. Solberg, and J. Rokka, "*Connectivity for autonomous ships: Architecture, use cases, and research challenges*," in 2017 International Conference on Information and Communication Technology Convergence (ICTC), Jeju, Korea (South), 2017.

[16] J. Panter, and J. Falcone, "*Feedback loops and fundamental flaws in autonomous warships,*" 24 June 2022. [Online]. Available: https://warontherocks.com/2022/06/feedback-loops-and-fundamental-flaws-in-autonomous-warships/

[17] U. S. G. A. Office, "*Uncrewed maritime systems (Report to Congressional Committees)*," 2022.

[18] J. Ye, "Deep learning in maritime autonomous surface ships: Current development and challenges," *Journal of Marine Science and Application,* vol. 22, no. 3, pp. 584-601, Sep 2023.

[19] J. Schneider, "*Blue hair in the gray zone,*" 10 January 2018. [Online]. Available: Retrieved from: https://warontherocks.com/2018/01/blue-hair-gray-zone/.

[20] H. Kara, "The usage of artificial intelligence in ships and legal issue," *Süleyman Demirel Law Review,* vol. 10, no. 1, pp. 17-51, Jun 2020.

[21] Z. Liu, Y. Zhang, X. Yu, and C. Yuan, "Unmanned surface vehicles: An overview of developments and challenges," *Annual Reviews in Control,* vol. 41, p. 71-93, 2016.

[22] A. Burilkov, and T. Geise, "Maritime strategies of rising powers: developments in China and Russia," *Third World Quarterly,* vol. 34, no. 6, pp. 1037-1053, 2013.

[23] W. P. Hughes, "Naval operations: A close look at the operational level of war at sea," *Naval War College Review*, vol. 65, no. 3, p. 44, 2012.

[24] R. O'Rourke, "*Navy large unmanned surface and undersea vehicles: background and issues for Congress*," Congressional Research Service Report, 2023.

RESEARCH ARTICLE

DOI: 10.54926/jnamt.2025.2410

J Nav Architect Mar Technol 2025;227(1):34-42

Exergy Based Ecological Performance Analysis of a Waste Heat-Powered Marine Refrigeration Cycle

Oğulcan Yılmaztürk, Asım Sinan Karakurt

Yıldız Technical University Faculty of Naval Architecture and Maritime, Deparment of Naval Architecture and Marine Engineering, İstanbul, Türkiye

To cite this article: O. Yılmaztürk, and A. S. Karakurt. Exergy based ecological performance analysis of a waste heat-powered marine refrigeration cycle. *J Nav Architect Mar Technol*. 2025;227(1):34-42.

Received: 22.11.2024 - **Revised:** 20.02.2025 - **Accepted:** 18.03.2025 - **Publication Date:** 29.05.2025

Abstract

The escalating costs of fuel, global fuel supply disruptions, and stringent international emissions regulations necessitate more efficient ship operations. A key component of environmentally sustainable, economical, and efficient marine transportation is the recovery and utilization of waste heat. This study investigates the potential of converting waste heat from ship exhaust gas into useful energy through an organic Rankine cycle and its subsequent integration into a refrigeration system. In this study, the thermodynamic performance of the refrigerants R717, R152a, R290, and R134a was investigated. The findings demonstrate that R717 exhibits superior performance in terms of utilization factor and second law efficiency (η_{II}), while R290 emerges as the optimal choice when minimizing total entropy generation (s_{gen_TOT}) is the primary objective. If the priorities are focused on maximizing useful work production, minimizing energy losses, and reducing environmental impacts, the advantages of the R717 refrigerant, which has the highest total ecological coefficient of performance (ECOP) and exergetic performance criteria (EPC) values, are clearly evident. The ideal operating temperatures for evaporator temperature (T_{Evap}) and turbine temperatures ($T_{Turbine}$) concerning *EPC* and *ECOP*, using R717 as the refrigerant, were investigated in the continuation of the study. During this investigation, changes in T_{Evap} and $T_{Turbine}$ were observed to have affected other components. When the T_{Evap} is kept constant, and the $T_{Turbine}$ amount is increased, an improvement was observed in EPC_{TOT}, $ECOP_{TOT}$, η_{II}, and utility factor values, while an increase in s_{gen_TOT} and exergy destruction (ExD_{TOT}) values. When the $T_{Turbine}$ is kept constant, a decrease is observed in the EPC_{TOT} value. At the same time, an improvement is seen in ExD_{TOT}, η_{II}, and $ECOP_{TOT}$ values, while an increase is noted in the s_{gen_TOT} value.

Keywords: ECOP, EPC, heat-powered refrigeration, temperature management, waste heat recovery

1. Introduction

Contemporary engineering systems must prioritize cost-effectiveness, efficiency, and environmental sustainability. To reach these objectives, various strategies for enhancing efficiency and minimizing environmental impact are implemented throughout land and marine vehicles' design and operational phases. In the maritime domain, common approaches include resistance reduction techniques, the adoption of alternative fuels, operational optimizations, design parameters such as energy efficiency design index and energy efficiency existing index, and the recovery and utilization of waste heat [1]. Ships often generate substantial waste heat from systems like main engine cooling, lubrication, and flue gas [2]. This heat can be harnessed for various applications, including direct heating of tanks or fuel, steam generation [3], power generation, or cooling

Address for Correspondence: Asım Sinan Karakurt, Yıldız Technical University Faculty of Naval Architecture and Maritime, Deparment of Naval Architecture and Marine Engineering, İstanbul, Türkiye

E-mail: asinan@yildiz.edu.tr

ORCID ID: orcid.org/0000-0002-6205-9089

Copyright© 2025 The Author. Published by Galenos Publishing House on behalf of UCTEA Turkish Chamber of Naval Architects and Marine Engineers.
Licensed under a Creative Commons Attribution-NonCommercial-NoDerivatives 4.0 (CC BY-NC-ND) International License

through different thermodynamic cycles [4]. However, ships also face significant cooling demands for spaces, food stores, and transported cargo [5]. To meet these cooling needs, engineers explore alternative approaches beyond traditional vapor compression refrigeration (VCR) systems. These include absorption or organic Rankine cycle (ORC) driven VCR systems utilizing waste heat, as well as hybrid methods combining both approaches.

The existing literature encompasses a diverse range of investigations into ORC-driven combined cooling systems or dual-cycle configurations for marine applications and low-temperature heat sources. Comparative performance assessments of various heat-powered refrigeration cycles, including absorption cycles, multi-stage arrangements, and combined heat-power systems, have been reported [6]. Thermodynamic analyses of ORC-VCR systems utilizing low-temperature source heat have been conducted for different working fluids and design parameters, leading to insights into optimal fluid selection and equipment [7-9]. Optimization studies have focused on refining design and operational parameters of ORC-VCR systems based on varying working fluids and heat source temperatures [10,11]. Exergy-based performance analyses have explored the impact of different working fluids, heat sources, and system layouts on ORC-VCR system efficiency [12-14]. Experimental investigations have been conducted to evaluate the performance of ORC-VCR systems recovering waste heat from internal combustion engines [15].

Exergetic performance analysis and optimization of air refrigeration cycles based on ecological coefficient of performance (ECOP) were studied by [16]. Analyses of exergy-based performance outputs, including exergetic performance criteria (EPC) analyses, of the multipurpose refrigeration system for different design conditions were performed by [17]. A recent research study was explored the optimization of simple Brayton refrigeration models using an exergy-based approach to improve ecological function by [18]. Exergy based thermodynamic analysis and optimizations of low temperature cascade refrigeration systems applications were presented by [19,20]. The performance analysis of the heat-powered refrigeration system using marine waste heat energy on the second law of thermodynamics was carried out depends on the different design parameters by [21]. This study will evaluate the performance of a refrigeration system driven by an ORC utilizing waste heat from a ship's diesel engine. The analysis will focus on key performance metrics, including utility factor (U_f), second law efficiency (η_{II}), total entropy generation (s_{gen_TOT}), exergy destruction ratio (y), *ECOP*, and *EPC*. These metrics will be assessed under various operating conditions, considering different working fluids and different evaporator temperatures (T_{Evap}), condenser, and turbine temperatures ($T_{Turbine}$).

2. Thermodynamic Model

The waste heat-powered ORC-VCR system can be conceptualized as two interconnected subsystems that utilize a single working fluid, which can be applied in such as industrial waste heat recovery systems, combined cooling and power systems, data center cooling, or marine systems. The ORC is a thermodynamic cycle that converts heat energy into mechanical work, similar to a steam Rankine cycle but using an organic working fluid (e.g., R134a, R717, 290, etc) instead of water. The ORC component comprises a condenser, pump, waste heat boiler, and steam turbine. The VCR cycle is a standard refrigeration process that absorbs heat from a low-temperature or cooled source and rejects it at a higher temperature. The VCR subsystem includes an evaporator, compressor, condenser, and expansion valve. Figure 1 illustrates the flow diagram of the ORC-VCR system. The ORC effectively converts waste heat from the main engine exhaust gases into a net work, driving the pump and compressor. In cases where the main engine is not operating or cannot provide exhaust gas with sufficient

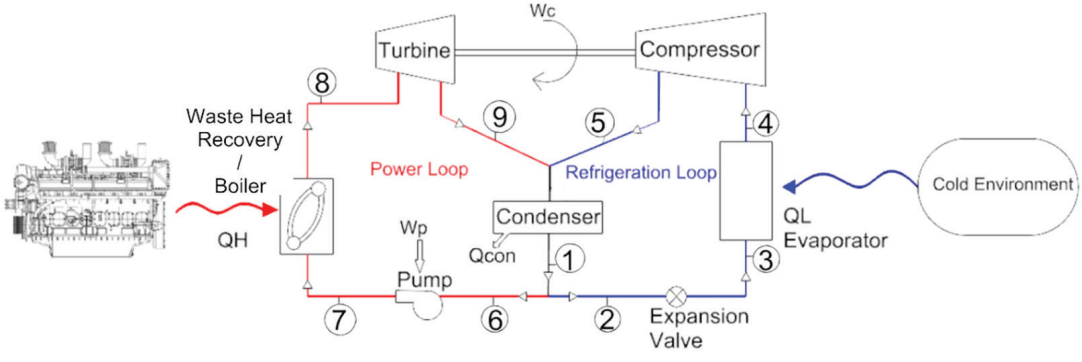


Figure 1. Thermodynamic model of the ORC-VCR system.

ORC: Organic Rankine cycle, VCR: Vapor compression refrigeration

thermal content, the boiler is activated and thus continuity in the cooling system is ensured. The VCR then leverages this energy to refrigerate the storage compartments.

The fundamental design parameters and associated assumptions are outlined below. The heat addition to the ORC, Q_H, is calculated based on exhaust gas properties, including mass flow rate and inlet temperature ($T_{exhaust,in}$). The specific heat capacity at constant temperature (Cp) of the exhaust gases was determined using Equation 1, considering the reference inlet and outlet temperatures.

$$Cp = 956 + \left(0.3389\ T_{exhaust,\,in}\right) - \left(2.476\ 10^{-5}\ T^{2}_{exhaust,\,in}\right) \quad (1)$$

Heat transfer (Q_{Con}, Q_L, and Q_H) values are calculated from the basic balance equations. The U_f, defined by Equation 2, represents the ratio of the refrigeration or cooling load of the VCR system (Q_L) to the heat input to the ORC (Q_H).

$$U_f = Q_L/Q_H \quad (2)$$

The η_{II} calculated with Equation 3 as the ratio of U_f and Carnot U_f (U_{f_Carnot}).

$$\eta_{II} = U_f/U_{f_Carnot} \quad (3)$$

s_{gen_TOT}, as defined by Equation 6, is the sum of the entropy generations from the environment, Equation 4, (Δs_{env}) and the system, Equation 5, (Δs_{sys}). The temperature difference between relevant environments and system points is denoted by ΔT. The heat transfer from the condenser unit (Q_{Con}) is the combined heat transfer from the power loop (PL) and the refrigeration loop (RL). T_{Con} and T_{avr} represent the temperature of condenser for power loop and the average value between condenser inlet and outlet temperature of RL, respectively.

$$\Delta s_{env} = \left(\left(\frac{Q_{con,\,PL}}{(T_{con} - \Delta T)}\right) + \left(\frac{Q_{con,\,RL}}{(T_{avr} - \Delta T)}\right)\right) - \left(\frac{Q_{con,\,PL}}{T_{con} + \left(\frac{Q_{con,\,RL}}{T_{avr}}\right)}\right) \quad (4)$$

$$\Delta s_{sys} = \left(\left(\frac{-Q_H}{(T_H + \Delta T)}\right) - \left(\frac{Q_L}{(T_L + \Delta T)}\right)\right) + \left(\frac{Q_H}{T_H}\right) + \left(\frac{Q_L}{T_L}\right) \quad (5)$$

$$s_{genTot} = \Delta s_{env} + \Delta s_{sys} \quad (6)$$

$$ex = h - h_0 - T_0\left(s - s_0\right) \quad (7)$$

The exergy density (ρ_{ex}) is a beneficial tool to compare the size and exergetic capacity of the system point which was defined the ratio of specific exergy to the specific volume of the system point in Equation 8 by [22].

$$\rho_{ex} = \frac{ex}{v} \quad (8)$$

The exergy destruction (ExD) of components is calculated with Equation 9 which depends on the flow rate and physical exergy of inlet and outlet conditions of components. The total ExD_{TOT} is the sum of all components of ExD as in Equation 10.

$$ExD = \dot{m}\left(ex_{in} - ex_{out}\right) \quad (9)$$

$$ExD_{TOT} = \sum ExD \quad (10)$$

The y can be defined for each component as the ratio of the ExD of components to the ExD_{TOT} of the system in Equation 11 [23].

$$y = \frac{ExD}{ExD_{TOT}} \quad (11)$$

$ECOP$ is defined as ratio of power output to the loss rate of availability in Equation 12 [24] and EPC defines the ratio of total exergy output to the loss rate of availability with Equation 13 [25].

$$ECOP = \frac{W}{T_0\, S_{gen_TOT}} \quad (12)$$

$$EPC = \frac{ex_{out}}{T_0\, s_{gen_TOT}} = \frac{ex_{out}}{ex_{in} - ex_{out}} \quad (13)$$

Some properties such as global warming potential, refrigerant concentration limit of working fluids (R717, R290, R134a, and R152a) according to the ASHRAE [26] were given in Table 1 Assumptions made for the analysis of the system were also shared in Table 2.

The thermodynamic analysis of the marine refrigeration system (MRS) was conducted for the following refrigerants: R717, R290, R134a, and R152a. The analysis relied on the following simplifying assumptions:

- All system components were assumed to operate under steady-state conditions.
- Chemical, kinetic, and potential energy, as well as their corresponding exergy terms, were disregarded.
- Pressure losses within the system's pipelines were considered negligible.
- Heat transfer to or from the compressor and expansion valve was assumed to be insignificant.
- The expansion of refrigerants in the expansion valves was assumed to be isenthalpic.

3. Results and Discussion

To evaluate the performance of the system under different refrigerant conditions, a parametric study was conducted using the established model (Equations 1-13). Four commonly employed refrigerants (R717, R290, R134a, and R152a) were selected. Their corresponding performance

Table 1. Properties of working fluids/refrigerants [26].

Fluid	*Atmospheric lifetime* (years)	*GWP* (100-yr)	ASHRAE [26] safety group	*RCL* (g/m^3)	Normal boiling point (°C)	*Critical temp.* (°C)	*Critical pressure* (kPa)
R717	0.019	0	B2L	320	-33.34	132.40	11.28
R290	13	3.3	A3	9.5	-42.10	96.70	4.25
R134a	14	1430	A1	210	-26.30	101.06	4.06
R152a	1.4	124	A2	32	-25	113.26	4.52

GWP: Global warming potential, *RCL*: Refrigerant concentration limit

Table 2. Assumptions made for the analysis of the system.

Parameters	Units	Values
Ambient temperature (T_0)	(K)	298
Ambient pressure (P_0)	(kPa)	101.325
Evaporator temperature (T_{evap})	(K)	258.15
Condenser temperature (T_{Con})	(K)	318.15
Turbine temperature ($T_{Turbine}$)	(K)	363.15
Temperature difference between cold space and evaporator (ΔT)	(K)	10

metrics, including the U_f, the η_{II}, the $ECOP_{TOT}$, the EPC_{TOT}, the s_{gen_TOT}, and the ExD_{TOT}, were calculated for different turbine and T_{Evap}. The Python 3.11.4 programming language, in conjunction with the CoolProp 8.3 library [27], was employed for the numerical simulations.

The results of this analysis, the information presented in Figure 2 compares the performance outputs of a waste heat-driven marine refrigeration cycle using four different refrigerants. It was observed that the optimal refrigerant choice is contingent upon the specific performance objective. R717 generally exhibits higher U_f, η_{II}, $ECOP_{TOT}$, EPC_{TOT}, and ExD_{TOT} and lower s_{gen_TOT} compared to R290, R152a, and R134a. This suggests that R717 is more efficient in converting waste heat into refrigeration, indicating that ammonia might be a slightly more efficient refrigerant in this specific application, despite its disadvantages for human health.

Temperature (T), pressure (P), specific enthalpy (h), specific entropy (s), mass flow rate (m), specific volume (v), specific exergy (ex), and exergy density (ρ_{Ex}) values of system points for the R717 are presented in Table 3 as thermophysical properties. Our priorities are to maximize practical work production, minimize energy losses, and reduce environmental impacts. In this case, the advantages of R717 refrigerant, which has the highest total *ECOP* and *EPC* values, are apparent.

To evaluate the system's overall performance, it would be helpful to calculate the performance outputs that would

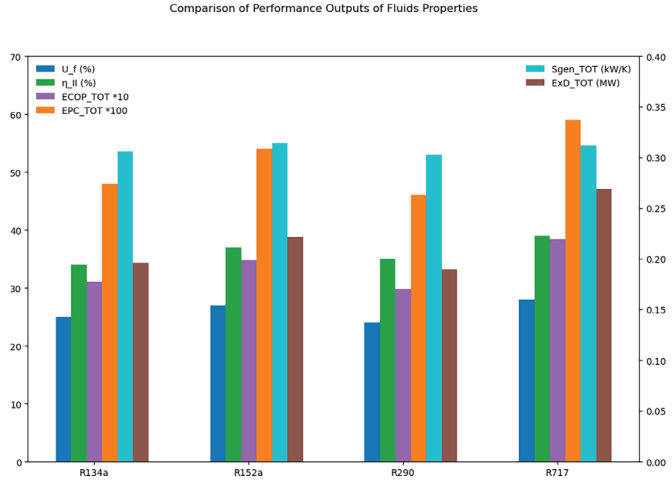


Figure 2. Comparison of performance outputs of different fluids.

η_{II}: Second law efficiency, s_{gen_TOT}: Total entropy generation, $ECOP_{TOT}$: Ecological coefficient of performance, EPC_{TOT}: Exergetic performance criteria, ExD_{TOT}: The exergy destruction, U_f: Utility factor

provide a comprehensive understanding of the system's losses and efficiencies. Table 4 represents performance outputs such as *ExD*, *EPC*, *y*, and η_{II} for the heat-powered MRS components (steam turbine, compressor, condenser, evaporator, expansion valve, pump, and boiler). The table shows that the evaporator has the highest ExD_{TOT} rate and the highest y value, with an almost 41% ratio, and the lowest *ExD* and *y* values belong to the pump unit. It can also be obtained from the table that the heat-related components (condenser, evaporator, and boiler) generate more ExD_{TOT}. Regarding the EPC value, the highest values are for pump and turbine units; the lowest are for heat-related units. By implementing design modifications and operational adjustments to the evaporator, condenser, and boiler units, the system's ExD_{TOT} can be reduced, leading to a notable increase in overall efficiency.

Figure 3 shows the effect of the $T_{Turbine}$ on the system components' *EPC*. As the $T_{Turbine}$ increases, the overall *EPC* generally decreases. Nevertheless, the individual *EPC* contributions of different components demonstrate different

Table 3. Thermophysical properties of system points.

No	*T* (K)	*P* (kPa)	*h* (kJ/kg)	*s* (kJ/kg K)	*m* (kg/s)	*v* (m³/kg)	*ex* (kJ/kg)	ρ_{ex} (MJ/m³)
1	318.15	1,781.67	560.67	2.20	1.654	0.002	324.84	185.62
2	318.15	1,781.67	560.67	2.20	0.348	0.002	324.84	185.62
3	258.15	236.11	560.67	2.33	0.348	0.11	288.72	2.600
4	258.15	236.11	1,589.68	6.31	0.348	0.51	129.92	0.260
5	429.71	1,781.67	1,896.97	6.44	0.348	0.11	452.88	4.050
6	318.15	1,781.67	560.67	2.20	1.306	0.002	324.84	185.62
7	319.47	5,116.42	566.81	2.21	1.306	0.002	330.73	189.65
8	363.15	5,116.42	1,604.99	5.11	1.306	0.02	504.59	21.95
9	318.15	1,781.67	1,483.68	5.16	1.306	0.06	384.43	6.050

T: Temperature, *P*: Pressure, *h*: Specific enthalpy, *s*: Specific entropy, *m*: Mass flow rate, *v*: Specific volume, *ex*: Specific exergy, ρ_{Ex}: Exergy density

Table 4. Performance outputs of the system using R717 for given conditions.

Component	*ExD* (kW)	*EPC*	*y*
Turbine	22.26	28.61	0.083
Compressor	13.41	11.74	0.05
Condenser	53.63	13.30	0.2
Evaporator	110.42	0.41	0.410
Expansion valve	12.56	7.99	0.047
Pump	1.27	340.22	0.005
Boiler	55.18	11.94	0.205

ExD: The exergy destruction, EPC: Exergetic performance criteria, *y*: Exergy destruction ratio

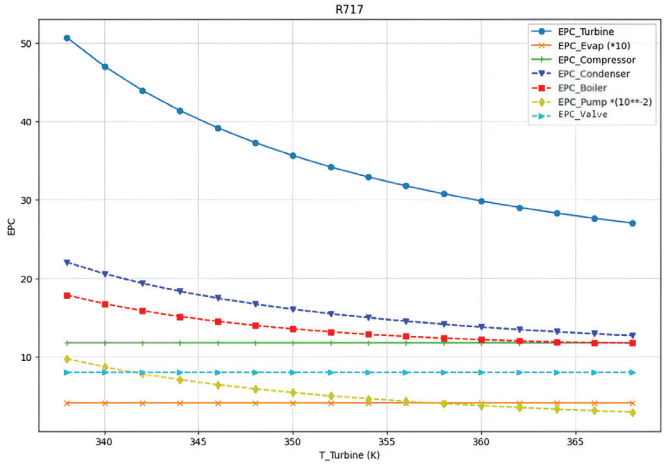


Figure 3. The turbine temperature effects on the EPC values.

EPC: Exergetic performance criteria

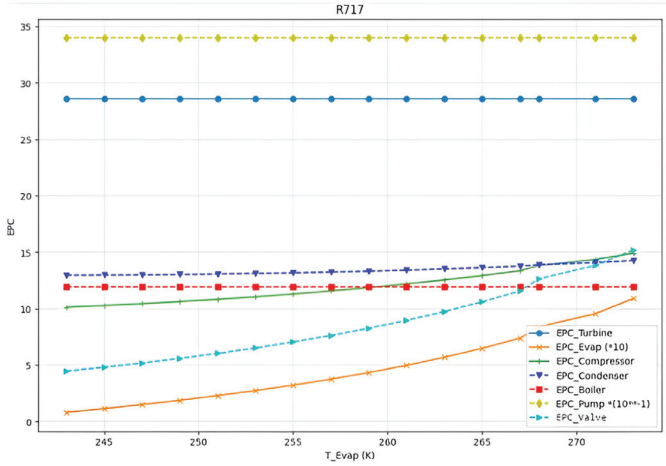


Figure 4. The evaporator temperature effects on the EPC values.

EPC: Exergetic performance criteria

trends. Significant decreases in $EPC_{Turbine}$, EPC_{Boiler}, and $EPC_{Condenser}$ between 340 and 355 K temperature and slight decreases in EPC_{Pump} are also observed. EPC_{Evap}, $EPC_{Compressor}$, and EPC_{Valve} remain relatively constant, as the evaporator's temperature does not directly affect the compressor's and valve's performance.

Figure 4 shows the effect of T_{Evap} on the *EPC* of the system components. As the T_{Evap} increases, the overall *EPC* generally increases. However, the individual *EPC* contributions of different components show different trends. $EPC_{Turbine}$, EPC_{Boiler}, and EPC_{Pump} remain relatively constant, as the turbine's, boiler's, and pump's performance are not directly

affected by the T_{Evap}. EPC_{Evap} and $EPC_{Condenser}$ increase slightly, $EPC_{Compressor}$ and EPC_{Valve} increases significantly with T_{Evap}.

Figure 5 shows the relationship between the U_f and the total EPC_{TOT} or EPC_{TOT} where the different lines represent various combinations of evaporator and $T_{Turbine}$. As the T_{Evap} increases, the EPC_{TOT} generally decrease for a given U_f, and the U_f increases for a given constant $T_{Turbine}$. However, there is a trade-off between T_{Evap} and cooling capacity. Higher T_{Evap} can reduce the cooling capacity of the system. Increasing the $T_{Turbine}$ generally increases EPC_{TOT} and U_f for constant T_{Evap}. Since improving EPC_{TOT} is the priority, the scenario in which It reaches its maximum improvement should be considered. Therefore, when the T_{Evap} was set to 243.15 K and the $T_{Turbine}$ to 368.15 K, an improvement of nearly 100% in EPC_{TOT} and almost 115% in U_f according to the values in $T_{Turbine}$ is 338.15 K.

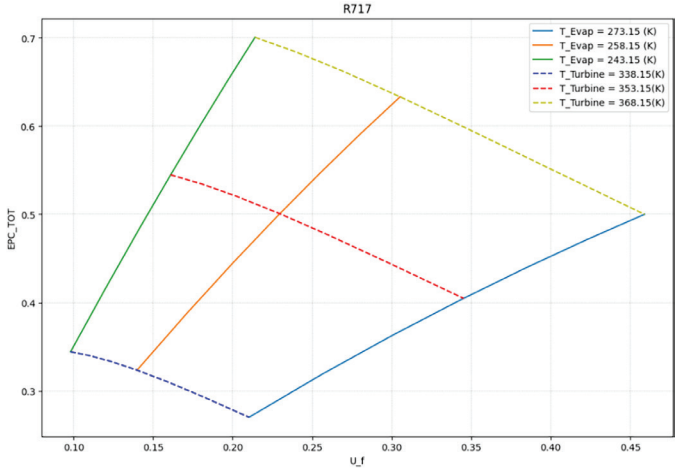


Figure 5. The turbine and evaporator temperatures effects on the U_f and EPC_{TOT}.

U_f: Utility factor, EPC_{TOT}: Exergetic performance criteria

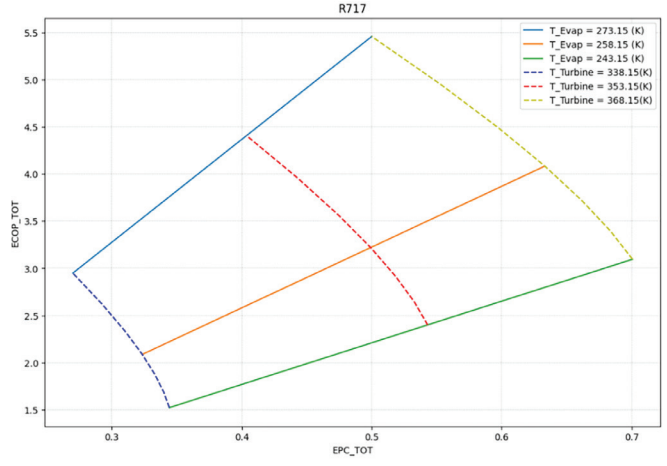


Figure 6. The turbine and evaporator temperatures effects on the EPC_{TOT} and $ECOP_{TOT}$.

EPC_{TOT}: Exergetic performance criteria, $ECOP_{TOT}$: Ecological coefficient of performance

Figure 6 depicts the effects of the evaporator and $T_{Turbine}$ on the relationship between $ECOP_{TOT}$ or $ECOP_{TOT}$ and EPC_{TOT}. As the T_{Evap} increases, the $ECOP_{TOT}$ generally increases for a given EPC_{TOT} or at a constant $T_{Turbine}$. However, increasing in T_{Evap} at constant $T_{Turbine}$ decreases the EPC_{TOT}. T_{Evap} and cooling capacity are inversely correlated, such that an increase in one leads to a decrease in the other. Increasing the $T_{Turbine}$ generally leads to a increase in $ECOP_{TOT}$ for a constant T_{Evap}. The ideal scenario is when the T_{Evap} is 258.15 K, and the $T_{Turbine}$ is 368.15 K to maintain optimal improvements in both $ECOP_{TOT}$ and EPC_{TOT}.

Figure 7 describes the relationship between EPC_{TOT} and η_{II} of the system using R717. As the T_{Evap} increases, η_{II} generally increases while EPC_{TOT} decreases for constant $T_{Turbine}$. Increasing the $T_{Turbine}$ generally increases both EPC_{TOT} and η_{II} for a given T_{Evap}. Since maximizing EPC_{TOT} is the primary objective, the scenario yielding its highest improvement should be considered. Accordingly, when the T_{Evap} was adjusted to 243.15 K and the $T_{Turbine}$ was 368.15 K, an enhancement of almost 170% in η_{II} was calculated by comparing it to the lowest scenario.

Figure 8 depicts the relationship between EPC_{TOT} and ExD_{TOT}. The different lines represent various combinations of evaporator and $T_{Turbine}$. As the T_{Evap} increases, the ExD_{TOT} generally increases for a given EPC_{TOT}, and EPC_{TOT} decreases with higher T_{Evap} at a constant $T_{Turbine}$ value. Increasing the $T_{Turbine}$ generally increases the ExD_{TOT} and EPC_{TOT}. By carefully selecting these temperatures, optimizing the system's performance in terms of both ExD_{TOT} and EPC_{TOT} is possible. While improving EPC_{TOT}, to keep ExD_{TOT} at its lowest level, two scenarios emerge: The most optimal

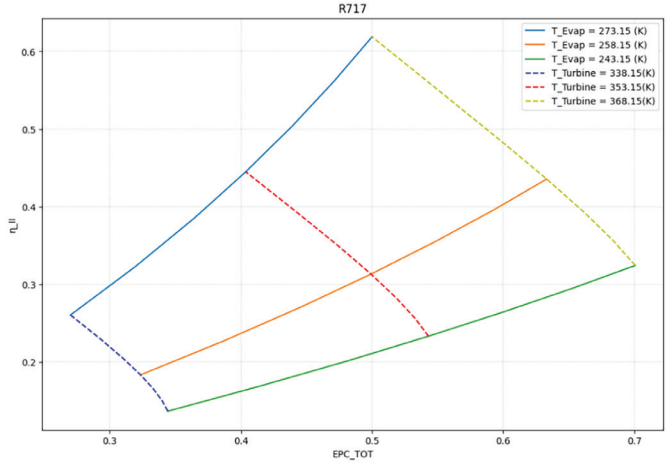


Figure 7. The turbine and evaporator temperatures effects on the η_{II} and EPC_{TOT}.

η_{II}: Second law efficiency, EPC_{TOT}: Exergetic performance criteria

balance between both values occurs when the T_{Evap} is 243.15 K and the $T_{Turbine}$ is 338.15 K. However, if the increase in ExD_{TOT} can be overlooked, the ideal temperature range for maximizing EPC_{TOT} is when the T_{Evap} is 243.15 K and the $T_{Turbine}$ is 368.15 K.

Figure 9 shows the relationship between EPC_{TOT} and s_{gen_TOT} for the system according to the different T_{Evap} (straight lines) and $T_{Turbine}$ (dotted lines). As the T_{Evap} increases, the s_{gen_TOT} generally increases for a given EPC_{TOT}. However, EPC_{TOT} also decreases with higher T_{Evap}. Higher T_{Evap} can lead to higher irreversibilities in the system, such as heat transfer across finite temperature differences and pressure drops in the components. Increasing the $T_{Turbine}$ generally leads to an increase in s_{gen_TOT} for a given EPC_{TOT}. Besides, EPC_{TOT} also

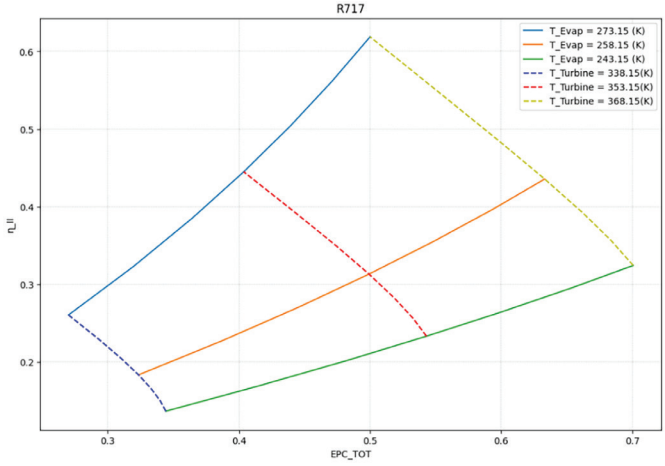


Figure 8. The turbine and evaporator temperatures effects on the ExD_{TOT} and EPC_{TOT}.

EPC_{TOT}: Exergetic performance criteria, ExD_{TOT}: The exergy destruction

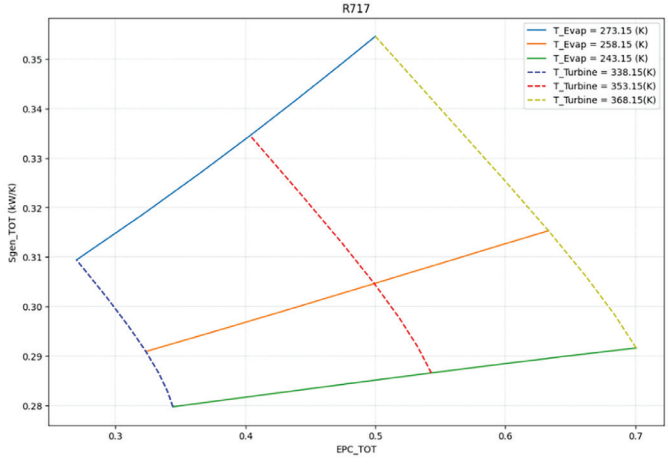


Figure 9. The turbine and evaporator temperatures effects on the s_{gen_TOT} and EPC_{TOT}.

s_{gen_TOT}: Total entropy generation, EPC_{TOT}: Exergetic performance criteria

increases with higher $T_{Turbine}$. The optimal combination of evaporator and $T_{Turbine}$ depends on the specific requirements of the heat-powered refrigeration system, which must balance between minimizing s_{gen_TOT} and maximizing EPC_{TOT}. For example, lower $T_{Turbine}$ and T_{Evap} might be suitable if the priority is to minimize entropy generation. If the priority is to maximize EPC_{TOT}, a lower v and a higher $T_{Turbine}$ might be better. It has been observed that the ideal scenario between EPC_{TOT} and s_{gen_TOT} occurs when the T_{Evap} is 243.15 K, and the $T_{Turbine}$ is 368.15 K.

4. Conclusion

This study investigated the feasibility of converting waste heat from ship exhaust gas into helpful energy through an ORC and subsequently utilizing this converted energy in a VCR cycle. The effects of the varying evaporator and condenser temperatures and different working fluids on the U_f, η_{II}, and s_{gen_TOT} production were analyzed. The results indicated that ammonia (R717) is the most suitable fluid for this system. Future research endeavors will focus on conducting detailed comparative performance analyses and exploring exergy-based environmental and economic assessments. Analyses have shown that the high *ECOP* and EPC values of R717 (ammonia) indicate their significant potential to enhance system efficiency. These results suggest that R717 could play an effective role in energy conversion processes, particularly optimizing energy efficiency. Furthermore, the high efficiency of R717 could lead to lower emissions and more sustainable energy solutions from an environmental perspective, while economically, it could reduce operating costs by lowering energy consumption. Future studies will further explore the broader application areas of R717 and its impact on environmental and economic assessments.

The optimal combination of e T_{Evap} and $T_{Turbine}$ depends on the specific requirements of the refrigeration system. For example, if the priority is to maximize cooling capacity, a lower T_{Evap} and a higher $T_{Turbine}$ might be suitable. If the priority is to minimize energy consumption, a higher T_{Evap} and a lower $T_{Turbine}$ might be better. Figures 5-9 show that the EPC_{TOT} of the heat-powered system using R717 is influenced by both the evaporator and $T_{Turbine}$. To optimize the total EPC, it is advantageous to operate at a lower T_{Evap} and a higher $T_{Turbine}$. The observations indicate that the optimal thermodynamic conditions for the EPC_{TOT}, occur at an T_{Evap} of 243.15 K and a $T_{Turbine}$ of 368.15 K which have almost 100% increment according to the lowest EPC_{TOT} value. By carefully selecting these temperatures, optimizing the system's performance for a given application is possible.

NOMENCLATURE

Symbol	Name
Cp	The specific heat capacity at constant pressure
ECOP	Ecological coefficient of performance
EPC	Exergetic performance criteria
η_{II}	Second law efficiency
ex	Specific exergy
ExD	Exergy destruction
GWP	Global warming potential,
h	Specific enthalpy
ORC	Organic Rankine cycle
m	Mass flow rate
MRS	Marine refrigeration system
P	Pressure
RL	Refrigeration loop
RCL	Refrigerant concentration limit
ρ_{ex}	Exergy density
s	Specific entropy
s_{gen_TOT}	Total entropy generation
T	Temperature
Q	The heat transfer ratio
U_f	Utility factor
W	Net work
v	Specific volume
VCR	Vapor compression refrigeration
y	Exergy destruction ratio
	Subscripts
0	Dead state conditions
avr	Average
c	Compressor
Con	Condenser
env	Environment
Evap	Evaporator
H	High temperature, Heat input
in	Inlet
L	Low temperature, Heat output
p	Pump
out	Outlet
sys	System
TOT	Total
Gen	Generated

Acknowledgement

The short version of this study was presented at the Fourth International Naval Architecture and Maritime Symposium (INTNAM-2023, YTÜ, İstanbul, 11-13.10.2023), the present paper is the improved version in terms of analysis and content. We would like to thank those who contributed to the symposium organisers and the journal publication process.

Footnotes

Authorship Contributions

Concept: O. Yılmaztürk, Design: O. Yılmaztürk, Data Collection or Processing: O. Yılmaztürk, and A. S. Karakurt, Analysis or Interpretation: A. S. Karakurt, Literature Review: O. Yılmaztürk, and A. S. Karakurt, Writing: O. Yılmaztürk, and A. S. Karakurt.

Conflict of Interest: No conflict of interest was declared by the authors.

Financial Disclosure: The authors declared that this study received no financial support.

References

[1] L. A. Díaz-Secades, R. González, N. Rivera, E. Montañés, and J. R. Quevedo, "Waste heat recovery system for marine engines optimized through a preference learning rank function embedded into a Bayesian optimizer," *Ocean Engineering*, vol. 281, 114747, Aug 2023.

[2] A. S. Karakurt, B. Başaran, and E. Z. Çubukçu, "Performance analyses of marine thermal oil system," *Gemi ve Deniz Teknolojisi,* no. 222, pp. 196-208, Jan 2023.

[3] B. Khan, and M.-H. Kim, "Energy and exergy analyses of a novel combined heat and power system operated by a recuperative organic rankine cycle integrated with a water heating system," *Energies*, vol. 15, no. 18, 6658, Jan 2022.

[4] T. Koroglu, I. Cavus, and M. U. Bayer, "Marine engine efficiency improvement with supercritical-CO2 Rankine waste heat recovery," *International Journal of Exergy,* vol. 40, no. 3, pp. 347-364, Jan 2023.

[5] V. Başhan, and A. Parlak, "Economic analysis of a ship refrigeration system in case of variable sea water temperature conditions," *Journal of ETA Maritime Science*, vol. 3, no. 2, pp. 67-74, 2015.

[6] R. Tozer, and R. W. James, "Heat powered refrigeration cycles," *Applied Thermal Engineering,* vol. 18, no. 9, pp. 731-743, Sep 1998.

[7] S. Khatoon, N. M. A. Almefreji, and M.-H. Kim, "Thermodynamic study of a combined power and refrigeration system for low-grade heat energy source," *Energies*, vol. 14, no. 2, pp. 410, Jan 2021.

[8] A. Elbir, F. A. Kodaloglu, I. Ucgul, and M. E. Sahin, "Thermodynamic analysis of refrigerants used in ORC-VCC combined power systems for low temperature heat sources," *Thermal Science,* vol. 26, no. 4 Part A, pp. 2855-2863, 2022.

[9] R. Zhar, A. Allouhi, A. Jamil, and K. Lahrech, "Performance analysis of combined power and refrigeration: ORC-VCC system," in *WITS 2020*, S. Bennani, Y. Lakhrissi, G. Khaissidi, A. Mansouri, and Y. Khamlichi, Eds., in Lecture Notes in Electrical Engineering. Singapore: Springer, 2022, p. 595-605.

[10] Y. Liang, Z. Yu, and W. Li, "A waste heat-driven cooling system based on combined organic rankine and vapour compression refrigeration cycles," *Applied Sciences*, vol. 9, no. 20, 4242, Jan 2019.

[11] X. Xia, Z. Liu, Z. Wang, T. Sun, and H. Zhang, "Multi-layer performance optimization based on operation parameter-working fluid-heat source for the ORC-VCR system," *Energy*, vol. 272, 127103, Jun 2023.

[12] O. Bounefour, A. Ouadha, and Y. Addad, "An exergy analysis of various layouts of ORC-VCC systems for usage in waste heat recovery onboard ships," *Marine Systems & Ocean Technology,* vol. 15, no. 1, pp. 26-44, Mar 2020.

[13] C. Aktemur, and G. Hacipasaoglu, "Assessment of an integrated organic rankine cycle (ORC)-vapor compression refrigeration (VCR) system using the energy, conventional exergy, and advanced exergy analysis," *Heat Transfer Research,* vol. 52, no. 15, 2021.

[14] M.-H. Kim, "Energy and exergy analysis of solar organic rankine cycle coupled with vapor compression refrigeration cycle," *Energies*, vol. 15, no. 15, Jan 2022.

[15] Y. Liang, A. Mckeown, Z. Yu, and S. F. K. Alshammari, "Experimental study on a heat driven refrigeration system based on combined organic Rankine and vapour compression cycles," *Energy Conversion and Management,* vol. 234, 113953, Apr 2021.

[16] Y. Ust, "Performance analysis and optimization of irreversible air refrigeration cycles based on ecological coefficient of performance criterion," *Applied Thermal Engineering,* vol. 29, no. 1, pp. 47-55, Jan 2009.

[17] Y. Ust, A. S. Karakurt, and U. Gunes, "Performance analysis of multipurpose refrigeration system (MRS) on fishing vessel," *Polish Maritime Research,* vol. 23, no. 2, pp. 48-56, 2016.

[18] L. Chen, Y. Ge, S. Shi, H. Feng, and P. Liu, "Exergetic efficiency and exergy-based ecological function performance optimizations for two irreversible simple Brayton refrigeration cycle models," *Results in Engineering*, vol. 22, 101967, Jun 2024.

[19] Md. M. Arefin, D. Mondal, and Md. A. Islam, "Optimizing cascade refrigeration systems with low GWP refrigerants for low-temperature applications: A thermodynamic analysis," *Energy Conversion and Management: X,* vol. 24, 100722, Oct 2024.

[20] Y. Ust, and A. S. Karakurt, "Analysis of a cascade refrigeration system (CRS) by using different refrigerant couples based on the exergetic performance coefficient (EPC) criterion," *Arabian Journal for Science and Engineering,* vol. 39, no. 11, pp. 8147-8156, Nov 2014.

[21] O. Yilmazturk, and A. S. Karakurt, "*Analyses of an ideal combined heat-powered marine refrigeration system,*" presented at the 4th International Naval Architecture and Maritime Symposium (Int-Nam 2023), İstanbul, Oct 2023. Accessed: Sep 13, 2024. [Online]. Available: https://avesis.yildiz.edu.tr/yayin/4e11e10f-2bff-4fea-b347-43e870e4a316/analyses-of-an-ideal-combined-heat-powered-marine-refrigeration-system

[22] A. S. Karakurt, and B. Sahin, "A new method for the size and performance analyses and optimization of thermal systems: The exergy density," *Sigma Journal of Engineering and Natural Sciences,* vol. 37, no. 2, pp. 573-583, Jul 2019.

[23] A. Bejan, "Entropy generation minimization: The new thermodynamics of finite-size devices and finite-time processes," *Journal of Applied Physics,* vol. 79, no. 3, pp. 1191-1218, Feb 1996.

[24] Y. Ust, B. Sahin, and A. Kodal, "Ecological coefficient of performance (ECOP) optimization for generalized irreversible Carnot heat engines," *Journal of the Energy Institute,* vol. 78, no. 3, pp. 145-151, Aug 2005.

[25] Y. Ust, B. Sahin, and T. Yilmaz, "Optimization of a regenerative gas-turbine cogeneration system based on a new exergetic performance criterion: Exergetic performance coefficient," *Proceedings of the Institution of Mechanical Engineers Part A-Journal of Power and Energy,* vol. 221, no. 4, pp. 447-456, Jun 2007.

[26] ASHRAE, *Designation and Safety Classification of Refrigerants*, Standart 34, Georgia, US., 2019. [Online]. Available: https://www.ashrae.org/technical-resources/bookstore/standard-34-designation-and-safety-classification-of-refrigerants

[27] I. H. Bell, J. Wronski, S. Quoilin, and V. Lemort, "Pure and pseudo-pure fluid thermophysical property evaluation and the open-source thermophysical property library CoolProp," *Industrial & Engineering Chemistry Research,* vol. 53, no. 6, pp. 2498-2508, Feb 2014.

RESEARCH ARTICLE

DOI: 10.54926/jnamt.2025.248

J Nav Architect Mar Technol 2025;227(1):43-51

Investigating the Torsional Vibration Behaviour of Composite Drive Shafts in Marine Propulsion Shaft Systems

Akile Neşe Halilbeşe

Ordu University Fatsa Faculty of Marine Sciences, Department of Marine Machinery Management Engineering, Ordu, Türkiye

To cite this article: Halilbeşe AN. Investigating the torsional vibration behaviour of composite drive shafts in marine propulsion shaft systems. *J Nav Architect Mar Technol*.

Received: 30.10.2024 - **Revision Requested:** 18.01.2025 - **Last Revision Received:** 11.03.2025 - **Accepted:** 02.06.2025 - **Publication Date:** 30.06.2025

Abstract

Within ship propulsion shaft systems, shafts function as crucial connecting elements, like springs, where their stiffness values significantly influence the overall vibration behavior of the system. Torsional vibration is particularly perilous in propulsion shaft systems due to the irregular forces exerted by the propeller. This study aims to enhance the integration of composite material in the construction of drive shafts used in the shipbuilding industry and to promote the use of composite materials while investigating torsional vibration behavior. To achieve this objective, a composite drive shaft is modeled using the ANSYS ACP Module, with production details such as ply angle and the number of layers meticulously defined within the ACP Module. The natural frequency of the drive shaft is determined through Modal Analysis, while the torsional angle is obtained using Static Structural Analysis. Optimization techniques are employed with ANSYS Direct Optimization Tool, involving precise adjustments to ply angles, to enhance overall performance. This study focuses on the effects of ply angles, thickness, and material on the torsional vibration behavior of the drive shaft, providing a comprehensive analysis that underscores the potential of composite materials and advanced manufacturing techniques in improving the efficiency and durability of propulsion systems in marine engineering.

Keywords: Composite shaft, torsional vibration, propulsion shaft system, optimization

1. Introduction

In the field of marine engineering, the design and analysis of propulsion shaft system components are crucial for ensuring the efficiency and durability of ships. A key component in this regard is the drive shaft, which is essential for transmitting torque and power between different parts of the propulsion system, exhibits vibrational behavior along various axes during its operation. Torsional vibration, resulting from oscillatory motion along the drive shaft's axis and considered the most dangerous type of vibration, is a significant area of study due to its potential to induce fatigue and failure during the drive shaft's operation. As technological advancements drive the demand for lightweight and high-performance materials, composite materials, particularly with the use of additive manufacturing, have emerged as promising alternatives to traditional metallic alloys in shaft construction. The unique mechanical properties of composites, such as high strength-to-weight ratios and tailored stiffness, provide an opportunity to improve the torsional behavior of shafts. However, optimizing composite shafts poses a challenge, requiring a thorough investigation of design factors such as layup angles, plate thicknesses, and stacking sequences to unlock their full potential.

Address for Correspondence: Akile Neşe Halilbeşe, Ordu University Fatsa Faculty of Marine Sciences, Department of Marine Machinery Management Engineering, Ordu, Türkiye
E-mail: akile.nese@gmail.com
ORCID ID: orcid.org/0000-0002-8182-4364

Copyright© 2025 The Author. Published by Galenos Publishing House on behalf of UCTEA Turkish Chamber of Naval Architects and Marine Engineers.
Licensed under a Creative Commons Attribution-NonCommercial-NoDerivatives 4.0 (CC BY-NC-ND) International License

The complexity of the design problem of the composite structure is compounded by numerous variables and constraints, potentially limiting the performance of the final structure [1]. Previous research on composite shafts has predominantly focused on the torsional behaviour of cylindrical structures subjected to vertical or horizontal forces, with fixed supports at both ends [2]. Various beam models and analysis methods, such as the Timoshenko theory [3-5] thin-walled beam theory [6], and finite element method [7], have been employed to examine the critical speed, natural frequencies, and stability under axial loads during whirling of the composite shaft [4,6,7]. Chang et al. [7] presented a model based on the first-order Timoshenko beam theory, while Badie et al. [8] utilized finite element analysis (FEA) to investigate the effects of fibre orientation angles and stacking sequences on torsional stiffness, natural frequencies, bending strength fatigue, life, and failure modes of composite tubes. Experimental tests were also conducted on a composite drive shaft to validate the FEA model [9]. Montagnier and Hochard introduced viscoelastic supports to mount composite shafts, and explored factors such as shaft length and support stiffness [10,11]. In contrast to linear system considerations, nonlinear studies investigating the spinning composite shafts based on the Bernoulli-Euler theory emphasized the presence of extensional, flexural, and torsional vibrations, by incorporating geometrical nonlinearity and linear couplings due to material anisotropy [12-15]. Overall, the exploration of composite shafts involves a comprehensive approach to design and analysis, considering various factors to optimize their performance in mechanical systems.

The literature on shaft torsional response mainly interests with the whirling analysis of axially loaded, simple or fixed supported composite shafts. These studies emphasize the axial loading-induced whirling phenomenon. However, as the integration of composite material into the shipbuilding industry gains prominence, there arises a need to revaluate the role of the shaft, considering its application as a joint element.

Within the propulsion shaft system, all constituent elements, including the crankshaft, intermediate shaft, propeller shaft, and any auxiliary shafts, are tasked with the transmission of torque. Torsional vibration manifests as a result of the engine torque, coupled with the inherent instability in propeller power output and power transmission dynamics [16-19]. In the context of passive vibration isolation, the system is systematically pre-tuned for torsional vibration by judiciously adjusting key parameters. These parameters encompass the torsional stiffness of the shafts, contingent upon their respective diameters, and the mass moment of inertia, potentially achieved through the incorporation of a flywheel [20,21]. Furthermore, alterations in torsional stiffness may be effectuated by the introduction of additional elements into the system, such as flexible shaft couplings [22,23].

The torsional vibration characteristics of a composite drive shaft have undergone thorough examination through systematic variation of pertinent parameters, including plate angle and material, within one side fixed supported configurations, as extensively documented in the literature. In the context of a shaft system; the composite shaft connects the components of the propulsion system (e.g. propeller, main engine) and has freedom of rotation. This study is motivated by elucidate the effects of various composite shaft parameters on the torsional vibration behaviour of the shaft system. To achieve this aim, the composite shaft is modeled with ANSYS Workbench ACP Module. The first naturel frequencies of the propulsion shaft system obtained with the help of ANSYS Workbench Modal Analysis, besides, the maximum torsional angle due to external moment is obtained with ANSYS Workbench Static Structural Analysis. The influence of the material, thickness and ply angle on naturel frequency and torsional angle is shared. In addition, employing the Direct Optimization tool within the ANSYS Workbench program, new permutations were made to attain the minimum torsion angle while varying ply angles. This approach aimed to systematically investigate the influence of these parameters on torsional vibration, and the findings of these analyses are subsequently elucidated.

2. Methodology and Numerical Model

This study investigates the torsional vibration of drive shaft which is a component of propulsion shaft system using single degree of freedom and ANSYS Software which is based on finite element method. Figure 1 provides an illustrative example of the appearance and structural configuration of a drive shaft.

Table 1 presents the detailed specifications of the drive shaft modeled using numerical method and ANSYS, and composite shaft details derived from the literature [24].

The torsional natural frequency of a shaft, with one end fixed and the other end free, can be approximated using the following expression [25];

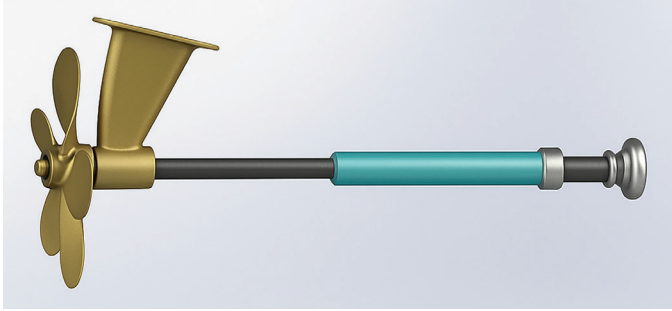


Figure 1. Drive shaft manufactured with steel.

Table 1. Mechanical details of the drive shaft [24]	
Length of the shaft	1200 mm
Inner diameter	75 mm
The transmitted torque	80 Nm
Fabric angle	0, ±30, ±45, ±60, 90
Fabric 1 (E-glass/Epoxy) thickness	3 mm
Fabric 2 (Carbon/epoxy) thickness	0.75 mm

$$f_n = \frac{1}{2\pi}\sqrt{\frac{K_T}{I}} \quad (1)$$

while K_T is torsional stiffness of the composite shaft [26], I is polar mass moment of inertia per unit length, and the torsional stiffness of the composite hallow shaft can be given as;

$$K_t = \frac{G_{eq}J}{L} \quad (2)$$

Here, J is polar moment of inertia of the hollow shaft which has 7 layer given with Equation 3 [27], and G_{eq} is shear modulus of the composite shaft and aproximatly calculated by considering the shear modulus of the meterials which are given with Table 2.

$$J = \frac{\pi}{32}\sum_{i=1}^{7}\left(d_{0,i}{}^4 - d_{i,i}{}^4\right) \quad (3)$$

$$G_{eq} = \frac{G_1 t_1 + G_2 t_2}{t_1 + t_2} \quad (4)$$

d_0 is outer diameter (m), d_i inner diameter (m) in Equation 3. The mechanical properties of the drive shaft is given in Table 1. The natural frequency obtained using Equation 1 is compared with the ANSYS Modal analysis results to first verify the accuracy of the ANSYS model.

For the ANSYS modal analysis, the SOLID185 element type was selected to construct the FEA model of the transmission. The model consists of 2904 nodes and 2880 elements after meshing. The boundary conditions specify that one end is a fixed support, while the other end is subjected to a transmitted torque. This is a seven-layer hybrid composite beam, and the first layer is of E-glass/Epoxy and upper layers are of Carbon/epoxy. ANSYS ACP model is used to create composite layers with varying orientation angles, as detailed in Figure 2. The green section represents the configuration without any composite material, whereas the red section demonstrates the layer-by-layer arrangement of composite materials. In this context, a represents the angle, and t represents the thickness of the plate. This representation is commonly used in composite manufacturing.

The [0/0/0/0/0/0/0] layup configuration was chosen to compare the numerical model and ANSYS. According to Equation 1, the natural frequency is 319.42 Hz, while the natural frequency obtained from the modal analysis is 339.82 Hz, as shown in Figure 3. Figures 3 and 4 present the mode shapes corresponding to these frequencies. The numerical analysis and ANSYS modal analysis have been observed to exhibit similar mode shapes at comparable natural frequency values.

The ANSYS model has been validated as accurate since it demonstrates similar natural frequency values and the same mode shape as the numerical analysis. Therefore, the study has proceeded using the ANSYS model. Various cases were examined to assess the impact of material type, ply angle and thickness on the natural frequency and torsional angle of the drive shaft. The materials utilized, along with their respective properties, are detailed in Table 2, and the thickness detail are shared with Table 1. To evaluate the effect of ply angle on the natural frequency and torsional angle, sequences with orientations of [0/0/0/0/0/0/0], [0/30/-30/30/-30/30/-30], [0/45/-45/45/-45/45/-45], [0/60/-60/60/-60/60/-60], [0/90/90/90/90/90/90] were employed.

3. Results and Discussion

To initially determine the effects of thickness and ply angle on natural frequency, an analysis was conducted with the inner tube diameter fixed at 75 mm. To measure the first naturel frequency of the drive shaft with different ply angle

Table 2. Mechanical properties of materials [24,28,29]				
	T300-934 Carbon/epoxy	**T300-7901 Carbon/epoxy**	**T300-12K Carbon/epoxy**	**ER1200-FW E-glass/Epoxy**
Density, (kg/m^3)	1500	1478	1760	1850
Young's Modulus (E_{11}), GPa	148	125	144.11	39.3
Young's Modulus (E_{22}), GPa	9.65	11.3	10.23	4.8
Shear Modulus ($G_{12,}$ G_{13}), GPa	4.55	5.43	6.12	4.0
Shear Modulus (G_{23}), GPa	4.55	3.98	6.12	4.0
Poisson ratio ($\nu_{12,}$ ν_{13})	0.30	0.30	0.246	0.25
Poisson ratio (ν_{23})	0.30	0.42	0.246	0.25

and ply number ANSYS Workbench Modal Analysis is used. The ply angle was varied at 0°, ±30°, ±45°, ±60°, and 90°, which are the most commonly used ply angles in manufacturing. The drive shaft thickness was increased in increments of 2 layers (0.75 mm), with the first layer being E-glass/Epoxy fixed, and the additional layers spanning from 6 layers to 14 layers (7.5 to 13.5 mm). The analysis results, depicted in Figure 5, indicate that the first natural frequency increased significantly with changes in ply angles. The indicators 0, 30, 45, 60, 90 in Figures symbolize 0°, ±30°, ±45°, ±60°, and 90°. Conversely, Figure 6 demonstrates that thickness has a relatively minor effect on natural frequency compared to ply angle. Additionally, Figure 6 shows that the increase in natural frequency becomes more pronounced as the ply angle increases. These findings suggest that ply angle is the most influential factor affecting natural frequency, rather than thickness.

Figure 7 shows that the torsional angle is the minimum at ±45 degrees for each ply number and the maximum at 90 degrees. The torsion angle values for complementary angles, such as 0 and 90 degrees or 30 and 60 degrees, are similar, though not identical. This pattern is not observed for natural frequency; however, it is evident that complementary angles result in comparable torsion angles.

Figure 8 indicates first naturel frequency for different material at ply angle ±30. Since similar results are seen at different ply angles, the result is shared only for ±30 degrees to avoid confusion in the figure. Even at different ply number of the shaft, the highest natural frequency is seen for T300-12K while the lowest natural frequency value is seen for T300-934.

Figure 9 illustrates the variation in natural frequency for different ply angles while maintaining a constant number of 10 plies. The natural frequency shows a slight increase from 0 degrees to 30 degrees. However, a sharp increase is observed from ±30 degrees to ±45 degrees, with the most significant rise occurring at ±60 degrees. Beyond ±60 degrees, up to 90 degrees, the natural frequency decreases slightly. These observations suggest that ply angles have a pronounced impact on natural frequency, with the most substantial effect occurring around ±60 degrees.

Figure 10 demonstrates that T300-12K has the highest density among the materials used, and the lowest torsion angle is observed in this high-density material. For each material, the lowest torsion angle occurs at ±45 degrees. Additionally, similar torsion angle values are observed at complementary angles (0,90, ±30, ±60), indicating a consistent pattern across different materials.

4. Optimization

This study investigates the effects of material, thickness, and ply angle on natural frequency and torsional angle. During the optimization phase, the objective is to minimize the torsion angle by modifying the arrangement angles in the

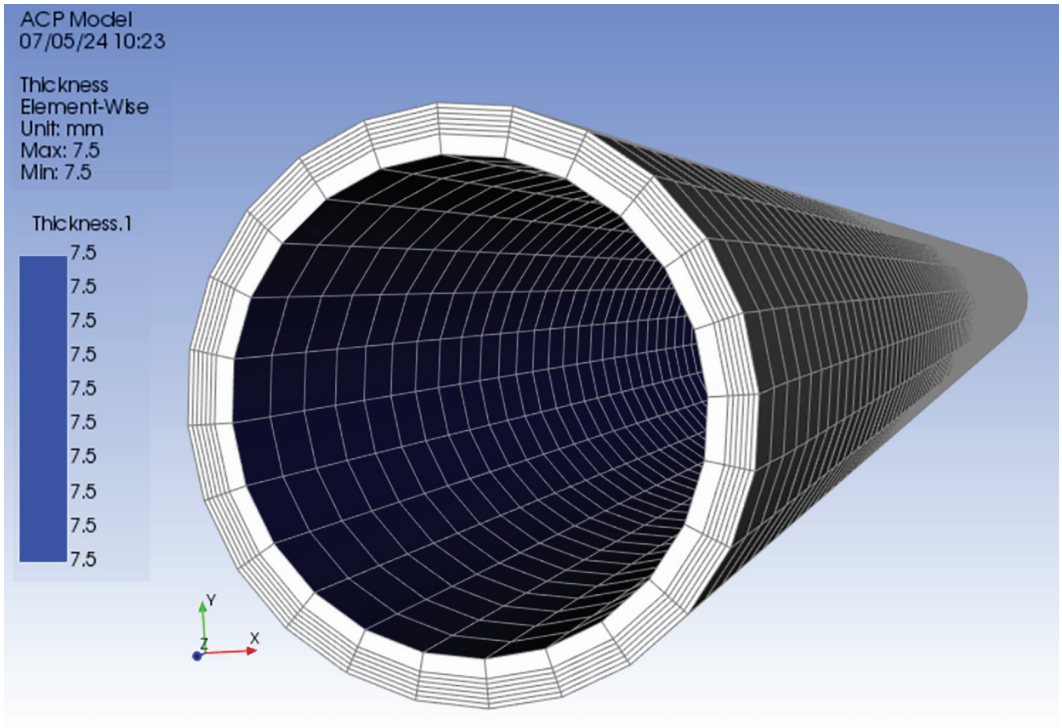


Figure 2. Details of the drive shaft with ANSYS ACP Module

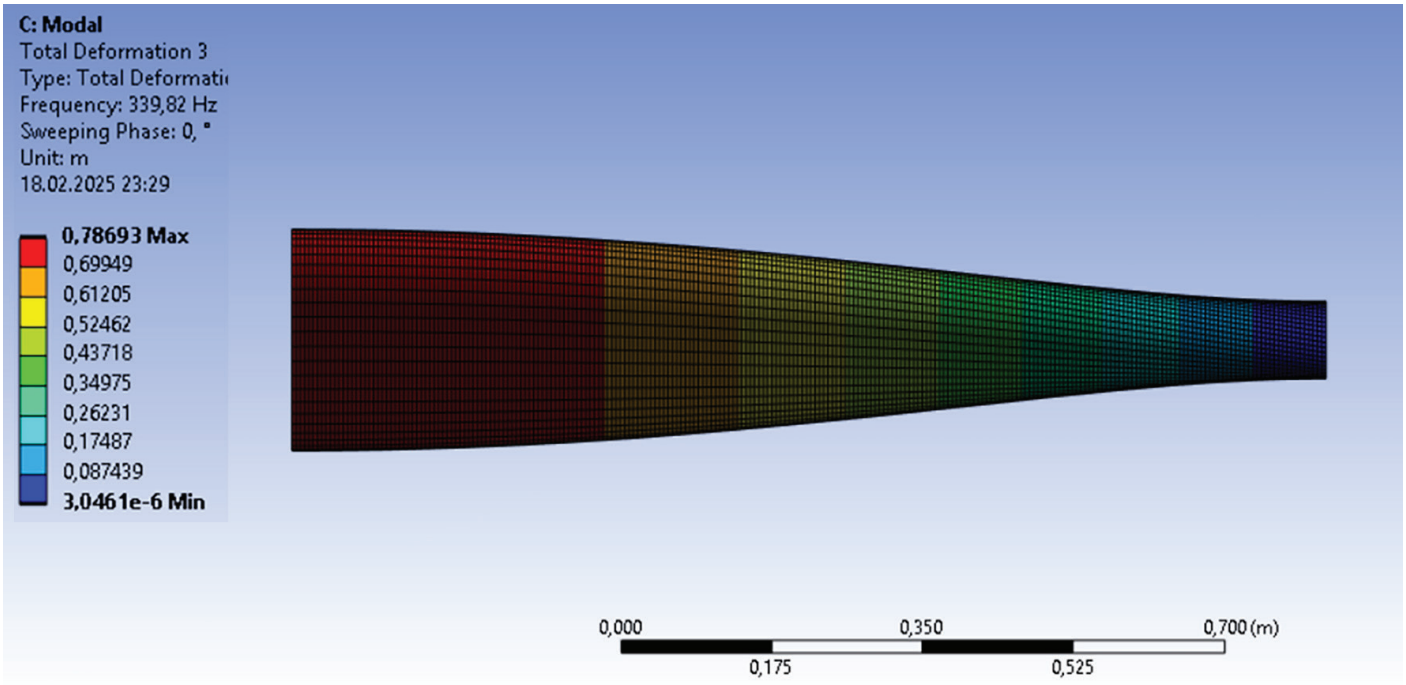


Figure 3. The mode shape of the composite shaft obtained with ANSYS Modal Analysis.

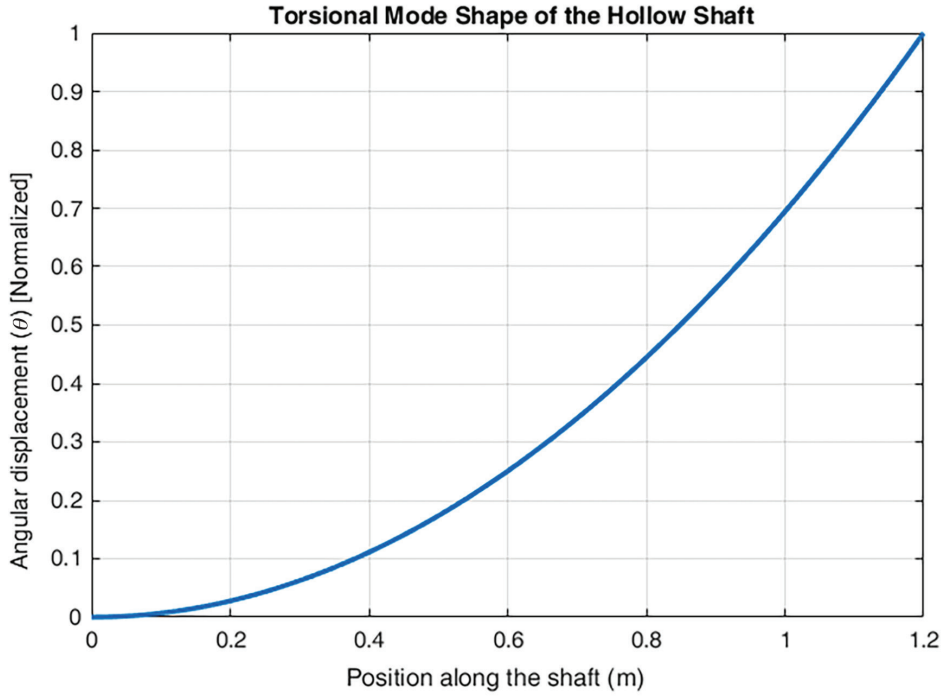


Figure 4. The mode shape of the composite shaft for 319.42 Hz.

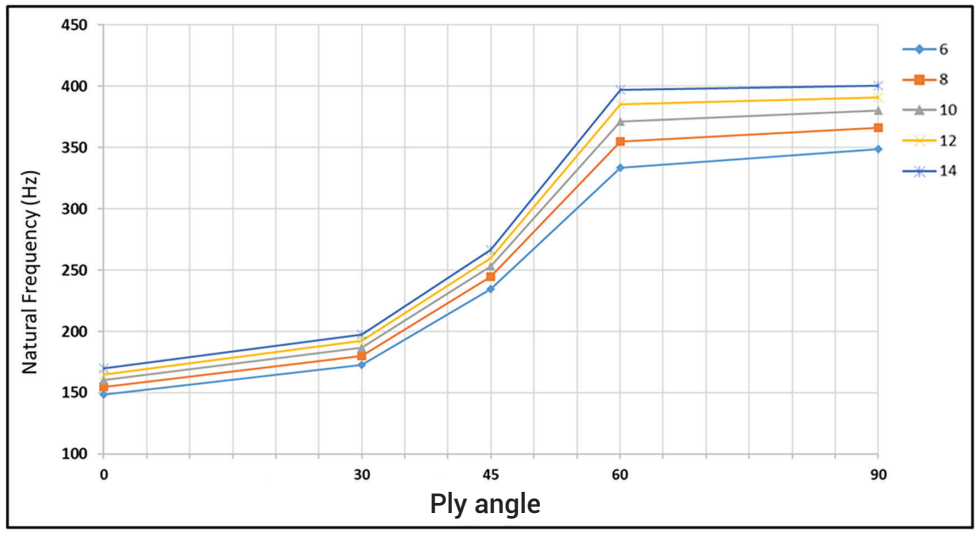


Figure 5. The layers of the composite drive shaft.

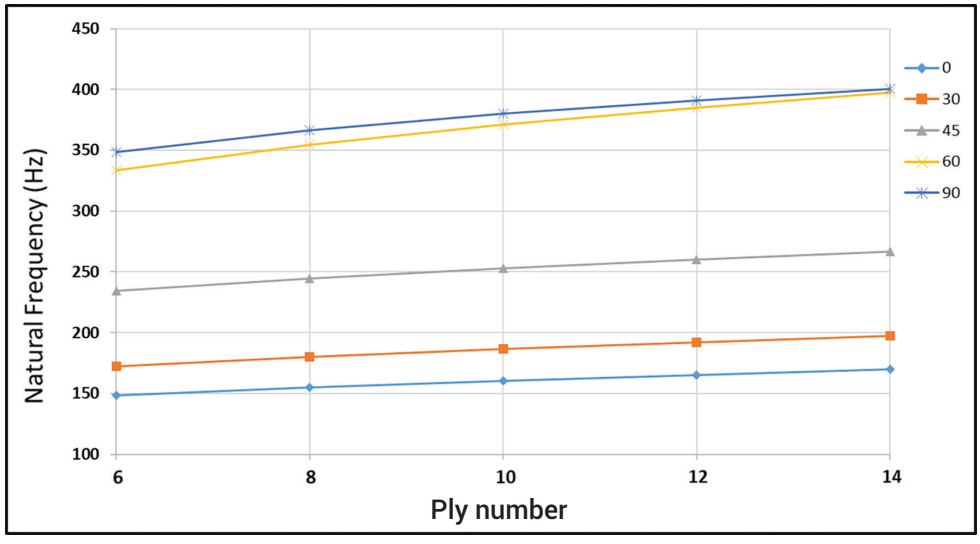


Figure 6. The layers of the composite drive shaft.

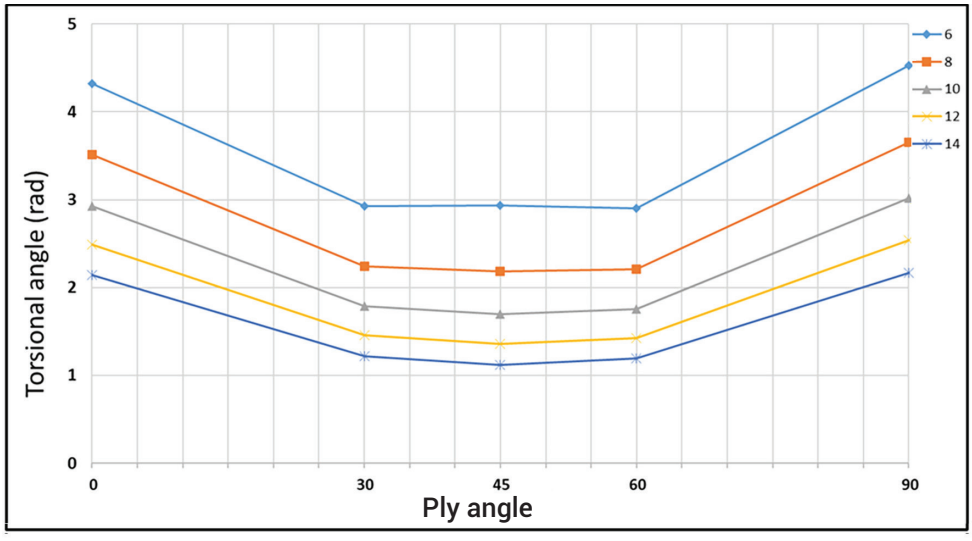


Figure 7. The layers of the composite drive shaft.

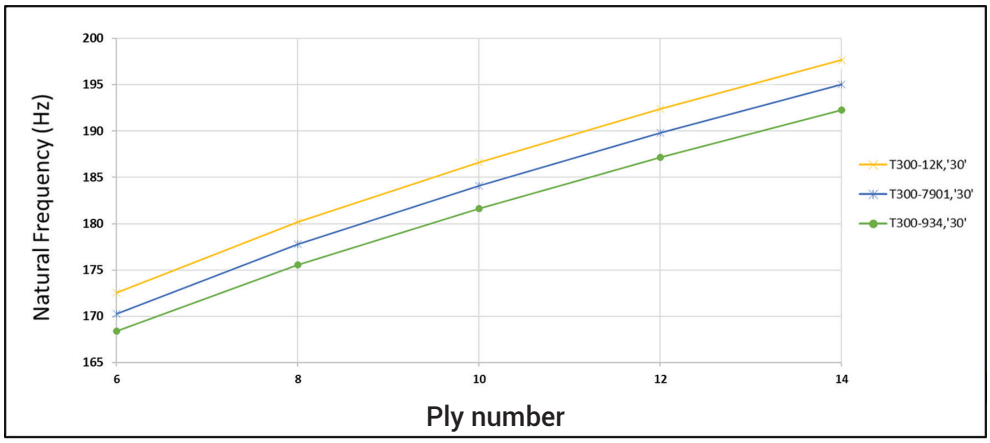


Figure 8. Natural frequencies with different material at ply angle ±30.

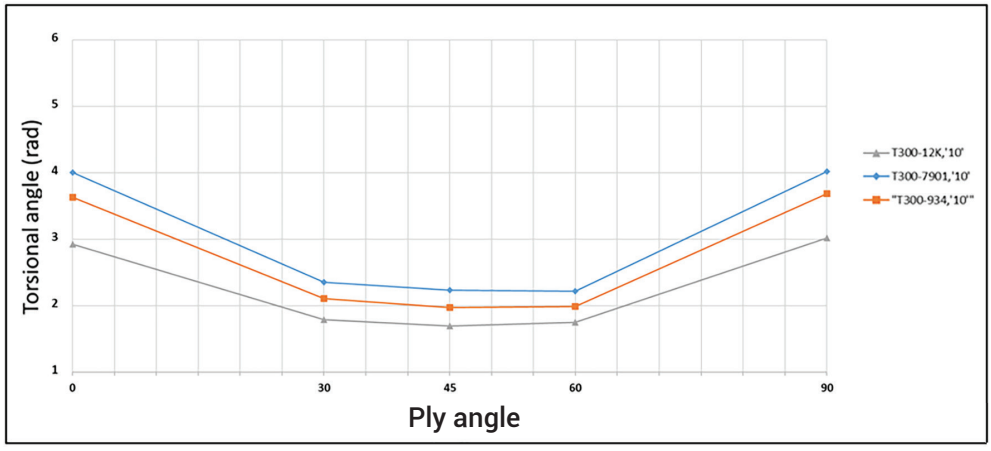


Figure 9. Natural frequencies with different material at different ply angle.

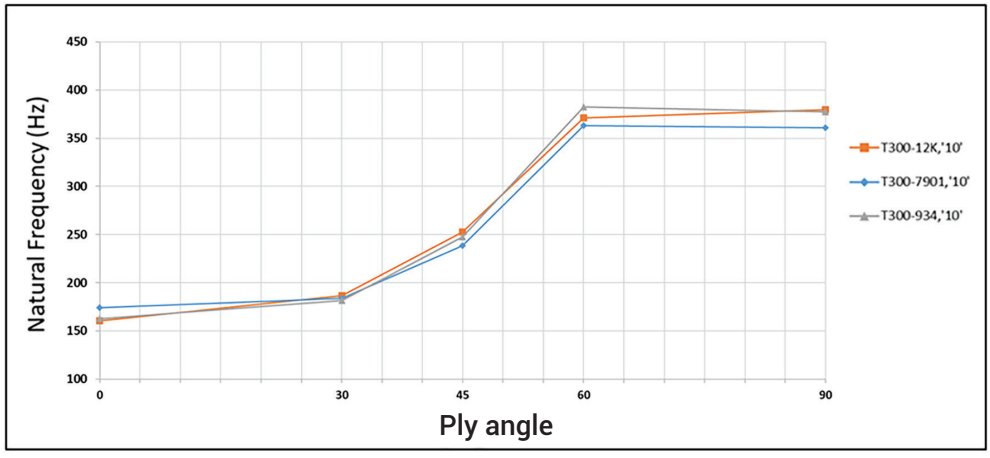


Figure 10. Torsional angle with different material at different ply angle.

[0/0/0/0/0/0/0] configuration for a composite shaft consisting of a first layer of E-glass/Epoxy and 6 layers of T300-12K. The goal is to achieve a torsion angle below 4.32 radians under the same applied moment for the specified configuration. Optimizations were conducted using the Direct Optimization module of the ANSYS Workbench program. Initially, the input and output parameters were identified using the ANSYS ACP module, which facilitated composite modeling with ply angle, and the Static Structural module, which provided torsion angle values. The allowable values for each input

parameter were determined, and an experimental matrix was created based on these values. Analysis was then performed for each combination in the matrix. A total of 728 different combinations were analyzed. As shown in Table 3, more optimal combinations were identified.

Table 3. Optimization results.

Combination	Layer angle	Torsional angle (rad)
1.	[0/0/0/0/0/0/0]	4.32
2.	[0/-30/45/-30/30/-30/0]	2.62
3.	[0/-30/30/-30/30/-30/-0]	2.65
4.	[0/-30/30/-30/45/-30/-0]	2.66

5. Conclusion

This study provides a comprehensive analysis of the effects of material composition, thickness, and ply angle on the natural frequency and torsional angle of composite drive shafts in marine propulsion systems. The findings underscore the critical influence of ply angle on the natural frequency, with variations in ply angles yielding significant changes in performance. Specifically, the analysis revealed that the first natural frequency increased substantially with changes in ply angles, while thickness exhibited a relatively minor effect. This highlights the importance of optimizing ply angles to enhance the dynamic behaviour of composite shafts.

The investigation demonstrated that the most significant increase in natural frequency occurred around ±60 degrees, suggesting that this ply angle configuration is particularly effective in shaft performance. Conversely, torsional angle analysis indicated that the lowest torsion angles were observed at ±45 degrees for all materials tested, with high-density materials such as T300-12K showing the most favorable results.

Optimization efforts focused on minimizing torsion angles by modifying the arrangement angles in the composite shaft's configuration. Utilizing the Direct Optimization module of ANSYS Workbench, a systematic approach was employed to identify the optimal ply angle combinations. The study successfully identified several configurations that significantly reduced the torsion angle, with the best-performing combination achieving a torsion angle of 2.62 radians, compared to the initial 4.32 radians.

In conclusion, this research highlights the potential of composite materials and advanced manufacturing techniques in enhancing the performance of drive shafts in marine engineering. The findings provide valuable insights into the optimal design parameters, paving the way for the development of more efficient and durable propulsion systems. Future work should continue to explore the interplay between different design variables to further optimize composite shaft performance in various operational contexts.

Footnote

Financial Disclosure: Dr. Akile Nese Halilbese's research is supported by the Scientific and Technological Research Council of Türkiye (TÜBİTAK) through the TÜBİTAK 2219 International Postdoctoral Research Fellowship Program.

References

[1] A. Cherniaevand, and V. Komarov, "Multistep optimization of composite drive shaft subject to strength, buckling, vibration and manufacturing constraints," *Applied Composite Materials*, vol. 22, no. 5, pp. 475-487, Oct 2015.

[2] S. A. A. Hosseini, "Dynamic stability and bifurcation of a nonlinear in-extensional rotating shaft with internal damping," *Nonlinear Dynamics*, vol. 74, no. 1-2, pp. 345-358, Oct 2013.

[3] S. A. A. Hosseini, M. Zamanian, S. Shams, and A. Shooshtari, "Vibration analysis of geometrically nonlinear spinning beams," *Mechanism and Machine Theory*,vol. 78, pp. 15-35, Aug 2004.

[4] L. W. Chen, and W. K. Peng, "Dynamic stability of rotating composite shafts under periodic axial compressive loads," *Journal of Sound and Vibration*, vol. 212, no. 2, pp. 215-230, Apr 1998.

[5] M. Y. Chang, J. K. Chen, and C. Y. Chang, "A simple spinning laminated composite shaft model," I*nternational Journal of Solids and Structures*, vol. 41, no. 3-4, 637-662, Feb 2004.

[6] O. Song, N. H. Jeong, and L. Librescu, "Implication of conservative and gyroscopic forces on vibration and stability of an elastically tailored rotating shaft modeled as a composite thin-walled beam," *The Journal of the Acoustical Society of America*, vol. 109, no. 3, pp. 972-981, Mar 2001.

[7] C. Y. Chang, M. Y. Chang, and J. H Huang, "Vibration analysis of rotating composite shafts containing randomly oriented reinforcements," *Composite Structures*, vol. 63, no. 1, pp. 21-32, Jan 2004.

[8] M. A. Badie, E. Mahdi, and A. M. S Hamouda, "An investigation into hybrid carbon/glass fiber reinforced epoxy composite automotive drive shaft," *Materials & Design*, vol. 32, no. 3, pp. 1485-1500, Mar 2011.

[9] P. F. Pai, X. Qian, and X. Du, "Modeling and dynamic characteristics of spinning Rayleigh beams," *International Journal of Mechanical Sciences*, vol. 68, pp. 291-303, Mar 2013.

[10] O. Montagnier, and C. Hochard, "Optimisation of hybrid high-modulus/high-strength carbon fibre reinforced plastic composite drive shafts," *Materials & Design,* vol. 46, pp. 88-100, April 2013

[11] O. Montagnier, and C. Hochard, "Dynamics of a supercritical composite shaft mounted on viscoelastic supports," *Journal of Sound and Vibration*, vol. 33, no. 2, pp. 470-484, Jan 2014.

[12] S. A. A. Hosseini, and S. E. Khadem, "Combination resonances in a rotating shaft," *Mechanism and Machine Theory*, vol. 44, no. 8, pp. 1535-1547, Aug 2009.

[13] M. Shahgholi, and S. E. Khadem, "Primary and parametric resonances of asymmetrical rotating shafts with stretching nonlinearity," *Mechanism and Machine Theory*, vol. 51, pp. 131-144, May 2012.

[14] S. A. A. Hosseini, and M. Zamanian, "Multiple scales solution for free vibrations of a rotating shaft with stretching nonlinearity," *Scientia Iranica*, vol. 20, no. 1, pp. 131-140, Feb 2013.

[15] H. S. A. Nezhad, S. A. A. Hosseini, and M. Zamanian, "Flexural–flexural–extensional–torsional vibration analysis of composite spinning shafts with geometrical nonlinearity," *Nonlinear Dynamics*, vol. 89, pp. 651-690, Mar 2017.

[16] H. S. Han, K. H. Lee, and S. H. Park, "Parametric study to identify the cause of high torsional vibration of the propulsion shaft in the ship," *Engineering Failure Analysis*, vol. 59, pp. 334-346, Jan 2016.

[17] J. Homišin, P. Kaššay, M. Urbanský, M. Puškár, R. Grega, and J. Krajňák, "Electronic constant twist angle control system suitable for torsional vibration tuning of propulsion systems," *Journal of Marine Science and Engineering*, vol. 8, no. 9, pp. 721, Sep 2020.

[18] N. Vulić, K. Bratić, B. Lalić, and L. Stazić, "Implementing simulationX in the modelling of marine shafting steady state torsional vibrations," *Polish Maritime Research*, vol. 28, no. 2, pp. 63-71, Jun 2021.

[19] Z. Korczewski, "A method to assess transverse vibration energy of ship propeller shaft for diagnostic purposes," *Polish Maritime Research*, vol. 24, no. 4, pp. 102-107, Dec 2017.

[20] H. Han, K. Lee, and S. Park, "Evaluation of the increased stiffness for the elastic coupling under the dynamic loading conditions in a ship". *Engineering Failure Analysis*, vol. 68, pp. 254-262, Oct 2012.

[21] P. Czech, "Determination of the course of pressure in an internal combustion engine cylinder with the use of vibration effects and radial basis function–preliminary research," In Telematics in the Transport Environment: 12th International Conference on Transport Systems Telematics, TST 2012, *Katowice-Ustroń, Poland,* vol. 12, pp. 175-182, Oct 2012.

[22] S. Neupauerová, "Investigation of stress allocation in the rubber-cord flexible element by FEF," *Acta Mechanica Slova*ca, vol. 9, pp. 27-30, Feb 2005.

[23] J. Homišin, "Contribution and perspectives of new flexible shaft coupling types–pneumatic couplings," *Zeszyty Naukowe Transport/ Politechnika Śląska,* Jun 2018.

[24] C. Kong, J Jeong, W. Yo, Y. Sugiyama, and C. Soutis, "Investigation of vibration characteristics of carbon/epoxy propeller shaft for vehicle," *Science and Engineering of Composite Materials*, vol. 10, no. 1, pp. 11-18, Feb 2002.

[25] N. O. Myklestad, Fundamentals of vibration analysis. Mineola, New York, ABD: *Courier Dover Publications*, 2018.

[26] A. N. Halilbese, and O. A. Özsoysal, "The coupling effect on torsional and longitudinal vibrations of marine propulsion shaft system," *Journal of ETA Maritime Science*, vol. 9, no. 4, Dec 2021.

[27] J. N. Reddy, *Mechanics of laminated composite plates and shells: theory and analysis*, (2nd Ed.). Boca Raton, Florida, ABD: CRC Press, 2004.

[28] E. Altunsaray, and İ. Bayer, "Deflection and free vibration of symmetrically laminated quasi-isotropic thin rectangular plates for different boundary conditions," *Ocean Engineering*, vol. 57, pp. 197-222, Jan 2013.

[29] H. Chunxing, H. Guibin, L. Cheng, "Experimental and numerical study of low-velocity impact and tensile after impact for CFRP laminates single-lap joints adhesively bonded structure," *Materials*, vol. 14, no. 4, 1016, Apr 2021.

RESEARCH ARTICLE

DOI: 10.54926/jnamt.2025.2517

J Nav Architect Mar Technol 2025;227(1):52-63

A Simple Combined Method for Parametric Generation of Ship Hull Variants

Marcelo de Oliveira Predes

Brazilian Navy, Rio de Janeiro, Brazil

To cite this article: M. O. Predes. A simple combined method for parametric generation of ship hull variants. *J Nav Architect Mar Technol*. 2025;227(1):52-63.

Received: 10.04.2025 - **Revision Requested:** 02.05.2025 - **Last Revision Received:** 24.06.2025 - **Accepted:** 08.07.2025 - **Publication Date:** 16.07.2025

Abstract

The ship's performance at sea can be influenced by multiple parameters, especially the hull design. Its geometry affects the vessel's behavior, structural integrity, and overall efficiency while crossing the water surface. While the process of hull form generation can involve complex mathematical models, sometimes requiring considerable computational effort, this paper presents a simple method based on the combination of polynomial functions with Lewis mapping techniques. Initially, using a frigate hull as the base model, a code was developed to generate variations of its geometry according to the proposed methodology. Through this approach, it was possible to derive variations of the original hull model, each differing in only one of the considered shape parameters, providing a valuable tool for hull geometry analysis in ship design.

Keywords: Lewis mapping, Hull geometry, Parametric hull design

1. Introduction

Developing methodologies to modify hull geometry plays a key role in optimization processes. When conducting performance analyses that involve global hull shape modifications, parameterizing the geometry using specific descriptors proves to be the most effective way to evaluate such changes.

Several studies have been conducted using different parameters and performance indicators [1] aimed to optimize the geometry of destroyer-type hulls by correlating seakeeping responses with certain shape parameters through regression analysis.

The studies published by [2] were based on an analytical method for seakeeping optimization. They developed a code to generate variations of a baseline hull model, which were evaluated based on performance under certain aspects, including the response of these models to specific types of motion [3]. Assessed the influence of hull geometry and dimensional variations on vertical response motions, as well as their effects on crew comfort and the risk of propeller emergence.

Aiming to generate geometric modifications to hulls and directly obtain an optimized solution [4], proposed a methodology combining polynomial functions with Lewis transformations. Although the results demonstrated significant performance improvements under the study's assumptions, the resulting hull shape was deemed impractical for real-world applications. All of these studies employed strip theory formulations to compute ship motions.

The study presented in [5] evaluated the performance enhancement of a catamaran vessel. In this work, geometric modifications of a baseline model were generated using the Lackenby algorithm, producing variations in the block

Address for Correspondence: Marcelo de Oliveira Predes, Brazilian Navy, Rio de Janeiro, Brazil
E-mail: marcelo.predes@marinha.mil.br
ORCID ID: orcid.org/0009-0001-2189-4088

Copyright© 2025 The Author. Published by Galenos Publishing House on behalf of UCTEA Turkish Chamber of Naval Architects and Marine Engineers.
Licensed under a Creative Commons Attribution-NonCommercial-NoDerivatives 4.0 (CC BY-NC-ND) International License

coefficient and the longitudinal position of the center of buoyancy within a 10% range. The results indicated that changes in specific hull parameters had a significant impact on the vessel's seakeeping performance.

Recent advancements in parametric hull modeling, optimization, and CFD-based performance evaluation have led to the development of several cutting-edge methodologies. These recent studies incorporate the latest technological innovations in the field [6]. Applied a parametric modeling approach combined with CFD simulations to optimize the hull geometry of containerships, focusing on minimizing resistance. This research is a prime example of how computational fluid dynamics can be utilized to improve vessel efficiency [7]. Introduced a novel hull modeler based on Generative Adversarial Networks, which are deep learning techniques capable of generating diverse hull forms. This approach represents a significant leap in the ability to design hulls using AI-driven methods. In [8], fully-parametric models of the hull, propeller, and rudder were used in an integrated optimization process aimed at improving overall hydrodynamic performance. The study highlights the benefits of employing a comprehensive, multi-component optimization framework for enhancing vessel performance. Finally, utilized deep neural networks to expedite the hull form optimization process for small vessels, offering an innovative solution for faster and more accurate optimization in smaller-scale applications [9].

The methodology presented in this article was originally used by [10] to analyze the effects of certain hull shape parameters on the occurrence of slamming, an event characterized by the violent impact of the vessel's structure on the sea surface. The results obtained in this study indicated the possibility of considerable performance improvements in seakeeping behavior through modifications of the analyzed geometric parameters. The detailing of the hull geometry variation process is presented in the following sections.

2. The Baseline Model and the Variation Process

This research used the hull configuration of the Dutch Friesland-class frigate as the baseline model, which has various published data, including its body plan and seakeeping performance measurements, as presented by [11] and [12]. Figure 1 represents the model through 21 bilge sections. The main characteristics are presented in Table 1.

A specific code was developed for generating new hull geometries, considering the following elements as constants relative to the original model: B, T, L_{PP} and the hull center-line profile (Figure 2 illustrates these constraints, highlighted on the baseline model).

Based on these premises, the mathematical description of the new hull geometries was obtained in two stages. Initially, the intersection curves between the flotation plane and the hull were modeled based on the variation of parameters S1, S2, and S3, using third-degree Bézier polynomial curves. For its definition, control points are established at the extremities, delimiting its beginning and end, as well as intermediate points to define the contour. The generic formulation of the

Table 1. Main characteristics

L_{pp}	112.4 m
B	11.74 m
T	4.01 m
C_B	0.562
CG	55; 0; 5 m
Displacement	3046 t

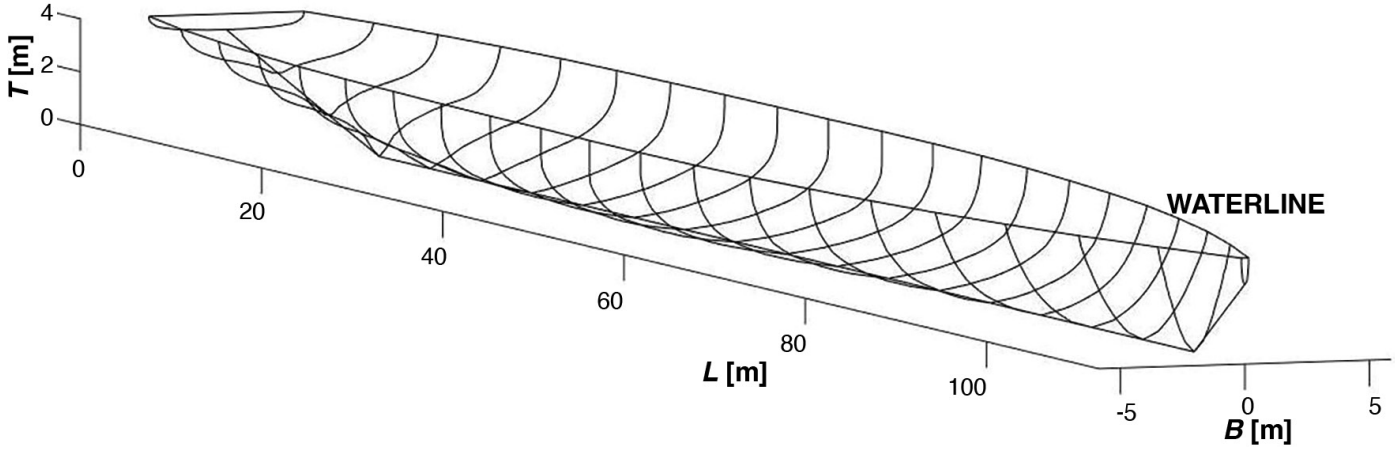


Figure 1. Hull model of the frigate "Friesland"

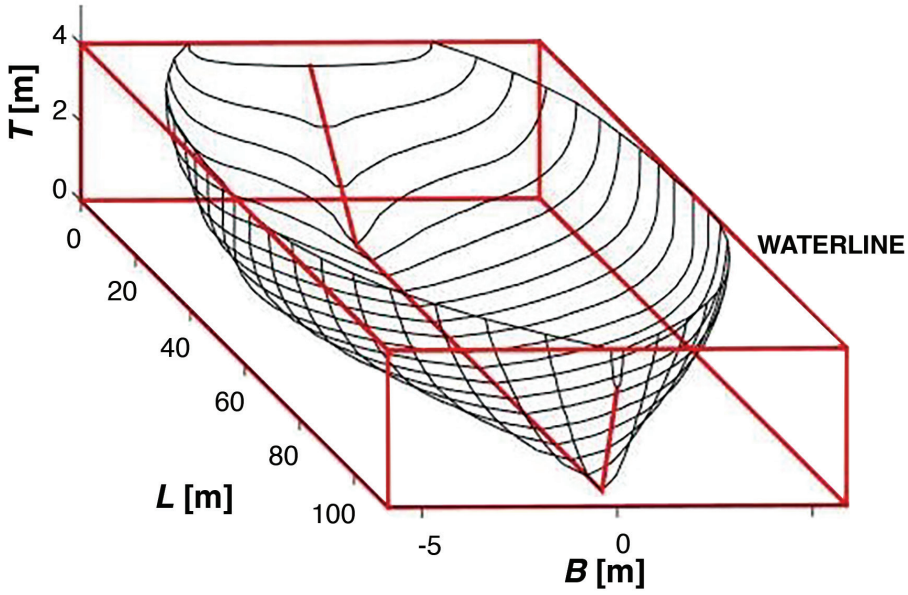


Figure 2. Variation limits on the baseline model

Bézier curve is presented in Equation 1, while its cubic form is represented in Equation 2.

$$B^n(t) = \sum_{i=0}^{n} B_i^n(t)\, b_i \quad (1)$$

$$B(t) = (1-t)^3 B_0 + 3t(1-t)^2 b_1 + 3t^2(1-t) b_2 + t^3 b_3 \quad (2)$$

Here, $B^n(t)$ are the Bernstein polynomials, b_i the control points defining the curve's shape, and t the interpolation parameter along the curve. Figure 3 illustrates a typical cubic Bézier curve and its control points.

The process of modeling the hull contour in the flotation plane is illustrated in Figure 4. The hull contour is defined by two Bézier curves connected at point B, which is fixed at the beam amidships. The first curve is governed by parameters S1 which also determines the stern width and S2, along with the fixed control points P1 and B. The second curve depends solely on parameter S3, with the other control points B, P2, and P3 held constant. Parameters S1, S2, and S3 vary only in the longitudinal direction. Figure 4 also shows five hypothetical positions for S2 and S3, highlighting the resulting variations in hull shape.

It is important to highlight that the method also constrained the Bézier curves in the transverse direction, ensuring they did not exceed the original beam (B). This restriction preserves the realistic proportions of the hull, maintaining its consistency with actual ship forms. The resulting hull contour, after applying this constraint, is shown in Figure 5.

Once the flotation contour was defined, the hull was modeled using Lewis transformations with two parameters for 21 transverse sections. This method was selected to simplify the hull generation process and reduce computational effort, while still capturing the essential geometric characteristics.

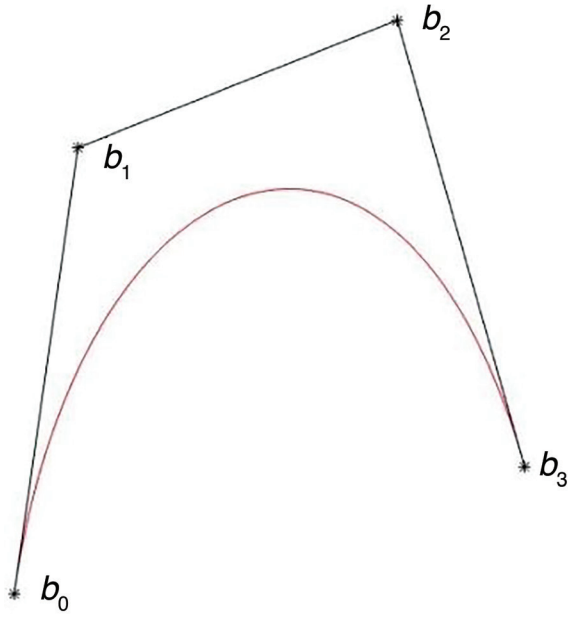


Figure 3. Cubic Bézier curve
Source: [10]

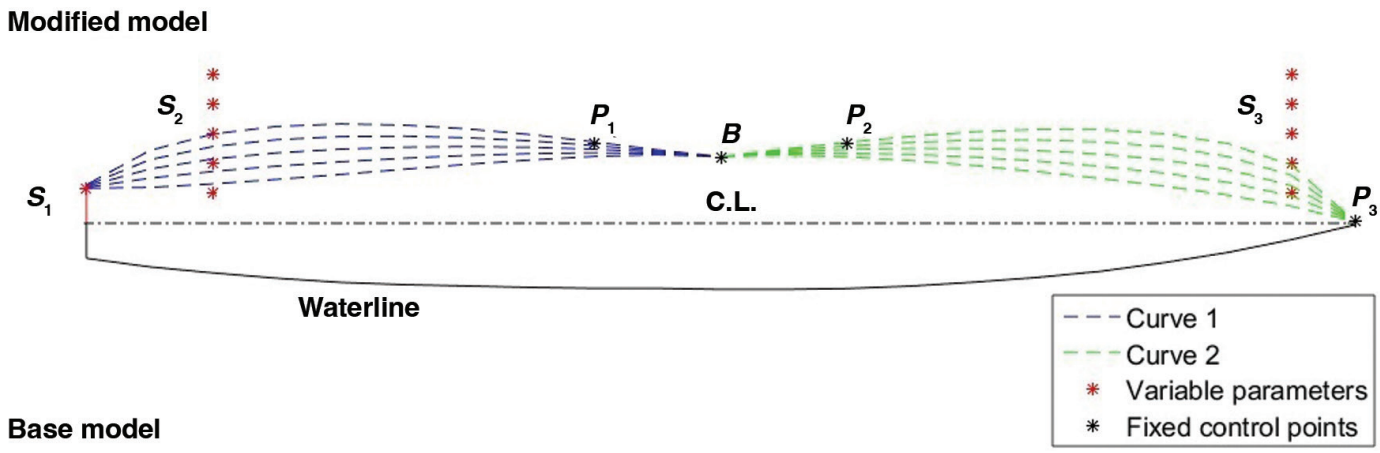


Figure 4. Variation of parameters S1, S2 and S3

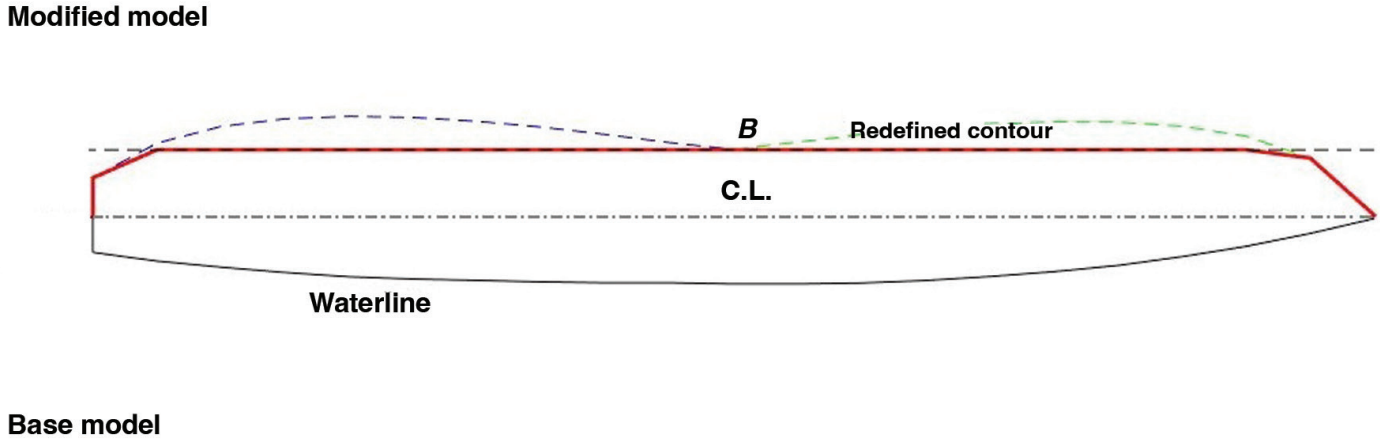


Figure 5. Limitation on the waterline contour

As discussed later in the text, a follow-up study is proposed to explore potential improvements introduced by incorporating a third parameter. The Lewis method [13] transforms a circular shape (Equation 3) into an arbitrary hull section (Equation 4):

$$\zeta = ie^{\alpha}e^{-i\theta} \tag{3}$$

$$z = x + iy \tag{4}$$

The transformation described in Equation 5 maps points from the ζ-plane to their corresponding locations in the z-plane, provided the coefficients of the mapping function are properly defined.

$$z = M_S(a_{-1}\zeta + a_1\zeta^{-1} + a_3\zeta^{-3} + a_5\zeta^{-5} + \ldots) \tag{5}$$

The Lewis formulation employs only two parameters, resulting in Equation 6:

$$z = M_S(a_{-1}\zeta + a_1\zeta^{-1} + a_3\zeta^{-3}) \tag{6}$$

By substituting Equations 3 and 4 into Equation 6 and separating the real and imaginary parts, one can obtain parametric equations that map the arbitrary shapes in the z-plane, as given by Equations 7 and 8:

$$y_S = M_S((1 + a_1)\sin\theta - a_3\sin 3\theta) \tag{7}$$

$$z_S = M_S((1 + a_1)\sin\theta - a_3\sin 3\theta) \tag{8}$$

Where M_S is the scaling factor and a_n the mapping function coefficients. For the shape of ship sections, the section ratio between the ship's half-beam and draft can be given by Equation 9, while the section area coefficient is obtained through Equation 10.

$$H = \frac{B_S/2}{D_S} = \frac{1 + a_1 + a_3}{1 - a_1 + a_3} \tag{9}$$

$$\sigma = \frac{Area}{B_S D_S} = \frac{\pi}{4}\left(\frac{1 - a_1^{\,2} - 3a_3^{\,2}}{(1 + a_3)^2 - a_1^{\,2}}\right) \tag{10}$$

Using the described formulations, hull-like curves can be generated with only two parameters: the H ratio and the sectional area coefficient. Figure 6 shows examples of curves produced by this method, where H is the beam-to-draft ratio and σ is the sectional area coefficient.

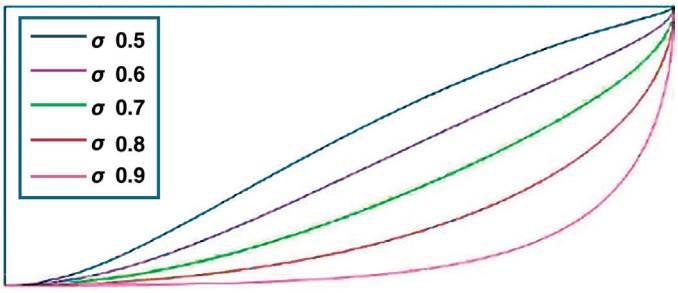


Figure 6. Typical geometries generated using Lewis' technique
Source: [10]

In each section, the H ratio is predetermined, since B_S follows the flotation contour obtained in the previous step, and the hull centerline profile remains fixed. Therefore, only the area coefficient needs to be specified. The coefficients for sections 1, 11, and 21 are directly provided (corresponding to input parameters B1, B2, and B3), while the coefficients for the remaining sections are automatically generated by the code using polynomial interpolation. This approach ensures smooth transitions between sections and prevents abrupt geometric variations. As a result, the entire process of generating hull variants requires only six input parameters.

3. Applying the Method to Obtain Specific Variations

3.1. Selection of Hull Shape Parameters

The described process combined simple formulations, enabling hull variant generation with low computational demands. This aspect is relevant when aiming to obtain a high number of variations, allowing for the filtering of characteristics in a specific manner.

In [10] work, the aim was to evaluate the effect of varying certain parameters on the slamming effect. To achieve this purpose, hull variants were used, each with only one of these parameters altered to an extreme maximum or minimum value.

For the analysis of hull geometry modification, the following shape parameters were selected:

- Dimensionless longitudinal center of buoyancy (LCB/L_{PP})
- Dimensionless longitudinal center of buoyancy (LCB/L_{PP})
- C_B
- C_{WP}

The objective of the method is to obtain variations of the original hull model in which only one of the four shape parameters differs from the baseline configuration. The resulting extreme cases, each isolating the influence of a single parameter, are designated as follows:

- LCB(+), with the center of buoyancy closer to the bow
- LCB(-), with the center of buoyancy closer to the stern
- C_B(+), with the highest block coefficient
- C_B(-), with the lowest block coefficient
- LCF(+), with the center of flotation closer to the bow
- LCF(-), with the center of flotation closer to the stern
- C_{WP}(+), with the highest waterplane area coefficient; and
- C_{WP}(-), with the lowest waterplane area coefficient

To generate these models, a large set of hull geometries was produced by systematically varying six input parameters S1, S2, S3, B1, B2, and B3 using a custom-coded routine. These parameters control the shape of the Bézier waterline curves and the Lewis section profiles. Although they do not directly correspond to high-level form coefficients, the code automatically filters the generated hulls, retaining only those in which a single coefficient C_B, C_{WP}, LCB, or LCF varies significantly, while the others remain within a narrow tolerance based on the form coefficients of the baseline hull. This indirect approach enables the construction of controlled geometry sets suitable for isolated parameter analysis, as illustrated in Figure 7.

The calculation of the four hull shape parameters is straightforward and accurate, given that the bilge and waterline contours are defined using Bézier and Lewis formulations. To compute these parameters, the generated hull is decomposed into simple geometric elements such as trapezoidal prisms whose centroids and volumes can be easily determined and integrated to obtain the desired characteristics.

3.2. Results

By varying the six parameters described earlier, approximately 10 million hull configurations were generated. Owing to the simplicity of the computational method, this process could be completed on a standard personal computer in approximately one hour. After applying the filtering criteria illustrated in Figure 7 which selected only the configurations falling within one of the four predefined ranges for each form coefficient just over 2,000 variations were retained. The remaining configurations were discarded for failing to preserve three of the dimensionless parameters at values approximately equal to those of the original model.

From the filtered dataset, eight extreme variations were selected for further analysis. Tables 2 to 5 present the highest

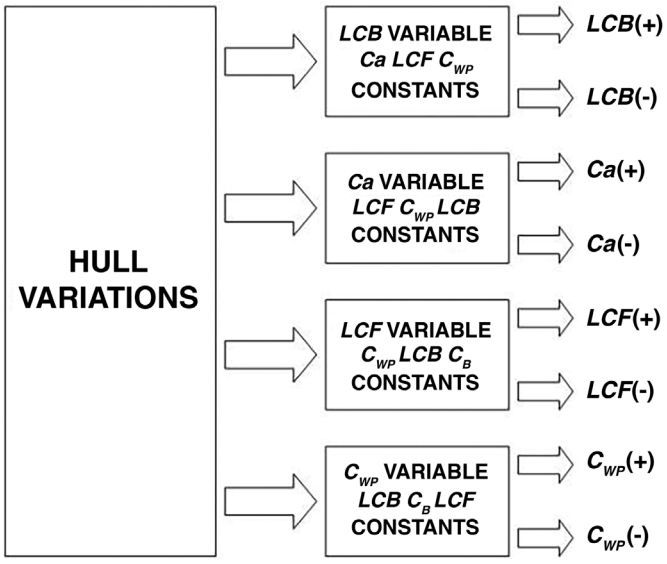


Figure 7. Variant selection process

(+) and lowest (-) non-dimensional values obtained for each form coefficient.

Figures 8-11 show the baseline plan of the 8 extreme variations obtained at the end of the process.

3.3. Stability Analysis

In order to ensure the basic feasibility of the generated hull models, the eight selected extreme configurations were subjected to initial and intact stability analyses. The initial equilibrium condition of the hull is assessed through the metacentric height (GM > 0), according to Equation 7:

$$GM = KB + BM - KG \tag{7}$$

The value of KB (Center of Buoyancy) was calculated based on the submerged geometry of the hull, while KG was previously established and fixed. The metacentric radius (BM) can be obtained from the relation in Equation 8, for small angles:

$$BM = \frac{I}{\nabla} \tag{8}$$

Where α is the heeling angle, I is the area moment of the waterplane about the ship's longitudinal axis, and ∇ is the volume displaced by the ship.

For intact stability assessment, the guidelines established by the International Maritime Organization (IMO) were adopted, according to resolution A749(18), (IMO, 1993). Basically, calculations are made based on the static stability curve for a given hull, briefly described in Table 6.

The results of the intact stability analysis for the eight hull variants are presented in Table 7, indicating compliance with the specified criteria.

Table 2. Variations (LCB/L_{PP})

261 variations	(%)	*LCB*(-)	Base	*LCB*(+)	(%)
LCB/L_{PP}	8.63	0.447	0.489	0.510	4.26
C_B	0.18	0.563	0.562	0.561	0.18
LCF/L_{PP}	0.24	0.462	0.461	0.461	0.14
C_{WP}	0.25	0.796	0.794	0.792	0.25

Table 3. Variations (C_B)

892 variations	(%)	C_B(-)	Base	C_B(+)	(%)
C_B	36.30	0.358	0.562	0.590	4.98
LCB/L_{PP}	0.21	0.490	0.489	0.489	0.06
LCF/L_{PP}	0.24	0.462	0.461	0.462	0.24
C_{WP}	0.25	0.796	0.794	0.796	0.25

Table 4. Variations (LCF/L_{PP})

168 variations	(%)	*LCF*(-)	Base	*LCF*(+)	(%)
LCF/L_{PP}	5.72	0.435	0.461	0.515	11.75
C_{WP}	0.13	0.793	0.794	0.793	0.13
LCB/L_{PP}	0.07	0.489	0.489	0.491	0.42
C_B	0.36	0.560	0.562	0.559	0.53

Table 5. Variations (C_{WP})					
790 variations	**(%)**	**C_{WL}(-)**	**Base**	**C_{WL}(+)**	**(%)**
C_{WP}	2.14	0.777	0.794	0.867	9.19
LCF/L_{PP}	0.34	0.463	0.461	0.460	0.28
LCB/L_{PP}	0.50	0.492	0.489	0.492	0.50
C_B	0.18	0.561	0.562	0.561	0.18

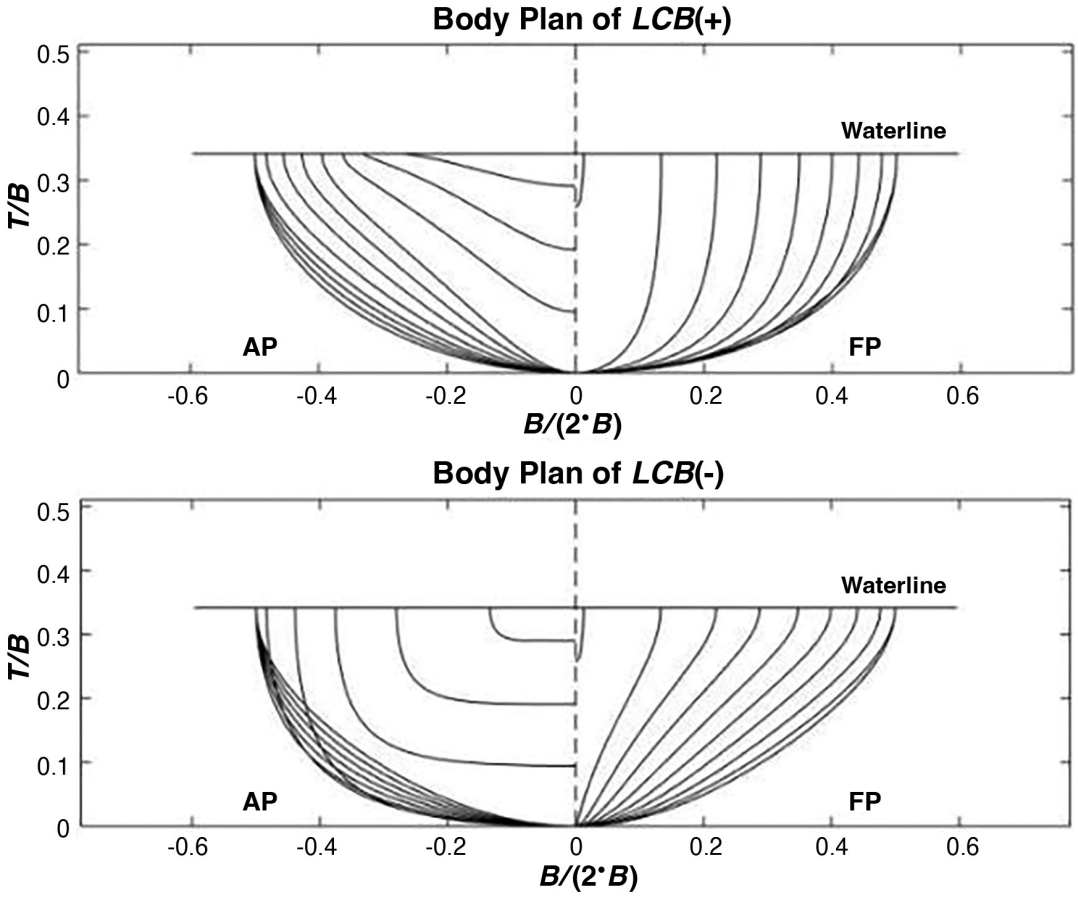


Figure 8. Extreme variations of *LCB*

3.4. Comparison with CAD-based Methods

Unlike CAD-based tools such as Rhino, Delftship, or Maxsurf, where geometric variations are usually introduced by manipulating control points or hull curves directly, the methodology presented here focuses on varying high-level form coefficients *(LCB, LCF,* C_{WP}, and C_B*)*. Since most CAD tools do not allow direct manipulation of these coefficients independently, achieving isolated variations in these parameters often requires manual trial-and-error. In contrast, the approach adopted in this paper automates this process through indirect parametric control, enabling the generation of hull forms where only one parameter varies significantly while the others remain near constant.

Table 6. IMO intact stability requirements		
No.	**Criteria**	**Requirement**
1	Area *GZ* < 30° (m.rad)	0.055
2	Area *GZ* < 40° (m.rad)	0.09
3	Area *GZ* 30° < < 40° (m.rad)	0.03
4	Max. angle *GZ* (°)	25
5	*GZ* at 30° (m)	0.2
6	Initial *GMt* (m)	0.15
7	Equivalent angle for crew concentration (°)	10
8	Equivalent angle for yawing (°)	10
IMO: International Maritime Organization		

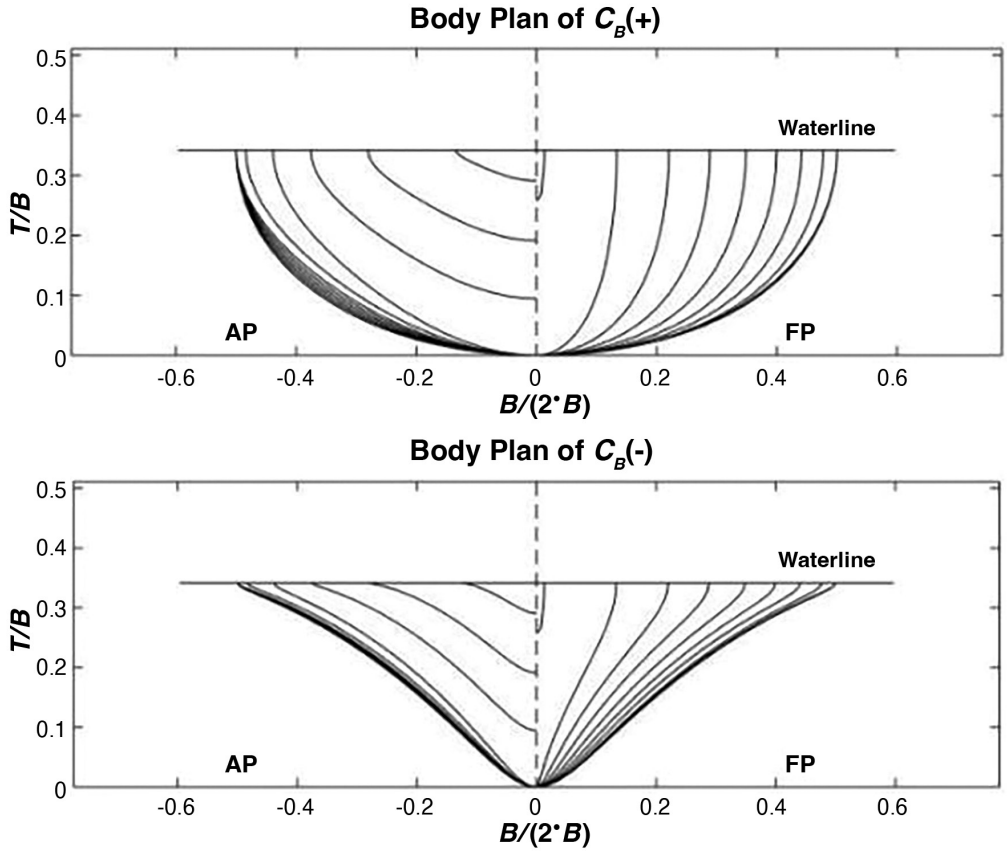


Figure 9. Extreme variations of C_B

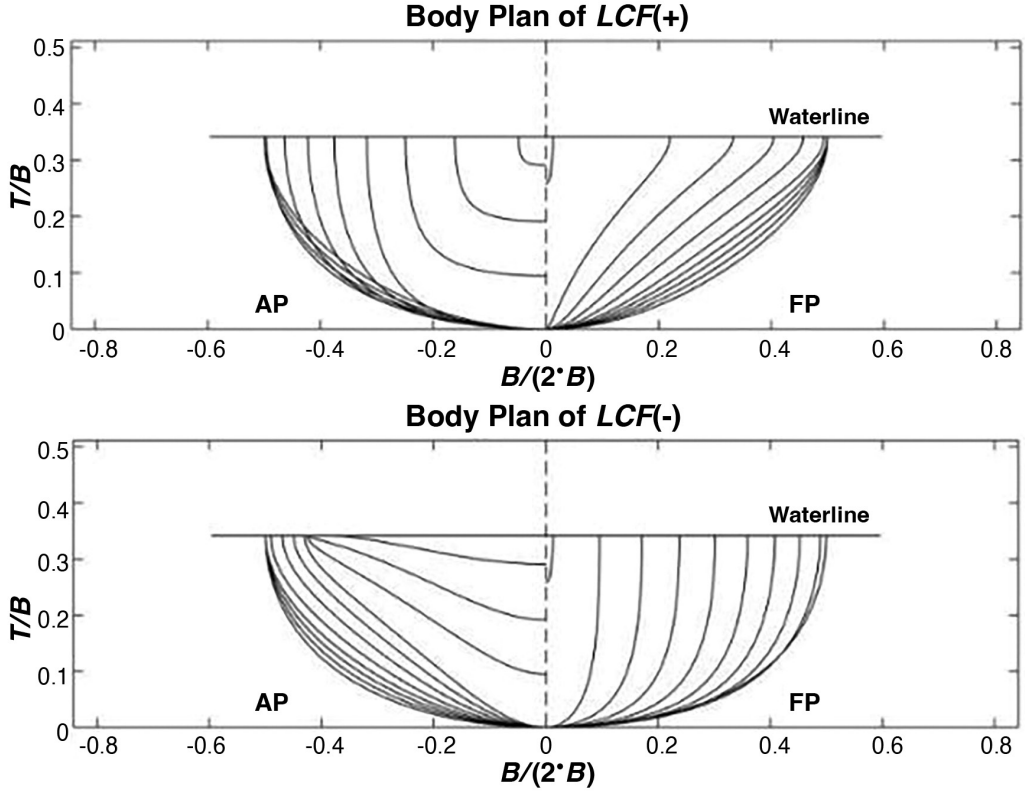


Figure 10. Extreme variations of *LCF*

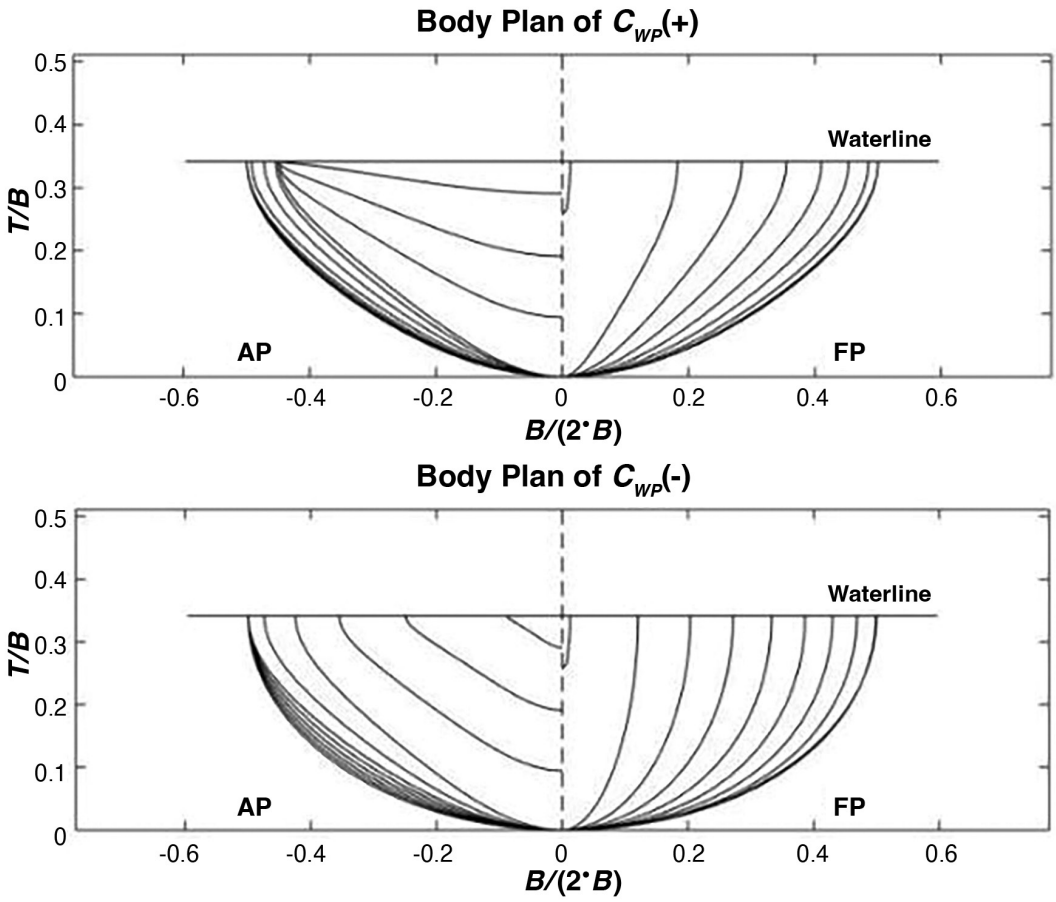


Figure 11. Extreme variations of C_{WP}

Table 7. Stability criteria results

Criteria	*LCB*(+)	*LCB*(-)	C_B(+)	C_B(-)	*LCF*(+)	*LCF*(-)	C_{WP}(+)	C_{WP}(-)
1	0.059	0.087	0.063	0.211	0.079	0.065	0.145	0.067
2	0.094	0.140	0.099	0.326	0.127	0.104	0.230	0.105
3	0.035	0.054	0.037	0.115	0.047	0.039	0.085	0.038
4	31.8	31.8	30.9	36.4	31.8	31.8	32.7	30.9
5	0.217	0.322	0.234	0.669	0.286	0.238	0.501	0.241
6	0.481	0.658	0.456	2.611	0.656	0.572	1.259	0.518
7	3.5	2.5	3.3	1.2	2.5	3.1	1.3	3.1
8	5.6	3.9	5.6	1.2	4.0	5.0	2.1	5.0

The ranges used for comparison in Table 8 are based on values typically found in naval architecture literature and CAD-based modeling tools. For instance, [14] indicate block coefficient values between 0.55 and 0.60 for fast naval vessels such as frigates, while typical waterplane coefficients range from 0.75 to 0.85. These values are consistent with those observed in parametric CAD platforms such as Maxsurf [15], reinforcing the validity of the generated hull forms.

To validate the effectiveness of the proposed methodology, a hull form was generated through automated variation of the six parametric inputs and compared against a reference model of the Friesland frigate, digitized from its original lines plan. As shown in Figure 12, the generated hull approximates the shape of the CAD-based reference model with reasonable accuracy. The original measurement points used for digitization are also shown to illustrate data fidelity. While some discrepancies are observed particularly in the aft sections where hull curvature is more complex the overall geometry is sufficiently close to support the feasibility of the approach.

Table 8. Comparison with typical design coefficient ranges

Dimensionless	Typical range (CAD/literature)	Range with proposed method	Relative variation [%]
LCB/L_{PP}	0.46-0.50	0.447-0.510	14.09
C_B	0.50-0.65 (frigates)	0.358-0.590	64.8
LCF/L_{PP}	0.45-0.49	0.435-0.515	18.39
C_{WP}	0.75-0.85	0.777-0.867	11.58

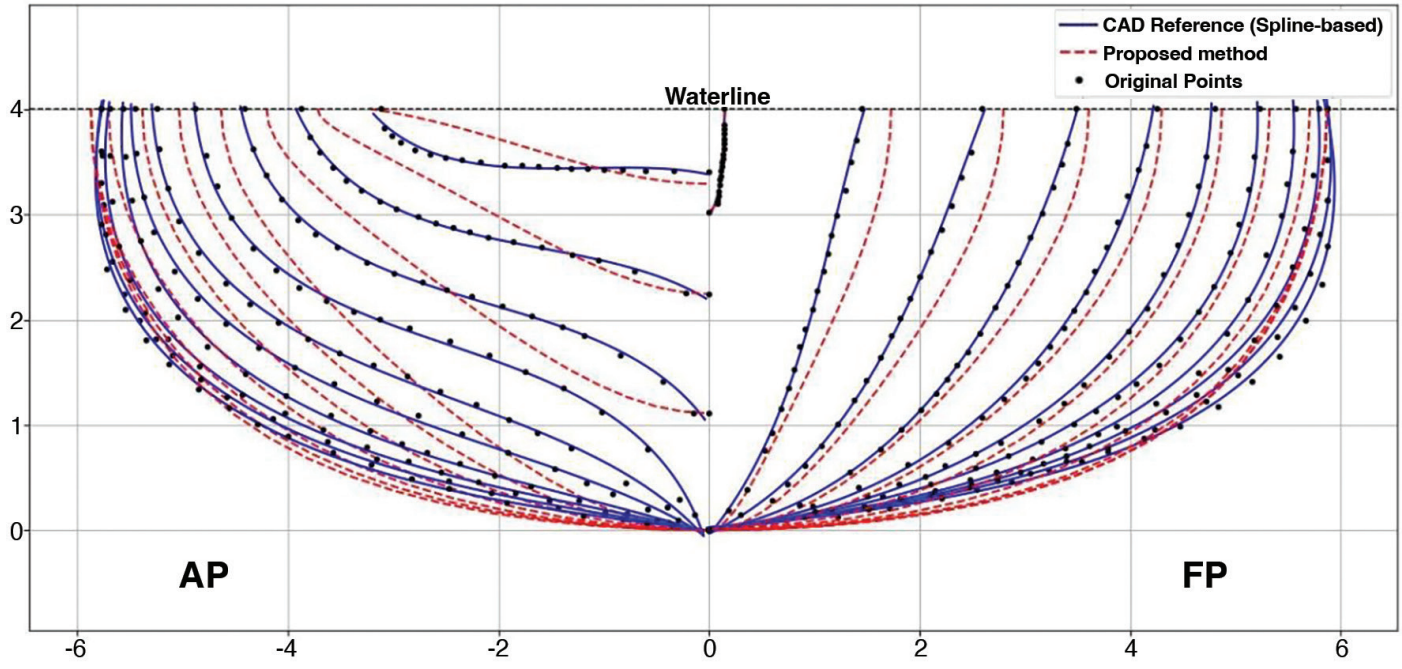


Figure 12. Body plan comparison

One noteworthy limitation observed is that Lewis sections are always tangent to the baseline and to the hull side at the waterline, which tends to produce vertical surfaces above the waterline. This behavior, visible in the comparative plots, can lead to unrealistic geometry in areas where the reference hull has more pronounced flare. It highlights the need for additional fairing if more complex hull shapes are to be accurately reproduced.

4. Practical Applications of the Proposed Method

4.1. Sensitivity Studies Using Simplified Performance Evaluation

The proposed method can support design investigations focused on understanding how individual geometric parameters affect ship behavior. A representative example is found in [4], who employed a parameterized hull model, defined through polynomial distributions and Lewis sections, to assess the influence of form modifications on seakeeping characteristics. By applying a linear strip theory solver, the study revealed that even moderate shape adjustments could lead to noticeable differences in vertical accelerations and bow motions. Such approaches demonstrate the practical value of simplified geometric tools when seeking directional insight during concept refinement or prior to detailed analysis.

A related application is presented in [5], where hull variants of a fast displacement catamaran were generated by varying form coefficients such as block coefficient and longitudinal center of buoyancy by ±10%. Seakeeping performance was assessed through strip theory codes (PDStrip, Maxsurf), and the study confirmed that relatively simple geometric changes can produce measurable improvements in motion behavior, particularly regarding vertical accelerations and seasickness index.

4.2. Parametric Hull Libraries and Design Space Exploration

The method is also well suited for generating systematic sets of hull variants to explore the influence of geometric characteristics. This is illustrated in [10], where a large number of configurations, produced using the same approach described in this article, were evaluated to estimate slamming probability for a frigate-type hull. Each variant featured the isolated modification of a single form parameter, enabling

a clear assessment of its effect on wave impact behavior. Simulations based on simplified seakeeping tools showed that even these targeted changes could significantly influence slamming occurrence. Figure 13 summarizes these findings, presenting results for both extreme and intermediate cases.

A similar strategy is adopted by [16], who developed multiple hull forms by systematically modifying form coefficients of reference designs. Using basic performance estimators, they analyzed resistance and motion behavior across the generated shapes and identified favorable trends for ship types such as destroyers and reefers. This type of exploration highlights the potential of automated variant generation methods to support informed design decisions from an early stage of development.

4.3. Integration with Simplified Estimators

The proposed method can also support early design workflows by supplying structured hull variants to simplified performance prediction tools. Its low computational cost and ability to isolate specific geometric characteristics make it suitable for integration into processes where a large number of alternatives must be screened before detailed analysis.

A related example is presented by [17], who employed a multiparameter conformal mapping technique, conceptually similar to the Lewis approach, to generate arbitrary hull section shapes. The generated variants were evaluated using low-order hydrodynamic tools, highlighting their utility for trend identification and pre-selection in exploratory studies. Although the resulting geometries were not immediately suitable for advanced solvers, they enabled efficient scanning of the design space and informed the refinement of promising configurations.

5. Conclusion

In this work, a simplified methodology for hull geometry modifications was presented. To verify its effectiveness, variants of a baseline model were generated by singular alterations of the established geometric parameters.

The use of the two-parameter Lewis formulation offered a simplified and analytically efficient means of generating sectional shapes for preliminary design studies. While this method facilitates the rapid production of hull variants, it presents inherent limitations in defining complex geometries, particularly above the waterline, due to its tangency constraints at the baseline and hull side. In this study, the focus remained on submerged shapes, with the understanding that the resulting point distributions are intended for early-stage exploration and can later be faired using external CAD or hull design tools prior to CFD or FEM applications. Each transverse section was defined using Bézier curves to ensure local smoothness and geometric control, and the sectional area coefficients were polynomially interpolated along the hull to maintain gradual shape transitions. For future work,

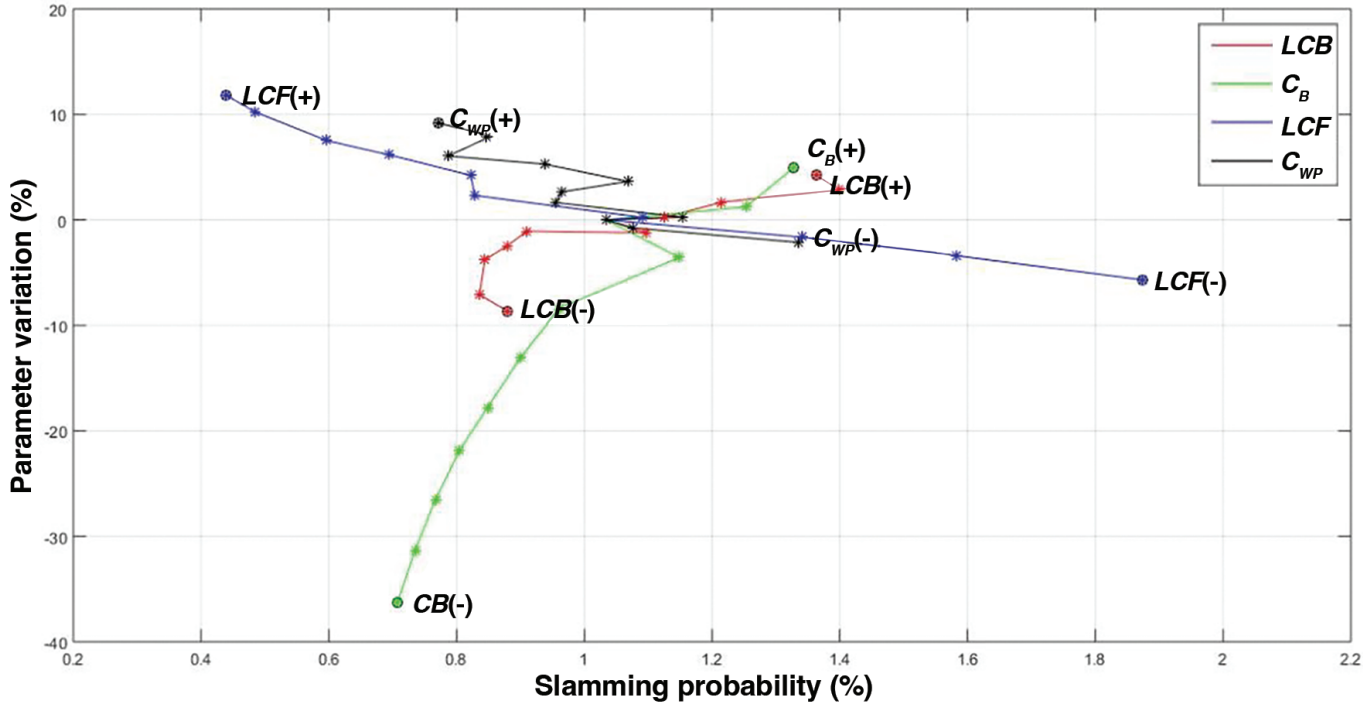


Figure 13. Slamming occurrence vs. parameter variation
Source: [10]

the adoption of the three-parameter Lewis technique may provide greater flexibility in capturing complex section profiles. Furthermore, the use of more advanced hull variation procedures such as Moor's method, in combination with a fair parent hull is recommended to enhance surface fairness and geometric realism in the generation of CFD-ready hull forms.

Footnote

Financial Disclosure: The author declared that this study received no financial support.

NOMENCLATURE

B	[m]	Beam at the waterline
L_{pp}	[m]	Length between perpendiculars
T	[m]	Draft
C_B	[-]	Block coefficient
C_{WP}	[-]	Waterplane area coefficient
CG	[m]	Center of gravity
LCB	[m]	Longitudinal center of buoyancy
LCF	[m]	Longitudinal center of flotation

References

[1] N. K. Bales, "Optimizing the seakeeping performance of destroyer-type hulls," in *Thirteenth Symposium on Naval Hydrodynamics*, Tokyo, Japan, 2018.

[2] G. J. Grigoropoulos, "A new method for developing hull forms with superior seakeeping qualities," in *CADMO '88 Conference*, Southampton, England, 1988.

[3] A. R. J. M. Lloyd, *Seakeeping: ship behavior in rough weather*. Chichester: Elis Horwood Limited, 1989. Available at: https://doi.org/10.1016/0951-8339(89)90012-9

[4] G. K. Kapsenberg, "Finding the hull form for given seakeeping characteristics," in *MARIN*, Wageningen, the Netherlands, 2005.

[5] F. C. Belga, "Seakeeping optimization of a fast displacement catamaran on the basis of strip-theory codes," M.Sc. dissertation, Instituto Superior Técnico, Lisboa, Portugal, 2017.

[6] Y. Feng, O. El Moctar, and T. E. Schellin, "Parametric hull form optimization of containerships for minimum resistance in calm water and in waves," *Journal of Marine Science and Application,* vol. 20, pp. 670-693, Dec 2021.

[7] S. Khan, K. Goucher-Lambert, K. Kostas, and P. Kaklis, "ShipHullGAN: a generic parametric modeller for ship hull design using deep convolutional generative model," *Computer Methods in Applied Mechanics and Engineering,* vol. 411, 116051, Jun 2023.

[8] X. Cheng, et al. "Ship optimization based on fully-parametric models for hull, propeller, and rudder," *Journal of Marine Science and Engineering,* vol. 12, no. 9, 1635, Sep 2024

[9] J.-H. Kim, M.-I. Roh, and I.-C. Yeo, "Hull form optimization of fully parameterized small ships using characteristic curves and deep neural networks," *International Journal of Naval Architecture and Ocean Engineering*, vol. 16, 100596, 2024.

[10] M. O. Predes, "Parametric analysis involving variations of form coefficients in slamming," Master's thesis, Federal University of Rio de Janeiro, Rio de Janeiro, Brazil, 2020. Available at: https://pantheon.ufrj.br/handle/11422/23176.

[11] W. Smith, *Equation of motion coefficients for a pitching and heaving destroyer model*. Delft, Netherlands: TUDelft, Ship Hydromechanics Laboratory, 1966.

[12] J. S. Gerritsma, W. E. Smith, "Full-scale destroyer motion measurements," *Journal of Ship Research,* vol. 11, no. 01, pp. 1-27, 1967.

[13] F. M. Lewis, "The inertia of water surrounding a vibrating ship," in *Transactions SNAME*, 1929.

[14] K. J. Rawson, and E. C. Tupper, *Basic ship theory-hydrostatics and strength*. 5th ed. Oxford: Butterworth-Heinemann, 2001.

[15] Bentley Systems. Maxsurf Modeler – User Manual. Bentley Systems, 2020.

[16] G. J. Grigoropoulos, "Hull form optimization for hydrodynamic performance," *Marine Technology and SNAME News,* vol. 41, no. 4, pp. 167-182, Oct 2004.

[17] M. Salehi, P. Ghadimi, and A. B. Rostami, "A more robust multiparameter conformal mapping method for geometry generation of any arbitrary ship section," *Journal of Engineering Mathematics,* vol. 89, pp. 113-136, Oct 2014.

RESEARCH ARTICLE

DOI: 10.54926/jnamt.2025.2518

J Nav Architect Mar Technol 2025;227(1):64-73

Wave-Induced Force Modeling on a Monopile Foundation at Gökçeada Using Spectral and Diffraction-Based Approaches

Deniz Bayraktar Bural

İstanbul Technical University Faculty of Naval Architecture and Ocean Engineering, Department of Shipbuilding and Ocean Engineering, İstanbul, Türkiye

To cite this article: D. Bayraktar Bural. Wave-induced force modeling on a monopile foundation at gökçeada using spectral and diffraction-based approaches. *J Nav Architect Mar Technol*. 2025;227(1):64-73.

Received: 05.05.2025 - **Revision Requested:** 14.06.2025 - **Accepted:** 10.07.2025 - **Publication Date:** 18.07.2025

Abstract

This study presents a numerical framework to reconstruct long-term wave-induced force histories on monopile foundations supporting offshore wind turbines in data-limited, fetch-limited marine environments. The methodology is demonstrated for the northeastern Aegean Sea near Gökçeada, where in-situ wave measurements are limited or not readily available. The objective is to model the wave-induced forces acting on offshore monopile-supported wind turbines under irregular sea states. By combining site-specific spectral wave data with diffraction-based force estimation, the study provides a detailed assessment of hydrodynamic load contributions across the frequency domain, offering critical insights for offshore wind energy infrastructure in the Northern Aegean Sea. A site-specific JONSWAP spectrum is constructed using a 10-year reanalysis dataset to characterize the local sea state. Wave loading on the monopile is estimated using MacCamy-Fuchs diffraction theory, which captures frequency-dependent hydrodynamic effects for large-diameter cylindrical structures. To ensure theoretical consistency, spectral components outside the applicable range are excluded with minimal energy loss. The resulting force spectrum is transformed into the time domain using inverse Fourier techniques with randomized phase, yielding a representative wave force signal for time-domain analysis. To assess extreme loading conditions, a statistical extreme value analysis is performed using threshold-based fitting. The proposed framework enables realistic wave load simulation in coastal regions lacking field measurements and supports applications such as fatigue assessment, reliability analysis, and offshore wind turbine design in semi-enclosed seas.

Keywords: Offshore wind turbines, MacCamy-Fuchs diffraction theory, wave-induced forces, JONSWAP spectrum, monopile foundations

1. Introduction

Offshore wind energy has become an increasingly vital component of sustainable energy strategies worldwide, driven by the urgent need to transition to renewable energy sources. In this context, Turkey, particularly the Aegean and Marmara Seas, holds significant offshore wind energy potential [1]. Among these regions, Gökçeada stands out as a promising site due to its strong wind resources and favorable water depths for offshore wind turbine installations [2,3]. Prior optimization studies, such as those by Şişbot et al. [4], have demonstrated that carefully planned turbine placement in Gökçeada can enhance energy production while maintaining structural and environmental feasibility. Recent technical feasibility assessments have further confirmed the suitability of the site for offshore wind development [5].

While wind energy availability is crucial for site selection, offshore structural design requires a thorough understanding of wave conditions, particularly in light of the growing

Address for Correspondence: Deniz Bayraktar Bural, İstanbul Technical University Faculty of Naval Architecture and Ocean Engineering, Department of Shipbuilding and Ocean Engineering, İstanbul, Türkiye
E-mail: bayraktard@itu.edu.tr
ORCID ID: orcid.org/0000-0002-4541-9089

Copyright© 2025 The Author. Published by Galenos Publishing House on behalf of UCTEA Turkish Chamber of Naval Architects and Marine Engineers.
Licensed under a Creative Commons Attribution-NonCommercial-NoDerivatives 4.0 (CC BY-NC-ND) International License

frequency of extreme weather events associated with climate change and the region-specific design criteria emphasized in offshore wind standards [6]. Accurate knowledge of wave height, peak period, and wave direction is fundamental for coastal and offshore engineering applications. Over the past decade, numerous studies have leveraged reanalysis data and numerical modeling to characterize wave climates and their variability across different maritime regions.

Sartini et al. [7] conducted a detailed analysis of 32 years of hindcast wave data in the North Tyrrhenian Sea, extracting critical parameters such as significant wave height, peak period, and dominant wave direction (VMDR). Similarly, Pillai et al. [8] analyzed long-term wave trends along the Emilia-Romagna coast, validating numerical results against field observations to improve nearshore wave climate representation. Ibrahim et al. [9] further highlighted an increasing trend in significant wave heights along the Mediterranean coastline, underscoring the growing influence of climatic shifts on coastal environments.

Understanding these evolving wave climates is essential not only for coastal resilience but also for the structural integrity of offshore wind turbines. The impact of extreme wave conditions on offshore foundations has been widely investigated through the application of wave spectra models. For instance, Fan [10] emphasized the need for accurate design wave height estimations to ensure structural resilience during extreme events such as typhoons. Li et al. [11] complemented these findings with experimental data on the hydrodynamic forces exerted on curved vertical structures, providing valuable insights into wave-structure interactions under varying sea states.

Recent advances in global climate reanalysis datasets, such as ERA5 and ECMWF products, have further enhanced the ability to characterize wave behavior on both regional and global scales. Napitupulu et al. [12] demonstrated how meteorological conditions strongly influence the spatiotemporal variability of significant wave heights, as observed in the Riau Archipelago, reinforcing the importance of accurate wave modeling for structural and navigational safety.

Given that real sea states consist of multiple interacting wave components, spectral analysis offers a more realistic representation of wave loads acting on marine structures compared to deterministic approaches. The design and stability of offshore wind turbines, particularly those supported by monopile foundations, depend critically on the accurate estimation of wave-induced forces under such irregular sea states [13]. Wave spectrum models provide insight into how energy is distributed across different frequency components, influencing the dynamic response of structures [14,15].

In this study, the JONSWAP spectrum has been selected to model the wave environment at Gökçeada. Originally developed for the North Sea, the JONSWAP spectrum remains highly applicable to semi-enclosed and fetch-limited environments when properly adapted. Recent studies support this approach: Vlachogiannis et al. [16] demonstrated the effectiveness of the JONSWAP model in predicting wave energy in shallow coastal areas when site-specific calibration is performed. Similarly, Spanoudaki et al. [17] confirmed that JONSWAP-based frameworks successfully capture the spatiotemporal variability of wave fields in the Aegean Sea. The importance of carefully selecting spectral parameters, particularly the peak enhancement factor γ, to accurately represent local conditions is also emphasized in sensitivity analyses by Barbariol et al. [18] and Xie et al. [19]. These findings collectively justify the application of the JONSWAP model in the Aegean Sea for reliable wave force estimation.

To further validate the fetch-limited characterization of the Gökçeada offshore site, wave climate data from the CMEMS were analyzed. The VMDR was compared with ERA5 wind data, confirming that the wave field in the region is primarily wind-driven with limited swell influence. The semi-enclosed nature of the Aegean Sea supports the classification of the study area as a fetch-limited environment, consistent with the modeling assumptions.

Based on these environmental conditions, wave force estimation for the monopile foundation at Gökçeada is approached using diffraction theory. When the monopile diameter is large relative to the incident wavelength, diffraction effects dominate the hydrodynamic response. In this study, MacCamy-Fuchs diffraction theory is employed to estimate wave-induced forces on the monopile. The validity of this approach is supported by key non-dimensional parameters: the diameter-to-wavelength ratio ($D/L>0.2$) and the water depth-to-wavelength ratio ($h/L>0.5$) indicate diffraction dominance, while the depth-to-diameter ratio ($h/D>1$) further supports the theoretical framework under the local site conditions.

The objective of this study is to model the wave-induced forces acting on offshore monopile-supported wind turbines at Gökçeada under irregular sea states. By combining site-specific spectral wave data with diffraction-based force estimation methods, the study provides a detailed assessment of hydrodynamic load contributions across the frequency domain, offering critical insights for the design and structural analysis of offshore wind energy infrastructure in the Northern Aegean Sea.

2. Site Characteristics and Data Collection

2.1. Location of the Study Area

This study focuses on the offshore region surrounding Gökçeada, the largest island in Türkiye, located in the northeastern Aegean Sea (~40.2 °N, 25.9 °E). The site offers technical suitability for offshore wind development due to its exposure to strong, persistent winds-particularly the seasonal Etesians that shape the local wave climate.

Figure 1 shows a screenshot from the CMEMS interface, where the island of Gökçeada is clearly labeled. The blue-shaded region indicates the spatial coverage of the available reanalysis wave data, while the black rectangle outlines the coordinate bounds used for data extraction. These bounds include the selected wind turbine location and are consistent with the spatial resolution of the CMEMS product.

Bathymetric data [20] from the CMEMS indicate an average water depth of ~48.3 m at the intended turbine site, supporting the use of fixed-bottom monopile foundations. The relatively uniform seabed and fetch-limited wave conditions justify the application of spectral wave modeling to estimate hydrodynamic forces.

2.2. Wave Climate and Wind Data

Wave climate data for the study area were obtained from the Copernicus Marine Service dataset (MEDSEA_MULTIYEAR_WAV_006_012), which provides a high-resolution hindcast of wave conditions in the Mediterranean Sea. The dataset has a spatial resolution of approximately 1/24° (~4.6 km) and covers the period from January 31, 2013, to May 31, 2023. The primary wave parameters extracted include significant wave height H_s, peak wave period T_p, and mean wave direction (VMDR), which are essential for characterizing the hydrodynamic environment of the Gökçeada offshore site.

Although no *in situ* buoy data are available directly offshore of Gökçeada, the Copernicus wave parameters have undergone extensive validation across the Mediterranean basin. According to the Product Quality and Validation Report [20] the modeled significant wave heights show strong agreement with buoy and satellite measurements, with root-mean-square errors (RMSE) of 0.25-0.35 m and correlation coefficients exceeding 0.90 in the Aegean region. Mean biases were typically below 0.1 m. These performance metrics confirm the reliability of Copernicus-derived wave parameters and justify their use in site-specific modeling where direct measurements are unavailable.

Given the region's semi-enclosed geometry and dominant wind-wave alignment, the Aegean Sea is considered fetch-limited. To describe the spectral distribution of wave energy at the site, a JONSWAP spectrum was developed using 10 years of reanalysis data. The long-term mean significant wave height of this data is approximately 0.54 m corresponds to Beaufort Force 4 (Moderate Breeze), providing a practical reference for the typical sea state. Details regarding the spectral formulation, parameter calibration, and validation procedures are provided in Section 3.1.

2.3. Wind Turbine and Monopile Design

The offshore wind turbine considered in this study is assumed to be supported by a monopile foundation, which is the most widely adopted substructure type for fixed-bottom offshore wind farms. Monopiles are preferred in moderate water depths (up to approximately 50 m) due to their structural simplicity, robustness, and cost-effectiveness.

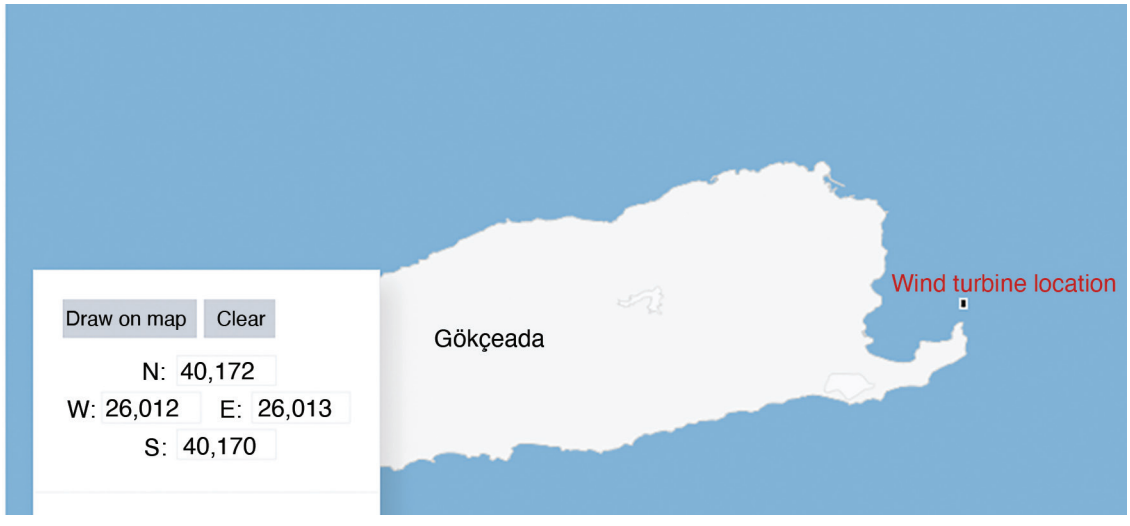


Figure 1. Screenshot from the Copernicus Marine Environment Monitoring Service, showing the study area near Gökçeada in the northeastern Aegean Sea. The blue-shaded region indicates reanalysis data coverage, and the black rectangle marks the coordinate bounds used for wave data extraction, including the wind turbine location.

A monopile diameter of D=2.5 m was selected for this study as shown in Figure 2, representing a practical dimension for offshore wind installations in similar bathymetric conditions. This diameter was directly incorporated into the diffraction-based wave force estimation using MacCamy-Fuchs theory to ensure accurate representation of wave-structure interaction effects. The analysis focuses exclusively on hydrodynamic loading induced by waves and does not consider the structural response of the wind turbine or aerodynamic forces associated with rotor operation.

Although turbine-specific aspects such as control systems, tower dynamics, or power generation are beyond the scope of this work, the computed wave-induced force signal is statistically analyzed to evaluate monthly variability, force magnitude distributions, and return-level estimates using a Peak Over Threshold (POT) approach fitted with a Generalized Pareto Distribution (GPD).

3. Methodology

The methodological framework of this study follows a structured approach to estimating wave-induced forces on the monopile foundation, incorporating site-specific wave conditions and diffraction-based force estimation. The overall procedure, from spectral input construction to time-domain force reconstruction, is summarized in Figure 3.

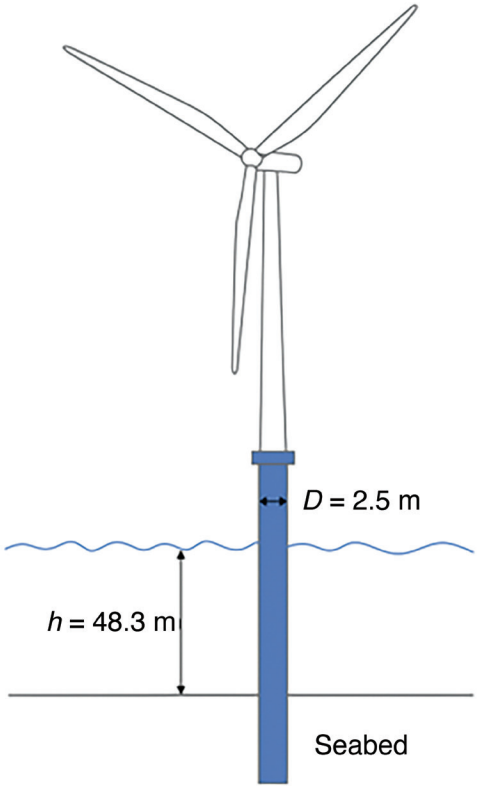


Figure 2. Schematic representation of the monopile-supported offshore wind turbine configuration.

The workflow begins with the acquisition of 10 years of reanalysis data for significant wave height (H_s), peak wave period (T_p), and mean wave direction (VMDR) from the Copernicus Marine Service. These parameters are used to construct a JONSWAP wave spectrum. The peak enhancement factor (γ) is selected adaptively based on the mean H_s, and the spectral width parameter (σ) is applied according to the standard JONSWAP formulation. The spectrum is then validated by comparing the estimated significant wave height ($H_{s,est}$) with the observed mean ($H_{s,mean}$), and an α-correction is applied to align spectral energy with reanalysis-based observations. To ensure the validity of MacCamy-Fuchs theory, a filtering step is applied to exclude spectral components where $ka>3$, and an energy retention check is performed. Spectral band contribution analysis is also conducted to quantify energy content in low, mid, and high frequency ranges.

Wave loading on the monopile is evaluated using MacCamy-Fuchs diffraction theory, which provides a frequency-dependent force transfer function suitable for vertical circular cylinders.

The wave-induced force contributions per frequency, obtained by applying the MacCamy-Fuchs transfer function to the site-specific JONSWAP spectrum, are numerically integrated over the retained frequency range to compute the total force in the frequency domain. This approach-combining a physically consistent diffraction model with validated spectral inputs-follows established practices in offshore hydrodynamic force estimation.

To evaluate the effects of irregular wave loading over time, a time-domain force signal is reconstructed using the inverse fast Fourier transform (IFFT) of the force spectrum,

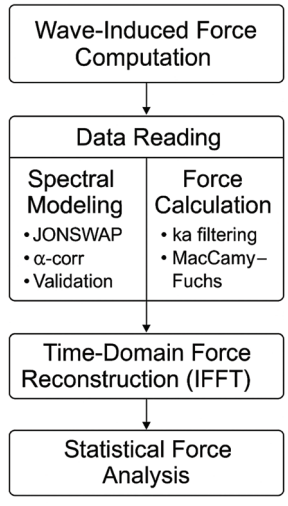


Figure 3. Computational workflow for modeling and reconstructing wave-induced forces.

generated by combining spectral magnitudes with randomly assigned phase values. This step enables the modeling of realistic, time-varying wave-induced loads acting on the monopile. The reconstructed signal is then subjected to statistical evaluation, including summary metrics such as mean, standard deviation, and percentiles, along with extreme value analysis based on the POT method. In this approach, force values exceeding the 95th percentile threshold are extracted and fitted to a GPD to estimate rare-event return levels. Further technical details related to wave spectrum formulation, diffraction theory, and numerical implementation are provided in subsequent sections. This methodological framework enables the generation of realistic, site-adapted force histories under irregular sea states and forms the basis for the statistical evaluations presented in Section 4.

3.1. Wave Spectrum Model Selection

To verify the fetch-limited nature of the study site, VMDRs extracted from the Copernicus Marine dataset were compared with prevailing wind directions from the ERA5 reanalysis product. The strong correlation between wind and wave directions, combined with the semi-enclosed geometry of the Aegean Sea, confirms that local wind forcing dominates wave generation, with negligible swell contribution. This finding justifies the use of the JONSWAP model.

A site-specific JONSWAP spectrum was then constructed using significant wave height (H_s) and peak period (T_p) values obtained from the reanalysis dataset. The spectral energy density $S(f)$ was computed according to Equation 1:

$$S(f) = \alpha g^2 f^{-5} \exp\left(-\frac{5}{4}\left(\frac{f_p}{f}\right)^4\right) \gamma^{\exp\left(-\frac{(f-f_p)^2}{2\sigma^2 f_p^2}\right)} \quad (1)$$

where α is a scaling parameter for spectral energy, f is the wave frequency in Hz, f_p is the peak frequency, g is the gravitational acceleration, σ is the spectral width parameter, and γ is the peak enhancement factor.

The peak enhancement factor γ was set to 1.8, consistent with the original JONSWAP formulation for moderately developed seas [21]. Although γ can range between 1 and 7 depending on wind and fetch conditions, values between 1.5 and 3 are typically used in engineering applications. The selected value was validated by comparing the modeled significant wave height $H_{s,est}$ with the observed mean $H_{s,mean}$ confirming the physical consistency of the spectrum.

The spectral width parameter σ was defined piecewise based on frequency relative to the spectral peak, as shown in Equation (2):

$$\sigma = \begin{cases} 0.07 \text{ for } f \leq f_p \\ 0.09 \text{ for } f > f_p \end{cases} \quad (2)$$

This asymmetric formulation reflects the structure of developing wind seas and was directly implemented in the numerical model.

To ensure consistency between the modeled spectrum and the observed wave energy, the spectral scaling coefficient α was iteratively adjusted so that the significant wave height estimated from the JONSWAP energy spectrum matched the long-term mean value obtained from the reanalysis dataset. This was performed using the standard relationship in Equation (3):

$$H_{s,\text{ estimated}} = \sqrt{16 \int S(f) df} \quad (3)$$

The final corrected spectrum was validated by comparing its peak frequency and total energy with reanalysis statistics. This validation was implemented using an in-house MATLAB code, and alignment was confirmed numerically with convergence of $H_{s,est}$ to $H_{s,mean}$=0.54 m.

As shown in Figure 4, the corrected spectrum exhibits a sharp peak around 0.34 Hz and steep decay at higher frequencies-characteristic of wind-driven waves in fetch-limited conditions.

This validated spectrum was used as input for wave force estimation. To ensure theoretical consistency within the MacCamy-Fuchs-based diffraction model [22], spectral components with non-dimensional wave number $ka>3$ were excluded.

3.2. Diffraction Theory for Wave Forces

The calculation of wave-induced forces on the monopile foundation is based on diffraction theory, which is appropriate for structures with large diameter-to-wavelength ratios.

To model wave diffraction around a vertical circular cylinder, the MacCamy-Fuchs linear diffraction theory [22] is applied. This approach defines a frequency-dependent transfer function $H_f(f)$ which modifies the hydrodynamic force according to diffraction behavior.

The wave-induced force contribution per frequency is then computed using Equation (4):

$$F(f) = \rho g D H_f S(f) \quad (4)$$

These per-frequency force contributions form the basis for calculating the total hydrodynamic load on the monopile. The integration of these contributions over the valid frequency range-along with the application of ka filtering and energy retention checks-is described in Section 3.3.

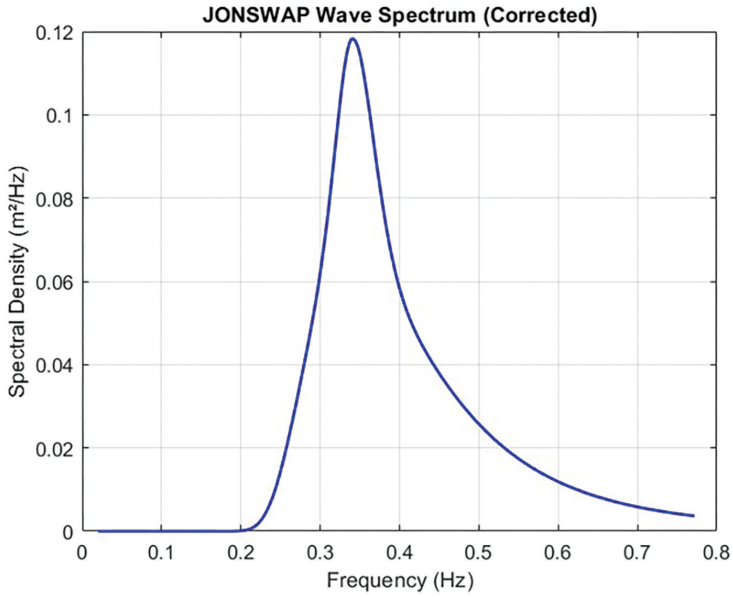


Figure 4. Corrected JONSWAP spectrum constructed from Copernicus reanalysis data for the Gökçeada offshore site, showing peak energy near 0.34 Hz under fetch-limited sea state conditions.

3.3. Numerical Implementation

The numerical implementation of MacCamy-Fuchs diffraction theory involves several computational steps to estimate wave-induced forces on the monopile foundation based on the JONSWAP spectrum. First, the wave number k is computed for each frequency by solving the linear wave dispersion relation given in Equation (5):

$$\omega^2 = gk\tanh(kh) \tag{5}$$

where $\omega = 2\pi f$ is the angular frequency and h is the water depth. This non-linear equation is solved numerically using a root-finding method with an initial guess based on deep-water approximation.

The transfer function H_f is computed using the MacCamy-Fuchs diffraction formulation for a vertical circular cylinder, as defined in Equation (6):

$$H_f = \left|1 - \frac{2J_1(kD/2)}{(kD/2)J_0(kD/2)}\right| \tag{6}$$

Here, J_0 and J_1 are Bessel functions of the first kind (orders 0 and 1), k is the wave number, and D is the diameter of the monopile. To prevent numerical instabilities and non-physical amplification in long waves, the transfer function is capped at an upper limit of $H_f = \min(H_f, 2)$. This cap reflects theoretical upper bounds found in classical diffraction theory [23].

For each frequency component, the wave-induced force contribution is calculated by multiplying the diffraction-based transfer function $H_f(f)$, the monopile diameter D and the spectral energy density $S(f)$. This computation captures the contribution of each frequency in the wave spectrum to the total hydrodynamic loading on the structure.

The total wave-induced force in the frequency domain is then obtained by numerically integrating these contributions using the trapezoidal rule, as shown in Equation (7):

$$F_{\text{total}} = \int \rho g D H_f S(f) df \tag{7}$$

This integration is performed over the valid frequency range defined by the diffraction theory limits.

Since MacCamy-Fuchs theory is applicable only when the non-dimensional wave number satisfies $ka \leq 3$, a filtering step is applied to enforce this condition, as stated in Equation (8):

$$ka = k\frac{D}{2} \leq 3 \tag{8}$$

Frequency components that do not satisfy this constraint are excluded to preserve the theoretical validity of the model.

To assess the effect of this filtering, a spectral energy retention check is performed. The total spectral energy before filtering is computed using Equation (9):

$$E_{all} = \int_{f_{min}}^{f_{max}} S(f) df \tag{9}$$

and the retained spectral energy, considering only frequencies within the valid set $F_{valid} \subset [f_{min}, f_{max}]$ is calculated as in Equation (10):

$$E_{retained} = \int S(f)df \quad (10)$$

The energy retention ratio is then determined from Equation (11):

$$Retention\ Ratio = 100\frac{E_{retained}}{E_{all}}(\%) \quad (11)$$

In this study, the retained energy after filtering exceeds 97%, indicating that the removal of high-frequency components has a negligible effect on the physical accuracy of the wave force computation.

All numerical procedures-including the computation of wave numbers via the dispersion relation, evaluation of the MacCamy-Fuchs transfer function, spectral energy filtering, numerical integration of force components, and time-domain reconstruction using IFFT with randomized phases-were implemented using an in-house MATLAB code. Built-in functions such as *fsolve*, *fft*, and *gpfit* were employed during relevant stages of the analysis.

4. Results and Discussion

This section presents the outcomes of the wave force modeling for the monopile-supported wind turbine in the Gökçeada offshore region. Using frequency-domain force components developed in Section 3, a time-varying wave-induced load signal was reconstructed to analyze load variability across the simulation period. These results were further processed to derive design-relevant statistics.

4.1. Time-Domain Wave Force Reconstruction

The wave force acting on the monopile was reconstructed in the time domain from frequency components obtained using the calibrated site-specific wave spectrum described in Section 3.1. The final spectral parameters yielded a significant wave height of H_s=0.5439 m, with a peak frequency of f_p=0.3407 Hz and corresponding peak period of T_p=2.935 s, representing typical sea conditions at the Gökçeada site.

To ensure model validity, the spectral force was truncated using the $ka \leq 3$ criterion described in Section 3.3, limiting energy loss to 2.51% and preserving the dominant hydrodynamic content. An IFFT with randomized phase angles was applied to reconstruct the time-varying force signal $F(t)$. The resulting record, shown in Figure 5, spans the entire 10-year simulation and captures both high-frequency variability and long-term modulations in wave loading. Although the applied diffraction model provides frequency-dependent amplitudes, conversion to the time domain was essential to evaluate load fluctuations, extreme values, and fatigue-relevant patterns that cannot be captured in the frequency domain alone.

A statistical comparison was performed between the frequency-domain force spectrum and the reconstructed time-domain signal obtained via IFFT with randomized phase. The frequency-domain force exhibited a standard deviation of 0.03 N and an RMS of 0.05 N, while the time-domain force signal yielded a standard deviation and RMS of 321.27 N. This apparent discrepancy arises from the inherent differences in how energy is distributed in the spectral versus time domains. The frequency-domain values are expressed per unit frequency (N²/Hz) and represent the square root of the integrated spectral force density. In contrast, the time-domain RMS force reflects the full amplitude of instantaneous loading over the reconstructed signal, normalized over time. The use of randomized phase in the IFFT ensures that the energy content is preserved, even though peak values differ

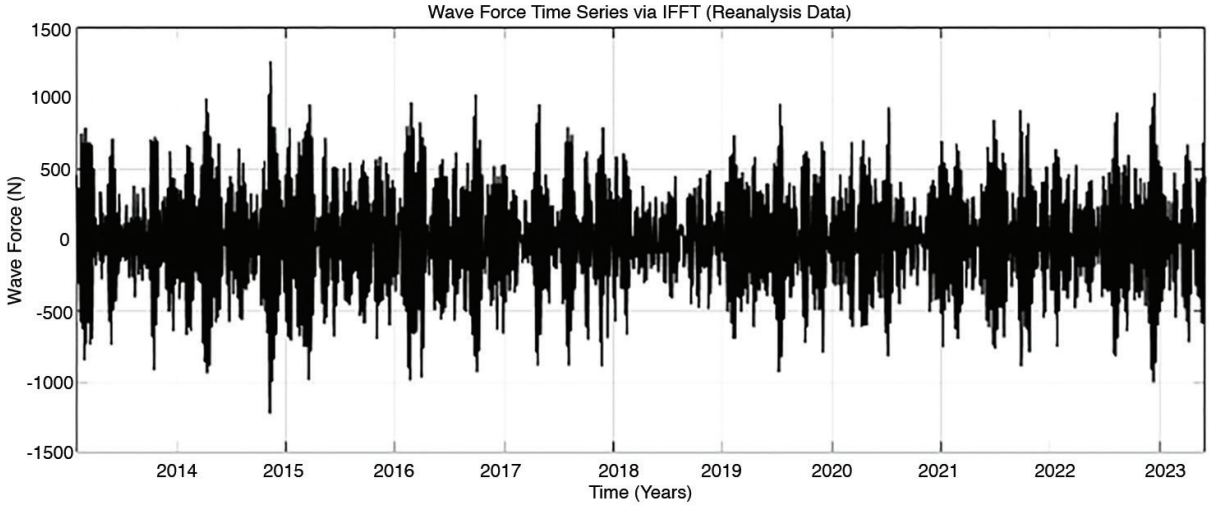


Figure 5. Reconstructed time-domain wave force signal via IFFT using site-specific JONSWAP spectrum, showing 10 years of irregular loading conditions.

substantially. Both metrics are valid within their respective domains and confirm the statistical representativeness of the reconstructed force signal. The reconstructed force time series, therefore, preserves the desired energy distribution for long-term statistical analyses and is considered suitable for further design load evaluations, including time-domain fatigue analysis, spectral bandwidth evaluation, and temporal clustering of load peaks, which cannot be assessed in the frequency domain alone.

4.2. Design Load Characterization

The reconstructed time-domain wave-induced force signal was statistically evaluated to extract load characteristics relevant for the structural design of a monopile-supported offshore wind turbine. As illustrated in Figure 6, the histogram of the reconstructed force signal reveals a near-symmetric distribution centered around zero, capturing the stochastic nature of irregular wave loading in the northeastern Aegean Sea. The force time series exhibited a maximum value of 1259.08 N, a minimum of -1226.58 N, and a standard deviation of 321.27 N. The mean value was effectively zero (-0.00 N), confirming the absence of a net directional bias in the long-term wave forcing. The histogram reveals that more than 99% of force amplitudes fall within ±3 standard deviations, indicating a bounded, stable force regime consistent with stochastic wave behavior. These results reflect realistic amplitude variability and confirm the suitability of the reconstructed signal for dynamic analysis.

To estimate extreme wave-induced loads, the POT method was applied using the 95th percentile of the reconstructed force signal as the threshold (u). This resulted in 519 exceedance values ($x>u$), which were fitted to a GPD. The cumulative distribution function of the GPD is given in Equation (12), and the corresponding return level expression is shown in Equation (13). The shape k and scale σ parameters of the GPD were estimated using MATLAB's built-in function *gpfit*, which applies maximum likelihood estimation to the exceedance data. For this study, the fitted parameters were k=0.0809 and σ=83.54 N. Using the estimated parameters and the annual rate of exceedance λ, the 50-year return force was calculated as 1351.7 N based on Equation (13).

$$F(x) = \begin{cases} 1 - \left(1 + \frac{k(x-u)}{\sigma}\right)^{-1/k} & \text{if } k \neq 0 \\ 1 - exp\left(-\frac{x-u}{\sigma}\right) & \text{if } k = 0 \end{cases} \quad \text{for } x > u \qquad (12)$$

$$z_T = u + \frac{\sigma}{k}[(T \cdot \lambda)^k - 1] \qquad (13)$$

It should be noted, however, that although the POT method is used here to estimate a 50-year return force for Ultimate Limit State (ULS) design considerations, the underlying wave conditions are derived from long-term average reanalysis data (mean $H_s \approx 0.54$ m). As such, the estimated ULS-level force primarily reflects rare high-end fluctuations within typical sea states, rather than forces associated with severe storm conditions. Future studies may incorporate design storm scenarios or higher percentile wave statistics to obtain more conservative estimates for ULS-level loading.

Figure 7 shows the empirical exceedance probability of the POT data (shown in blue) along with the fitted GPD model (shown as a red dashed line). The 50-year return level is

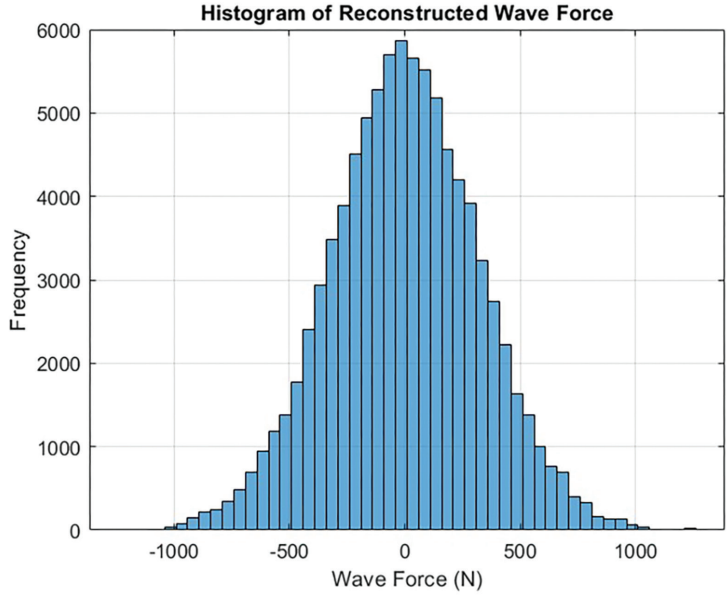


Figure 6. Histogram of reconstructed wave-induced force signal. The y-axis indicates the statistical frequency (count) of force amplitudes observed over the 10-year simulation period.

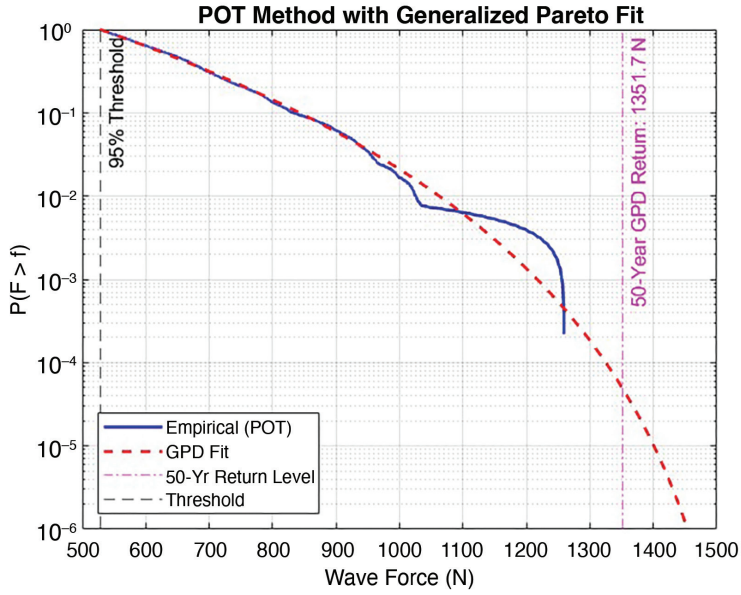


Figure 7. Exceedance probability plot of wave-induced forces above the 95th percentile threshold, fitted with a Generalized Pareto Distribution.

marked with a vertical magenta line. A strong agreement is observed in the upper tail, confirming the statistical validity of the model for extrapolating rare wave loading events. Minor stepwise features and curvature in the empirical curve at very low exceedance probabilities are attributed to the limited number of high-magnitude observations -a typical behavior in data-limited POT applications. This analysis highlights the advantage of using a continuous statistical model for reliable ULS-level force estimation under data-limited conditions.

To generalize the findings and facilitate comparisons across different monopile diameters, the wave force signal was normalized by the monopile diameter (D=2.5 m), resulting in a unit-diameter force representation (F_{norm} in N/m). The normalized signal exhibited a maximum of +503.63 N/m, a minimum of -490.63 N/m, and a standard deviation of 128.51 N/m. These values can be directly applied in parametric studies, load extrapolation efforts, and design evaluations involving geometrically scaled foundations, while remaining consistent with the assumptions of linear wave diffraction theory.

5. Conclusion

This study developed a numerical framework for reconstructing wave-induced forces on a monopile-supported offshore wind turbine located off the coast of Gökçeada in the northeastern Aegean Sea. A site-specific JONSWAP wave spectrum was calibrated using a decade of Mediterranean reanalysis data to represent the irregular sea states typical of fetch-limited environments.

To account for diffraction effects associated with the large monopile diameter, the MacCamy-Fuchs diffraction theory was applied. Spectral components with a non-dimensional wave number exceeding $ka>3$ were excluded to maintain theoretical consistency, resulting in an energy retention rate of approximately 97.5%. The filtered spectrum was then used to reconstruct a 10-year time-domain wave force signal via IFFT, capturing both short-term variability and long-term statistical trends.

The reconstructed signal exhibited a standard deviation of 321.27 N and a peak amplitude of 1259.08 N. To evaluate extreme loading, a POT analysis was conducted using the 95th percentile threshold, with exceedances fitted to a GPD. The resulting 50-year return force was estimated as 1351.7 N, providing a statistically consistent upper bound within the context of long-term average sea states (mean $H_s \approx 0.54$ m). Therefore, while the estimated force captures upper-bound fluctuations under typical wave conditions, it does not represent severe storm-induced loading that would be expected in conservative ULS design.

Spectral energy analysis showed that 88.4% of the wave energy was concentrated in the high-frequency band $f>0.3$ Hz, emphasizing the dominant role of short-period waves in monopile loading. For generalized application, the force signal was normalized by the monopile diameter, yielding a maximum unit-diameter force of 503.63 N/m.

This study focuses on the reconstruction of long-term, realistic wave-induced force histories on offshore monopile foundations in data-limited, fetch-limited regions by

relying solely on reanalysis wave data and diffraction-based modeling. Although previous studies have employed spectral wave models or diffraction theory independently, the integration of these approaches for time-domain force reconstruction under typical sea conditions remains limited-particularly in semi-enclosed basins such as the Aegean Sea. Addressing this gap, the present study introduces a physically consistent and scalable framework that combines a site-specific, validated JONSWAP spectrum with MacCamy-Fuchs diffraction theory and randomized-phase IFFT. This novel approach enables the generation of statistically representative wave load histories without requiring in-situ measurements, offering a robust tool for structural design, fatigue assessment, and reliability analysis of offshore wind turbine foundations in regions with limited observational resources.

In addition, the validated force time series provides a foundation for further investigations into long-term structural performance, especially in the context of fatigue and probabilistic reliability. While the present study focuses on average sea states, future work may incorporate storm conditions or extreme wave events to support more conservative ULS design assessments.

Footnote

Financial Disclosure: The author declared that this study received no financial support.

References

[1] M. Argin, V. Yerci, N. Erdogan, S. Kucuksari, and U. Cali, "Exploring the offshore wind energy potential of Turkey based on multi-criteria site selection," Energy Strategy Reviews, vol. 23, pp. 33-46, Jan 2019.

[2] S. Tolun, S. Mentese, Z. Aslan, and M. A. Yukselen, "The wind energy potential of Gökçeada in the Northern Aegean Sea," Renewable Energy, vol. 6, no. 7, pp. 679-685, Oct 1995.

[3] N. Eskin, H. Artar, and S. Tolun, "Wind energy potential of Gökçeada Island in Turkey," Renewable and Sustainable Energy Reviews, vol. 12, no. 3, pp. 839-851, Apr 2008.

[4] S. Şişbot, Ö. Turgut, M. Tunç, and Ü. Çamdalı, "Optimal positioning of wind turbines on Gökçeada using multi-objective genetic algorithm," Wind Energy, vol. 13, no. 4, pp. 297-306, Apr 2009.

[5] M. D. Akyol, E. Şahin, and S. Güçlüer, "Technical feasibility of offshore wind power plant for Gökçeada region in Türkiye," in 2023 12th International Conference on Renewable Energy Research and Applications (ICRERA), pp. 1016-1020, Aug 2023.

[6] American Bureau of Shipping (ABS), Design standards for offshore wind farms, Final Report, Contract No. M10PC00105, U.S. Department of the Interior, Bureau of Ocean Energy Management, 2011.

[7] L. Sartini, L. Mentaschi, and G. Besio, "Sub-mesoscale wave height return levels on the basis of hindcast data: the North Tyrrhenian Sea," Coastal Engineering Proceedings, vol. 1, no. 34, p. 39, Oct 2014.

[8] U. P. A. Pillai et al. "Wind-wave characteristics and extremes along the Emilia-Romagna coast," Natural Hazards and Earth System Sciences, vol. 22, no. 10, pp. 3413-3433, 2022.

[9] A. S. Ibrahim, A. El-Molla, and H. G. I. Ahmed, "Long-term trends in significant wave heights in the Mediterranean as an indicator of climate change," Transactions on Maritime Science, vol. 13, no. 2, Oct 2024.

[10] Y. Fan, "Analysis of long-term changes in extreme waves in the northwest pacific over the past 60 years," The EGU interactive community platform [Preprint], 2025.

[11] Z. Li, Z. Wang, B. Liang, and X. Wang, "Experimental study on hydrodynamic performance and structural forces of curved and vertical front face pile-supported permeable breakwaters," Physics of Fluids, vol. 36, no. 11, Nov 2024.

[12] G. Napitupulu, A. Tarya, I. G. M. Y. Pratama, and I. S. Winardhie, "Variability analysis of significant wave heights and wind waves in Riau Archipelago Sea Part ALKI 1," Jurnal Pesisir Dan Laut Tropis, vol. 10, no. 3, pp. 341-355, Oct 2022.

[13] A. Aggarwal, M. A. Chella, A. Kamath, and H. Bihs, "Irregular wave forces on a large vertical circular cylinder," Energy Procedia, vol. 94, pp. 172-181, Sep 2016.

[14] S. P. León, J. H. Bettencourt, and N. Kjerstad, "Simulation of irregular waves in an offshore wind farm with a spectral wave model," Continental Shelf Research, vol. 31, no. 15, pp. 1541-1557, Oct 2011.

[15] S. Kalvig, E. Manger, B. H. Hjertager, and J. B. Jakobsen, "Wave influenced wind and the effect on offshore wind turbine performance," Energy Procedia, vol. 53, pp. 202-213, 2014.

[16] P. Vlachogiannis, C. Peyrard, A. C. Pillai, M. Collu, and D. Ingram, "A comparison of the influence of using empirical or mathematically pre-defined wave energy spectra for tower base bending fatigue calculations," in Proceeding ASME 2023 5th International Offshore Wind Technical Conference, 2023.

[17] K. Spanoudaki, A. K. Chuchmala, and E. A. Varouchakis, "An integrated geostatistical and numerical modelling framework for spatiotemporal analysis of wave energy fields in the Aegean Sea," EGUsphere, 2025.

[18] F. Barbariol, A. Benetazzo, F. Bergamasco, S. Carniel, and M. Sclavo, "Stochastic space-time extremes of wind sea states: validation and modeling," in Proceeding ASME 2014 33rd International Conference on Ocean, Offshore and Arctic Engineering, vol. 8B, 2014.

[19] B. Xie, X. Ren, X. Jia, and Z. Li, "Research on ocean wave spectrum and parameter statistics in the northern South China Sea," in Proceeding Offshore Technology Conference, Houston, TX, USA, May 2019.

[20] Copernicus Marine Service, Product User Manual for Mediterranean Sea Waves Reanalysis (MEDSEA_MULTIYEAR_WAV_006_012), Issue 2.4, Mercator Ocean International, 2024. [Online]. Available: https://marine.copernicus.eu

[21] K. Hasselmann et al., "Measurements of wind-wave growth and swell decay during the Joint North Sea Wave Project (JONSWAP)," Ergänzungsheft zur Deutschen Hydrographischen Zeitschrift, A8, Hamburg: Deutsches Hydrographisches Institut, 1973.

[22] R. C. MacCamy, and R. A. Fuchs, Wave forces on piles: a diffraction theory, Technical Memorandum No. 69, Beach Erosion Board, U.S. Army Corps of Engineers, 1954.

[23] R. G. Dean, and R. A. Dalrymple, Water wave mechanics for engineers and scientists, vol. 2. World Scientific, 1991.

RESEARCH ARTICLE

DOI: 10.54926/jnamt.2025.2524

J Nav Architect Mar Technol 2025;227(1):74-93

Numerical Investigation into the Effects of Initial Stability on the Flooding Dynamics in a Damaged Ro-Pax Ship Model

Mehmet Zeki Şener[1], Hyeon Kyu Yoon[2], Ercan Köse[1], Thi Thanh Diep Nguyen[3], Aeri Cho[4]

[1]Karadeniz Technical University, Department of Naval Architecture and Marine Engineering, Trabzon, Türkiye
[2]Changwon National University, Department of Naval Architecture and Ocean Engineering, Gyeongsangnam-do, South Korea
[3]Changwon National University, Industrial Technology Research Center, Gyeongsangnam-do, South Korea
[4]Changwon National University, Smart Ocean Mobility Engineering, Gyeongsangnam-do, South Korea

To cite this article: M. Z. Şener, H. K. Yoon, E. Köse, T. T. D. Nguyen, and A. Cho. Numerical investigation into the effects of initial stability on the flooding dynamics in a damaged Ro-Pax ship model. *J Nav Architect Mar Technol*. 2025;227(1):74-93.

Received: 03.08.2025 - **Revision Requested:** 10.10.2025 - **Last Revision Received:** 14.10.2025 - **Accepted:** 17.11.2025 - **Publication Date:** 26.12.2025

Abstract

Structural damage to the hull that causes internal flooding poses a significant risk to ship stability, potentially compromising operational integrity and, in severe cases, resulting in capsizing, grounding, or sinking. When water enters through breached compartments, it reduces overall buoyancy and introduces a free-surface effect. Progressive flooding may also occur as water spreads into adjacent compartments through structural openings or failed watertight barriers. The movement of floodwater, combined with fluid–structure interactions, generates complex, nonlinear forces that are difficult to predict. This study employs numerical simulations using a damaged Ro-Pax ship model to examine how initial stability influences flooding behavior and motion response. The analyses are carried out until flooding reaches a quasi-steady state. A Computational Fluid Dynamics methodology is used to accurately capture the fluid–structure interactions during flooding. Two flooding scenarios were simulated with identical damage extents and environmental conditions, but different metacentric height (*GM*) values, to isolate the effect of initial stability. The model's time-dependent linear and angular motions, along with floodwater levels, were monitored throughout the flooding period. Although the affected tanks were not fully filled, the ship model still reached a quasi-steady state. Results indicated that initial *GM* had minimal impact on the total volume of ingress water during the simulation period. This suggests that, given the specific damage geometry and boundary conditions, hydrostatic and hydrodynamic forces primarily govern water ingress, reducing the influence of initial stability. However, notable differences were observed in the motion response. The configuration with lower *GM* exhibited significantly larger roll and yaw motions and lower damping rates. While these dynamic behaviors may not directly affect the volume of floodwater, they have important operational implications, including a higher risk of cargo shift, increased passenger discomfort, and reduced controllability.

Keywords: Damaged stability, flooded ship, Ro-Pax ship, ship dynamics, ship stability

Address for Correspondence: Asst. Prof. Mehmet Zeki Şener, Karadeniz Technical University, Department of Naval Architecture and Marine Engineering, Trabzon, Türkiye
E-mail: senermehmetzeki@ktu.edu.tr
ORCID ID: orcid.org/000-0002-9794-4811

**An earlier version of this paper appeared in the Proceedings of the 3rd International Congress on Ship and Marine Technology (GMO-SHIPMAR 2024, oper source https://www.gmoshipmar.org), 10-12.12.2024, Trabzon, pp. 247–259. The present article is an extended and revised version in which the text and methodology have been refined, and the results are presented in greater detail.*

Copyright© 2025 The Author. Published by Galenos Publishing House on behalf of UCTEA Turkish Chamber of Naval Architects and Marine Engineers.
Licensed under a Creative Commons Attribution-NonCommercial-NoDerivatives 4.0 (CC BY-NC-ND) International License

1. Introduction

Maritime transport is widely used for the carriage of goods and passengers over long distances. The continuous growth in the size and structural complexity of modern ships has increased the importance of damage stability assessments. Among various types of ship damage, flooding is addressed in regulatory frameworks, as it directly influences stability and survivability. Flooding occurs when water enters internal spaces due to structural failure or hull breach. This reduces overall buoyancy and introduces a free-surface effect, both of which affect stability. If not adequately controlled, flooding can result in capsizing, grounding, or total loss of the vessel. To limit the consequences of such events, ships are designed with watertight subdivision and optimized weight distribution to preserve residual stability.

Accurate evaluation of damaged ship stability requires understanding the dynamic interaction between floodwater and ship motion. Progressive flooding through multiple compartments, the location and size of damage openings, the ingress rate of seawater, and the presence of non-watertight internal boundaries all influence the flooding process. Additionally, environmental conditions also introduce dynamic forces that complicate the assessment. These factors necessitate modelling capable of capturing fluid–structure interaction under transient and nonlinear conditions.

Three main approaches are commonly used to evaluate damage stability: experimental, theoretical, and numerical. Each has specific advantages and limitations. Among them, numerical methods offer flexibility in simulating complex geometries and damage scenarios. Computational Fluid Dynamics (CFD), in particular, enables detailed modelling of the fluid behavior and its interaction with ship motion during flooding. CFD has been increasingly applied in maritime research due to improvements in computational capacity. While its predictive capability has been demonstrated in various contexts, further validation is ongoing to ensure its applicability in real-case damage scenarios and regulatory frameworks. The study by Cheng et al. [1] investigated the coupled dynamics between flooding water and damaged ship motion using experimental methods and Smoothed Particle Hydrodynamics (SPH). A refined SPH framework incorporating improved boundary treatments and visualization techniques is developed and validated against physical experiments. The effects of variables such as opening size, position, the number of flooded cabins, and wave conditions were investigated in relation to fluid behavior and ship responses. Results revealed that complex flow structures, including inflow jets, sloshing, and vortex shedding, significantly affect ship stability and motion. Cao et al. [2] developed a SPH model based on strip theory to simulate the dynamic response of a damaged ship in beam seas, accounting for nonlinear interactions between external waves, internal sloshing, and flooding water. The study validated the model using experimental data and conducted parametric analyses on factors such as damage opening size, wave direction, and internal liquid loading. Results showed that flooding-induced damping effects reduced roll motion, and that wave direction relative to the damage opening critically influenced the severity of ship response. Notably, the presence of internal liquid cargo was found to substantially alter sloshing behavior, with a 50% filling ratio minimizing rolling amplitude. Hu et al. [3] conducted a numerical investigation employing a CFD approach that integrates the Navier-Stokes equations with the Volume of Fluid (VOF) method and a dynamic mesh strategy. The simulations were applied to a damaged barge and a rectangular cabin, and the computed results were verified against experimental measurements. The study demonstrated that the applied method effectively captured fluid-structure interaction and flooding dynamics within a time-domain framework. Although not exhaustive, these studies show that as modelling techniques advance, the need for simplifying assumptions decreases.

The complexity of ship flooding increases reliance on CFD-based simulations. However, recent advancements in CFD techniques have broadened their range of applications. To implement CFD effectively in these scenarios, a thorough understanding of the available numerical methods is essential. Wang and Wan [4] reviewed the advancements in CFD for predicting complex viscous flows around floating structures, highlighting techniques such as the VOF method, dynamic overset grid, and fluid-structure coupling. Similarly, Xu et al. [5] discussed numerical simulation techniques for various hydrodynamic coupling problems, including hull-propeller-rudder coupling, wave-floating structure coupling, aerodynamic-hydrodynamic coupling, fluid-structure coupling, and fluid-noise coupling. The paper emphasizes the importance of accurately predicting these coupling effects to optimize ship and ocean engineering designs. In this context, Çakıcı et al. [6] utilized the URANS method to compute hydrodynamic coefficients for heave motion of a Wigley hull with forward speed, demonstrating that viscous flow solutions offer higher accuracy than potential flow methods, particularly regarding damping characteristics. These studies underscore the advancements in CFD methods for resolving complex fluid-structure interactions and improving computational efficiency.

1.1. Aim of the Study

Structural breaches in the hull can lead to flooding, which may subsequently spread through internal openings and failed doors and hatches. The spread of floodwater decreases buoyancy and induces a free-surface effect, both of which significantly impair stability. Assessing the stability of

a damaged ship is inherently complex due to the coupled dynamics between internal flooding and ship motion. The resulting fluid–structure interactions generate nonlinear forces that are difficult to model using conventional assessment methods.

The International Maritime Organization (IMO) provides a regulatory framework for damage stability assessment by prescribing standardized damage scenarios and probabilistic calculation methods. These approaches typically assume instantaneous flooding and do not incorporate the time-dependent progression of water ingress or the associated motion responses of the ship. As a result, such methods may not adequately represent the physical realities of damaged ship behavior, particularly in dynamic sea states or during complex flooding events.

This study aims to address these limitations by applying numerical simulations based on CFD to evaluate the dynamic behavior of a Ro-Pax ship model under two distinct initial metacentric height (*GM*) conditions. The simulations are conducted under identical external and internal damage parameters, enabling a controlled comparison of vessel responses. The objective is to provide a detailed representation of stability under damaged conditions, thereby supporting the potential use of CFD in early-stage ship design and contributing to the refinement of performance-based stability assessment methods.

2. Materials and Methods

Stability analysis of damaged ships under flooding conditions requires accurate modeling of fluid–structure interaction and motion response. Depending on the objectives and constraints of a given study, different methodological frameworks may be employed. In this study, internal flooding and resulting ship motions are simulated using a Unsteady Reynolds-Averaged Navier-Stokes-URANS-based CFD approach. This section provides a detailed explanation of the materials and methods used in this study, along with their application procedures.

2.1. Damage Stability of Ships

Damage stability is the capacity of a vessel to remain afloat and maintain equilibrium after sustaining structural damage that allows water to ingress into one or more watertight compartments while complying with regulatory standards set by International Convention for the Safety of Life at Sea-SOLAS and IMO guidelines. When the watertight hull is breached, floodwater increases the weight of the vessel and reduces the buoyant volume. This can significantly compromise stability and pose serious risks to the ship, the passengers, the crew, and the cargo. Under severe flooding conditions, uncontrolled flooding leads to insufficient buoyancy and a high probability of capsizing or sinking.

Major maritime disasters acted as pivotal moments that shaped the development of modern damage stability regulations. High-profile incidents revealed the catastrophic consequences of inadequate subdivision and insufficient flood survivability, prompting a global shift in regulatory priorities. As a result, international safety frameworks such as SOLAS Chapter II-1 and guidelines set forth by the IMO require ships to be designed with sufficient watertight subdivision and residual stability. The goal is to ensure that vessels can remain afloat and upright even after sustaining damage. These regulations are not only essential for passenger ships but also apply to cargo vessels, tankers, and specialized offshore units. Through both deterministic and probabilistic approaches, naval architects must demonstrate that a vessel can survive specific damage conditions without exceeding allowable heel angles or stability thresholds, thereby safeguarding human life, cargo, and the marine environment.

Understanding stability in normal conditions is essential for evaluating how a vessel reacts to damage. Stability refers to the ability of a ship to resist heeling caused by external forces and to return to an upright position once those forces are removed. This behavior depends on the relationship between the center of gravity, the center of buoyancy, and the metacenter. When a vessel is upright, the center of gravity and the center of buoyancy are vertically aligned. As the vessel heels, the center of buoyancy shifts laterally due to the change in the shape and distribution of the submerged volume. The intersection between the vertical line of buoyant force and the initial centerline defines the metacenter.

GM, defined as the distance between the center of gravity and the metacenter, is a parameter for evaluating initial ship stability. Greater *GM* typically results in stronger resistance to heeling and faster righting action in response to disturbances. Beyond static considerations, *GM* also plays a role in the vessel response during compartment flooding. When a vessel experiences asymmetrical flooding, internal water movement creates free-surface moments that reduce effective transverse stability. This reduction in *GM* leads to greater roll angles and can increase the risk of capsizing. While the amount of water entering damaged compartments is mainly governed by factors such as breach geometry and hydrostatic pressure, *GM* significantly affects the motion response of the vessel. Characteristics such as roll amplitude, period, and damping behavior are strongly influenced by *GM*, especially during transient flooding conditions. Reduced *GM* are more susceptible to rapid capsize following flooding incidents. In such cases, safety margins decrease, and the time available for evacuation is often insufficient. Therefore, assessing *GM* within both static and dynamic frameworks is essential for comprehensive damage stability analysis.

CFD simulations are important for advancing ship design and safety evaluation. They enable the creation of a virtual yet realistic environment for the effective testing of various conditions. In this study, CFD simulations were used to assess the impact of two different initial stability conditions on a Ro-Pax vessel model. The primary aim was to examine how these conditions influence the progression of flooding and, in turn, affect the motion response. Since initial stability plays a major role in ship dynamics, analyzing this parameter is essential for enhancing overall ship safety.

2.2. Numerical Methodology

Fluid dynamics investigates the motion of substances such as liquids and gases, which do not resist deformation when subjected to external shear forces. To analyze fluid flow, the control volume approach provides a practical and convenient framework. By focusing on a defined control volume, fundamental conservation laws, such as mass, momentum, and energy, can be systematically derived.

The Navier-Stokes equations, named after Claude-Louis Navier [7] and George Gabriel Stokes [8], offer a comprehensive description of the motion of viscous fluids. These equations define how velocity, pressure, temperature, and density interact in a moving fluid. The conservation of momentum expressed in the Navier-Stokes equations corresponds to Newton's second law applied to a fluid element, incorporating forces due to pressure, viscosity, and external influences such as gravity. Although these nonlinear partial differential equations are widely applied in science and engineering, they remain one of the most challenging aspects of fluid dynamics due to their mathematical complexity.

The Navier-Stokes equations for an incompressible three-dimensional flow can be written as follows (Equation 1):

$$\frac{\partial \vec{U}}{\partial t} + (\vec{U} \cdot \nabla)\vec{U} = g - \frac{1}{\rho}\nabla P + \nu \nabla^2 \vec{U} \quad (1)$$

where "∇^2" is the Laplacian or Laplace operator.

Applying the Navier-Stokes equations in practical scenarios often requires the use of numerical methods due to the inherent complexity of obtaining analytical solutions. CFD techniques enable the approximation of solutions to the Navier-Stokes equations across a wide range of flow regimes and geometries. Despite their effectiveness, these methods reveal the inherent complexity of the equations, and finding exact solutions remains a major challenge. This difficulty is embodied in one of the most renowned unsolved problems in mathematics: the Navier-Stokes existence and smoothness problem.

The Navier–Stokes equations form the basis for describing fluid motion. However, due to the mathematical complexity of these equations, simplifications are often required to enable practical implementation in engineering applications. This need for simplification leads to the use of the Reynolds-Averaged Navier-Stokes (RANS) equations. Named after Osborne Reynolds [9], these equations provide a framework for addressing the challenges of turbulent flow analysis. By averaging flow properties over time, RANS equations reduce the complexity of the system while still capturing the essential effects of turbulence. This approach enables the prediction of the average behaviour of turbulent flows.

The RANS equations are derived from the original Navier-Stokes equations using Reynolds decomposition, which separates flow variables into a time-averaged component and a fluctuating component. This methodology removes instantaneous turbulent fluctuations and replaces them with their averaged effect, thereby simplifying the equations. The momentum equation for incompressible flow can be expressed as follows (Equation 2):

$$\frac{\partial}{\partial t}(\rho \overline{u}_i) + \frac{\partial}{\partial x_j}(\rho \overline{u}_i \overline{u}_j) = -\frac{\partial P}{\partial x_i} + \frac{\partial}{\partial x_i}[\mu(\frac{\partial \overline{u}_i}{\partial x_j} + \frac{\partial \overline{u}_j}{\partial x_i} - \frac{2}{3}\delta_{ij}\frac{\partial \overline{u}_i}{\partial x_i})] + \frac{\partial}{\partial x_j}(-\rho \overline{u_i'}\,\overline{u_j'}) \quad (2)$$

In these equations, $\overline{u}_i$ and $\overline{u}_j$ represent the mean average flow velocities, $\overline{u_i'}$ and $\overline{u_j'}$ denote the fluctuating velocities, μ is the dynamic viscosity, ρ is the fluid density, δ_{ij} is the Kronecker delta function, and P is fluid pressure.

The conservation of mass refers to the principle that the total mass within a system remains constant over time. This fundamental concept forms the basis for understanding and analysing fluid flow in a wide range of engineering and physical applications. It is commonly expressed through the continuity equation, which states that the mass entering a control volume must equal the mass exiting it, assuming there is no accumulation or loss of mass within the volume.

For Newtonian fluids, the mass continuity equation can be expressed as follows (Equations 3-5):

$$\dot{m} = \frac{\partial m}{\partial t} = \int_v \frac{\partial \rho}{\partial t} dv = 0 \quad (3)$$

$$\int_v \left[\frac{\partial \rho}{\partial t} + \nabla \cdot \left(\rho \vec{U}\right)\right] = 0 \quad (4)$$

$$\frac{\partial \rho}{\partial t} + \nabla \cdot \left(\rho \vec{U}\right) = 0 \quad (5)$$

where ρ is the density, $\vec{U}$ is the vector for flow velocity in three-dimensional cartesian coordinates. ∇ represents the divergence operator, and Equation (5) can be expanded as (Equation 6):

$$\frac{\partial \rho}{\partial t} + \frac{\partial (\rho u)}{\partial x} + \frac{\partial (\rho v)}{\partial y} + \frac{\partial (\rho w)}{\partial z} = 0 \quad (6)$$

In fluid dynamics, certain scenarios permit the assumption of constant fluid density, giving rise to the concept of

incompressible flow. This assumption greatly simplifies the governing equations and serves as the foundation for many practical applications. Incompressibility is commonly associated with liquids, which exhibit very low compressibility. Although the incompressible flow model is widely used, it should only be applied when compressibility effects are negligible. In this study, the incompressible flow model is employed for understanding the process of compartment flooding in damaged ships. By reducing the complexity of the governing equations, the incompressible flow model offers a more practical approach.

A fluid is considered incompressible when its density remains constant, as expressed by the following condition (Equation 7):

$$\frac{\partial(\rho u)}{\partial x} + \frac{\partial(\rho v)}{\partial y} + \frac{\partial(\rho w)}{\partial z} = 0 \quad (7)$$

Turbulence closure models account for the Reynolds stresses by modelling the transfer of energy between the mean and turbulent flows, addressing the closure problem in the Reynolds-averaged equations. To achieve closure, higher-order terms must be expressed in terms of lower-order quantities, ensuring the number of equations matches the number of unknowns.

Boussinesq [10] proposed that turbulence fluctuations could be modelled using the concept of eddy viscosity, a flow property rather than a physical property of the fluid. Prandtl [11] extended this idea by introducing the notion that eddy viscosity is not constant but varies depending on the local rate of strain and turbulence scale. This development led to the formulation of turbulence models, where additional transport equations are solved to determine local turbulence characteristics. One-equation turbulence models solve a single transport equation for turbulent kinetic energy (k), offering reasonable accuracy for many turbulent flows while maintaining computational efficiency. In comparison, two-equation models solve two transport equations, typically for turbulent kinetic energy and a second variable related to the turbulence length scale.

In this study, ANSYS Fluent was used to simulate the flooding process by combining the VOF model with the overset grid technique and a six-degree-of-freedom solver. The VOF model enables the simulation of two or more immiscible fluids by tracking the volume fraction of each. The overset grid method offers flexibility in handling complex geometries and moving boundaries without requiring frequent remeshing. This combination facilitated the simulation of fluid-structure interactions during compartment flooding and captured the ship's motion response. The continuity and momentum equations, along with the k-omega Shear Stress Transport (SST) turbulence model, were employed to analyse fluid flow, while the VOF model determined the volume fractions of air and water. This methodology provided an accurate representation of the turbulent, multiphase flow dynamics involved in the flooding scenario.

The k-ω SST model defines both turbulent kinetic energy (k) and the specific dissipation rate (ω). The modelled transport equations for the k-ω SST formulation are as follows (Equations 8 and 9) [12]:

$$\frac{\partial}{\partial t}(\rho k) + \frac{\partial}{\partial x_i}(\rho k \overline{u_i}) = \frac{\partial}{\partial x_j}\left[\left(\mu + \frac{\mu_t}{\sigma_k}\right)\frac{\partial k}{\partial x_j}\right] + G_k - Y_k + S_k \quad (8)$$

$$\frac{\partial}{\partial t}(\rho \omega) + \frac{\partial}{\partial x_i}(\rho \omega \overline{u_i}) = \frac{\partial}{\partial x_j}\left[\left(\frac{\mu + \mu_t}{\sigma_\omega}\right)\frac{\partial \omega}{\partial x_j}\right] + G_\omega - Y_\omega + D_\omega + S_\omega \quad (9)$$

In these equations, G_k represents the generation of turbulence kinetic energy due to average velocity gradients, while G_ω denotes the production of ω. The terms Y_k and Y_ω account for the dissipation of k and ω due to turbulence, respectively. The source terms are represented by S_k and S_ω which representing external influences affecting k and ω. The turbulence Prandtl numbers for k and ω are given by σ_k and σ_ω. Additionally, D_ω is the cross-diffusion term. The turbulent viscosity (μ_t) for the SST k-ω model is given by (Equation 10) [11]:

$$\mu_t = \frac{(\rho k/\omega)}{max\left[\frac{1}{\alpha^*}, \frac{\Omega F_2}{\alpha_1 \omega}\right]} \quad (10)$$

In this equation, Ω represents the strain rate magnitude, and α^* is a coefficient used to dampen turbulent viscosity. The turbulent Prandtl numbers σ_k ve σ_ω for k and ω are used as follows: $\sigma_{k,1} = 1.176$, $\sigma_{\omega,1} = 2.0$, $\sigma_{k,2} = 1.0$, $\sigma_{\omega,2} = 1.168$, $\alpha_1 = 0.31$.

2.3. Geometry and Mesh Structure

Accurate model design is required for reliable structural assessment and flooding analysis. Model must include all dimensions and structural elements that directly affect hydrostatic and hydrodynamic behavior, such as hull shape and compartment boundaries. The numerical model should apply appropriate boundary conditions and capture fluid–structure interaction relevant to flooding scenarios.

Table 1. Main dimensions of the ship model

Main dimensions	
Overall length, L_{OA}	1.435 m
Length between perpendiculars, L_{PP}	1.310 m
Beam, B	0.250 m
Draft, T	0.054 m
GM_1	0.03121 m
GM_2	0.02455 m

GM: Metacentric height

Table 2. Main dimension of the compartments			
Compartments	**Length [m]**	**Width [m]**	**Depth [m]**
Compartment 1	0.119	0.250	0.066
Compartment 2	0.119	0.250	0.066
Compartment 3	0.066	0.250	0.066

This study uses a model of a 162-meter Ro-Pax vessel [13] developed by Meyer Turku Shipyard [14], in accordance with SOLAS safety standards [15]. Ro-Pax vessels are frequently used in flooding studies due to their open vehicle decks, which allow water accumulation and can significantly reduce transverse stability under asymmetric damage. The vessel's main dimensions and compartment configuration are provided in Table 1 and Table 2.

The first step in numerical simulations is the generation of model geometry. At this stage, the physical system is simplified into a form suitable for numerical analysis. The components and features of the system are defined in accordance with the objectives of the study, ensuring that the model accurately represents the essential aspects of the problem while omitting irrelevant details. The model prepared for simulation is illustrated in Figures 1a and 1b.

It is recommended to represent the damage opening using a simple geometric shape, such as a triangle, a rectangle, or a trapezoid [16]. Accordingly, compartments 2 and 3

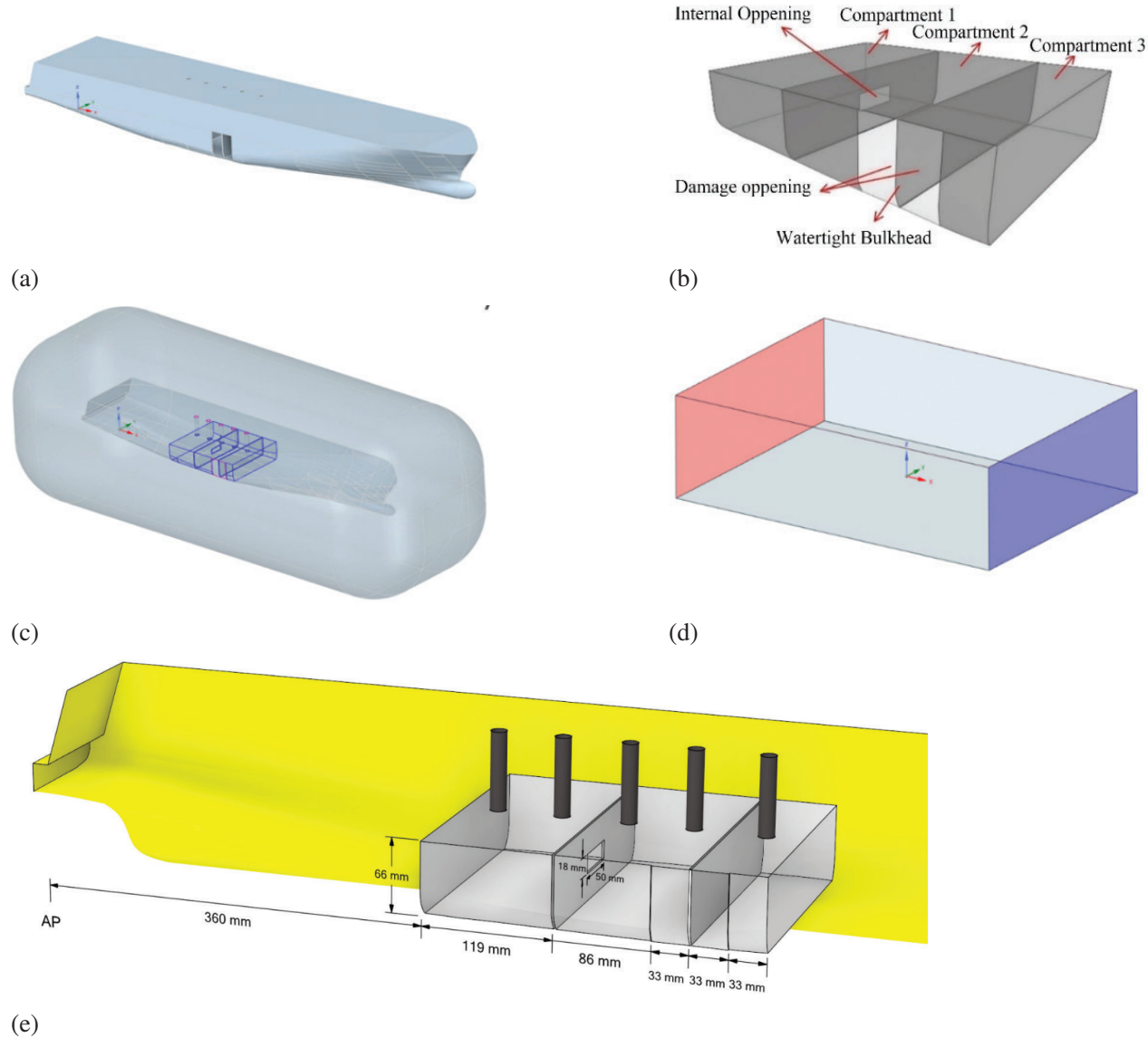


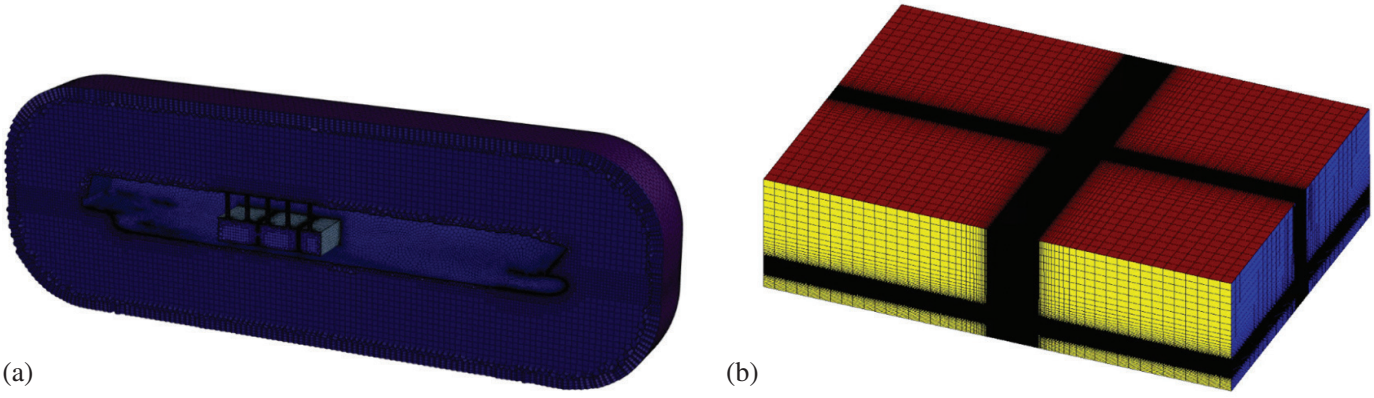
Figure 1. Illustrations of ship structure and zones: **(a)** ship model, **(b)** flooding compartments, **(c)** component zone, **(d)** background zone, and **(e)** compartment layout

in the ship's hull each include a continuous opening with a width of 33 mm to represent the damaged area. The height of the damage extends from the top to the bottom of the compartment, allowing unobstructed water ingress. To ensure proper ventilation and prevent air entrapment, airflow channels with a diameter of 15 mm have been incorporated.

Mesh generation is the process of discretizing the physical domain into smaller, finite cells, enabling the numerical solution of the governing equations over the computational domain. The mesh quality and resolution directly affect both the accuracy of the numerical solution and the computational cost. Higher mesh density is applied in regions with complex flow behavior or strong fluid-structure interactions, such as near the hull surface, inside the damaged compartments, and along the free surface interface. In contrast, lower mesh density is used in areas with relatively uniform flow, such as regions distant from the hull or away from the free surface. This mesh distribution improves accuracy in zones where large velocity or pressure gradients are expected, while limiting the total cell count and maintaining computational efficiency. The mesh structure was configured to balance numerical precision with simulation performance. An overset mesh approach is employed to simulate interactions between components exhibiting relative motion, including translation and rotation. In this method, individual mesh zones are generated for separate parts of the domain, and data is exchanged between them through interpolation. This strategy supports simulations involving time-dependent geometries and enables localized refinement. In the present study, two mesh zones were created, as shown in Figures 1c and 1d. The component mesh consists of 1,671,554 cells, and the background mesh, which covers a domain of 20 m×14 m×1.8 m, comprises 1,476,620 cells, as illustrated in Figure 2.

2.4. Boundary Conditions and Numerical Setup

The definition of boundary conditions involves specifying the physical and environmental constraints applied to the model to reflect the conditions of the actual system. These inputs influence the flow behavior and solution stability within the computational domain and affect the reliability of the simulation results. The selection of boundary conditions is based on the characteristics of the system and the specific objectives of the simulation. This includes the assignment of parameters such as pressure, temperature, velocity, and turbulence properties at relevant boundaries. Once defined,



(a) (b)

Figure 2. Meshes for the **(a)** component zone and **(b)** background zone

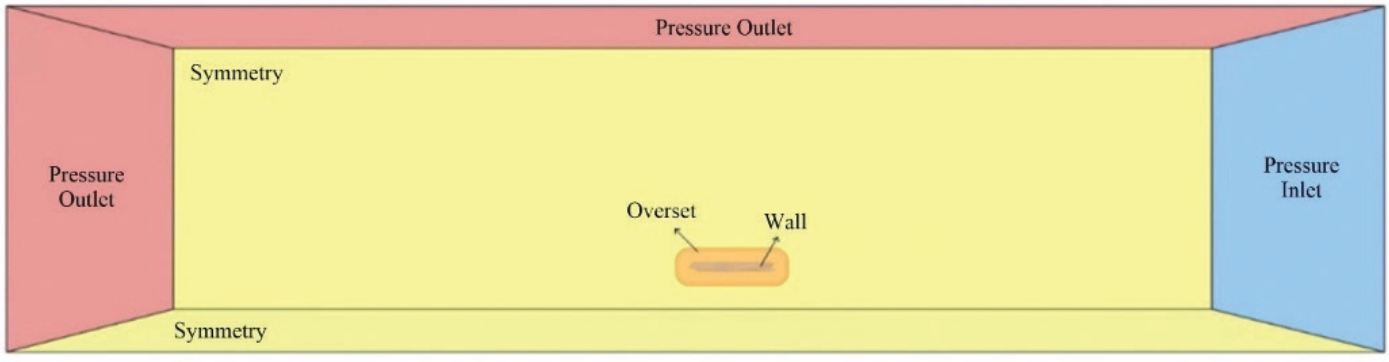


Figure 3. Boundary conditions for the computational domain

the boundary conditions are implemented in the simulation environment. The boundary conditions applied in this study are shown in Figure 3.

The turbulence model employed in the simulations is the k-ω SST model. This model combines the advantages of the standard k-ε and k-ω formulations and is suitable for capturing the behavior of boundary layers under adverse pressure gradients and separating flows. It solves transport equations for the turbulent kinetic energy (k) and the specific dissipation rate (ω), enabling accurate representation of turbulence effects both near the wall and in the free stream. The k-ω SST model is widely used in engineering applications due to its robustness in handling a broad range of Reynolds numbers and its ability to model complex flow features, including wall-bounded flows, flow separation, and recirculation.

Analytical solutions of non-linear partial differential equations are generally not feasible for most practical flow problems. Therefore, CFD relies on numerical methods, such as the finite volume method, to obtain approximate solutions. In this approach, the flow domain is discretized into control volumes, over which the governing equations are integrated to yield algebraic equations defined at the centroids of the volumes. Interpolation schemes are applied to estimate variable values at the control volume faces using the centroid values. In this study, a second-order upwind scheme is used to improve the spatial accuracy of the convective terms. For transient simulations, the solution is advanced in time using a fixed time step of 0.002 s to capture unsteady flow behavior. The coupled algorithm, an iterative pressure-velocity coupling method, is employed to solve the resulting system of equations until convergence is achieved.

3. Results and Discussion

This study examines the influence of initial GM on the flooding behavior and motion response of a damaged Ro-Pax vessel through RANS-based CFD simulations. The objective is to evaluate how variations in initial stability affect the rate of water ingress and the ship's dynamic response during flooding. Two stability configurations, GM_1 and GM_2, are analyzed to compare the temporal evolution of floodwater and the corresponding motion characteristics of the vessel. This section presents the simulation results, including trends in floodwater accumulation and ship motion, and discusses their implications for the damaged stability performance of Ro-Pax ships.

The mass of floodwater increases over time for both GM_1 and GM_2 cases, with no significant deviation observed between the two configurations. This indicates that, within the tested range, variations in initial GM have a negligible effect on the rate of water ingress. As shown in the figure, the floodwater mass stabilizes at approximately 3.6 kg for both cases after around 10 seconds (Figure 4). The close alignment of the two curves suggests that the initial stability condition does not substantially influence the flooding progression within the considered timeframe.

The angular motion responses under the initial stability conditions GM_1 and GM_2 are presented in Figure 5. As shown in Figure 5a, GM_2 exhibits a higher initial roll amplitude compared to GM_1, reflecting the influence of lower GM on roll behavior. Over time, both configurations display roll damping, with decreasing roll amplitudes that converge to near-zero values by approximately 8 seconds. The comparison indicates that higher initial GM_1 results in reduced maximum roll angles during the flooding process. These findings

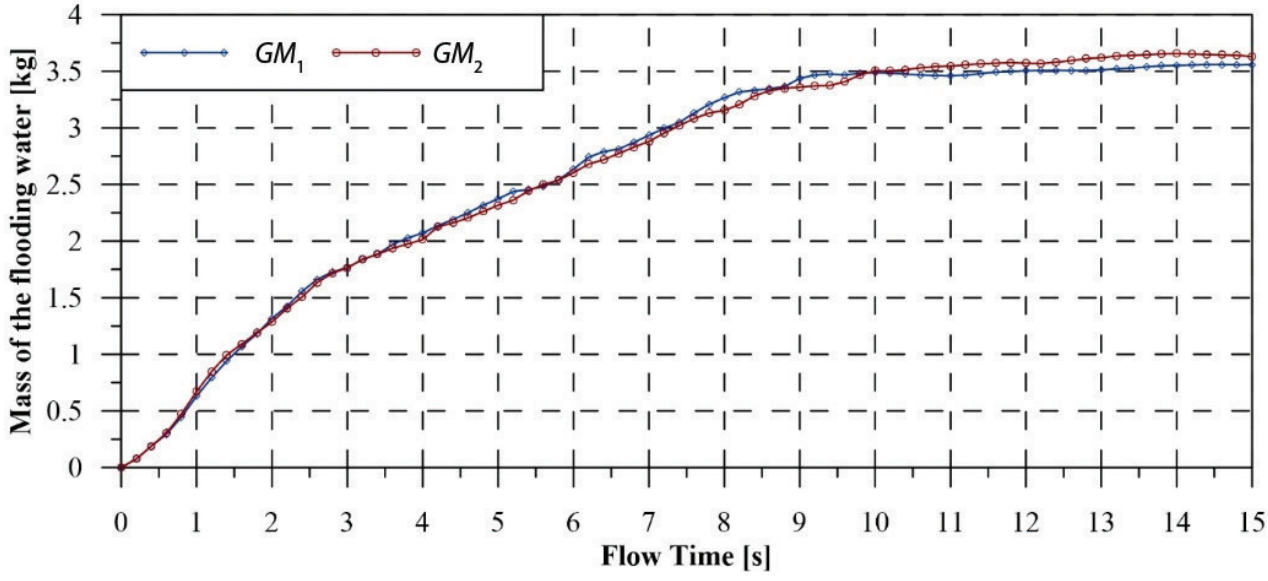


Figure 4. Mass of the flooding water under the initial stability conditions of GM_1 and GM_2

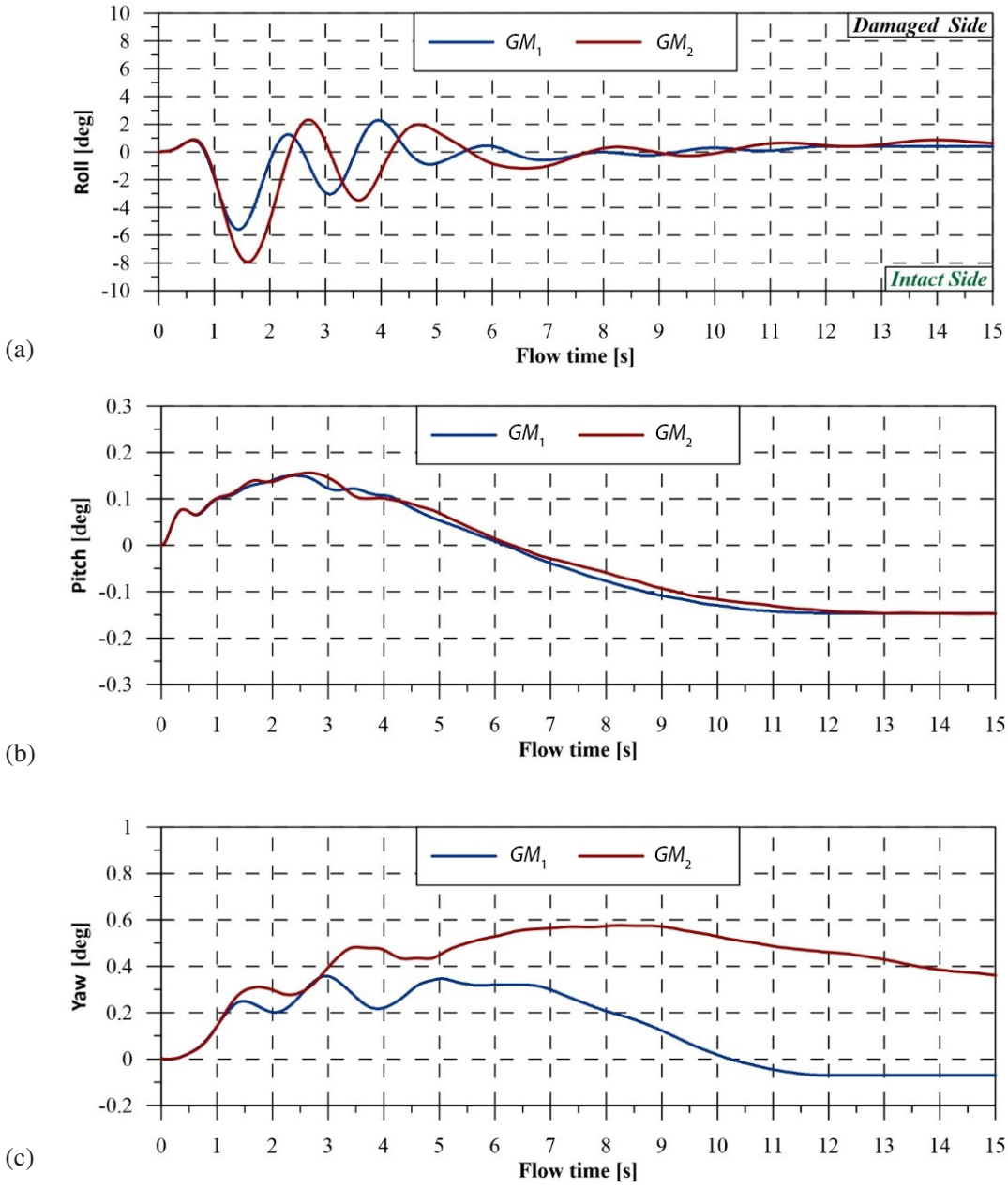


Figure 5. The angular motion responses during flooding under the initial stability conditions of GM_1 and GM_2: **(a)** roll, **(b)** pitch, and **(c)** yaw

highlight the role of initial stability in determining the ship's roll response under damaged conditions. A higher *GM* value contributes to lower roll amplitudes in the early stages of flooding, which may reduce the likelihood of cargo shift, particularly for wheeled cargo commonly transported on Ro-Pax vessels. However, maintaining an optimal *GM* must be considered in the context of overall vessel design and operational constraints, as excessively high stability can lead to reduced comfort and operational flexibility.

The linear motion responses for the initial stability conditions GM_1 and GM_2 are presented in Figure 6. In the surge direction, both configurations exhibit similar behavior throughout the flooding event. During the initial phase (0-3 seconds), surge displacements remain close to zero with minor oscillations. As flooding progresses, the surge response increases in both cases, reaching a peak near 8 seconds. After this point, a gradual reduction is observed, with surge displacement stabilizing around -7 mm by the end of the simulation period. In contrast, the sway motion response reveals more notable differences between the two configurations. While initial displacements are comparable, divergence becomes evident as flooding continues. GM_2,

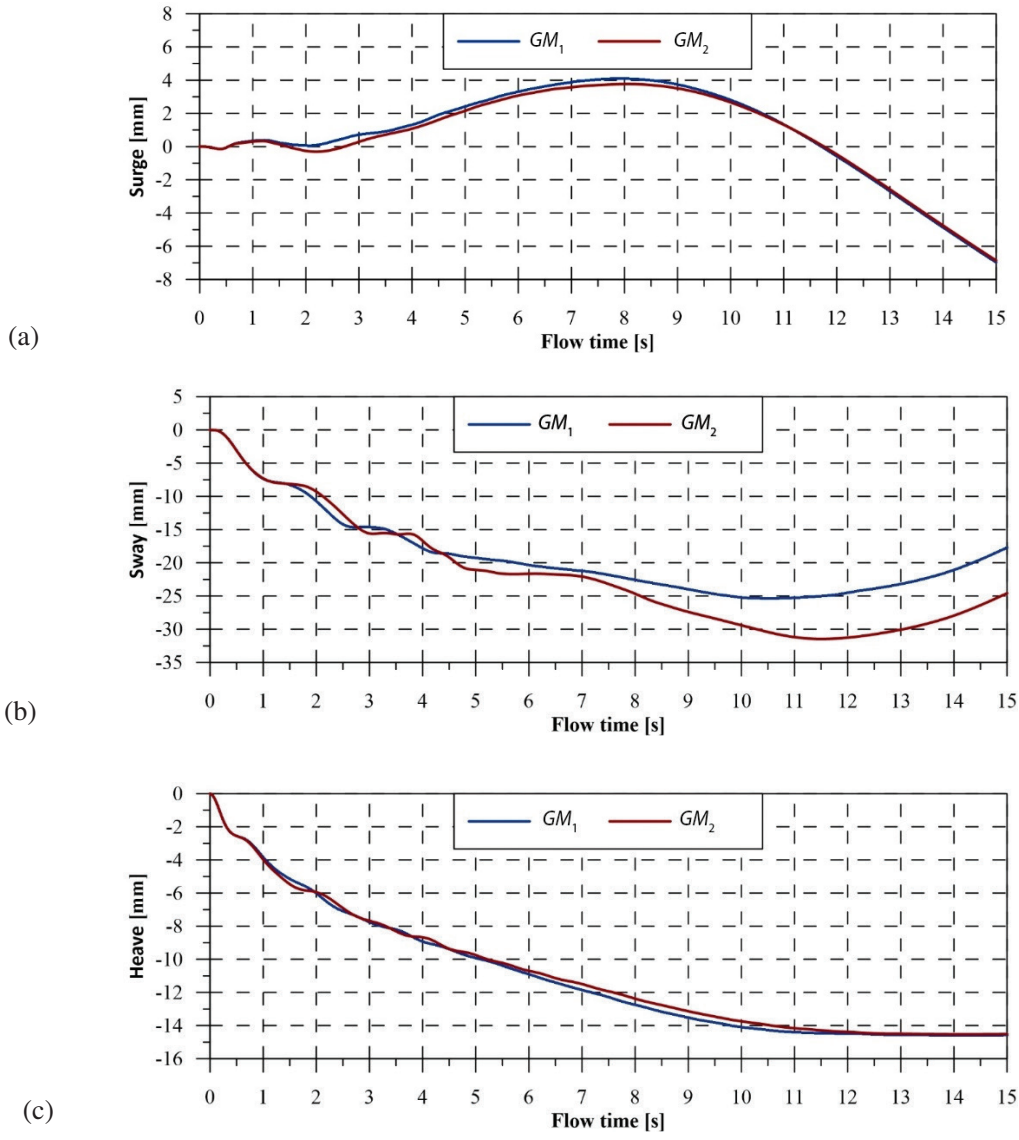
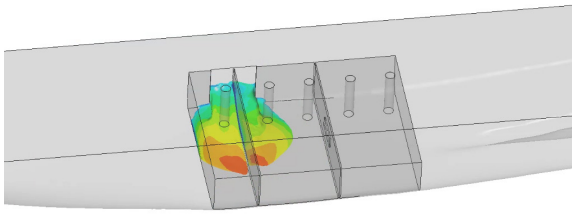


Figure 6. The linear motion responses during flooding under the initial stability conditions of GM_1 and GM_2: **(a)** surge, **(b)** sway, and **(c)** heave

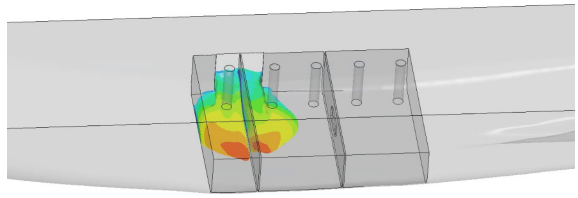
representing the lower initial stability case, reaches a maximum negative sway displacement of over -30 mm at approximately 7 seconds, whereas GM_1 reaches around -25 mm at the same time. This suggests that lower initial *GM* is associated with greater lateral movement during flooding. In the later stages, both configurations exhibit damping behavior, with sway displacements gradually returning toward less negative values.

The heave motion response shows a consistent trend for both GM_1 and GM_2. Initially, both cases experience a gradual downward (negative) displacement, which continues until approximately 10 seconds, reaching around -14 mm. Toward the end of the simulation period, the heave displacement stabilizes at approximately -15 mm for both configurations, indicating convergence and a steady-state condition.

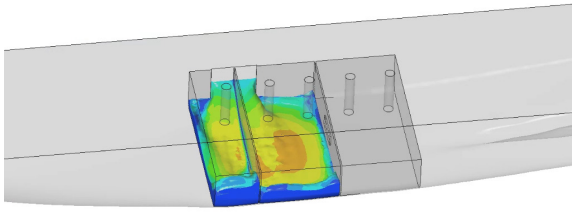
Figure 7 and Figure 8 presents the temporal evolution of the flooding process for the initial stability configurations GM_1 and GM_2. The velocity field of the floodwater (Figure 7) is visualized using a color scale, where blue represents low velocities and red indicates high velocities. At the onset of flooding, water enters the empty compartments through the damaged opening, resulting in a rising water level and increasing flow velocity. As the flooding progresses, the flow becomes more uniformly distributed across Compartments 2 and 3. With continued ingress, water enters Compartment 1, during which the velocity magnitudes begin to decrease. Once Compartment 1 is substantially flooded, the flow field stabilizes. In the final stages, the flooding reaches a quasi-steady state, characterized by relatively uniform water distribution and reduced velocity variations across the compartments.



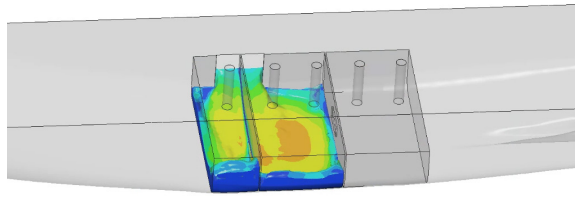
GM_1, t=0.2 s



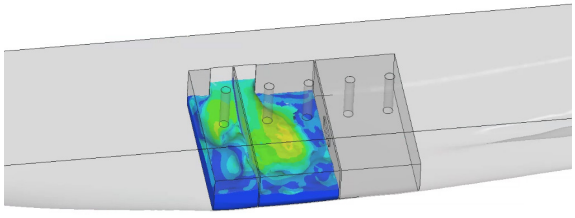
GM_2, t=0.2 s



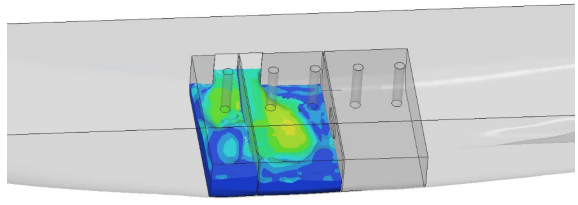
GM_1, t=0.6 s



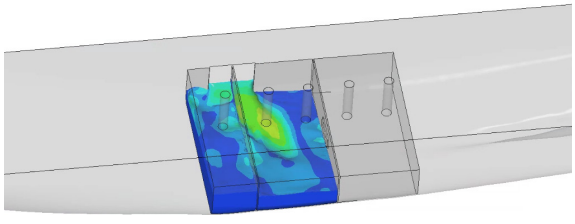
GM_2, t=0.6 s



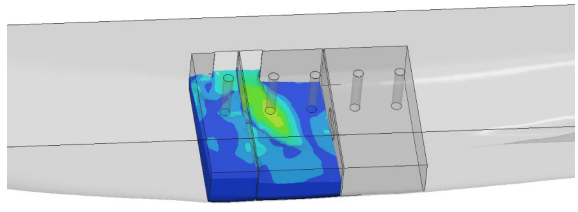
GM_1, t=1.0 s



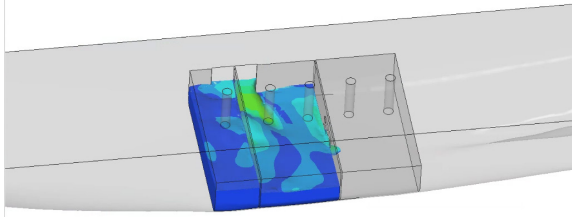
GM_2, t=1.0 s



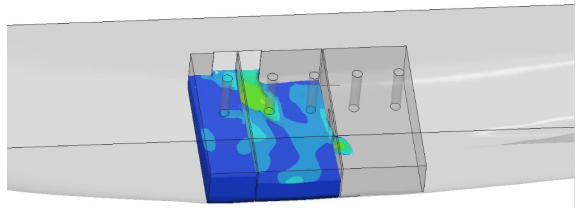
GM_1, t=1.4 s



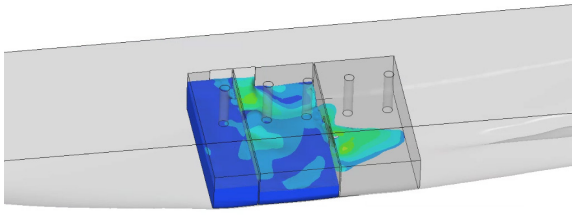
GM_2, t=1.4 s



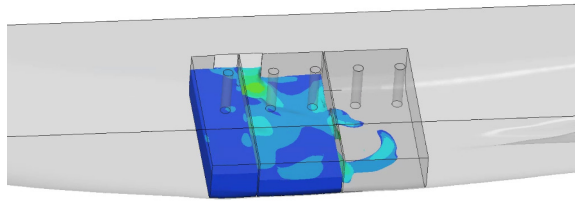
GM_1, t=1.8 s



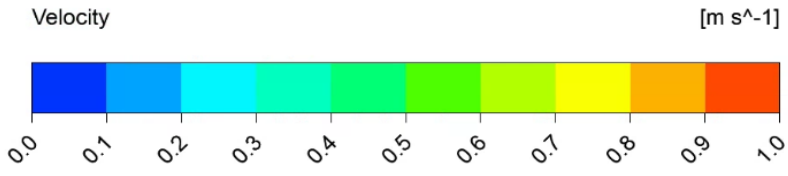
GM_2, t=1.8 s

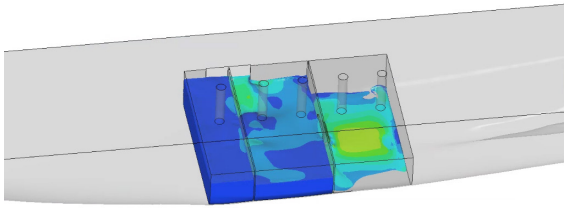


GM_1, t=2.2 s

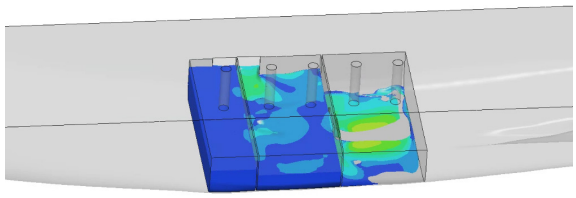


GM_2, t=2.2 s

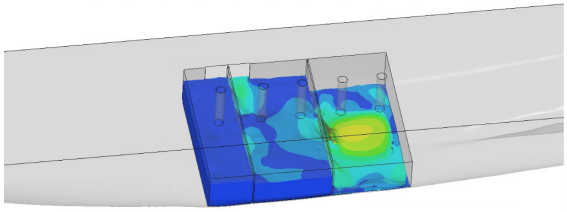




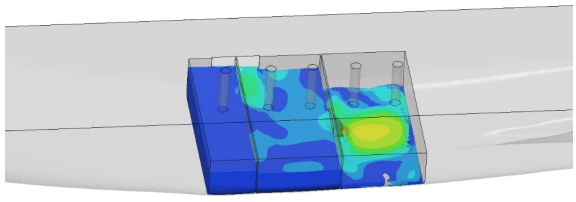
GM_1, t=2.6 s



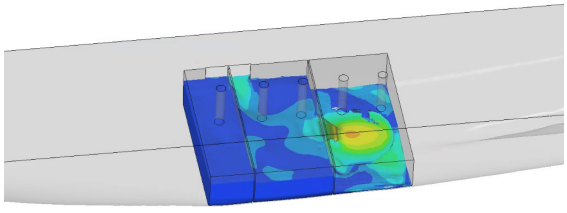
GM_2, t=2.6 s



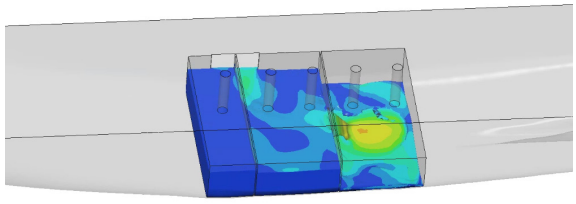
GM_1, t=3.0 s



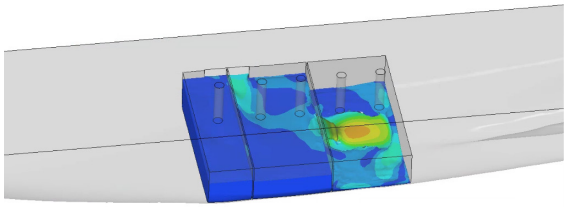
G GM_2, t=3.0 s



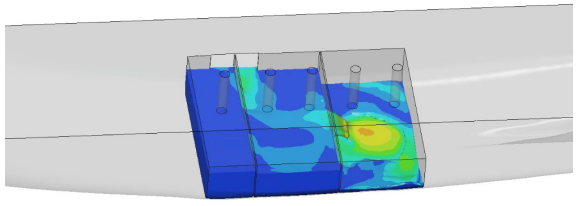
GM_1, t=3.4 s



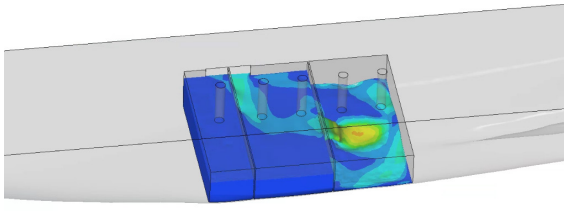
GM_2, t=3.4 s



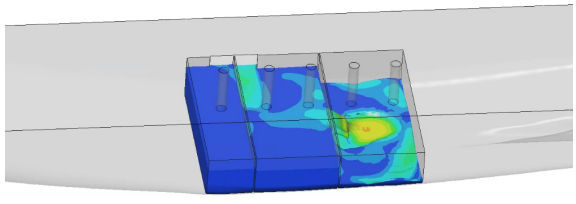
GM_1, t=3.8 s



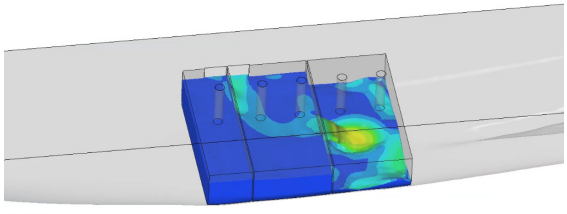
GM_2, t=3.8 s



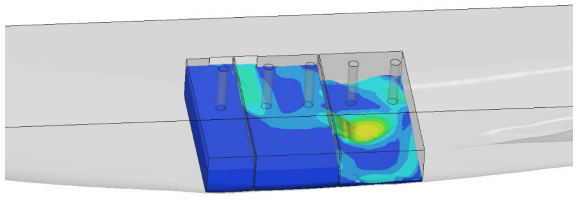
GM_1, t=4.2 s



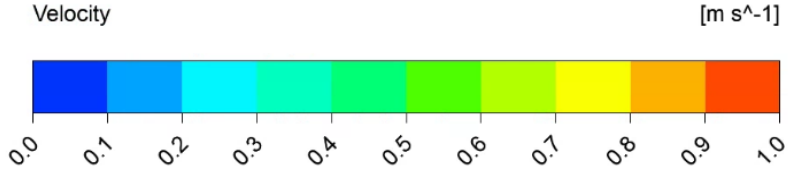
GM_2, t=4.2 s

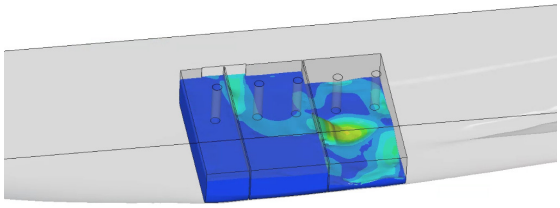


GM_1, t=4.6 s

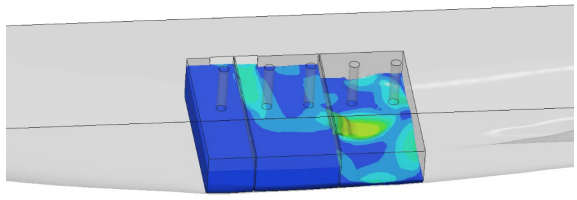


GM_2, t=4.6 s

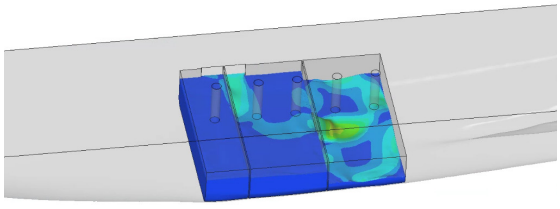




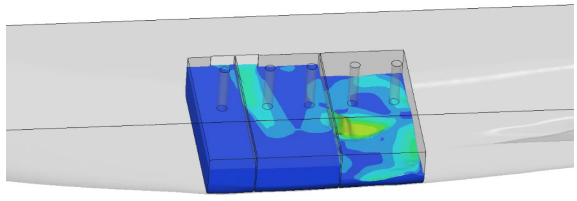
GM_1, t=5.0 s



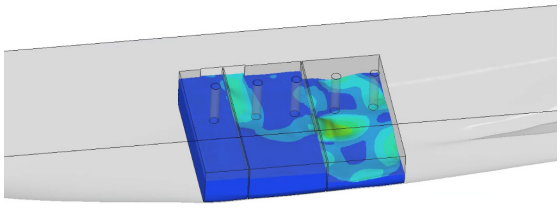
GM_2, t=5.0s



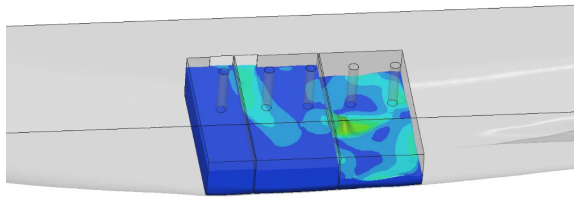
GM_1, t=5.4 s



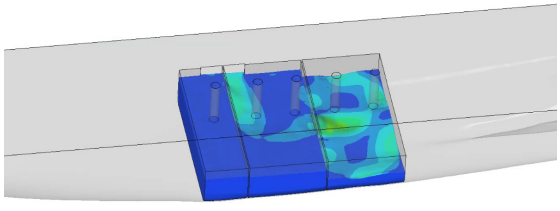
GM_2, t=5.4 s



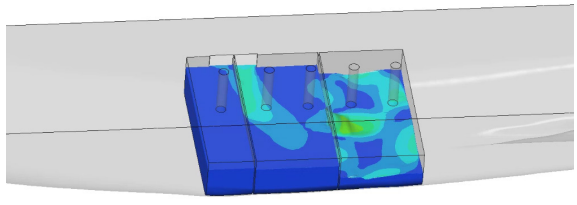
GM_1, t=5.8 s



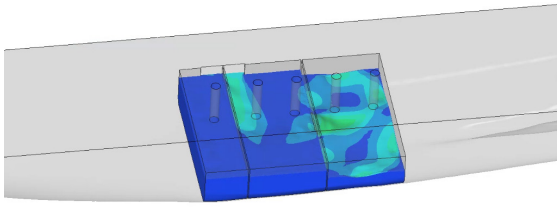
GM_2, t=5.8 s



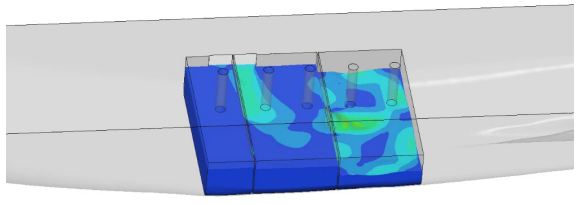
GM_1, t=6.2 s



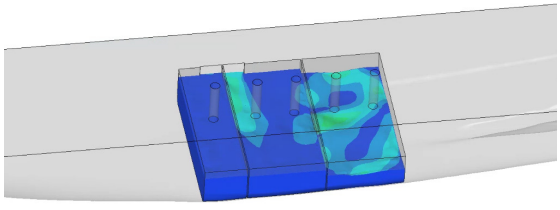
GM_2, t=6.2 s



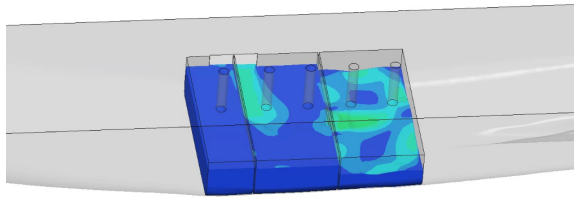
GM_1, t=6.6 s



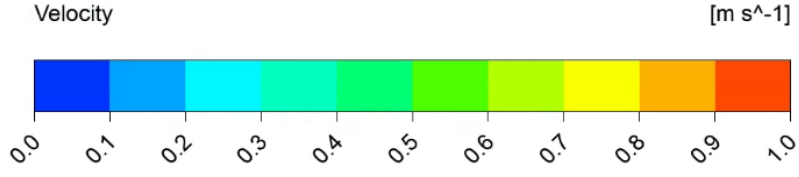
GM_2, t=6.6 s

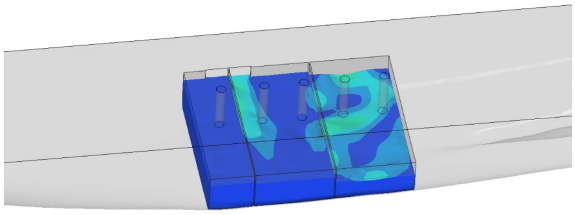


GM_1, t=7.0 s

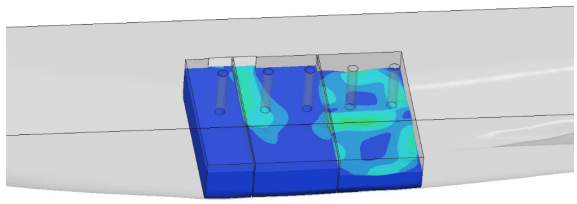


GM_2, t=7.0 s

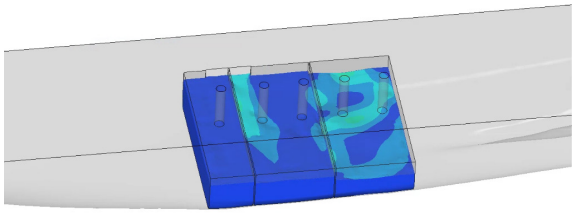




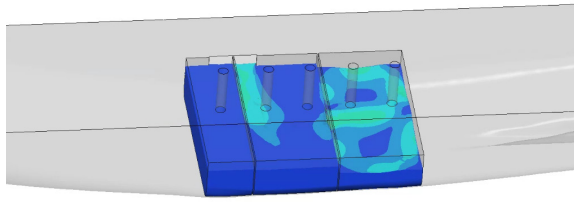
GM_1, t=7.4 s



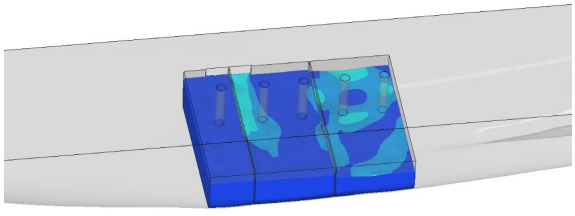
GM_2, t=7.4s



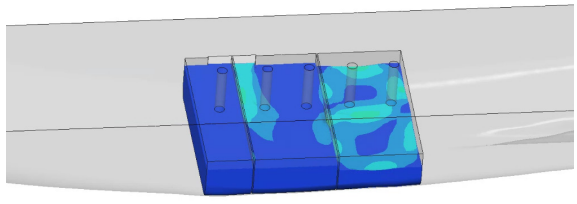
GM_1, t=7.8 s



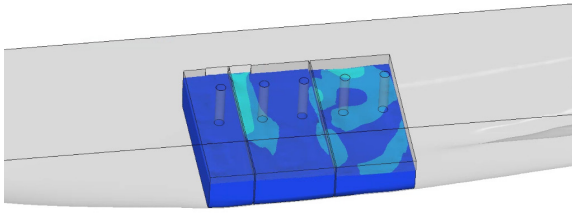
GM_2, t=7.8 s



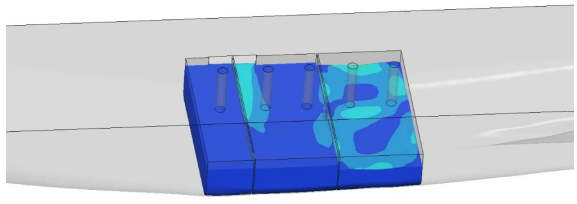
GM_1, t=8.2 s



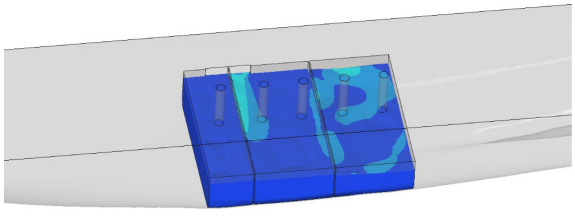
GM_2, t=8.2 s



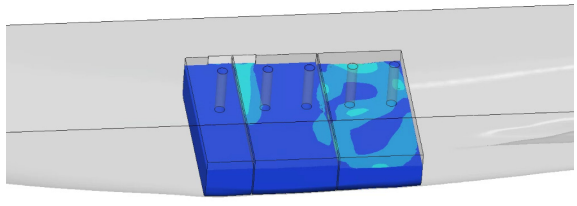
GM_1, t=8.6 s



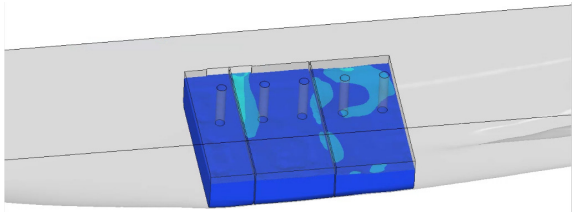
GM_2, t=8.6 s



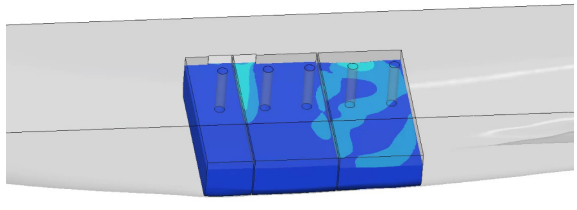
GM_1, t=9.0 s



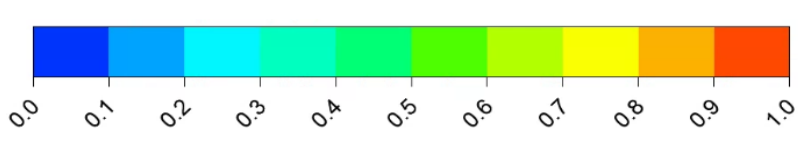
GM_2, t=9.0 s



GM_1, t=9.4 s



GM_2, t=9.4 s



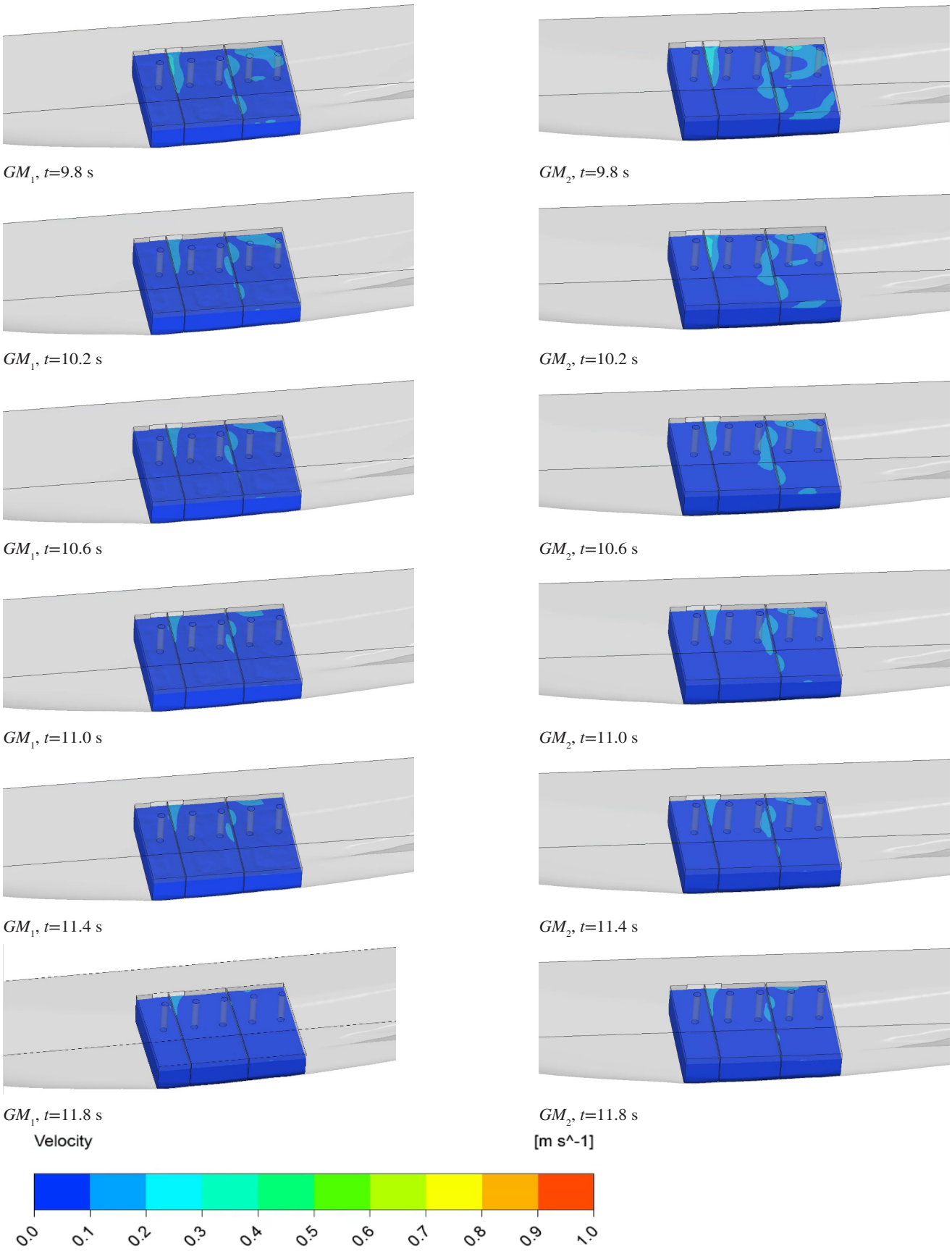
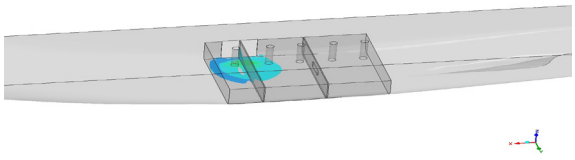
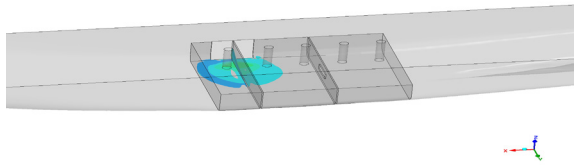


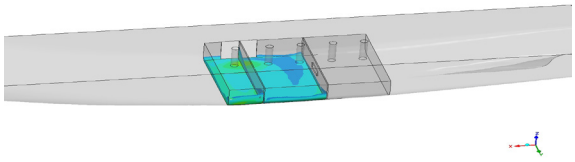
Figure 7. Visuals of the velocity colored flooding process for the initial stability conditions of GM_1 and GM_2



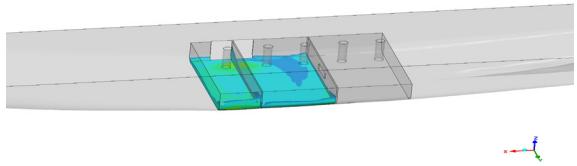
GM_1, t=0.2 s



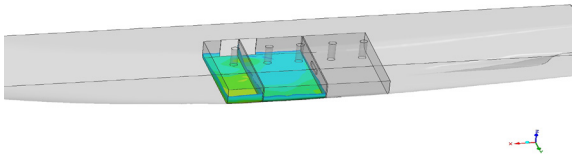
GM_2, t=0.2 s



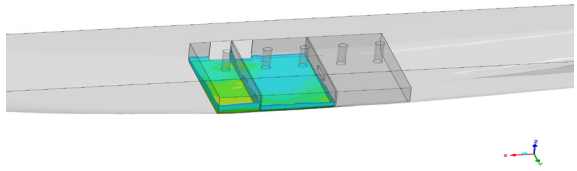
GM_1, t=0.6 s



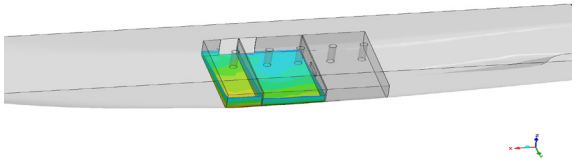
GM_2, t=0.6 s



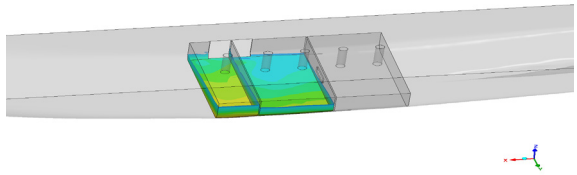
GM_1, t=1.0 s



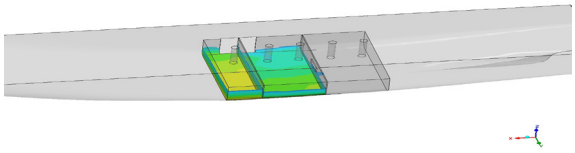
GM_2, t=1.0 s



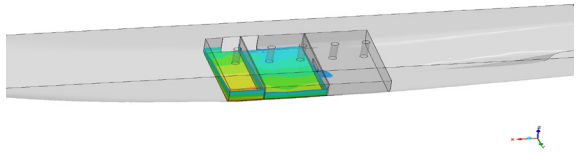
GM_1, t=1.4 s



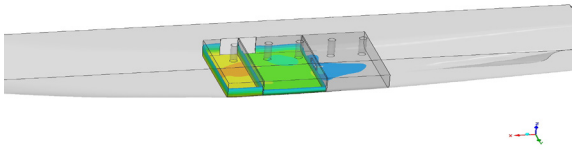
GM_2, t=1.4 s



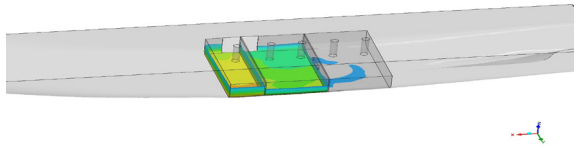
GM_1, t=1.8 s



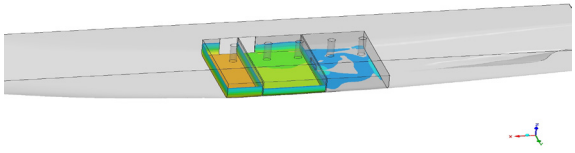
GM_2, t=1.8 s



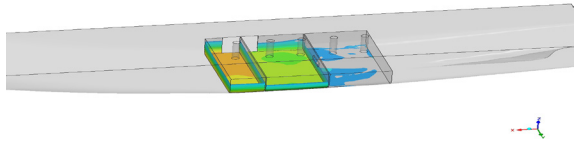
GM_1, t=2.2 s



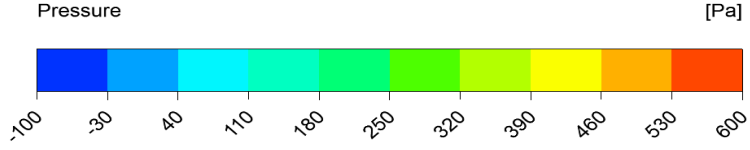
GM_2, t=2.2 s

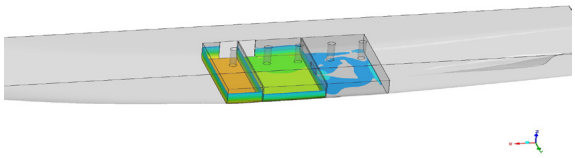


GM_1, t=2.6 s

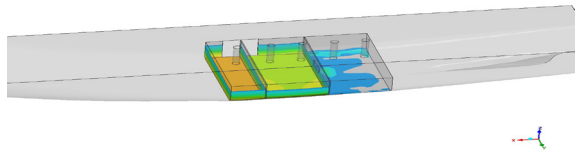


GM_2, t=2.6 s

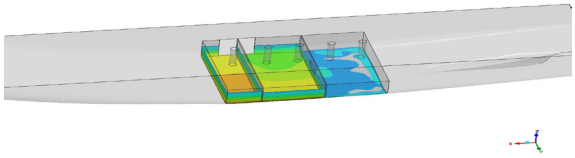




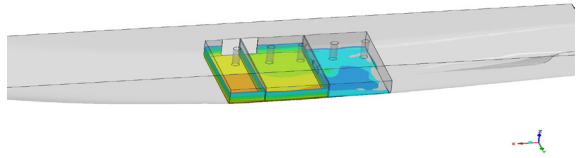
GM_1, t=2.6 s



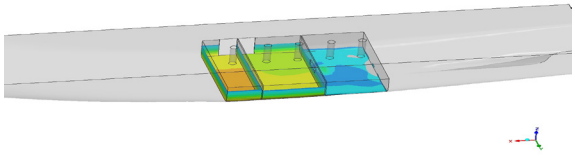
GM_2, t=2.6 s



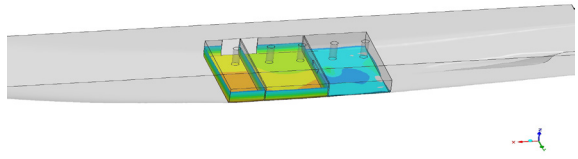
GM_1, t=3.0 s



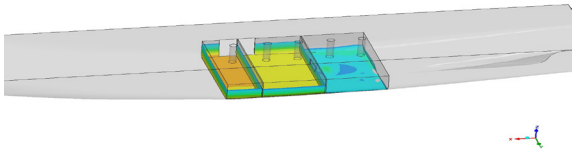
GM_2, t=3.0 s



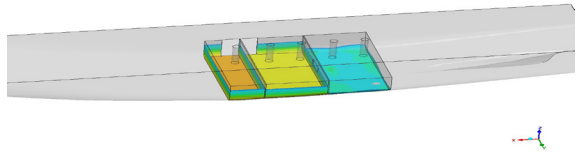
GM_1, t=3.4 s



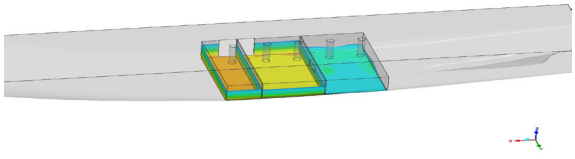
GM_2, t=3.4 s



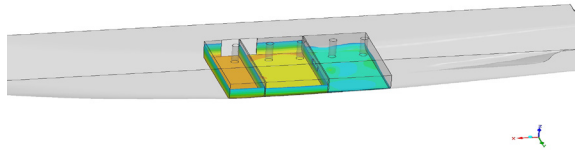
GM_1, t=3.8 s



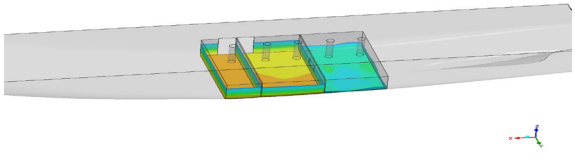
GM_2, t=3.8 s



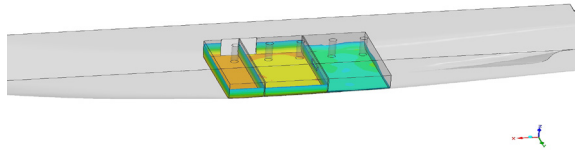
GM_1, t=4.2 s



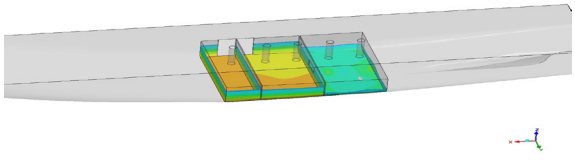
GM_2, t=4.2 s



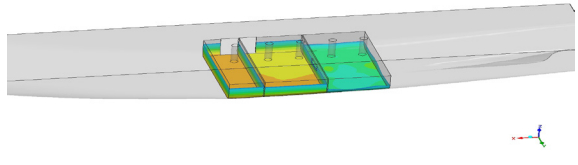
GM_1, t=4.6 s



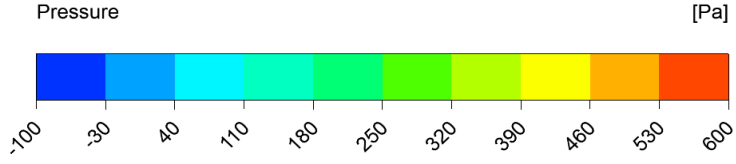
GM_2, t=4.6 s

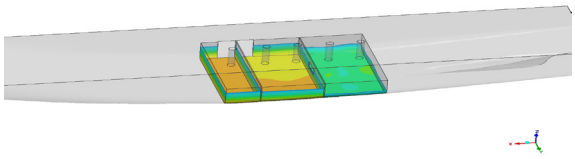


GM_1, t=5.0 s

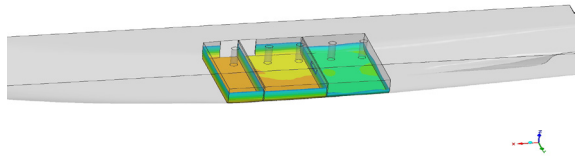


GM_2, t=5.0s

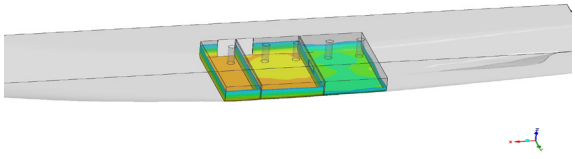




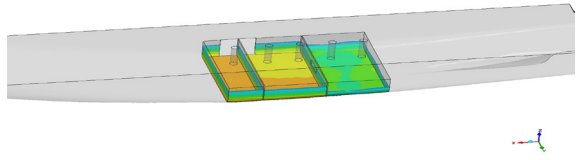
GM_1, t=5.4 s



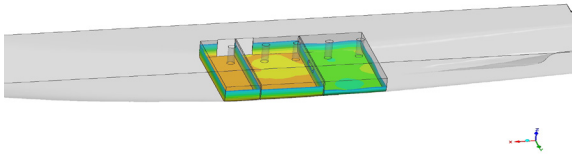
GM_2, t=5.4 s



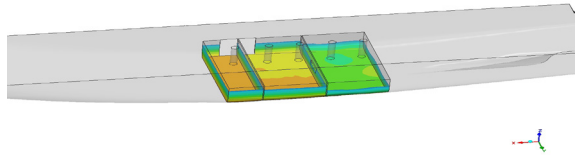
GM_1, t=5.8 s



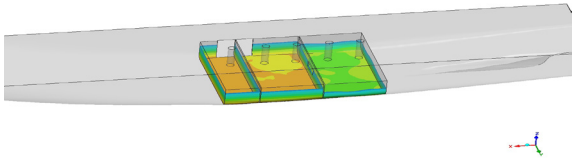
GM_2, t=5.8 s



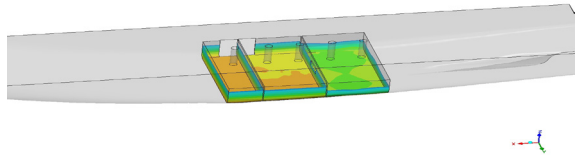
GM_1, t=6.2 s



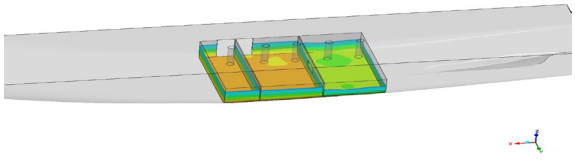
GM_2, t=6.2 s



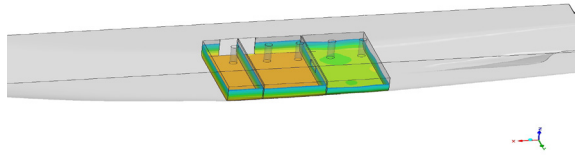
GM_1, t=6.6 s



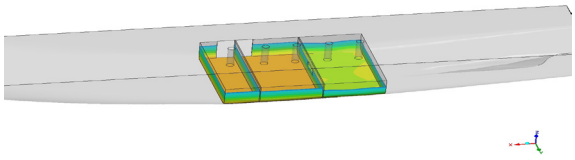
GM_2, t=6.6 s



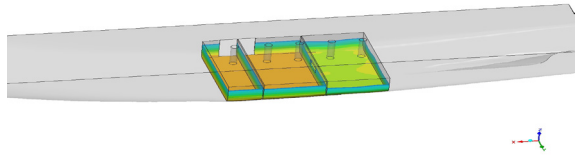
GM_1, t=7.0 s



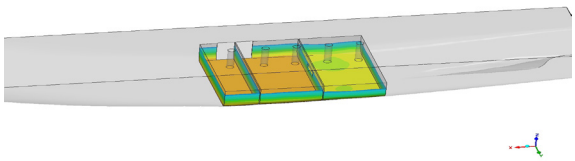
GM_2, t=7.0 s



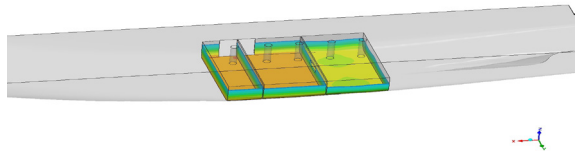
GM_1, t=7.4 s



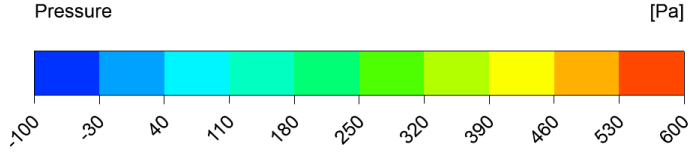
GM_2, t=7.4s



GM_1, t=7.8 s



GM_2, t=7.8 s



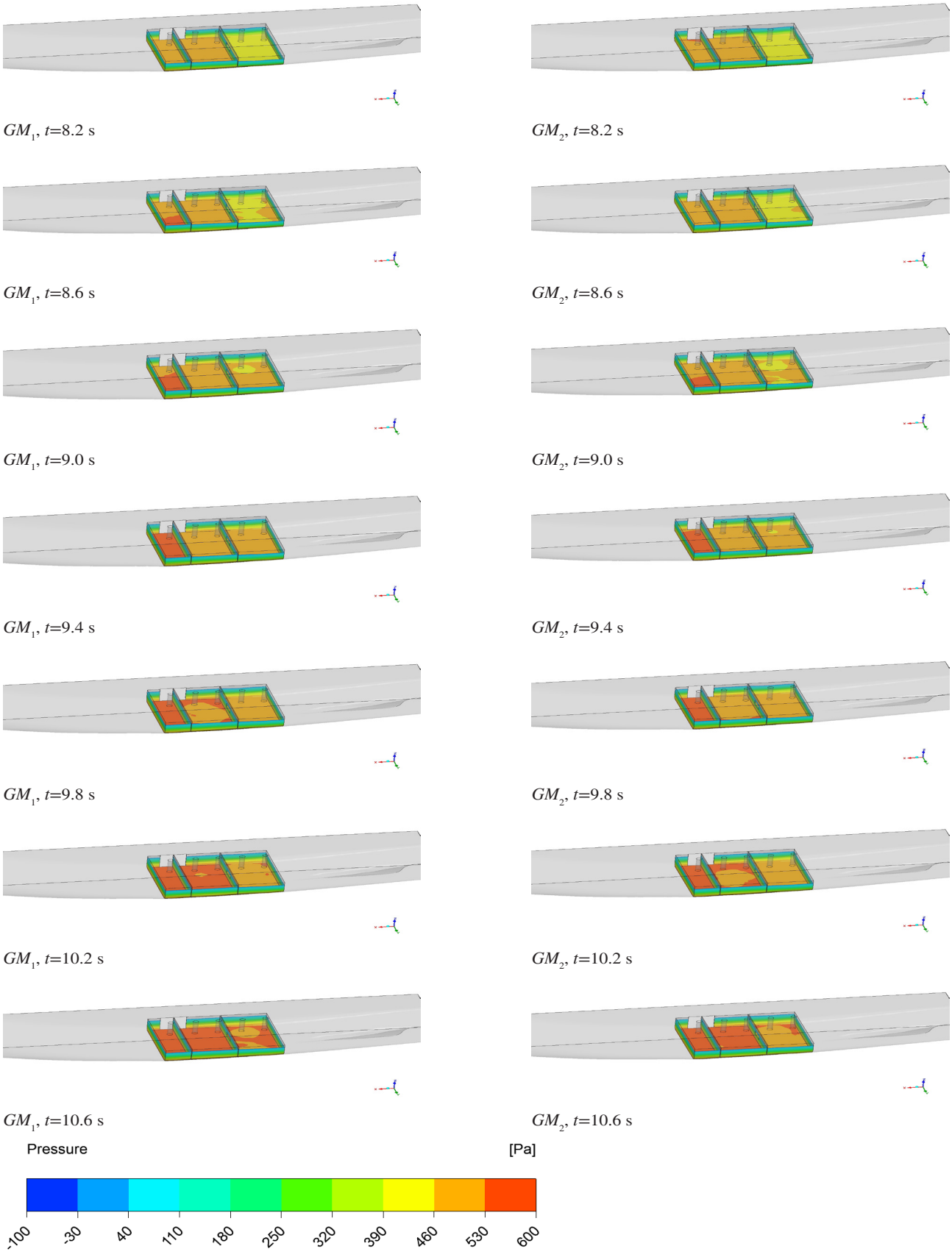


Figure 8. Visuals of pressure distributions on the walls of the damaged compartments caused by floodwater, under the initial stability conditions GM_1 and GM_2

4. Conclusion

This study investigated the influence of initial *GM* on the flooding behavior and motion response of a damaged Ro-Pax ship using RANS-based CFD analysis. The results show that differences in initial *GM* (GM_1 and GM_2) have a limited effect on the rate of water ingress. Both configurations reached similar floodwater masses, stabilizing at approximately 3.6 kg after 10 seconds, indicating that the flooding dynamics remained largely unaffected by *GM* variations within the observed period. In contrast, *GM* had a more pronounced impact on the vessel's motion response. Although both GM_1 and GM_2 configurations exhibited effective roll damping and ultimately converged to minimal roll angles, GM_1 showed reduced maximum roll amplitudes during the early stages of flooding. This behavior is associated with improved resistance to roll excitations induced by internal fluid motion, which is relevant for maintaining cargo security and dynamic stability. The effects of *GM* on pitch and heave motions were negligible, whereas yaw motion was more pronounced and less damped under lower stability conditions (GM_2). These findings highlight the relevance of selecting an appropriate *GM* in the damaged condition. Increasing *GM* can reduce roll and yaw motions during flooding, thereby lowering the risk of cargo displacement and subsequent instability. However, *GM* selection should also account for operational and comfort considerations, as excessive stability may lead to undesirable motion characteristics under normal operating conditions. Balancing these factors is essential to maintain both intact and damaged stability performance for Ro-Pax vessels.

Footnotes

Authorship Contributions

Concept: M. Z. Şener, H. K. Yoon, E. Köse, T. T. D. Nguyen, and A. CHO, Design: M. Z. Şener, H. K. Yoon, E. Köse, T. T. D. Nguyen, and A. CHO, Data Collection or Processing: M. Z. Şener, and T. T. D. Nguyen, Analysis or Interpretation: M. Z. Şener, and T. T. D. Nguyen, Literature Review: M. Z. Şener, H. K. Yoon, and E. Köse, Writing: M. Z. Şener, H. K. Yoon, E. Köse, T. T. D. Nguyen, and A. CHO.

Conflict of Interest: No conflict of interest was declared by the authors.

Financial Disclosure: The Scientific and Technological Research Council of Türkiye (TÜBİTAK) for the 2214-A International Doctoral Research Fellowship Programme for the first author, the Ship Dynamics and Control Laboratory of Changwon National University, and Karadeniz Technical University are all acknowledged for their support to make this work possible. This work was supported by the National Research Foundation of Korea (NRF) grant funded by the Korea government (MSIT) (NRF-2022R1A2C1093055).

5. References

[1] H. Cheng, A. M. Zhang, and F. R. Ming, "Study on coupled dynamics of ship and flooding water based on experimental and SPH methods," *Physics of Fluids,* vol. 29, no. 10, 107101, Oct 2017.

[2] X. Y. Cao, L. Tao, A.-M. Zhang, and F. R. Ming, "Smoothed particle hydrodynamics (SPH) model for coupled analysis of a damaged ship with internal sloshing in beam seas," *Physics of Fluids,* vol. 31, no. 3, 032103, Mar 2019.

[3] L.-F. Hu, H. Qi, Y. Li, W. Li, and S. Chen, "The CFD method-based research on damaged ship's flooding process in time-domain," *Polish Maritime Research,* vol. 26, no. 1, pp. 72-81, Mar 2019.

[4] J. Wang and D. Wan, "Application progress of computational fluid dynamic techniques for complex viscous flows in ship and ocean engineering," *Journal of Marine Science and Application,* vol. 19, pp. 1-16, Jun 2020.

[5] M. Xu, et al. "Advances in the application of intelligent algorithms to the optimization and control of hydrodynamic noise: Improve energy efficiency and system optimization," *Applied Sciences,* vol. 15, no. 4, pp. 2084, Feb 2025.

[6] Çakıcı, F., Kahramanoğlu E., Duman S., and Alkan, A. D. (2021) "Computational prediction of hydrodynamic coefficients for heave motion," *Seatific Journal*: Vol. 1: Iss. 1, Article 2.

[7] C. L. Navier, "Mémoire sur les lois du mouvement des fluides," *Mémoires de l'Académie Royale des Sciences de l'Institut de France,* pp. 389-440, 1823.

[8] G. G. Stokes, "On the theories of the internal friction of fluids in motion and of the equilibrium and motion of elastic solids," *Trans. Cambridge Philos. Soc.,* vol. 8, pp. 287-319, 1845.

[9] R. Osborne, "On the dynamical theory of incompressible viscous fluids and the determination of the criterion," *Philos. Trans. R. Soc. Lond.,* vol. 186, pp. 123-164, 1895.

[10] J. Boussinesq, "Essai sur la théorie des eaux courantes," *Mém. Présentés Divers Savants Acad. Sci.,* vol. 23, no. 1, pp. 1-680, 1877.

[11] A. Busemann, "Ludwig Prandtl, 1875-1953," *Biogr. Mem. Fellows R. Soc.,* vol. 5, pp. 193-205, Feb 1960.

[12] ANSYS, Inc., Ansys Fluent Theory Guide: Shear-Stress Transport (SST) k-ω Models. Canonsburg, PA: ANSYS, Inc., 2009.

[13] P. Ruponen, et al. "Results of an international benchmark study on numerical simulation of flooding and motions of a damaged ropax ship," *Applied Ocean Research*, vol. 123, 103153, Jun 2022.

[14] Meyer Turku Shipyard, "Meyer Turku Shipyard," Accessed: Jul 17, 2025. [Online]. Available: https://www.meyerturku.fi/en/index.jsp

[15] International Maritime Organization, SOLAS: Consolidated Edition, 2020. London, U.K.: International Maritime Organization, 2020.

[16] ITTC, Model Tests on Damage Stability in Waves, 7.5-02-07-04.2, ITTC Quality System Manual, Recommended Procedures and Guidelines, 2017.